Open Access Dissertations

Theses and Dissertations

Spring 2015

Laboratory studies on the production of alpha-pinene-derived organic nitrates and their atmospheric fate

Joel David Rindelaub
Purdue University

PURDUE UNIVERSITY
GRADUATE SCHOOL
Thesis/Dissertation Acceptance

This is to certify that the thesis/dissertation prepared

By Joel David Rindelaub

Entitled LABORATORY STUDIES ON THE PRODUCTION OF ALPHA-PINENE-DERIVED ORGANIC NITRATES AND THEIR ATMOSPHERIC FATE

For the degree of   Doctor of Philosophy

Is approved by the final examining committee:

Paul B. Shepson

Garth J. Simpson

David R. McMillin

Peter T. Kissinger

To the best of my knowledge and as understood by the student in the Thesis/Dissertation Agreement, Publication Delay, and Certification/Disclaimer (Graduate School Form 32), this thesis/dissertation adheres to the provisions of Purdue University's "Policy on Integrity in Research" and the use of copyrighted material.

Paul B. Shepson

Approved by Major Professor(s): _____

_____

Approved by: R. E. Wild   04/17/2015

Head of the Department Graduate Program   Date

LABORATORY STUDIES ON THE PRODUCTION OF ALPHA-PINENE-DERIVED

ORGANIC NITRATES AND THEIR ATMOSPHERIC FATE

A Dissertation

Submitted to the Faculty

of

Purdue University

by

Joel David Rindelaub

In Partial Fulfillment of the

Requirements of the Degree

of

Doctor of Philosophy

May 2015

Purdue University

West Lafayette, Indiana

To my parents, George and Mary Ann Rindelaub, for their continuous love and support.

ACKNOWLEDGMENTS

TABLE OF CONTENTS

LIST OF TABLES

LIST OF FIGURES

Figure   Page

Figure   Page

ABSTRACT

Rindelaub, Joel David. Ph.D., Purdue University, May 2015. Laboratory Studies on the Production of Alpha-Pinene-Derived Organic Nitrates and Their Atmospheric Fate. Major Professor: Paul B. Shepson.

Currently, the formation yields of organic nitrates from the oxidation of biogenic volatile organic compounds, such as α-pinene, is highly uncertain, negatively impacting our knowledge on tropospheric ozone production and the fate of atmospheric NO_x. To lower this uncertainty, we quantified the organic nitrate yield from the OH radical oxidation of α-pinene under high NO_x conditions. The α-pinene-derived nitrates created in chamber experiments readily partitioned to the aerosol phase and underwent particle phase hydrolysis, indicating that these processes are likely a sink for atmospheric NO_x. The hydrolysis of organic nitrates was found to be specific acid-catalyzed and proceeded via unimolecular mechanisms under acidic conditions. The hydrolysis lifetime of a synthesized α-pinene nitrate standard was well within the lifetime of an atmospheric particle. Previously unreported α-pinene oxidation products from chamber studies were identified using mass spectrometry, and, for the first time, individual α-pinene-derived nitrates were identified in a complex mixture. In addition, paper spray ionization was adapted for the direct detection of organosulfates from filter samples and a Raman technique was developed to directly measure the pH of single aerosol particles, for the first time.

CHAPTER ONE: INTRODUCTION

1.1 The Evolution of Earth's Atmosphere

Earth's solar system was created roughly 4.6 billion years ago from a

gravitational collapse of an unstable molecular cloud left over from previous solar

supernovae, mainly comprised of hydrogen and helium (Taylor, 2001). Along with this

gravitational collapse to form the current Sun, a protoplanetary disk emerged, believed to

be responsible for the current solar system's planar and elliptical shape. Photographs

from Atacama Large Millimeter/submillimeter Array (ALMA), released in 2014, give a

snapshot of a similar event from the Taurus Molecular Cloud (Fig. 1.1). The accretion of

dust from such a protoplanetary disk would eventually form the early earth. However, the

large amount of heat in the early inner solar system, coupled with earth's undeveloped

magnetosphere needed to shield solar wind, led to high velocities of volatile compounds

in the early atmosphere (Walker, 1982) and compounds such as water, methane, and

ammonia were able to reach earth's escape velocity, v_e, and "break free" (Eq. 1.1):

$$v_e = \left(\frac{G\,M}{r} \right)^{1/2}$$

(1.1)

where G is the gravitational constant, M is the planetary mass, and r is the radius from the

center of the earth to the point where the escape velocity is calculated. Current ice-giant

planets in the outer solar system, such as Uranus and Neptune, were cold enough to allow

for the condensation of such volatiles and were able to grow to the large sizes currently observed. As the mass of these planets grew, the atmospheric escape velocity also increased (Eq. 1.1), contributing the retention of small molecules like H_2 and He. Thus, unlike earth, the atmospheric composition of the gas giant planets are largely unchanged from their original formation, due to their large size and low temperatures, and represent the primordial material of the solar system (Denlinger, 2005).
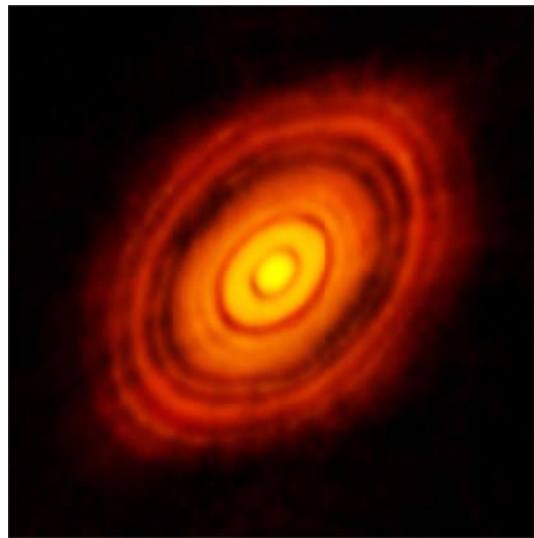
Figure 1.1. The protoplanetary disk of the young star HL Tauri in the Taurus Constellation. This image was taken by the Atacama Large Millimeter/submillimeter Array in Northern Chile (http://www.almaobservatory.org/en/press-room/press-releases/771-revolutionary-alma-image-reveals-planetary-genesis).

After most of the earth's mass had been accrued from hot planetesimal accretions, the beginning of earth's current atmospheric composition started to evolve, taking place around 4.0 billion years ago. During this period, volcanism expelled large amounts of water, carbon dioxide, and nitrogen into the atmosphere (Martin, 2007). Additionally, contributions from asteroid impact from the Late Heavy Bombardment (LHB) also likely

played a role in the accretion of volatiles to the earth's crust and atmosphere (Shaw, 2008). The contribution to present day water on earth from cometary impact may not have been significant, as indicated by very high deuterium/hydrogen ratios detected in water from Comet 67P in 2014 (Altwegg et al., 2015). The oldest known rock sediments on earth, some of which are water-related, have a cut off at 3.8 billion years old, the same age as lunar samples, which indicates that asteroid impact from the LHB may also have had an impact on the earth's current water composition (Shaw, 2008).

The earth's atmosphere did not contain molecular oxygen until roughly 3.0 billion years ago (Lyons et al., 2014). Before life existed on earth, molecular oxygen was first produced via reaction of O + OH --> O_2 + H, originating from the photolysis of water and carbon dioxide (Wayne, 1992; Eq. 1.2-1.4). Once photosynthetic life emerged in the planet's oceans, CO_2 and H_2O were converted into biologically relevant compounds and molecular oxygen (O_2).

$$H_2O \; + \; h\nu \, (\lambda{<}240nm) \; \rightarrow \; OH \; + \;\; H \tag{1.2}$$

$$CO_2 \; + \; h\nu \, (\lambda{<}175nm) \; \rightarrow \; CO \; + \; O \tag{1.3}$$

$$O \;\; + \;\;\;\; OH \;\;\;\;\;\; \rightarrow \; O_2 \; + \; H \tag{1.4}$$

The production of oxygen from oceanic photosynthetic life did not immediately lead to a sharp increase in atmospheric oxygen concentrations, according to analysis of sediment records (Catling, 2005). Large concentrations of ferrous iron within the oceans reacted with the newly produced oxygen to form ferric oxides, which sank to the bottom of the ocean and are found in "banded iron formations", aging at least 2.0 billion years

old (Cairns-Smith, 1978). Once the ocean's ferrous iron was depleted, molecular oxygen reacted with reduced terrestrial minerals to form oxidized sediments, such as "red beds" from the oxidation of pyrite (FeS_2), which date up to 2.0 billion years old (Canfield, 2005). Only once the oceanic and terrestrial reservoirs were depleted did atmospheric oxygen begin to rapidly increase in the atmosphere, roughly 0.5 billion years ago (Lyons et al., 2014).

The increased abundance of O_2 and decrease of CO_2 in the atmosphere had a large impact on the evolution of life on the planet earth. The irradiance of short wavelength UV light from the sun photolyzed oxygen to create ozone (Eq. 1.5-1.6).

$$O_2 + h\nu \ (\lambda<240nm) \rightarrow 2\ O(^3P) \tag{1.5}$$

$$O_2 + \quad O(^3P) \quad \rightarrow \quad O_3 \tag{1.6}$$

Earth's development of the stratospheric ozone layer was essential in the expansion of life to land because ozone absorbs harmful short wavelength radiation that damages biologically relevant molecules, such as deoxyribonucleic acid (DNA; Wayne, 1992). The rise of oxygen was also essential for the evolution of aerobic life and the progression of eukaryotic species. The oldest known terrestrial plant fossils are ~460 million years old (Rubinstein et al., 2010) and the oldest animal fossil is ~350 million years old (Gess, 2013), both of which occur shortly after the oxygen concentration in the earth's atmosphere is believed to level off, 0.5 billion years ago (Catling, 2005). This event allowed for complex plant and animal life to flourish.

1.2 Major Gas Phase Constituents of Current Atmosphere

Since oxygen levels stabilized roughly 500 million years ago, the main chemical

composition of the dry atmosphere has remained similar to today's structure (see Table

1.1 below). Molecular nitrogen is very stable and thus is the most abundant molecule in

the atmosphere by volume at 78%. It is also believed that denitrification of organic

material by soil microbes has contributed to present day nitrogen levels in the atmosphere

(Jacobson, 2000). Molecular oxygen is the second most abundant molecule at 21% while

the noble gas argon contributes 0.93% of the current atmosphere. The remaining trace

gases include CO_2, Ne, He, and CH_4. Water vapor can vary significantly by location from

less than 1% (e.g. polar regions) to ~5% (e.g. tropical environments), with a global

average of about 0.5%. Most of the earth's atmosphere, 80% by mass, resides in the

troposphere, the atmosphere's lowest layer, which ranges from the surface to

approximately 17 km. Thus, the chemistry described within this thesis will focus on this

important layer of the atmosphere.

Table 1.1. The major constituents of Earth's present day dry atmosphere. Taken from http://nssdc.gsfc.nasa.gov/planetary/factsheet/earthfact.html.

Compound	% by vol.
Nitrogen	78.1
Oxygen	20.9
Argon	0.934
Carbon Dioxide	0.0397
Neon	0.00182
Helium	0.000524
Methane	0.000179

1.3 Tropospheric Components

1.3.1 Greenhouse Gases

Despite relatively low concentrations atmospherically, trace gases can have a strong influence on earth's climate and biosphere. Greenhouse gases such as H_2O, CO_2, and CH_4 have strong absorption in the infrared region, trapping outgoing long wave surface radiation and warming the atmosphere to an average global surface temperature 33^oC above what would be expected for earth's surface given its solar irradiance (IPCC, 2007). The greenhouse effect on earth allows for liquid water to exist and, thus, is essential for life to flourish. Recent greenhouse gas contributions to the atmosphere from anthropogenic sources have led to an increase in global surface temperatures at a rate significantly faster than previous climate variations unrelated to catastrophic events (IPCC, 2013). As seen in Fig. 1.2, where the yellow scheme indicates incoming short wave radiation and the red scheme indicates outgoing long wave radiation, greenhouse gases, clouds, and aerosol are responsible for capturing 86% of outgoing surface radiation (Wild et al., 2013), and thus are majors contributor to the current imbalance in the earth's radiative budget at the top of the atmosphere, $0.5\text{-}1.0$ W m^{-2} (Trenberth et al., 2014).
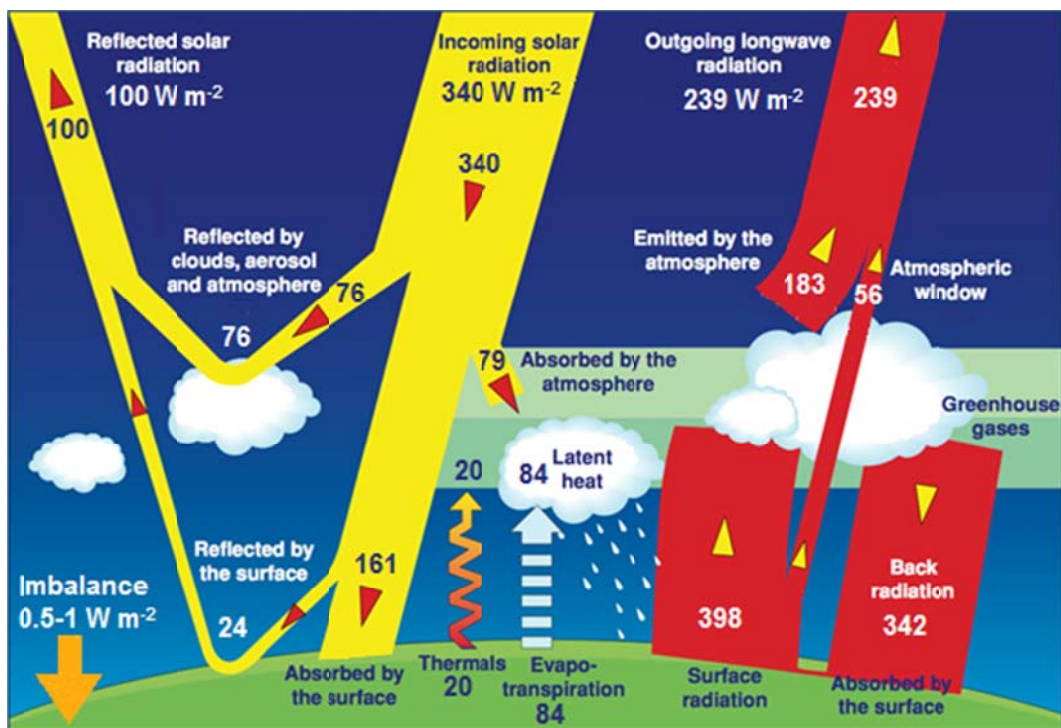
Figure 1.2. The global radiation budget of the earth including incoming solar radiation and outgoing terrestrial radiation. The figure is adapted from Kiehl and Trenberth (1997) using updated data from Wild et al. (2014) and Trenberth et al. (2014).

The contribution of each greenhouse gas to total radiative forcing is shown in Fig. 1.3, with CO_2 having the greatest impact relative to pre-industrial conditions (1.68 W m^{-2}) at "very high" (90%) certainty (IPCC, 2013).

Emitted compound	Resulting atmospheric drivers	Radiative forcing by emissions and drivers	Level of confidence

Well-mixed greenhouse gases / Anthropogenic:

- CO_2 — CO_2 — 1.68 [1.33 to 2.03] — VH
- CH_4 — CO_2 H_2O^{str} O_3 CH_4 — 0.97 [0.74 to 1.20] — H
- Halo-carbons — O_3 CFCs HCFCs — 0.18 [0.01 to 0.35] — H
- N_2O — N_2O — 0.17 [0.13 to 0.21] — VH

Short lived gases and aerosols / Anthropogenic:

- CO — CO_2 CH_4 O_3 — 0.23 [0.16 to 0.30] — M
- NMVOC — CO_2 CH_4 O_3 — 0.10 [0.05 to 0.15] — M
- NO_x — Nitrate CH_4 O_3 — -0.15 [-0.34 to 0.03] — M
- Aerosols and precursors (Mineral dust, SO_2, NH_3, Organic carbon and Black carbon) — Mineral dust Sulphate Nitrate Organic carbon Black carbon — -0.27 [-0.77 to 0.23] — H
- Cloud adjustments due to aerosols — -0.55 [-1.33 to -0.06] — L
- Albedo change due to land use — -0.15 [-0.25 to -0.05] — M

Natural:

- Changes in solar irradiance — 0.05 [0.00 to 0.10] — M

Total anthropogenic RF relative to 1750:

- 2011 — 2.29 [1.13 to 3.33] — H
- 1980 — 1.25 [0.64 to 1.86] — H
- 1950 — 0.57 [0.29 to 0.85] — M

Radiative forcing relative to 1750 (W m^{-2})

Figure 1.3. The 2011 estimates for radiative forcing (RF) relative to the pre-industrial era (1750 A.D.) for both gas and particle phase anthropogenic emissions. The confidence level scale is as follows: VL-very low, L-low, M-medium, H-high, VH-very high (IPCC, 2013).

1.3.2 Particulate Matter

1.3.2.1 Climate Forcing

Earth's radiative budget is also affected by particulate matter, which can be created by the condensation of low-volatility products derived from trace gas oxidation or from primary sources of both natural (e.g. mineral dust, sea spray, volcanos) and

anthropogenic origin (e.g. combustion) (IPCC, 2013). Suspended particulate matter, known as aerosols, can directly scatter radiation as well as seed cloud formation, which can also interact with solar radiation (see Fig. 1.2). Each cloud droplet is generated by the condensation of water vapor onto an aerosol particle. The reflection of incoming solar radiation back to space will have a net cooling effect on the planet while the absorption of outgoing terrestrial infrared radiation will have a warming effect (Fig. 1.2).

Different types of aerosol will have different impacts on earth's radiative budget. Inorganic particles, such as mineral dust, can lead to cloud formation and have a net cooling effect on the planet by reflecting incoming solar radiation while black carbon, emitted from combustion sources, will readily absorb radiation and have a warming effect (IPCC, 2013). Organic carbon emissions can act as aerosol precursors via atmospheric oxidation and conversion to SOA, and, like inorganic particles, also have a negative climate forcing effect (Fig. 1.3). Overall, the net impact of aerosols on climate is believed to be a cooling one, however, as seen from the error bars in Fig. 1.3, the overall impact still has a high degree of uncertainty at this time (IPCC, 2013).

1.3.2.2 Health Impacts

In addition to impacts on climate and visibility (Fig. 1.4), aerosol particles can also lead to serious health effects such as respiratory illness, cardiovascular disease, lung cancer, and premature death (EPA, 2010). Especially harmful is the inhalation of particulate matter in the fine ($<2\mu$m diameter) and ultrafine (<10 nm diameter) range that are small enough to bypass filtering from the nose cilia and throat mucus to lodge deep into the lungs and enter the bloodstream by diffusion through the aveoli (Araujo et al.,

2008). A recent study by Raaschou-Nielsen et al. (2013) showed that exposure to particulate matter less than 2.5 μm in diameter resulted in a 36% increase in lung cancer rate for every 10 μg cm^{-3} in aerosol emission. The US estimates that particulate matter less than 2.5 μm in diameter accounts for 39,000 to 130,000 premature deaths annually (EPA, 2010). Another prominent example of aerosol pollution occurs in present day Beijing during the winter (Fig. 1.4) when combustion processes, such as burning coal, produce excessively high aerosol concentrations, up to 75 times greater than the Environmental Protection Agency (EPA) standard (15 μg cm^{-3}). These high aerosol loadings, comprised mostly of organic material, SO_4^{2-}, NO_3^- and NH_4^+ (Sun et al., 2014), leads to a peak in respiratory-related illnesses and deaths (Li et al., 2013).

Figure 1.4. A photograph of Beijing, China during a particulate matter "smog" event in the winter of 2013 is shown on the right while normal ambient conditions are shown on the left. (Photo by: Bobak Ha'Eri/Creative Commons 2.5; http://news.mongabay.com/2013/0819-hance-china-air-pollution.html)

1.3.2.3 Aerosol Characterization

The particulate matter created from the condensation of atmospheric oxidation products is known as secondary aerosol while particles directly emitted from sources are primary aerosol. One method used to differentiate between primary and secondary aerosol is to measure the size of the particles, due to the proclivity of primary aerosols to have large diameters in the coarse mode (> 2μm; Fig. 1.5). This measurement is most often accomplished using a scanning mobility particle sizer (SMPS; see Chapter 2). The size distributions of ambient aerosols are shown in Fig. 1.5, displaying the modes for both fine (< 2μm) and coarse (> 2μm) particles. Coarse mode particles are primarily produced by mechanical processes such as grinding (e.g. construction) and wind-induced erosion, and, due to their large size, will be rapidly removed from the atmosphere via gravitational settling (Finlayson-Pitts and Pitts, 1999).
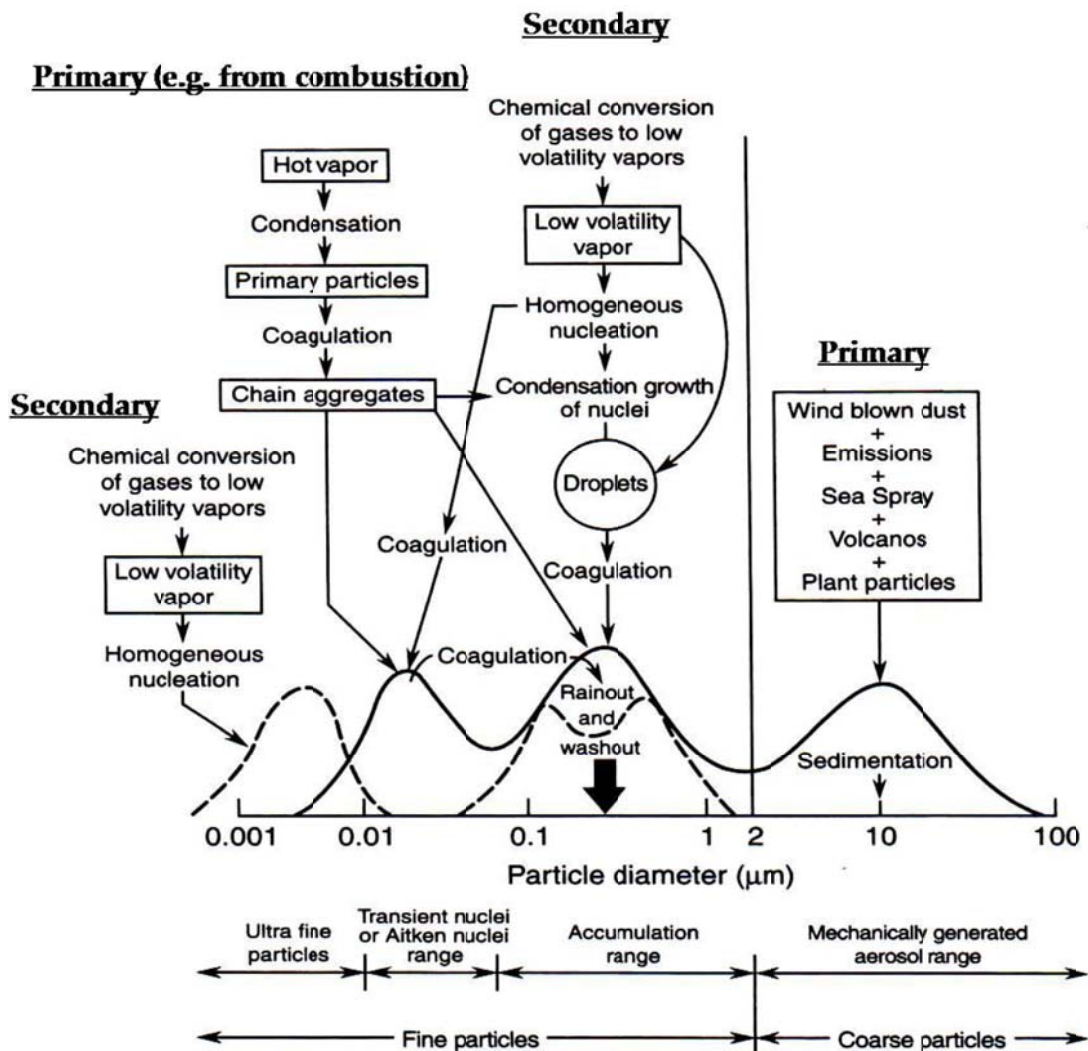
Figure 1.5. The size distributions and aging processes of primary and secondary aerosol particles in the ambient atmosphere (Finlayson-Pitts and Pitts, 1999).

The distribution of fine particles has three distinct modes: ultrafine (< 10nm), Aitken mode (10-100nm), and accumulation range (100-2000nm). Ultrafine particles are created through homogeneous nucleation of low-volatility vapor and can grow through continued condensation of vapors as well as coagulation with other fine particles to reach the Aitken mode size. Continued growth of Aitken mode particles happens quickly,

leading to accumulation size particles, which are more likely to uptake water and act as

cloud condensation nuclei (CCN) due to the reduced surface tension effects at the particle

surface (Köhler, 1936). Salt aerosol, which acts as a dissolved solute on the particle

surface, also contributes to the ability of accumulation mode particles to act as CCN by

lowering the vapor pressures of water at the surface (Ueno, 1976). Accumulation mode

particles will have longer diffusion times and comparatively longer atmospheric lifetimes

compared to other fine mode particles and, due to their increased ability to form CCN,

will be removed from the atmosphere by both dry and wet deposition.

1.3.2.4 Partitioning of Gas Phase Components

The partitioning of volatile compounds into aerosols has traditionally been

modeled assuming equilibrium between the gas and particle phases (Pankow, 1994). The

degree to which a compound, i, will partition to the particle phase is described by its

partition coefficient (K_p). Experimentally this is determined using Eq. 1.7 and measuring

the mass concentration of total suspended particles (M) along with the concentration of

the target compound, i, in both the gas (A_i) and particle (F_i) phases (Fig. 1.6). A larger

partition coefficient corresponds to a higher concentration of a compound in the particle

phase at equilibrium. Both adsorptive and absorptive partitioning of a compound to the

aerosol particle is dependent on several factors including its vapor pressure, p_L^o, and

temperature, T (Eq. 1.8).

Gas　　Particle　　　　　　Partition Coefficient (K_p)

Experimental:

$$K_{p,i} = \frac{F_i}{A_i\,M} \qquad (1.7)$$

Theoretical:

$$K_{p,i} = \frac{1}{p_L{}^o}\left(\frac{N\,a_{tsp}\,T\,e^{\frac{\Delta H_d - \Delta H_v}{RT}}}{1600} + \frac{f_{om}\,760RT}{MW_{om}\,\zeta_i\,10^6}\right) \qquad (1.8)$$

Adsorptive Term　　　Absorptive Term

$A_i \rightleftharpoons F_i$

M
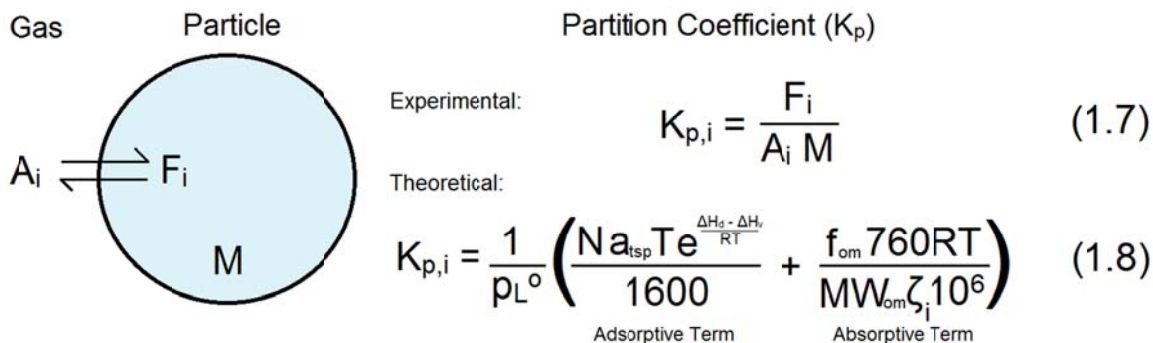
Figure 1.6. The gas-particle equilibrium partitioning model as described by Pankow (1994). Partition coefficients ($K_{p,i}$) are determined experimentally using Eq. 1.7 where F_i is the concentration of compound, i, in the particle phase, A_i is the gas phase concentration, and M is the total aerosol mass concentration. Theoretical determination of the partition coefficient ($K_{p,i}$) is shown in Eq. 1.8 where $p_L{}^o$ is the vapor pressure of compound, i, N is the surface concentration of aerosol sorption sites, a_{tsp} is the surface area concentration, T is the temperature, R is the gas constant, ΔH_d is the enthalpy of desorption, ΔH_v is the enthalpy of vaporization of the aerosol absorbing phase, f_{om} is the weight fraction of total suspended particles that is the absorbing phase, MW_{om} is the mean molecular weight of the absorbing phase, and ζ_i is the activity coefficient of the compound, i.

The partitioning of gas phase compounds into the particle phase may also be dependent on the chemistry within the aerosol. For instance, the amount of SO_2 dissolved in aqueous solution, similar to a cloud droplet, is highly dependent on pH due to its equilibrium with the bisulfite ion (HSO_3^-) in water (Eq. 1.9-1.10; Seinfeld and Pandis, 2006). The effective Henry's law constant of SO_2, which is defined as the ratio of the aqueous phase SO_2 concentration to its equilibrium partial pressure, increases by approximately seven orders of magnitude as solution pH increases from 1 to 8 (Fig. 1.7; Seinfeld and Pandis, 2006), displaying the potentially immense importance that the chemical nature of the particle phase can have on the gas-particle equilibrium of the system.

$$SO_2 \ + \ H_2O \ \rightarrow \ \ SO_2 \cdot H_2O \tag{1.9}$$

$$SO_2 \cdot H_2O \ \ \ \ \rightarrow \ H^+ \ + \ HSO_3^- \tag{1.10}$$
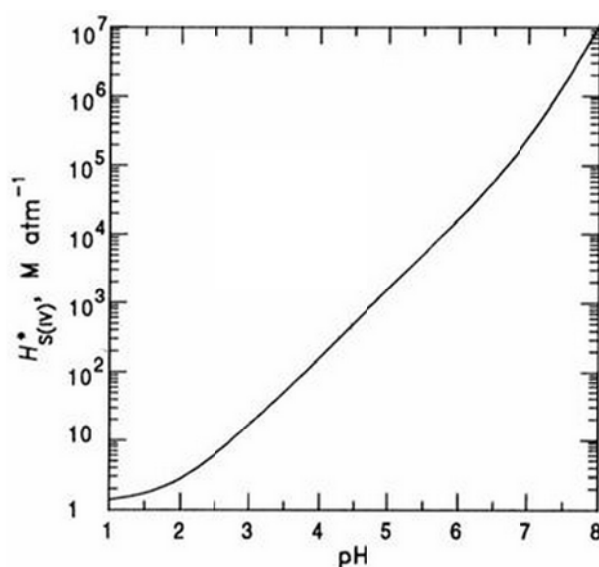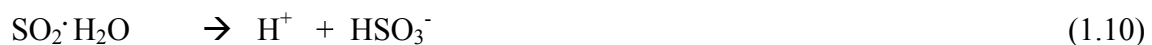
Figure 1.7. The effective Henry's law constant (M atm^{-1}) for SO$_2$ in water as a function of pH (Seinfeld and Pandis, 2006).

Recent research has suggested that non-equilibrium partitioning of organic species may also exist in the gas-particle partitioning system (Perraud et al., 2012). This type of partitioning is suggested to occur at low relative humidity when aerosols can be hard and viscous instead of a homogeneous liquid as assumed in the traditional model (Virtanen, 2010), leading to irreversible partitioning of gas phase compounds into the particle phase, due to the large increase in diffusion times. Evidence for non-ideal mixing of particles, where a liquid-liquid phase separation can divide the aerosol into aqueous and organic layers (You et al., 2013), brings further question into the phase state of

particulate matter and how it affects the partitioning of volatiles to the particle phase (Shiraiwa et al. 2013).

1.3.3 Biogenic Volatile Organic Compounds

Biogenic volatile organic compounds (BVOCs), emitted at ~1100 Tg yr^{-1} (Guenther et al., 2012), are the most important global contributor to the atmospheric non-methane organic carbon budget, accounting for 88% of all non-methane VOCs emitted annually (Goldstein and Galbally, 2007). The BVOC with the highest global emission rate is isoprene, also known as 2-methyl-1,3-butadiene, at ~535 Tg yr^{-1} (Guenther et al., 2012), which is largely released from vegetation (e.g. deciduous forests) during heat stress and as a possible oxidative scavenger (Sharkey and Singsaas, 1995; Loreto et al., 2001). Isoprene (Fig. 1.8) is the simplest of the terpene species, a C_5H_8 building block that is the basis for other BVOCs emissions such as monoterpenes ($C_{10}H_{16}$) and sesquiterpenes ($C_{10}H_{24}$). Due to its high emission rate and two double bonds, it is highly reactive in the atmosphere and has a major impact on the oxidative capacity of the atmosphere (see below; e.g. Starn et al., 1998). Due to its small size and high volatility, its oxidation products do not have as significant of a contribution to aerosol production compared to higher carbon number BVOCs like the monoterpenes (Carlton et al., 2009).
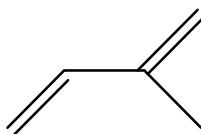
Figure 1.8. The structure of isoprene.

Monoterpenes are emitted at ~157 Tg yr^{-1} (Guenther et al., 2012), mainly as a natural insecticide and a possible oxidative scavenger for conifers (De Moraes et al., 1998; Loreto et al., 2001), and are a C_{10} BVOC that is also important with respect to atmospheric oxidation. Their olefinic nature (from 1-3 double bonds) allows them to quickly react with atmospheric oxidants (see below; e.g. O_3, OH, NO_3) to form low volatility compounds that significantly contribute to secondary organic aerosol (SOA) production (e.g. Cahill et al., 2006). Globally, fine aerosol is dominated by organics (Jimenez et al., 2009), accounting for 20-90% of all particulate mass in the lower troposphere (Kanakidou et al., 2005), and biogenic SOA makes up >59% of all organic aerosol, both primary and secondary (Hallquist et al., 2009). Additionally, the presence of biogenic SOA increases global mean CCN concentrations by up to 21%, which is estimated to contribute to global radiative forcing by -0.07 to -1.55 W m^{-2} from the combined direct scattering and indirect cloud cover effects (Scott et al., 2014).

Due to large variations in connectivity, monoterpenes can have very different atmospheric oxidation rates and contribution to SOA. One compound that has significant reactivity and contribution to aerosol production is α-pinene (Lee et al., 2006). α-Pinene (Fig 1.9) also has the largest emission rate for monoterpenes globally, with annual emissions at ~66 Tg yr^{-1} (Guenther et al., 2012).
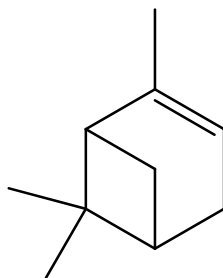
Figure 1.9. The structure of the monoterpene α -pinene.

1.3.4 Atmospheric Oxidants

The earth's atmosphere is very oxidizing and its main oxidizing agents, hydroxyl

(OH) radical, ozone (O_3), and nitrate (NO_3) radical, control the removal of gas phase

compounds, e.g. volatile organic compounds (VOCs), NO_x, SO_2, H_2S, NH_3. Due to rapid

photolysis, the nitrate (NO_3) radical tends to have much larger concentrations at night.

During the day, the hydroxyl (OH) radical is the most important oxidant (see Table 1.2)

due to its ability to both abstract atoms from and oxidize atmospheric compounds, despite

having low tropospheric concentrations on the order of 10^6 molecules cm^{-3} (~0.1 ppt)

(Prinn et al., 1995). The hydroxyl radical is produced from the photolysis of ozone in the

presence of water vapor (Eq. 1.11-1.12).

Table 1.2. The α-pinene rate constants for reaction with O_3, OH and NO_3 radical in cm^3 molecule^{-1} s^{-1} (Atkinson et al., 2003).

k_{O3}	k_{OH}	k_{NO3}
8.11×10^{-17}	5.33×10^{-11}	6.16×10^{-12}

$$O_3 \quad + \quad h\nu \ (300{<}\lambda{<}320nm) \ \rightarrow \ O_2 \quad + \quad O(^1D) \tag{1.11}$$

$$O(^1D) \ + \quad\quad H_2O \quad\quad\quad \rightarrow \quad\quad 2\,OH \tag{1.12}$$
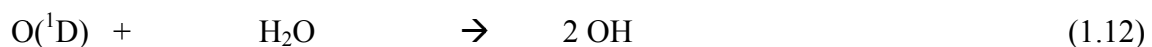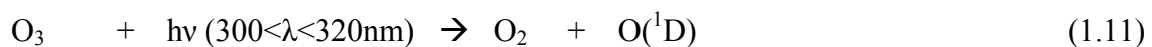
Ozone has the highest atmospheric concentration of the main oxidants, ranging from ~2-8 ppm on average in the stratosphere to 20-45 ppb in the troposphere (Vingarzan, 2004). Stratospheric ozone, at altitudes ranging from ~17 to 50 km (Fig. 1.10), is created from the photolysis of molecular oxygen (see Eq. 1.5-1.6) while tropospheric ozone, which is partially derived from downward transport from the stratosphere, is mainly produced via efficient photolysis of NO_2 at near visible wavelengths (Eq. 1.13-1.14).
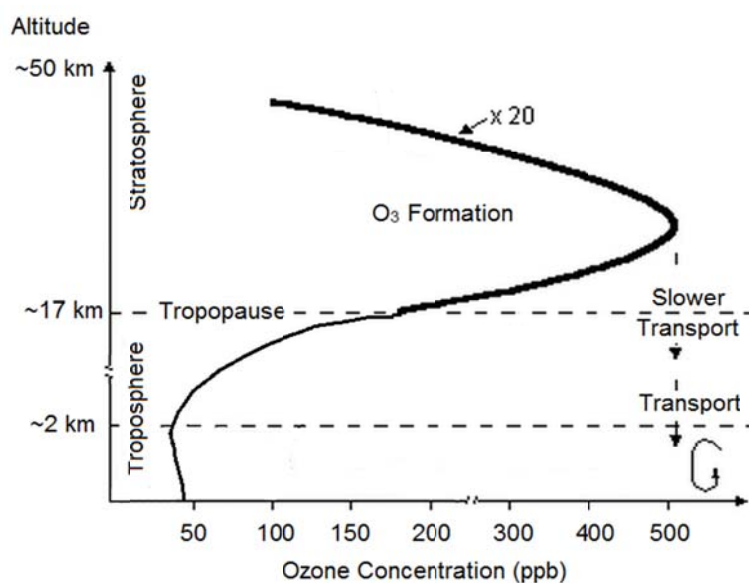
Figure 1.10. The ozone concentration profile as a function of altitude for the stratosphere and troposphere. The figure is adapted from Schurath (1984).

$$NO_2 \quad + \quad h\nu\ (\lambda<420nm) \quad \rightarrow \quad O(^3P) \quad + \quad NO \tag{1.13}$$

$$O(^3P) \quad + \quad O_2\ (+M) \quad \rightarrow \quad O_3 \tag{1.14}$$
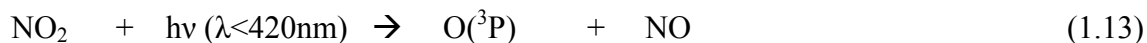
Tropospheric NO_x ($NO + NO_2$) is mainly produced from anthropogenic combustion processes, however, NO_x can also be produced from soil microbes and lightning (Penner et al., 1992). At high heat from lightning and combustion reactions, molecular nitrogen and oxygen are split into the atomic form and further react to form nitric oxide (NO), shown in Eq. 1.15-1.16, which can be further oxidized to form NO_2 and eventually NO_3 in the absence of sunlight (Eq. 1.17-1.18).

$$N \quad + \quad O_2 \rightarrow NO \quad + \quad O \tag{1.15}$$

$$O \quad + \quad N_2 \rightarrow NO \quad + \quad N \tag{1.16}$$

$$NO \quad + \quad O_3 \rightarrow NO_2 \quad + \quad O_2 \tag{1.17}$$

$$NO_2 \quad + \quad O_3 \rightarrow NO_3 \quad + \quad O_2 \tag{1.18}$$

The main production pathway for tropospheric ozone is from the OH initiated oxidation of VOCs under high NO_x conditions. "High NO_x" conditions can vary greatly based on HO_x ($OH + HO_2$) and VOC concentrations (see below), however, high NO_x concentrations are usually considered to be at levels greater than 1-10ppb (Trainer et al., 2000; Thornton et al., 2002). The OH radical can either abstract a hydrogen from the VOC (Eq. 1.19a) or undergo addition in the case of alkenes (Eq. 1.19b). The resulting radical will quickly react with oxygen to produce a peroxy radical (Eq. 1.20).

R-H $\quad\quad$ + $\cdot$OH $\quad$ → $\quad$ R$\cdot$ + H$_2$O $\qquad\qquad\qquad$ (1.19a)

 $\quad$ + $\cdot$OH $\quad\quad$ → $\quad$ $\qquad\qquad$ (1.19b)

R$\cdot$ $\quad\quad\quad$ + O$_2$ (+M) → $\quad$ ROO$\cdot$ $\qquad\qquad\qquad$ (1.20)
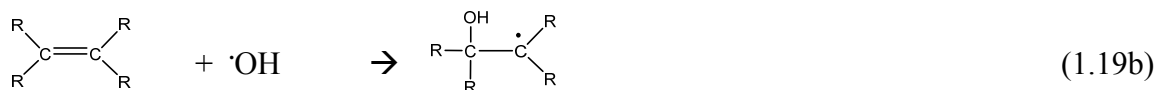
In the presence of nitric oxide (NO), the peroxy radical can react to form organic nitrates in a chain termination step or react to form the alkoxy radical and NO$_2$, an ozone precursor (Eq. 1.13-1.14). The ratio of the rate of organic nitrate (RONO$_2$) formation (Eq. 1.21b) compared to the sum of both ROO + NO reaction pathway rates (Eq. 1.21a,b) is known as the organic nitrate branching ratio, $k_{1.14a}/(k_{1.14a}+k_{1.14b})$.

ROO$\cdot$ + $\quad$ $\cdot$NO $\quad\quad$ → $\quad$ RO$\cdot$ + $\cdot$NO$_2$ $\qquad\qquad\qquad$ (1.21a)

ROO$\cdot$ + $\quad$ $\cdot$NO (+M) → $\quad\quad$ RONO$_2$ $\qquad\qquad\qquad$ (1.21b)
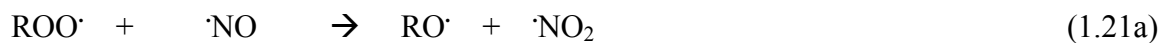
The alkoxy radical (RO) will further react with oxygen to form a carbonyl compound (R=O) and HO$_2$ (Eq. 1.22). HO$_2$ can react with NO to regenerate the OH radical and NO$_2$ (Eq. 1.23). This reaction pathway is catalyzed by the OH radical and, in the absence of any other chemistry, produces two molecules of ozone per cycle via NO$_2$ photolysis (Eq. 1.13-1.14). An example of the cyclic nature of the OH initiated oxidation of the BVOC isoprene under high NO$_x$ conditions is outlined in Fig. 1.11.

RO$\cdot$ + $\quad\quad$ O$_2$ $\quad\quad$ → $\quad\quad$ R=O + HO$_2$$\cdot$ $\qquad\qquad\qquad$ (1.22)

HO$_2$$\cdot$ + $\quad$ $\cdot$NO $\quad\quad$ → $\quad\quad$ $\cdot$OH + $\cdot$NO$_2$ $\qquad\qquad\qquad$ (1.23)
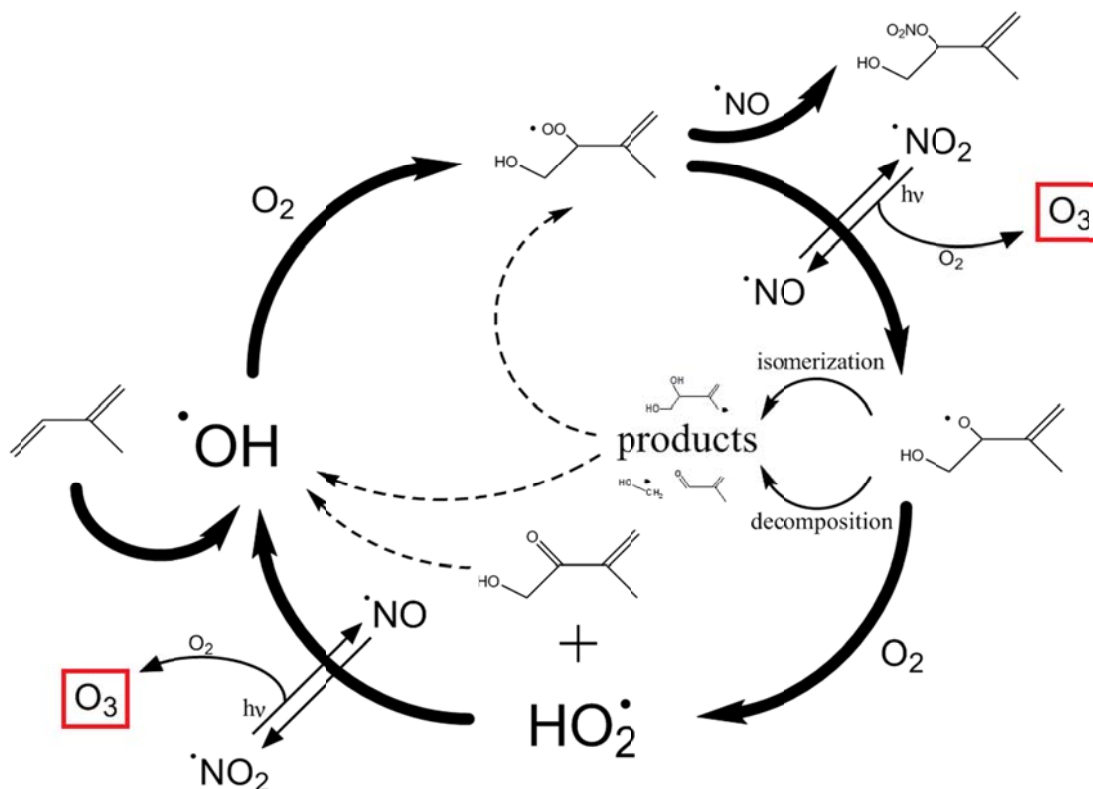
Figure 1.11. The atmospheric OH radical oxidation of the BVOC isoprene under high NO_x conditions. One complete oxidation cycle can produces two molecules of NO_2 (and thus ozone) if the radical termination step involving organic nitrate ($RONO_2$) formation does not occur.

The actual production of ozone from this chemical pathway can vary greatly based on several factors, including the potential reactivity from the isomerization and/or decomposition product(s) of the alkoxyl radical produced from Eq. 1.21a (see Fig. 1.11), the further reactivity of the carbonyl compound (R=O) formed in Eq. 1.22 with the OH radical, and the branching ratio of the $RONO_2$ produced from Eq. 1.21b (Fig. 1.11). Additionally, the ozone production efficiency (OPE) from this pathway, defined as the moles of ozone produced per mole of NO_x (Liu et al., 1987), can vary greatly based on both HO_x (OH + HO_2) and VOC concentrations, with values as high as ~20 (Hudman et

al., 2004). Typical OPE values in the United States range from 1-8 (Kleinman et al., 2002).

The VOC/NO_x concentrations and relative rates of HO_x and NO_x radical chain termination pathways have a major impact on the ozone production chemistry described in Fig. 1.9. When the RH + OH reaction (Eq. 1.15) reaction rate is large and the peroxy radical ($HO_2 + RO_2$) concentrations are high compared to [NO_x], the primary chain termination steps are controlled by HO_x self-reactions (Eq. 1.20-1.22). Thus variations in NO_x concentration do not have a large impact on the fate of the peroxy radical. As NO_x concentrations increase so too does the O_3 production under this NO_x-sensitive regime (Thornton et al., 2002).

$$\cdot OH \quad + \quad HO_2\cdot \quad \rightarrow \quad H_2O \quad + \quad O_2 \tag{1.20}$$

$$HO_2\cdot \quad + \quad HO_2\cdot \ (+M) \rightarrow \quad H_2O_2 \quad + \quad O_2 \tag{1.21}$$

$$HO_2\cdot \quad + \quad ROO\cdot \quad \rightarrow \quad ROOH \ + \ O_2 \tag{1.22}$$
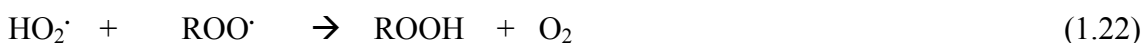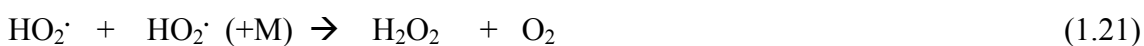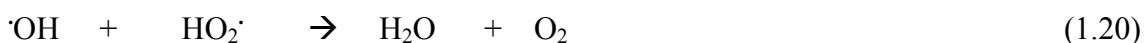
As the [HO_x]:[NO_x] shifts toward [NO_x], the chain termination pathways start to favor the formation of the NO_x sequestering reactions (Eq. 1.17b, 1.23). When the production of $RONO_2$ and HNO_3 outcompetes the HO_x chain termination reactions, the regime is NO_x-saturated (VOC-sensitive) and ozone production decreases with increases in [NO_x], due to the termination of both of the OH and NO radical regeneration chains (Fig. 1.9; Thornton et al., 2002).

$$ROO\cdot \quad + \quad \cdot NO \ (+M) \quad \rightarrow \quad RONO_2 \tag{1.17b}$$

$$\cdot OH \quad + \quad \cdot NO_2 \ (+M) \rightarrow \quad HNO_3 \tag{1.23}$$

The shifting of ozone production with [NO] can be better understood by observing Fig. 1.12. This plot shows the ozone production of the atmosphere at a middle-Tennessee field site as a function of NO concentration. At low NO concentrations, when conditions are NO_x-sensitive, ozone production increases almost linearly as a function of increasing [NO]. This positive correlation levels off at around 1000 ppt [NO] at the Tennessee field site before ozone production begins to decline as NO concentrations continue to increase. The figure shows clearly that when conditions go from NO_x-sensitive to VOC-sensitive there is a maximum in ozone production.
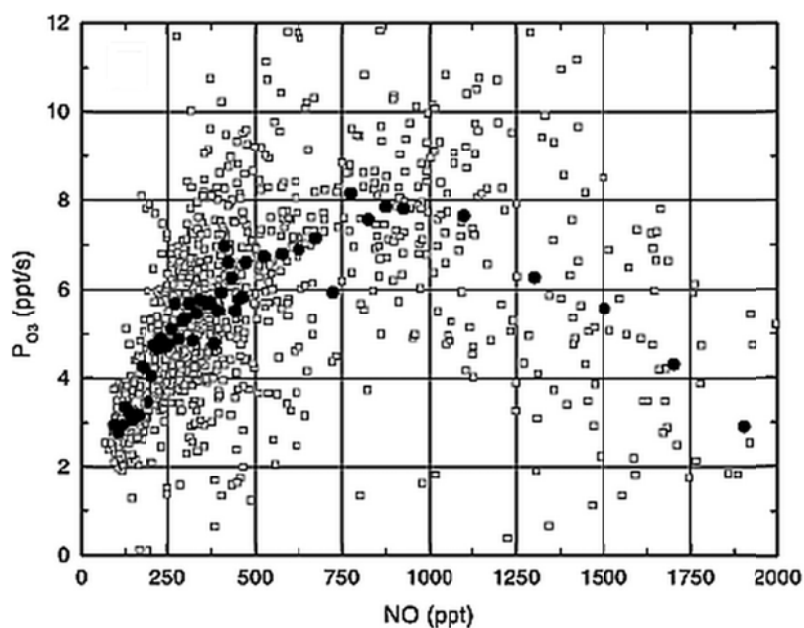
Figure 1.12. The ozone production rate (ppt/s) plotted as a function of nitric oxide (NO) concentration (ppt) for a middle-Tennessee field site. The open squares represent raw data points and the closed circles are the averaged data. The figure is adapted from Thronton et al. (2002).

Understanding the conditions that maximize ozone production is very important because ozone, which can benefit life by blocking harmful low wavelength radiation in the stratosphere, has a negative impact on human and environmental health at the tropospheric level. The inhalation of ozone can cause several respiratory issues such as lung lining inflammation and lung tissue scaring (EPA, 2010). Ozone has also been related to increased mortality rates (Jerrett et al., 2009) and is regulated by the US EPA at 75 ppb average over an 8 hour period (EPA, 2010). Additionally, tropospheric ozone is also a known greenhouse gas that has contributed to an increase of $0.28^{\circ}C$ to average global surface temperatures since the industrial revolution (Mickley et al., 2004).

Using the chemistry described above, the maximum ozone production potential has been modeled to help provide insight into the identification of NO_x-sensitive and VOC-sensitive regimes (Fig. 1.13; Sillman and He, 2002). The dotted blue line in Fig. 1.13 separates the two regimes and represents the conditions that yield maximum ozone production, with the NO_x-sensitive on the lower portion of the figure and the VOC-sensitive on the upper portion. The figure shows that under NO_x-sensitive conditions, for example, changes in VOC concentrations will have minimal impact on the O_3 production of the oxidation system.
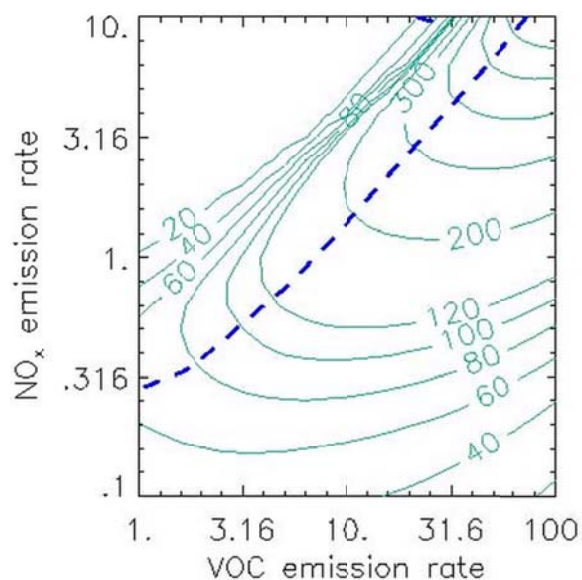
Figure 1.13. The isopleth plot from Sillman and He (2002) showing the effect different VOC/NO$_x$ ratios have on ozone production in polluted environments. Both the x- and y-axes are in 10^{12} molecules cm^{-2} s^{-1}.

Thanks to this knowledge, efforts by the US EPA to regulate NO$_x$ and VOC emissions have been successful in reducing tropospheric ozone concentrations by 25% since 1980 (Fig. 1.14; EPA, 2011). NO$_x$ emissions, which are regulated by the EPA at 53 ppb NO$_2$ averaged annually, have been reduced from both power plants (e.g. using staged combustion) and vehicles (e.g. using catalytic converters) (Skalska et al, 2010), which has had a strong impact on ozone concentrations as the US is mostly in a NO$_x$-sensitive regime (Lamarque et al., 2005). Certain VOC-sensitive regions, such cities like Los Angeles, have also seen decreases in ozone concentrations due to VOC emission regulations (Lei and Wang, 2014). Additionally, the reduction in harmful emissions, thanks to the Clean Air Act amendments in 1990, has been estimated to save the US

almost 2 trillion dollars by the year 2020 from increased American worker production

and ease on the health care system (EPA, 2011).
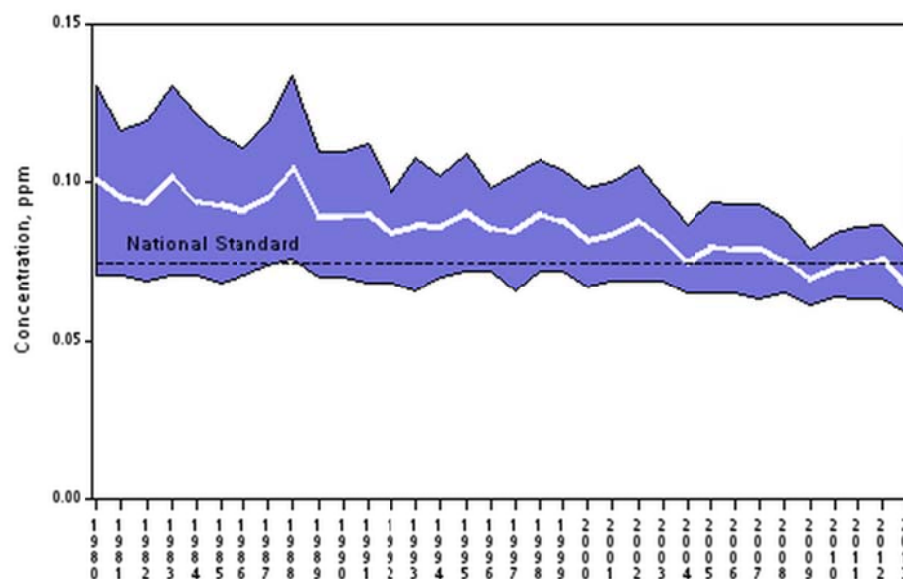
Figure 1.14. The average tropospheric ozone concentrations from 222 sites across the US (EPA, 2013).

1.3.5 Organic Nitrates

The formation of organic nitrates is an important reaction pathway with regards to

human health and the oxidative capacity of the atmosphere because it is a chain

termination step in the oxidation of VOCs that limits ozone production (Eq. 1.17b).The

gas phase production of organic nitrates was first measured in the laboratory by Darnall

et al. (1976) and ambient alkyl nitrates were later observed by Atlas (1988), both using

gas chromatography. Since these first measurements, much research has focused on the

formation of organic nitrates and their atmospheric reactivity.

The main pathway for organic nitrate production is from the addition of nitric oxide (NO) to the peroxy radical (RO$_2$). The mechanism responsible for the formation of organic nitrates (RONO$_2$) was initially unclear, due to uncertainty in the step following the creation of the initial peroxy nitrite intermediate (ROONO*). The simplest mechanism would involve a dissociation-recombination step, however, dissociation would produce a highly reactive alkoxy radical (RO) that likely would not recombine with NO$_2$ at atmospheric pressures (Ellison et al., 2004). Clarity on the issue was provided when Zhao et al. (2004) reported that the *cis*-conformation of the ROONO* intermediate could lead to a three-membered ring transition state capable of producing ground state NO$_2$ along with the alkoxy radical (Fig. 1.15). Reaction through the same isomerization transition state is also responsible for RONO$_2$ formation (Ellison et al., 2004). The system cross-over that describes the internal recombination and formation of RONO$_2$ (or ground state NO$_2$) is shown in the energy diagram in Fig. 1.16.

Figure 1.15. The nitric acid (NO) + peroxy radical (RO$_2$) reaction and the three membered ring transition state responsible for the formation of organic nitrate (RONO$_2$) species.

Figure 1.16. The energy diagram for the transition of FONO to FNO$_2$, showing the analogous rearrangement and system cross-over that occurs to form RONO$_2$ compounds. The figure is adapted from Ellison et al. (2004).

Further support of reaction via the isomerization transition state in Figs. 1.15 and 1.16 can be seen with the organic nitrate yield's dependence on both pressure and temperature (Fig. 1.17). Atkinson et al. (1983) found that organic nitrate yields increased with pressure for the pentyl peroxy radicals, due to increased collisional deactivation of the RONO$_2$* intermediate (Fig. 1.15). Atkinson et al. (1983) also observed larger organic nitrate yields with decreasing temperature (Fig. 1.17). High temperatures will lead to more energy in the vibrational modes of the transition state, making dissociation a more likely reaction pathway. The temperature and pressure dependence observed is typical for complex reaction mechanisms with activated chemical species (Atkinson et al., 1983).
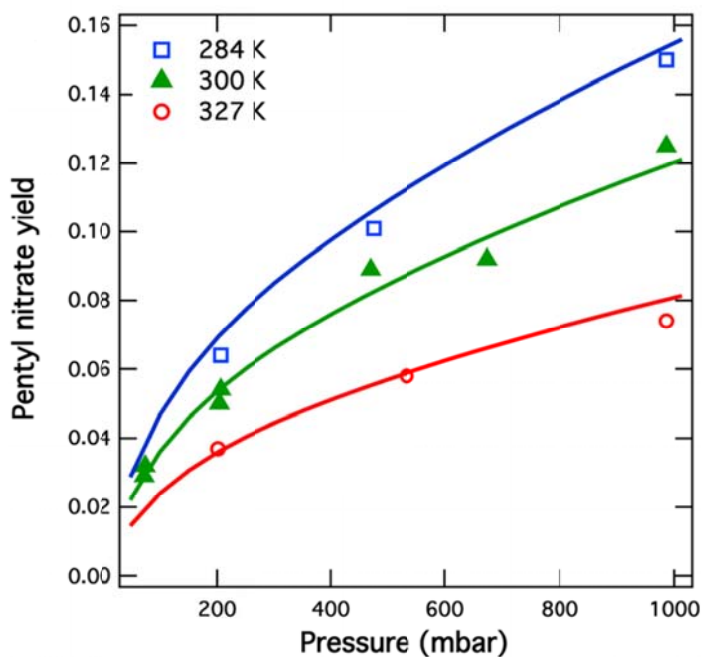
Figure 1.17. The organic nitrate yield for the OH radical initiated oxidation of *n*-pentane under high NO_x conditions as a function of pressure at three different temperatures, 284, 300, and 327 K. The figure is adapted from Atkinson et al. (1983).

The $RONO_2$ branching ratio from the $NO + RO_2$ reaction pathway is also dependent on the size of the peroxy radical. For OH initiated oxidation of alkanes, Arey et al. (2001) found that organic nitrates increased approximately linearly with carbon chain length (Fig. 1.18). Larger molecules have more vibrational degrees of freedom to help stabilize the transition state and allow for $RONO_2$ formation.
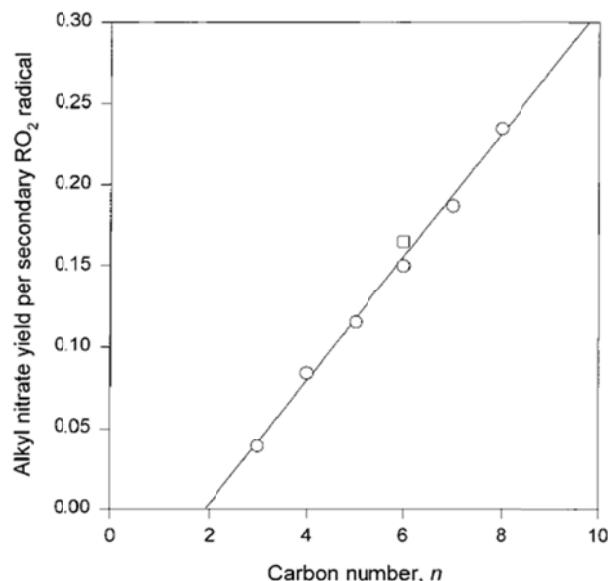
Figure 1.18. The fractional organic nitrate yield from the NO addition to the alkyl peroxy radical as a function of carbon number for the original VOC species. The figure is adapted from Arey et al. (2001).

The functionality of the peroxy radical may also affect the $RONO_2$ branching ratio. Reported $RONO_2$ yields of straight chain alkenes, which will favor the addition of OH across the double bond as opposed to H-abstraction, are lower than those of straight chain alkanes (Tuazon et al., 1990; O'Brien et al., 1998). This phenomenon has been attributed to the hydrogen bonding of the adjacent β-hydroxy group with the peroxy linkage in the ROONO* adduct to weaken the O-O bond and increase the rate of dissociation (O'Brien et al., 1998). Since BVOCs have large emission rates, and OH rate constants for olefinic carbon compounds are significantly faster than for alkanes, β-hydroxy organic nitrates are expected to be more atmospherically important than the analogous alkyl nitrate compounds. Aromatic compounds also have been shown to have a reduced organic nitrate yield compared to similar sized straight chain alkanes (Elrod,

2011). Additionally, the $RONO_2$ yields reported by Elrod (2011) did not show a pressure dependence, indicating that there may be other mechanisms responsible for the creation of $RONO_2$ compounds.

One specific compound that currently has an uncertain organic nitrate yield is the monoterpene α-pinene, due to disagreement between the only reported $RONO_2$ yields, ranging from ~1% (Aschmann et al., 2002) to 18±9% (Noziere et al., 1999). The oxidation of α-pinene can lead to significant secondary organic aerosol production (Lee et al., 2006) and, with emissions accounting for 42% of all monoterpenes (Guenther et al., 2012), the formation of organic nitrates from α-pinene will have important contributions to the ozone and aerosol production potential of forest environments. An α-pinene organic nitrate yield close to the reported value of Noziere et al. (1999), 18±9%, would be much larger than expected based on the β-hydroxy nitrate trend described previously by O'Brien et al. (1998) and may indicate that radical rearrangement is occurring to produce final $RONO_2$ products without the β-hydroxy nitrate functionality. Study of that process is one objective of this thesis..

1.3.5.1 Fate of Organic Nitrates

Once created in the gas phase, organic nitrates can undergo several atmospheric processes such as deposition, partitioning to aerosol, photolysis, and further oxidation. The uptake of organic nitrates to plants for the use of amino acid synthesis has also been demonstrated (Lockwood et al., 2008). In comparison to dry deposition, reaction with the OH radical, and known photolysis rates, Shepson et al. (1996) calculated wet deposition to account for 26-60% of the removal of non-olefinic β-hydroxy organic nitrates, after

determining Henry's law constants to be four orders of magnitude larger for the multi-functional nitrates compared to analogous alkyl nitrate species. Taking these values into account, Treves and Rudich (2003) estimated the lifetime of β-hydroxy nitrates to be between 0.5 and 4 days.

The photolysis of organic nitrates can vary drastically based on functionality. Short chain alkyl nitrates have a measured lifetime of 15-30 days (Luke et al., 1989) while dinitrate compounds are estimated at ~6 days (Barnes et al. 1993). The fastest measured photolysis rates for organic nitrate compounds are carbonyl nitrates, which have recently been measured to have lifetimes on the order of hours, making photolysis the most probable pathway of removal for these species (Müller et al., 2014). The photolysis of organic nitrates breaks the O-N bond at near unity quantum efficiency, to produce the alkoxy radical and NO_2, thus, the photolysis of carbonyl nitrate species is very important with regard to ozone production potential (Müller et al., 2014).

The oxidation of organic nitrates has also been studied, however, the NO_x recycling efficiency from gas phase reactions is still uncertain for many atmospherically relevant compounds. The NO_x recycling efficiency of an organic nitrate is defined as the fractional difference between the amount of NO_x released from the reaction of an $RONO_2$ and the amount of NO consumed. For photolysis of carbonyl nitrates, the NO_x recycling efficiency is ~100%. An example of the OH radical oxidation of an isoprene-derived 1,4-δ-hydroxy nitrate is shown in Fig. 1.19 (Lee et al., 2014).
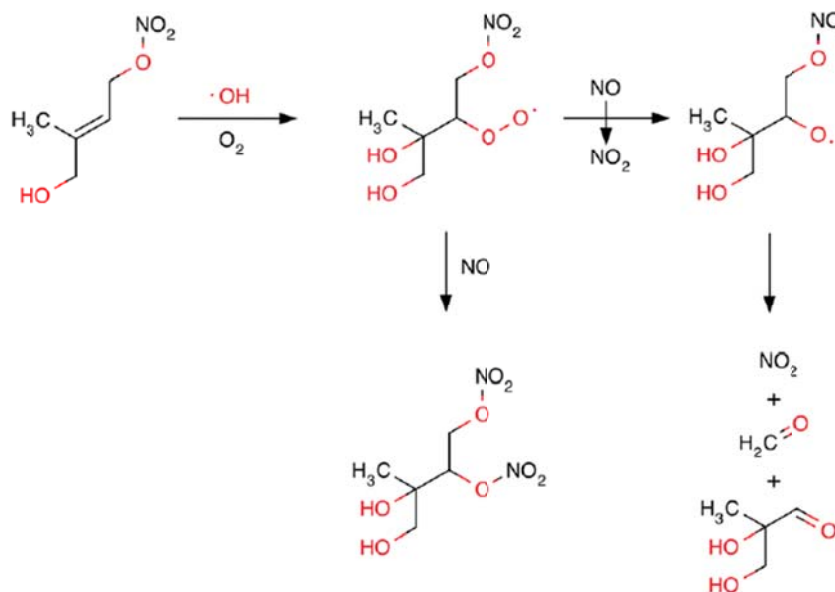
Figure 1.19. Selected pathways of OH radical initiated oxidation of an isoprene-derived 1,4-δ-hydroxy nitrate is shown. The figure is adapted from Lee et al. (2014).

Reaction rate constants for selected isoprene-derived β- and δ-hydroxy nitrates with O_3 and OH were recently measured to be on the same order of magnitude as isoprene + OH rate constants, if not faster (Lee et al., 2014), displaying the importance of the OH radical's atmospheric reactivity with alkenes. The lone exception to the very fast $RONO_2$ rate constants measured by Lee et al. (2014) was the β-hydroxy nitrate + O_3 reaction, which had a rate constant two orders of magnitude smaller than that of the δ-hydroxy nitrate. This discrepancy was believed to be at least partially explained by a lack of functionality on the alkene group. A simple methyl group can have an order of magnitude difference on ozonolysis rate constants (Greene et al., 1992; Avzianova et al., 2002), thus the functionality of an organic nitrate is very important when considering its atmospheric oxidation. Due to the diverse level of functionality and connectivity of

atmospheric $RONO_2$ species, there is still much research needed to improve our understanding of the gas phase oxidation of organic nitrates.

The NO_x recycling efficiencies of the isoprene-derived nitrates studied in Lee et al. (2014) were as low as -25%, indicating that, overall, NO_x was consumed instead of released in the continued oxidation of organic nitrates by forming multi-nitrate species (Fig. 1.19). Previous NO_x recycling estimates for isoprene-derived nitrates were at +50% (Paulot et al., 2009), displaying the large degree of uncertainty in the NO_x sequestration ability of organic nitrates and the effects on potential ozone production from their oxidation.

The aerosol phase partitioning of low-volatility organic nitrates, such as those derived from α-pinene, allows the opportunity for condensed phase and surface chemistry to govern the fate of $RONO_2$ compounds. Previous studies have shown that α-pinene-derived nitrates can readily partition to the particle phase (Perraud et al., 2012). Many condensed phase processes, such as oligomerization (Chan et al., 2013) and oxidation (Daumit et al., 2014), are likely to occur within an aerosol, however, there is currently very little research that has investigated the chemical mechanisms governing the fate of $RONO_2$ compounds within the particle phase.

Concerning the fate of organic nitrates, one chemical pathway that is likely to contribute to its particle phase reactivity is the hydrolysis mechanism. The hydrolysis of alkyl nitrates is not a recently discovered phenomenon (Klason and Carlson, 1907) and product analysis has shown that, under basic conditions, three products can be formed from the original $RONO_2$ species via bimolecular mechanisms (Baker and Eatsy, 1950): the analogous alcohol, olefin, or carbonyl compound (Fig. 1.20).
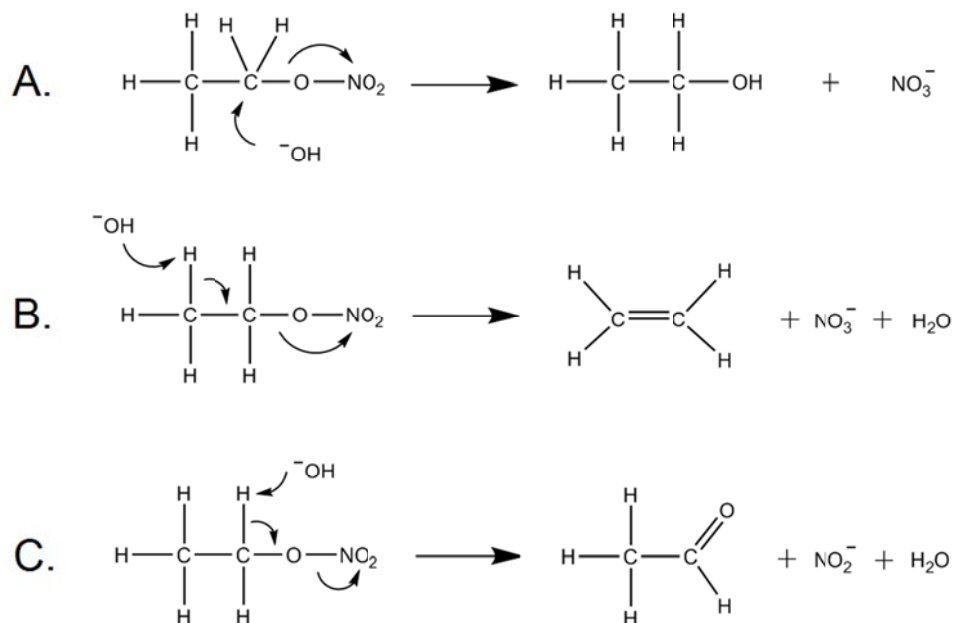
Figure 1.20. The different pathways of ethyl nitrate hydrolysis mechanism under basic conditions.

The hydrolysis of ethyl nitrate is shown in Fig. 1.19 under basic conditions. The mechanism in Fig.1.20a shows the bimolecular nucleophilic substitution (S_N2) of the OH anion to the α-carbon to create ethanol and the nitrate anion. Fig 1.20b shows the bimolecular elimination (E2) mechanism where the OH anion attacks the β-hydrogen to form ethylene along with the nitrate anion and water. The mechanism in Fig. 1.20c is also an E2 mechanism, but, in this instance, attack occurs at the α-hydrogen to produce acetaldehyde along with the nitrate anion and water. In each case, the $RONO_2$ functionality is removed from the organic compound to produce a comparatively less reaction nitrate anion. This transformation could have large implications on the fate of NO_x from organic nitrate production. It is also important to note that bimolecular mechanisms are not favored to occur on tertiary nitrates, in polar protic solvents, or with

weak nucleophiles, and thus other mechanisms, such as unimolecular substitution and elimination, will likely contribute to the hydrolysis chemistry of organic nitrates. This process will be a focus of this thesis.

The hydrolysis of atmospherically relevant β-hydroxy organic nitrates has been a focus of condensed phase studies, with rate constants positively correlated to solution acidity (Darer et al., 2011). Darer et al. (2011) also reported that tertiary organic nitrates hydrolyzed significantly faster (lifetimes of ~4min) than primary organic nitrates (lifetime of >2500 hr). These results imply that an S_N1 mechanism is responsible for the hydrolysis at neutral and low pH, despite Darer et al. (2011) attributing the chemistry to an S_N2 mechanism. Three years later, Jacob et al. (2014) reported the hydrolysis lifetimes of a primary isoprene-derived δ-hydroxy nitrate to be faster than that of a secondary isoprene-derived β-hydroxy nitrate species, indicating that the rate and mechanism of hydrolysis also has a strong dependence on the stability of the carbocation intermediate, which is consistent with a unimolecular mechanism. Interestingly, Jacob et al. (2014) did not see a reaction rate that correlated with acidity, leading to unanswered questions about the acid-catalyzed nature of the hydrolysis reaction mechanism. Along with the gas phase OH oxidation mechanism, the large degree of functionality and connectivity of organic nitrates leaves much room for study in the hydrolysis chemistry of $RONO_2$ species and the effect on the fate of NO_x.

The hydrolysis mechanism has been suggested to be responsible for a lack of aerosol phase organic nitrate measurements in a previous laboratory study (Liu et al., 2012) and may help explain the relative dearth of organic nitrate measurements from field campaigns (e.g. Day et al., 2010). Extended sampling times, which may allow for

hydrolysis to unintentionally occur on filters, and the lack of properly heated inlet lines may also contribute the lack of ambient organic nitrate measurements.

The uncertainty in the organic nitrate yields of important atmospheric compounds coupled with the lack of knowledge on the partitioning and particle phase fate of $RONO_2$ species currently has a large negative impact on our understanding of the sinks/reservoirs of NO_x and their effect on tropospheric ozone production. One reactive pathway of particular interest is the OH initiated oxidation of α-pinene, due to its relatively high global emissions, potential for a high $RONO_2$ branching ratio, and the contribution of its oxidation products to secondary organic aerosol formation.

1.4 Research Goals

The main objective of this thesis is to study the atmospheric chemistry of α-pinene in the presence of the OH radical and nitric oxide (NO) to gain a better understanding of organic nitrate chemistry in forest environments. Chemistry research will focus on reactions that govern the fate of NO_x and ozone production potential. α-Pinene was selected as a model BVOC for experiments based on its relatively large annual emissions, ~66 Tg yr^{-1} (Guenther et al., 2012), and its relatively large SOA yields (Lee et al., 2006).

This study was able to determine the organic nitrate yield from the OH radical oxidation of α-pinene under high NO_x conditions, helping to lower the uncertainty in ozone production potential of this reaction pathway and providing insight into the chemistry of monoterpene species. Further study of α-pinene-derived nitrates, as well as other model compounds, allowed for valuable understanding of the rates and chemical

mechanisms responsible for the particle phase hydrolysis chemistry of organic nitrates and other α-pinene-derived species. Additionally, the data gathered has potentially significant implications on the fate of gas-phase NO_x.

CHAPTER TWO: PHOTOCHEMICAL CHAMBER STUDIES OF ALPHA-PINENE-DERIVED NITRATE PRODUCTION AND HUMIDITY-DEPENDENT LOSS IN THE PARTICLE PHASE

2.1 Introduction

This study used photochemical reaction chamber experiments, involving the OH radical initiated oxidation of α-pinene in the presence of nitric oxide (NO), to investigate the formation of organic nitrates from simulated day-time atmospheric chemistry above coniferous forests. The formation mechanism of α-pinene-derived organic nitrates from this experiment is shown in Fig. 2.1. The organic nitrate ($RONO_2$) branching ratio, k_A/k_A+k_B, was measured as a function of chamber relative humidity under three different seed aerosol scenarios: neutral seed, acidic seed, and without seed aerosol. Data from these measurements gives better understanding of the ozone production potential of the monoterpene oxidation pathway as well as insight into the mechanisms that govern the fate of $RONO_2$ compounds in the aerosol phase with respect to acid-catalyzed hydrolysis.
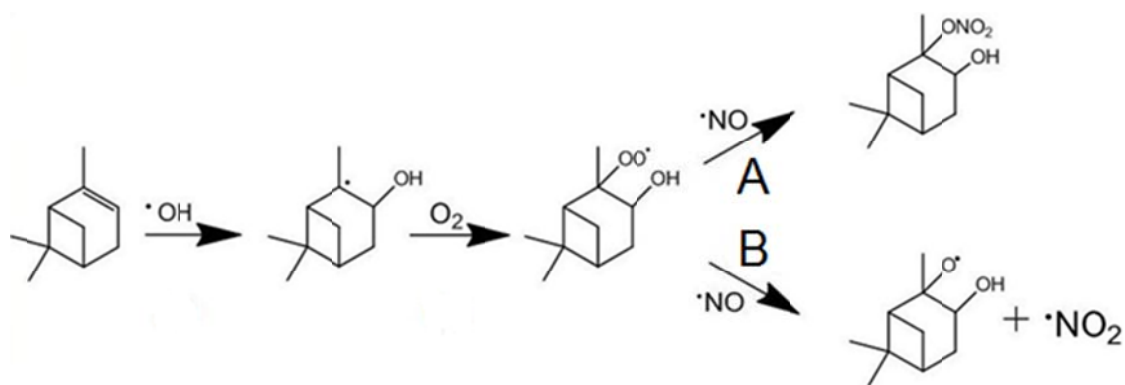
Figure 2.1. The mechanistic pathway for the hydroxyl radical initiated oxidation of α-pinene in the presence of nitric oxide (NO).

2.2 Experimental

2.2.1 Photochemical Reaction Chamber

A 5500 L all-Teflon photochemical reaction chamber was used for α-pinene oxidation experiments (Fig. 2.2). The chamber was built in conjunction with the Jonathan Amy Facility for Chemical Instrumentation in 1996 and has been used in previous "smog" chamber studies (Chen et al. 1998; Lockwood et al. 2010; Espada et al., 2005a,b). The chamber is equipped a Teflon-coated mixing fan and surrounded by 16 UV solar simulator lamps (Q-Lab, UVA-340) that have a maximum output at 340 nm (Fig. 2.3).

Figure 2.2. The Shepson group all-Teflon photochemical reaction chamber at Purdue University.
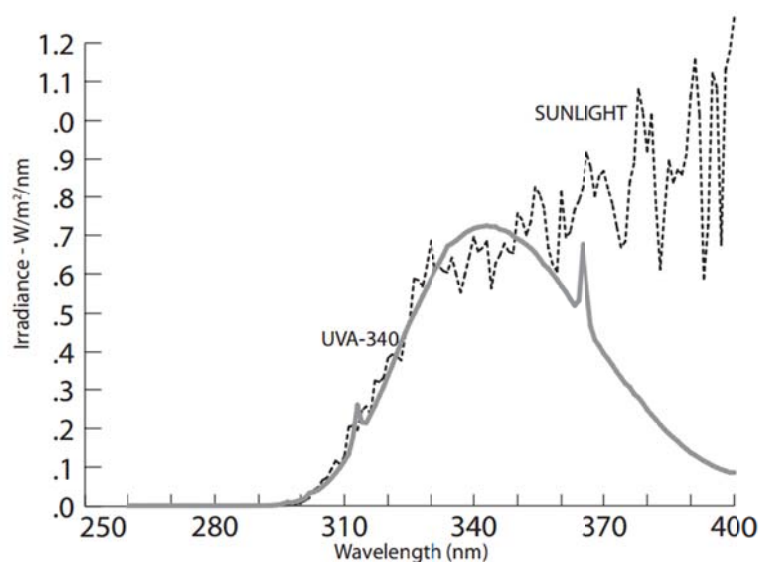
Figure 2.3. The irradiance (W m^{-2} nm^{-1}) of the photochemical chamber UV lamps compared to solar irradiance as a function of wavelength (nm). The figure is taken from www.Q-Lab.com.

2.2.2 Introduction of Reagents

Reagents were introduced into the chamber using reagent-specific methods. Water and hydrogen peroxide were bubbled into the chamber under a stream of ultra-pure air, volatile organic compounds (VOCs) and nitric oxide were injected using a syringe and glass tee under a stream of ultra-pure air, and seed aerosol was injected using an aerosol generator. For more detail on each method, see the corresponding section below.

Order of Injection into the Chamber

1. H_2O (if necessary)

2. H_2O_2 (OH radical precursor)

3. Seed aerosol

4. Reactive tracer compound (if necessary)

5. α-Pinene

6. Nitric oxide

Once all reagents were injected into the chamber, the contents were allowed to mix for ten minutes before the fan was turned off and the UV lights were initiated (t=0). The lights were turned off when roughly half of the α-pinene was consumed, marking the end of an experiment. This was done in effort to focus on first-generation products of the α-pinene oxidation pathway.

2.2.3 Hydrogen Peroxide

Hydrogen peroxide (30% in H_2O, Sigma Aldrich, Inc.) was used as the OH radical precursor (Eq. 2.1). Hydrogen peroxide has a very low absorption cross section at the peak output wavelength of the solar simulator lamps (Fig. 2.4), thus, high concentrations of precursor H_2O_2 were needed in these experiments. Hydrogen peroxide was bubbled into the chamber under ultra-pure air prior to injection of seed aerosol, α-pinene, and nitric oxide.

$$H_2O_2 \quad + \quad h\nu \quad \rightarrow \quad 2\,^{\cdot}OH \tag{2.1}$$
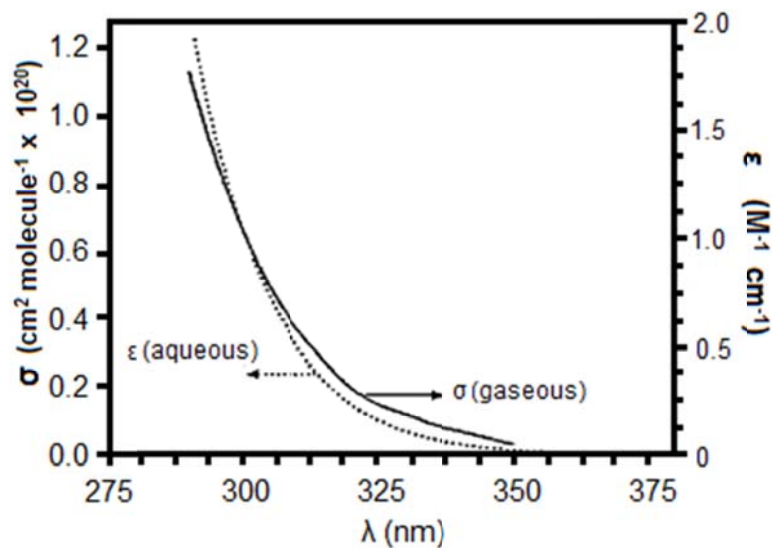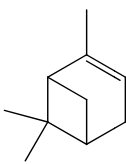
Figure 2.4. The absorption cross section of gas phase H_2O_2 (σ) and aqueous H_2O_2 (ε). The figure is adapted from Vione et al. (2003).

2.2.4 Volatile Organic Compounds

α-Pinene (98%, Sigma Aldrich, Inc.) and the reactive tracer compound, isooctane (99%, Sigma Aldrich, Inc.), were introduced into the chamber via ultra-pure air using a glass tee and gentle heat. Selected experiments involved the use of a reactive tracer compound to determine OH radical concentrations. Isooctane was selected as a reactive tracer compound because its OH radical rate constant is roughly an order of magnitude lower than that of α-pinene (Table 2.1), allowing for minimal contribution to the observed chemistry of the chamber experiment. The OH radical concentrations were determined using Eq. 2.2 (Tuazon et al., 1984), which assumes that OH radical concentrations were essentially constant over the irradiation period. The OH radical concentrations in chamber experiments ranged from 1×10^6 cm^{-3} to 1×10^7 cm^{-3}.

Table 2.1. The α-pinene and isooctane OH rate constants from Atkinson et al. (2003).

Compound	Structure	OH Rate Constant (cm^3 molecule^{-1} s^{-1})
α-Pinene		5.33×10^{-11}
Isooctane		3.34×10^{-12}

$$[OH] = \frac{1}{k_{OH}(t_2 - t_1)} \ln\left(\frac{[\text{isooctane}]_{t_1}}{[\text{isooctane}]_{t_2}}\right)$$

(2.2)

Volatile organic compound measurements were made using a gas chromatograph

(5890 Series II, HP, Inc.) coupled to a flame ionization detector (GC-FID; see Fig. 2.5).

In these experiments, a capillary column gas chromatograph was used to separate organic

compounds based on both volatility and polarity. Specifications for the RTX-1 (Restek,

Inc.) column used are as follows: dimethylpolysiloxane stationary phase, 30 m length,

0.52 mm i.d., and a 1.0 μm film thickness. Helium was used as the carrier gas at a column

flow rate of 10mL/min.
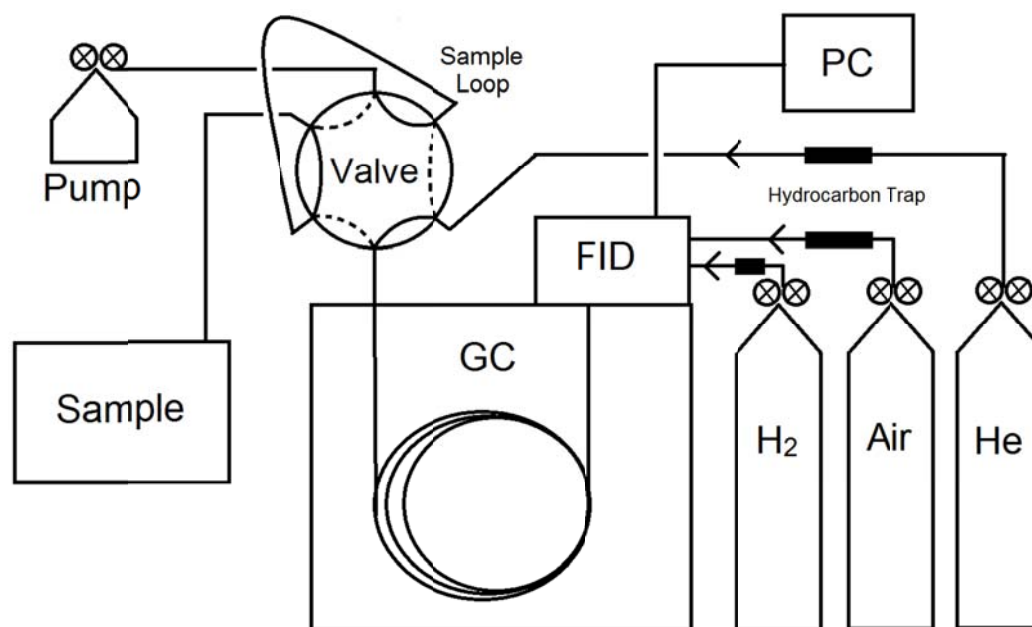
Figure 2.5. Schematic for quantifying gas phase α-pinene and other organic compounds
using the GC-FID. The 6-port valve is shown in LOAD mode. See Fig. 2.6 for further
information on the 6-port valve.

Gas phase injection of the analyte was made possible by the use of a 6-port valve

(Valco Instr. Co., Inc.). A double-diaphragm vacuum pump was used to fill the sample

loop (stainless steel, 10 cm^3) using the "LOAD" setting (Fig. 2.6). By switching to the

"INJECT" setting, the carrier gas transferred the analyte from the sample loop to the

column. The sample line was wrapped in heating tape (120°C) and insulated with

fiberglass tape, to prevent sample line loss.
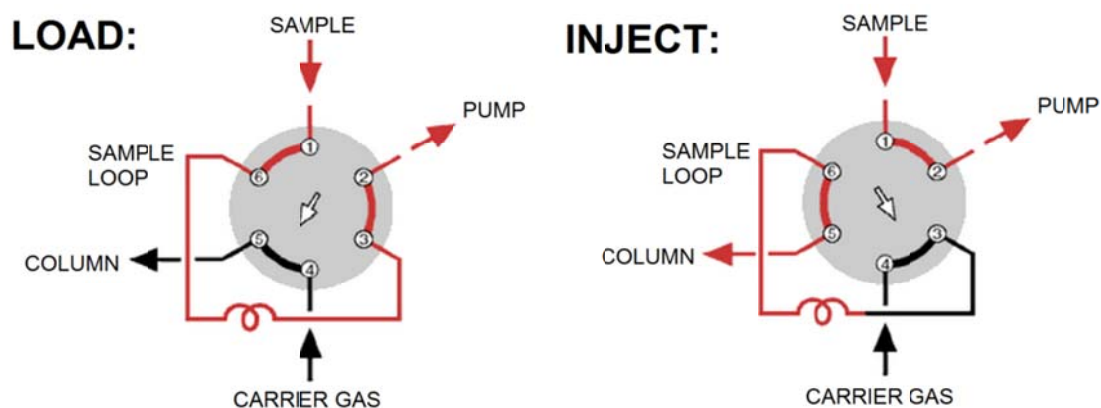
Figure 2.6. The schematic for the 6-port valve (Valco Instr. Co., Inc.) used for gas phase injection of the analyte into the GC-FID showing both the "LOAD" and "INJECT" modes.

The column oven for the GC-FID used a temperature ramp starting at 55°C for 1

minute followed by a 50°C/min increase to 255°C. Under the column conditions listed

previously, α-pinene eluted the column at 182s and was easily separated from the relative

rate compound, isooctane, which eluted at 100s (Fig. 2.7).
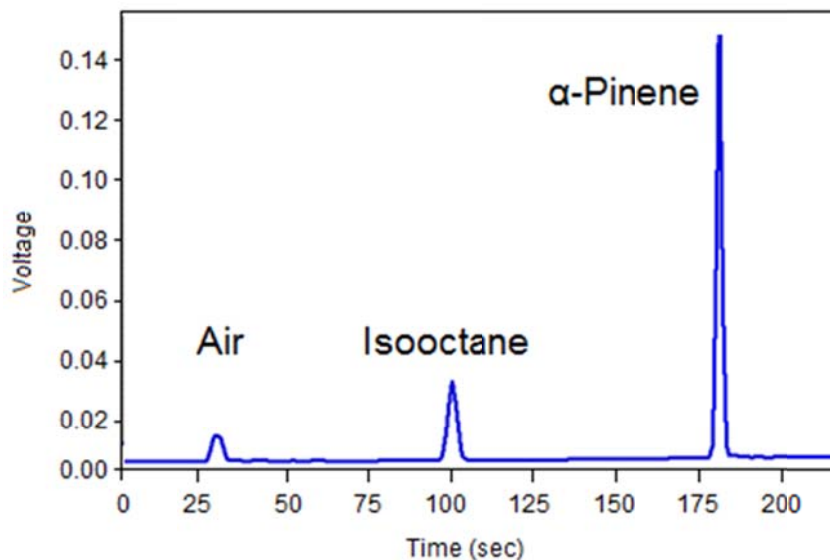
Figure 2.7. A GC-FID chromatogram showing the elution of isooctane (100s) and α-pinene (182s).

Once separated by the GC, the analyte was detected using an FID. Flame ionization detectors combust organic samples using a hydrogen/air flame to produce ions and electrons. The hydrogen gas flow rate was kept at 20mL/min while the air flow rate was 325 mL/min. The application of a voltage on an electrode above the flame (Fig. 2.8) allows for ions to move to the electrode collector (cathode), which creates a measurable current. The most abundant ion product from the combustion of organics in an FID is the CHO^+ ion (Holm, 1999). The signal of the FID is proportional to the reduced carbon atoms of a species and is not sensitive to noncombustible gases such as water, CO_2, and inert gases.
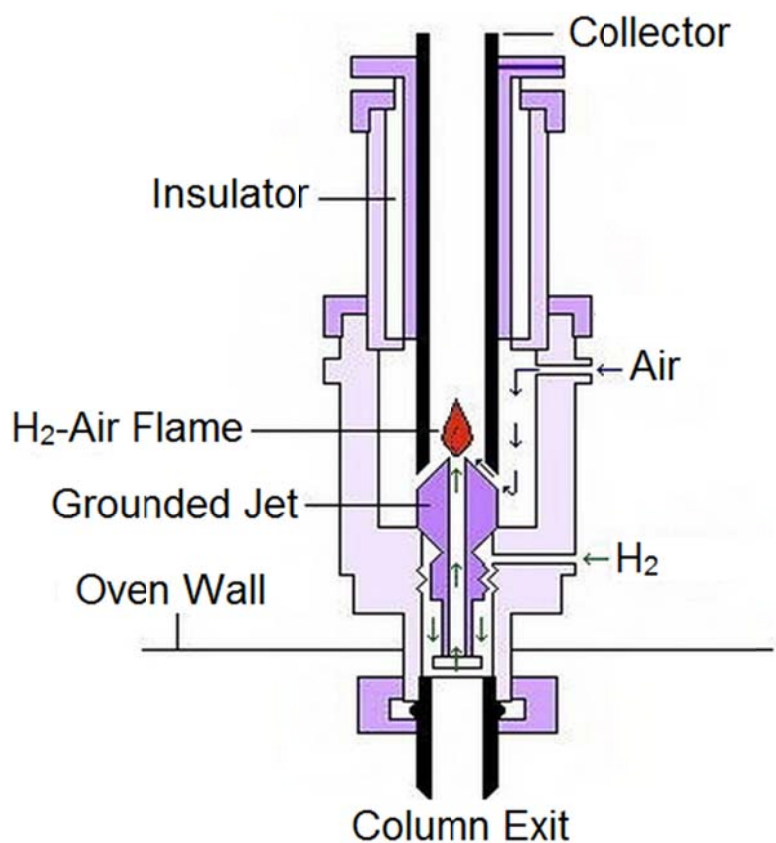
Figure 2.8. The flame ionization detector (FID**)** schematic. This figure is adapted from www.chem.agilent.com.

GC-FID calibration curves for both α-pinene and isooctane are shown below in Fig. 2.9. The relative sensitivity of the GC-FID to α-pinene/isooctane (29450/23975=1.23) was very close to the α-pinene/isooctane carbon number ratio (10/8=1.25), as expected (Scanlon and Willis, 1985).
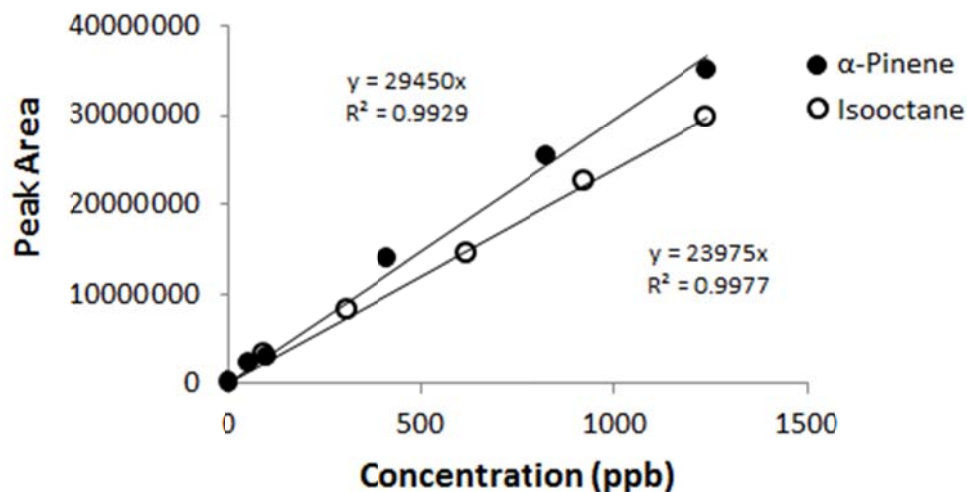
Figure 2.9. GC-FID calibration curves for α-pinene (●) and isooctane (○).

2.2.5 Seed Aerosol

Seed aerosol used for chamber experiments was created by passing air into an aerosol generator to create a polydisperse aerosol flow stream that was then dried using a diffusion dryer. A known charge distribution was applied on the particles using an aerosol neutralizer before injection into the chamber (Fig. 2.10).
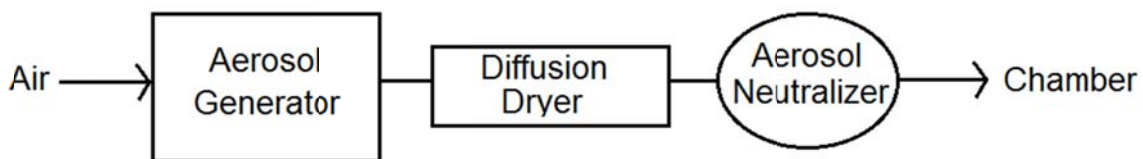
Figure 2.10. The scheme for generation of seed aerosol and injection into the photochemical reaction chamber.

Three different seed aerosol conditions were used in this experiment to determine the effect of particle acidity on organic nitrate yields. Neutral seed consisted of $(NH_4)_2SO_4$ and acidic seed consisted of $MgSO_4/H_2SO_4$ while the third set of experiments was completed without the use of seed aerosol. The use of sulfate salts as seed aerosol is common in chamber experiments, due to the sulfate ion's ubiquity in the ambient atmosphere. Typical seed aerosol mass concentrations ranged from 50 to 150 µg/m^3 and number concentrations ranged from approx. 5.0×10^4 to 1.5×10^5 cm^{-3}. A typical seed aerosol size distribution is shown in Fig. 2.11.
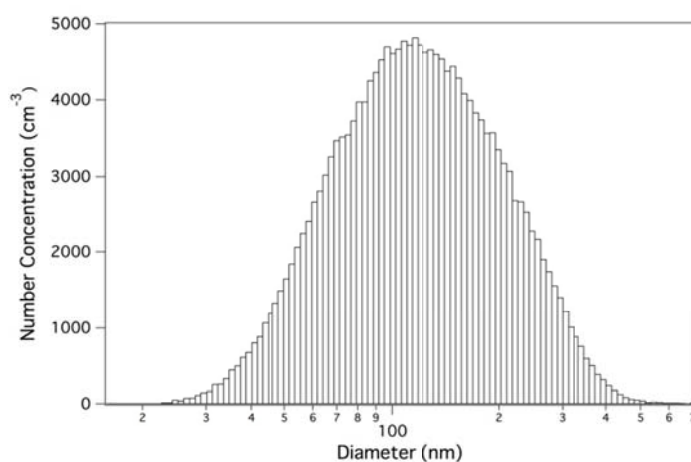
Figure 2.11. A seed aerosol size distribution showing aerosol number concentration (cm^{-3}) as a function of particle diameter (nm).

The generation of seed aerosol particles was accomplished using a Constant Output Atomizer (Fig. 2.12; Model 3076, TSI, Inc.). A constant stream of air (3.0 L/min) is passed through a 0.0135" diameter orifice in the nozzle disk, causing the air to expand and create a high-velocity jet capable of drawing up liquid solution from the reservoir.

Large droplets are impacted on the adjacent wall and are deposited back into the reservoir while fine spray flows out of the atomizer. The atomizer is capable of generating a polydisperse aerosol flow at a concentration of 2×10^6 particles cm^{-3} (Liu and Lee, 1975). For neutral seed aerosol, the reservoir was filled with a solution of 15mM $(NH_4)_2SO_4$ and for acidic seed aerosol experiments, a solution of 30 mM $MgSO_4$/50 mM H_2SO_4 was used. Seed aerosol conditions were based on Surratt et al. (2008).
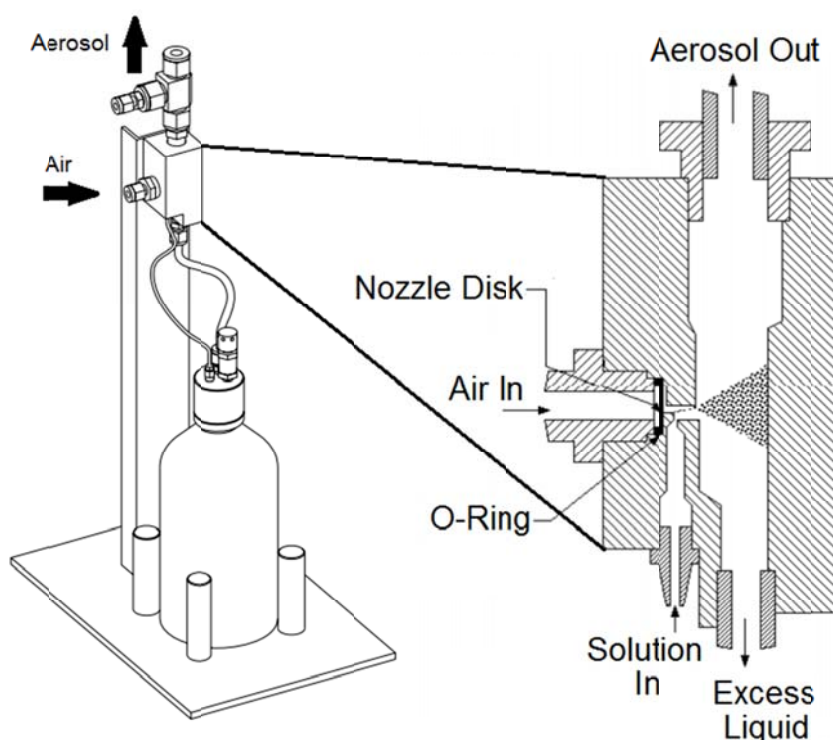
Figure 2.12. The 3076 Constant Output Atomizer (TSI, Inc.) schematic. This figure is adapted from www.tsi.com.

Once created, seed aerosol is passed through a diffusion dryer to remove excess water from the particles. The diffusion dryer consists of a cylindrical wire screen

surrounded by silica gel (Fig. 2.13). Water diffuses from the gas stream and particles to the silica to create dry aerosol.
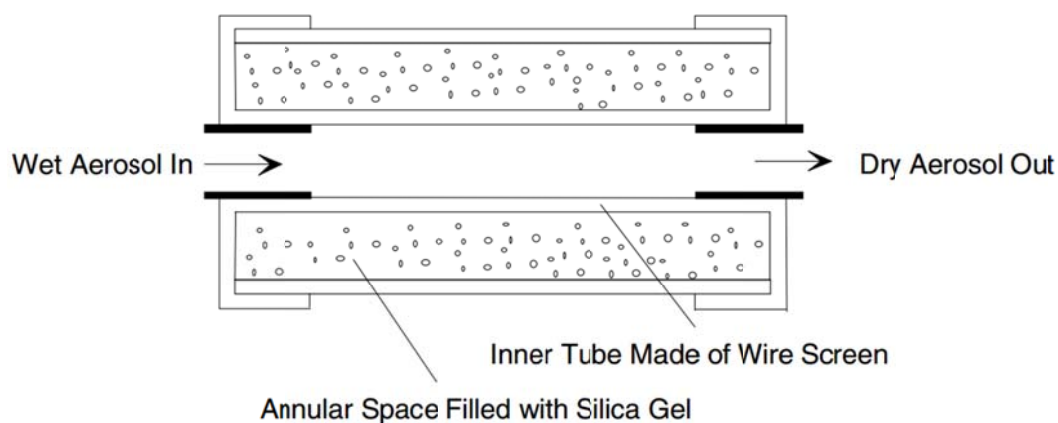
Figure 2.13. The diffusion dryer schematic. This figure was taken from www.tsi.com.

Before dry seed aerosol was injected into the chamber for experiments, it was passed through an aerosol neutralizer to create a known bipolar charge distribution of particles. The creation of aerosol can lead to an asymmetric charge distribution across particles because particle generation is a stationary system where charge is not in equilibrium (Fuchs, 1963). The Kr-85 source in the aerosol neutralizer creates an equilibrium distribution of charge across particles, which is important because only a known bipolar charge distribution will produce reliably measured aerosol size distributions (Wiedensohler, 1988).

2.2.6 Scanning Mobility Particle Sizer

The measurement of aerosol particle size distributions and concentrations was accomplished using a scanning mobility particle sizer (SMPS). The SMPS consists of an electrostatic classifier (Model 3080, TSI, Inc.), which separates particles based on size, and a condensation particle counter (CPC; Model 3775, TSI, Inc.), which measures particle concentrations.

As polydisperse aerosol enters the electrostatic classifier, it first passes through an impactor to remove particles above a certain particle diameter based on inertial impaction. The aerosol stream is accelerated through a nozzle and large particles with high inertia collide with the impaction plate while smaller particles continue with the flow stream and exit the impactor (Fig. 2.14). This technique allows for the removal of large, unwanted particles that are more likely to be multiply charged (Wang and Flagan, 1990).
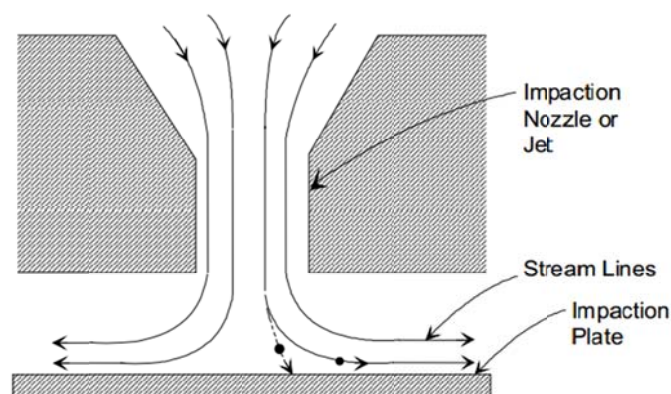
Figure 2.14. A schematic for the impactor used to eliminate large particles from the aerosol stream (Hinds, 1982).

After the removal of large particles from inertial impaction, the polydisperse aerosol stream was passed through a Kr-85 neutralizer to create a bipolar charge distribution (see above) necessary for electrostatic analysis using the differential mobility analyzer (DMA). The DMA, shown on the right in Fig. 2.15, consists of two cylindrical coaxial rods that, when a known voltage is applied between them, can separate particles based on both electronic mobility of the particle, which is a function of aerosol diameter and charge, and instrumental parameters, such as flow rate and radius of annular space between the rods. The relationship between particle diameter and DMA voltage is described by Eq. 2.3 below:

$$\frac{D_p}{C} = \frac{2\,n\,e\,V\,L}{3\,\mu\,q_{sh}\,\ln\frac{r_2}{r_1}}$$

(2.3)

Here D_P is the particle diameter, C is the Cunningham slip correction, n is the number of elementary charges, e is the elementary charge of an electron (1.6×10^{-19} C), V is the voltage on the inner rod, L is the length between exit slit and aerosol inlet, μ is the gas viscosity, q_{sh} is the sheath air flow, r_2 is the outer radius of annular space, and r_1 is the inner radius of annular space. Scanning a range of DMA voltages will yield an aerosol size distribution of the particle stream.
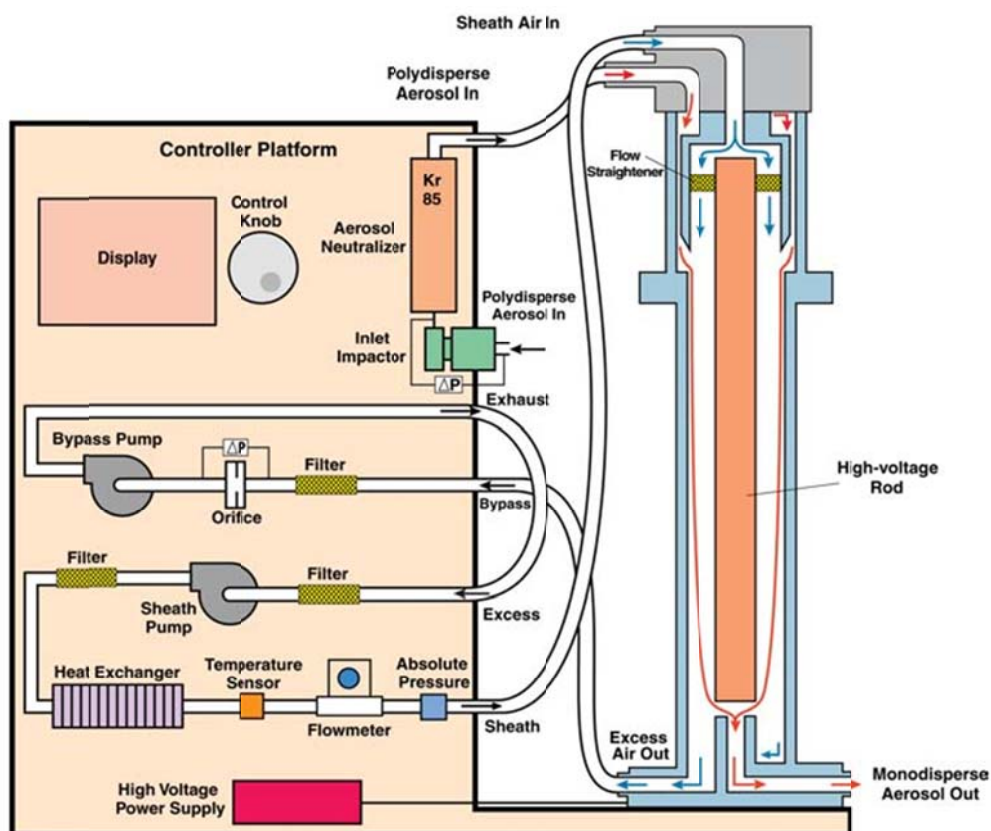
Figure 2.15. The flow system schematic for the electrostatic classifier (Model 3080, TSI, Inc.) with the differential mobility analyzer (DMA) pictured on the right.

The aerosol concentration of the monodisperse aerosol stream created by the DMA is measured using a condensation particle counter (CPC). Aerosol entering the CPC is passed through vaporized butanol before the stream is cooled to allow for the particles to act as efficient condensation nuclei for the vapor. The resulting droplets are easily detected optically by use of a laser and photodiode detector. The scattering of light by the large droplets creates a light pulse at the photodiode detector that is converted to an aerosol number concentration measurement (particles/cm^3). The aerosol number concentration can be used to calculate aerosol mass concentration using the measured

particle diameter from the DMA measurement and a particle density estimate, which, for the α-pinene oxidation experiments herein, a density of 1.3 g/cm^3 was used (Ng et al., 2007).

2.2.7 Nitric Oxide

Nitric oxide (NO) was injected into the chamber under a stream of nitrogen using the glass tee. Concentrations of NO were kept above 100 ppb to keep ozone levels low, via Eq. 2.4, and ensure that the OH radical was the sole initial oxidizing agent in the experiments.

$$NO \quad + \quad O_3 \quad \rightarrow \quad NO_2^* \quad + \quad O_2 \qquad\qquad (2.4)$$
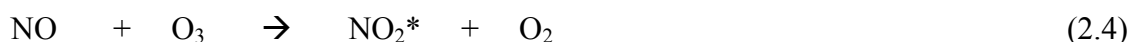
Nitric oxide concentration measurements were accomplished using a commercial NO/NO$_y$ detector (Model 42C, Thermo Sci., Inc.). The NO/NO$_y$ detector uses a chemiluminescence technique to measure the light emitted from the transition of excited state NO$_2^*$ back to the ground state. The activated NO$_2$ is produced from NO reaction with O$_3$ within the instrument, via Eq. 2.4, and decays to release near infrared light (Eq. 2.5). The resulting light is measured using a photomultiplier tube (PMT) and the signal is proportional to the original NO concentration of the sample.

$$NO_2^* \qquad\qquad \rightarrow \quad NO_2 \quad + \quad h\nu \qquad\qquad (2.5)$$

A schematic for the NO/NO$_y$ instrument is shown in Fig. 2.16. Ozone needed for the reaction chamber (Eq 2.4) is produced from filtered, dry air by an ozonator, which uses a high voltage to split oxygen and create ozone (Eq. 2.6-2.7).

$$O_2 + \quad energy \quad \rightarrow 2\,O(^3P) \tag{2.6}$$

$$O_2 + \quad O(^3P) \quad \rightarrow \quad O_3 \tag{2.7}$$
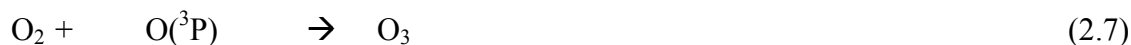
To measure NO, the sample is directly injected into the reaction chamber, while in "NO_y mode", the sample air is passed into a converter to catalytically convert NO_2 (and often other reactive nitrogen species) into NO ($NO_2 \rightarrow NO + O$) before injection into the reaction chamber. The converter, made of molybdenum, is heated to $325^\circ C$ and designed to convert NO_2 to NO, which can then react with ozone in the reaction chamber and create measureable radiation (Eq. 2.4-2.5). Due to the high temperature of the converter, however, it will also produce NO_2 from the decomposition of other NO_y species (Fig. 2.17), such as peroxynitrates ($ROONO_2$; Eq. 2.8), organic nitrates ($RONO_2$; Eq. 2.9), and nitric acid (HNO_3; Eq. 2.10), and, thus, the measurement of solely gas phase NO_2 concentrations, as designed, is not possible during photochemical oxidation reactions.
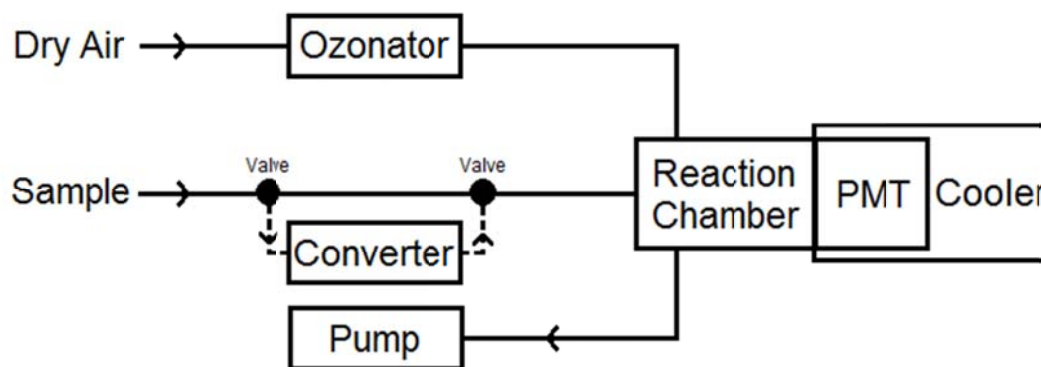
Figure 2.16. The NO/NO_y analyzer schematic.
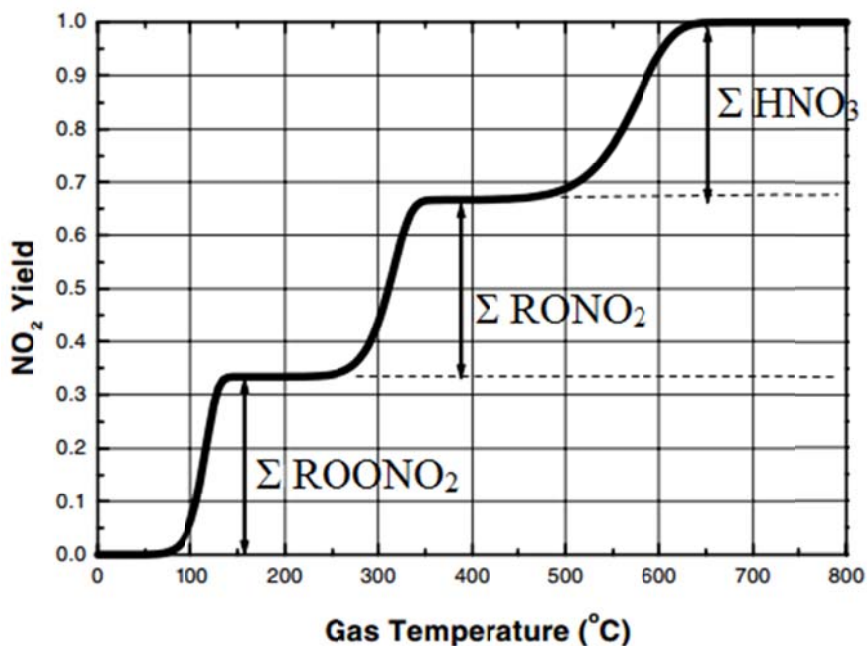
Figure 2.17. The modeled NO_2 yields plotted versus decomposition temperature for various NO_y species. The figure is adapted from Day et al. (2002).

$$ROONO_2 \; + \; heat\,(>100^oC) \; \rightarrow \; ROO^{\cdot} \; + \; {}^{\cdot}NO_2 \qquad\qquad (2.8)$$

$$RONO_2 \; + \; heat\,(>250^oC) \; \rightarrow \; RO^{\cdot} \; + \; {}^{\cdot}NO_2 \qquad\qquad (2.9)$$

$$HNO_3 \; + \; heat\,(>500^oC) \; \rightarrow \; HO^{\cdot} \; + \; {}^{\cdot}NO_2 \qquad\qquad (2.10)$$
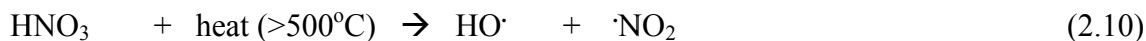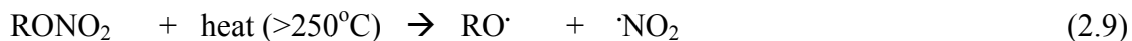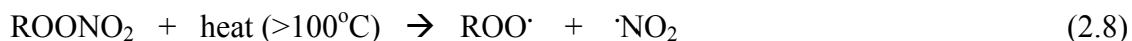
The NO/NO_y detector was calibrated for nitric oxide by diluting a standard NO cylinder (4.94 ppm in N_2, Praxair, Inc.) flow stream with varying nitrogen gas flow rates to produce a range of NO gas concentrations. The NO_y channel was not calibrated for this study. A calibration curve for NO is shown in Fig. 2.18.
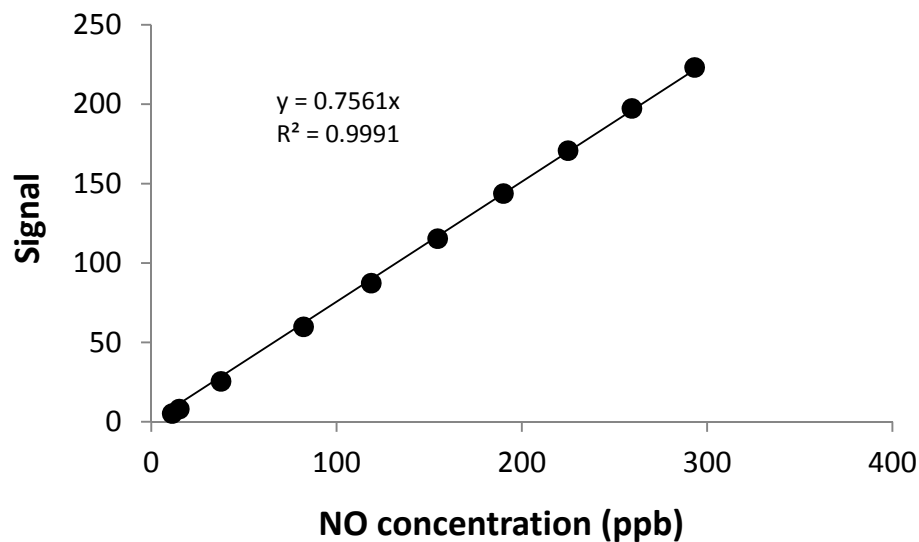
Figure 2.18. The NO/NO$_y$ detector calibration curve for nitric oxide.

2.2.8 Water Vapor

The introduction of H$_2$O vapor into the chamber was used in selected experiments to observe the dependency of the α-pinene-derived nitrate yield on chamber RH. Water was bubbled under a stream of ultra-pure air and chamber concentrations were measured using a commercial CO$_2$/H$_2$O analyzer (LI- 7000, LI-COR, Inc.), which uses differential absorption of infrared light centered at 2.59μm to determine water concentrations. Ultra-pure air passed through a DrieRite filter (CaSO$_4$) was used as the dry reference gas stream.

Calibration of the LICOR-7000 was accomplished by creating air streams with known water vapor concentrations. Water streams were produced by flowing dry air over a saturated solution of K$_2$SO$_4$ in an Erlenmeyer flask. The air above enclosed saturated salt solutions produces a constant relative humidity (below 100% RH), which, for K$_2$SO$_4$

at 25°C, is 97% RH (Wexler, 1992). Mass flow controllers (MFCs) were used to adjust

the relative flow rates of each air stream to produce a combined stream with a known

water vapor concentration. A schematic for the H_2O analyzer calibration is shown in Fig.

2.19. Before entering the H_2O analyzer, each line was vented to ensure that the reference

and sample cells were sampling atmospheric pressure air, as for the sample. A calibration

curve for the instrument is shown in Fig. 2.20.
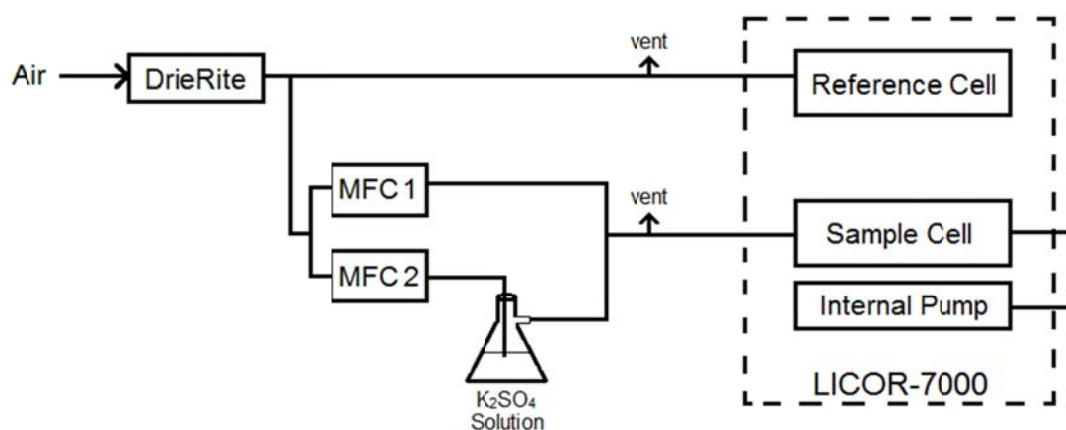
Figure 2.19. The calibration set-up for the LICOR-7000 H_2O analyzer involving a
saturated K_2SO_4 solution. Water/air concentrations were created by using the mass flow
controllers (MFCs) to adjust the air stream flow rates.
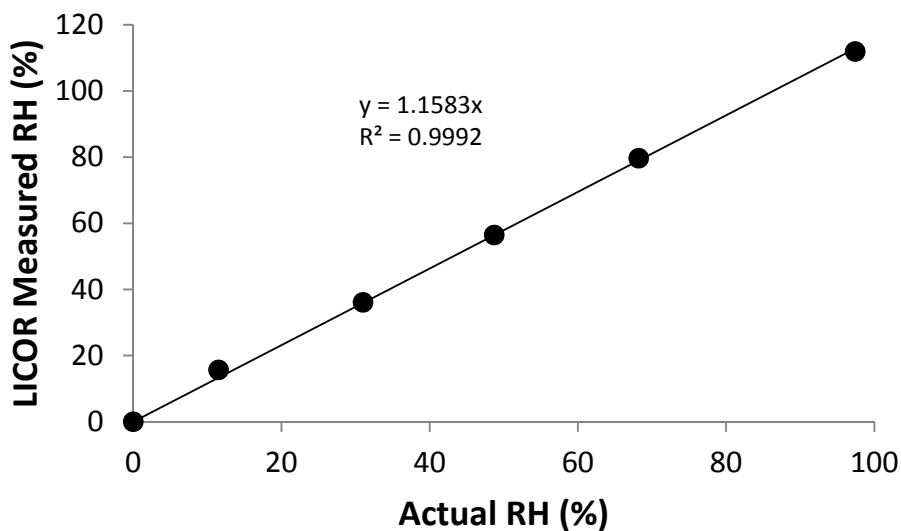
Figure 2.20. A calibration curve for the LICOR-7000 H$_2$O analyzer.

2.2.9 Procedure

Prior to experiments, the reaction chamber was flushed with the lights on for at least five chamber volumes with ultra-pure air. Blank samples from each instrument were collected prior to injection. Real-time samples were collected every 5 minutes for the SMPS, every 15 minutes for both the GC-FID and NO/NO$_y$ analyzer, and at both the beginning and end of the experiment for the H$_2$O analyzer. Experiments were concluded when approximately half of the α-pinene was consumed, which, on average, was one hour in length. All samplings lines used were 1/4" PFA Teflon except for the SMPS sampling line, which was copper, to prevent the buildup of static charge.

The average sampling rate from the reaction chamber, accounting for all instruments making real-time measurements, was calculated to be 0.51 L/min. For a 60 minute experiment, 31 L of the chamber would be consumed, which is less than 1% of

the total chamber volume (5500 L). Thus, a dilution correction was not applied to the real-time data.

2.2.10 Post-Experiment Sampling and Analysis

After experiments were completed, denuder-based filter samples were acquired for off-line analysis. The use of a denuder-based filter pack (Fig. 2.21) allowed for separate analysis of gas and particle phase products. The residence time within the annular denuder (20cm, XAD-4 coated, URG, Inc.) was sufficient for gas phase compounds to diffuse to and adsorb to the denuder walls while allowing particle phase component to pass to the filter. For clarification, based on a 0.74 second residence time, the root mean square distance (Z_{rms}) traveled by a gas phase product within the denuder was calculated to be 1.7 cm (Eq. 2.11), which is more than an order of magnitude greater than the distance between denuder annuli (Fig. 2.22). The filter pack consisted of a Teflon front filter (47mm, VWR, Inc.) to directly collect aerosol mass and a carbon-infused back-up filter (Grade 72, VWR, Inc.) to collect any gas phase artifacts that desorbed from the front filter.

$$Z_{rms} = (2Dt)^{1/2} \tag{2.11}$$

Here Z_{rms} is root mean square distance traveled of a gas phase compound for a given time (t) and D is the diffusion coefficient. For an α-pinene-derived organic nitrate, a diffusion coefficient of $2.06 \times 10^{-6}\,m^2\,s^{-1}$ was used.
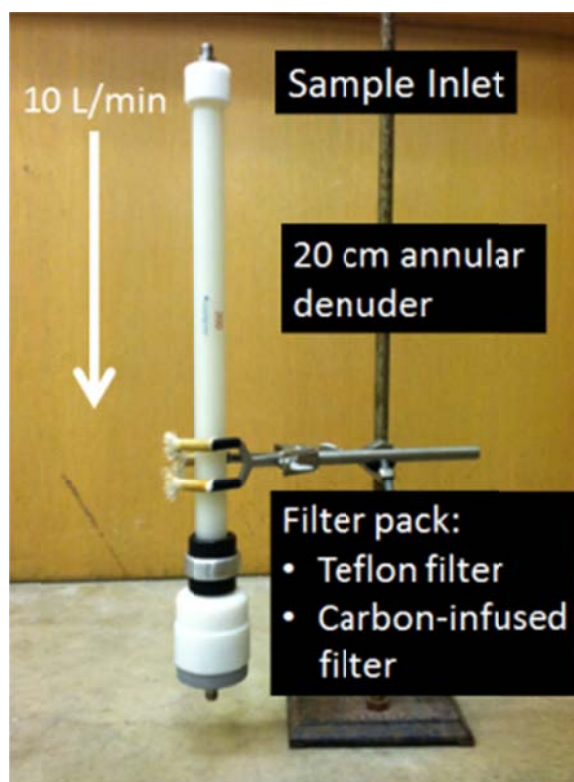
Figure 2.21. The denuder-based filter pack used for collection of gas and particle phase products from the photochemical chamber experiments.
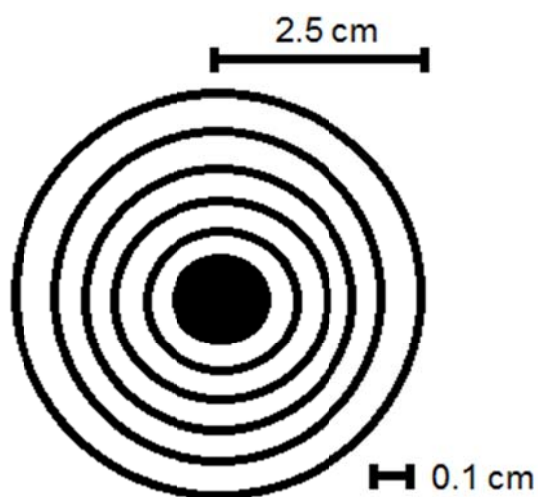
Figure 2.22. The cross section of the annular denuder. Concentric cylindrical sheaths were spaced 0.1 cm apart and the denuder radius was 2.5 cm.

Before the determination of organic nitrate concentrations was accomplished using liquid-sample Fourier transform infrared spectroscopy (FT-IR), the filters were extracted with tetrachlroethylene (C_2Cl_4) and sonicated for 45 minutes while the evaporated under nitrogen to ~25% of the original volume, and transferred into C_2Cl_4. Tetrachloroethylene was selected as a solvent due to its minimal absorption features in the infrared regions of interest.

Quantification of the total organic nitrate concentration was accomplished by integrating its unique asymmetric $-NO_2$ stretch at ~1640 cm^{-1} (Nielsen, 1995) in conjunction with the Beer-Lambert law (Eq. 2.12). The other two distinct bands related to the infrared absorption of organic nitrates, 1280 and 845 cm^{-1}, were not used in this study after Bruns et al. (2010) showed that quantitative results do not vary when integrating over one band compared the use of all three. The molar absorptivity of the α-pinene-derived nitrates produced in this study was assumed to be identical to that for an isobutyl nitrate standard. A previous study analyzing molecular extinction coefficients of alkyl nitrates observed a standard deviation of less than 7% among the compounds studied (Carrington, 1960), indicating that variability in the absorption cross section of organic nitrates in our study is likely not a significant source of error. A typical spectrum produced by the FT-IR spectrometer (Tensor 27, Brucker, Inc.) showing a filter extract and a blank extract is displayed in Figure 2.23, while a calibration curve for the instrument is shown in Fig. 2.24.

$$A \quad = \quad a \, b \, c \qquad\qquad\qquad\qquad (2.12)$$

Here A is the measured absorbance, a is the absorption cross section (L mol^{-1} cm^{-1}), b is the path length (cm), and c is the analyte concentration (mol L^{-1}).
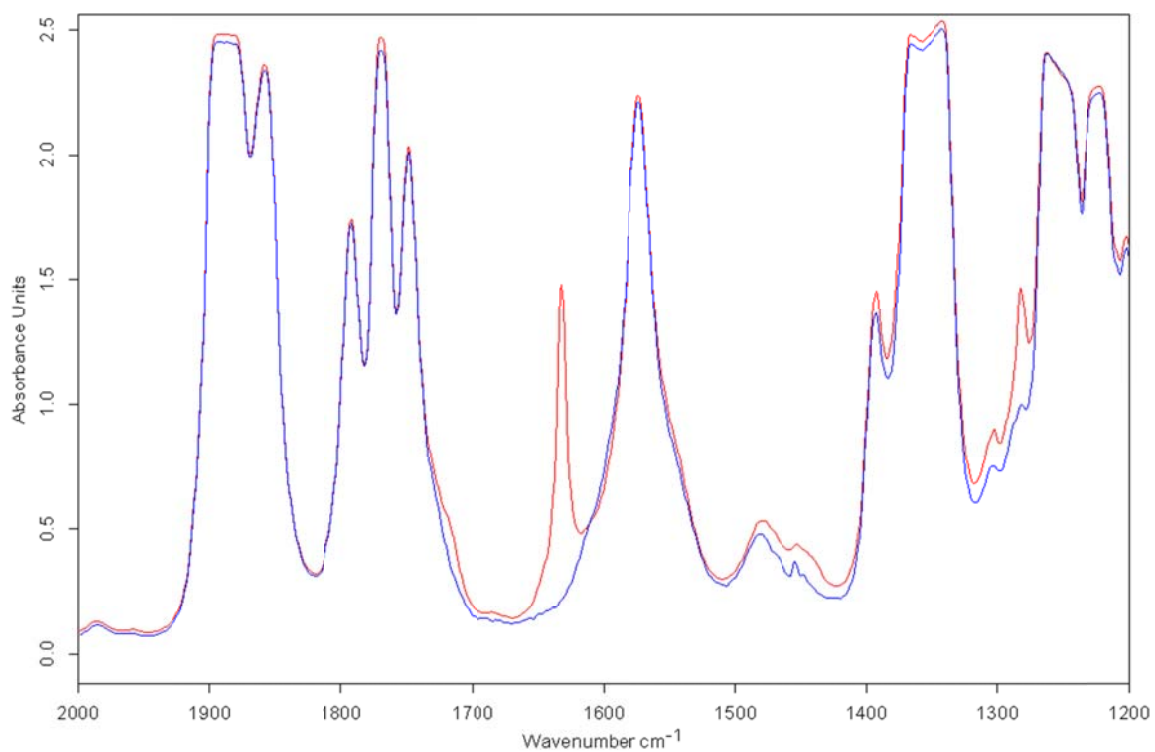
Figure 2.23. The FT-IR spectrum of a filter sample extracted in C_2Cl_4 (red) and a filter blank (blue). The peak at ~1640 cm-^{1} corresponds to the asymmetric $-NO_2$ stretch of organic nitrates.
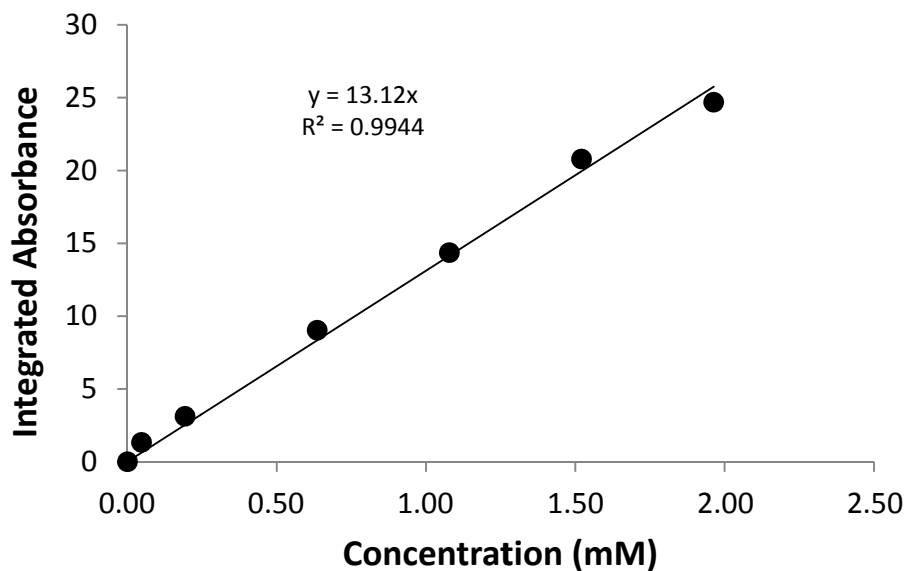
Figure 2.24. An FT-IR calibration curve using isobutyl nitrate.

The denuder was calibrated for both gas phase collection efficiency and particle transmission efficiency. Gas phase photochemical chamber isopropyl nitrate concentrations were measured using a GC-ECD (see Appendix I) both upstream and downstream of the denuder to conclude that the denuder had a gas phase collection efficiency of $\geq 98\%$. The particle transmission efficiency, determined to be $>99\%$, was measured at the conclusion of selected experiments using the SMPS to collect aerosol mass concentration measurements both upstream and downstream of the denuder.

To confirm that laminar flow was occurring within the denuder, its Reynolds number was calculated, R=312 (Eq. 2.13; Possanzini et al., 1983). Reynolds numbers ≤ 2000 indicate laminar flow.

$$R = \frac{v\,\delta}{\mu}$$

(2.13)

Here R is the Reynolds number, ν is the mean velocity of the air, μ is the air viscosity, and δ is the equivalent diameter of the denuder (defined as four times the ratio of denuder cross sectional area to its perimeter).

2.2.11 Data Corrections

The measured organic nitrate yields were corrected for chamber wall loss in both the gas and particle phases. Organic nitrate loss from consumption by the OH radical was not taken into consideration due to the current uncertainty in NO_x recycling efficiency from this reaction pathway, which ranges from -50% (Paulot et al., 2009) to +24% (Lee et al., 2014) for isoprene-derived nitrate reactions, meaning that the reaction of organic nitrates with the OH radical could produce a multi-nitrate species instead of breaking the $RONO_2$ bond to reform gas phase NO_x. It is important to note that measured organic nitrate yields in this study did not vary as a function of fractional α-pinene consumed, as shown in Fig. 2.25, which displays the fractional organic nitrate yields as a function of fraction of α-pinene consumed for all seeded experiments at low RH (0-20%).
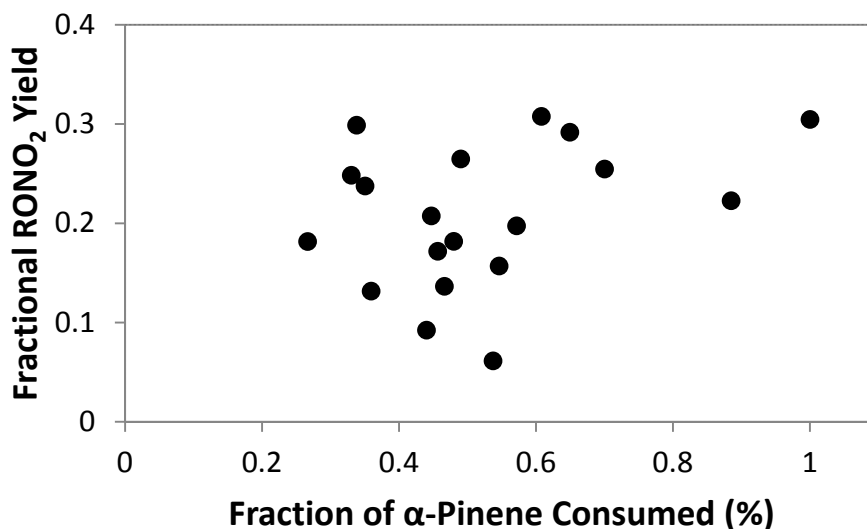
Figure 2.25. The fractional organic nitrate yields as a function of fractional α-pinene consumed for all seeded experiments at low RH (0-20%).

Both gas and particle phase wall loss processes followed first order kinetics (Eq. 2.14). The determination of wall loss rate constants was accomplished by manipulating Eq. 2.14 to form Eq. 2.15 and plotting the $\ln(A_o/A_t)$ term versus time. A linear regression of the plot derived from Eq. 2.15 will yield a slope equal to k, the first order wall loss rate constant.

$$A_t = A_o \exp(-kt) \tag{2.14}$$

Here A_t is the organic nitrate concentration at time t, A_o is the original organic nitrate concentration, and k is the first order wall loss rate constant

$$\ln(A_o/A_t) = kt \tag{2.15}$$

The particle phase wall loss rate constant was determined using the SMPS to measure aerosol mass concentrations as a function of time following an α-pinene

oxidation experiment within the chamber, with the lights off. Data for particle phase wall loss and the determination of the first order rate constant (8.18×10^{-5} s^{-1}) are shown in Fig. 2.26. The wall loss corrected organic nitrate concentrations can be calculated by solving for A_o in Eq. 2.14. The time used in this correction calculation is one-half the total experiment and sampling time.
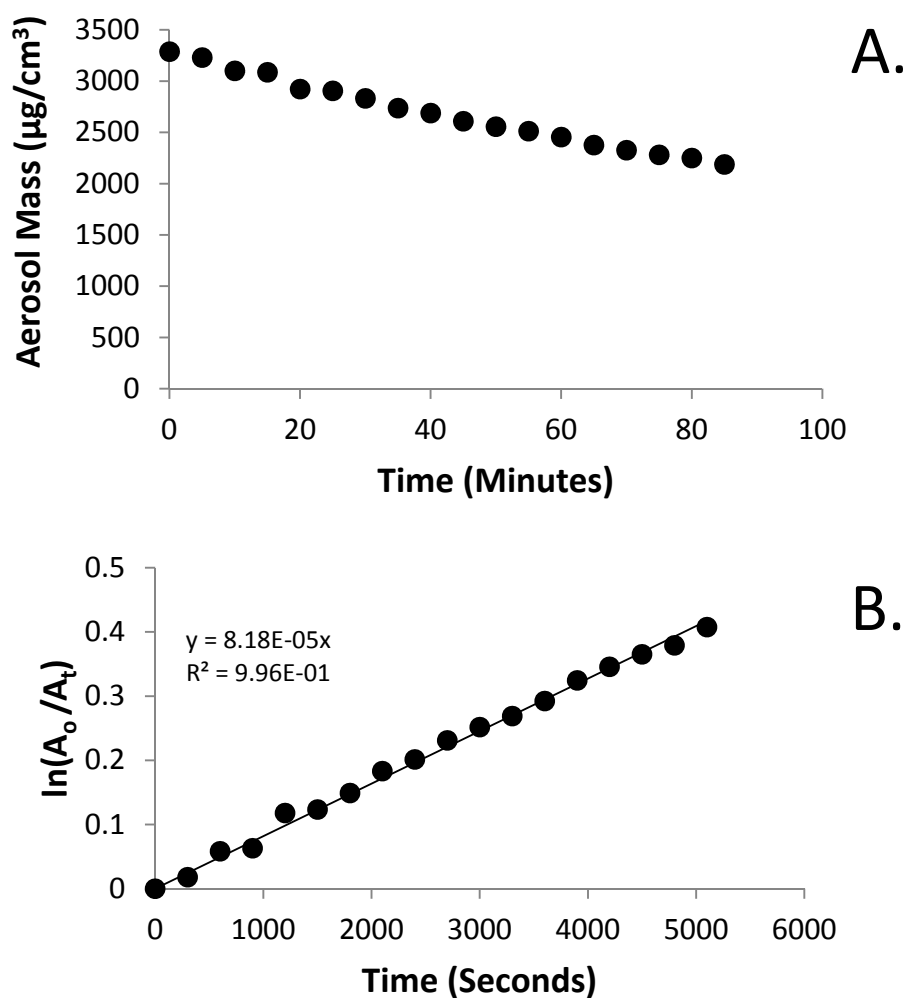
Figure 2.26. The (A) loss of aerosol mass as a function of time within the reaction chamber and (B) the plot determining the first order wall loss rate constant.

Gas phase wall loss rate constants were determined in a similar manner as the particle phase wall loss rate constants except a GC-(NICI)-MS (see Chapter 3) was used to identify organic nitrates using the *m/z* 46 ion in the negative ion mode (Worton et al., 2008). Figure 2.27 displays both the total ion current chromatogram (TIC) and the *m/z* 46 extracted ion current chromatogram (EIC) from the GC-(NICI)-MS at the end of an experiment, showing four main organic nitrates peaks in the EIC. The loss of each organic nitrate peak (retention times: 11.85, 12.23, 12.57, and 12.91 minutes) was measured as a function of time and an average wall loss rate constant was determined to be $2.3 \times 10^{-4} \, s^{-1}$.
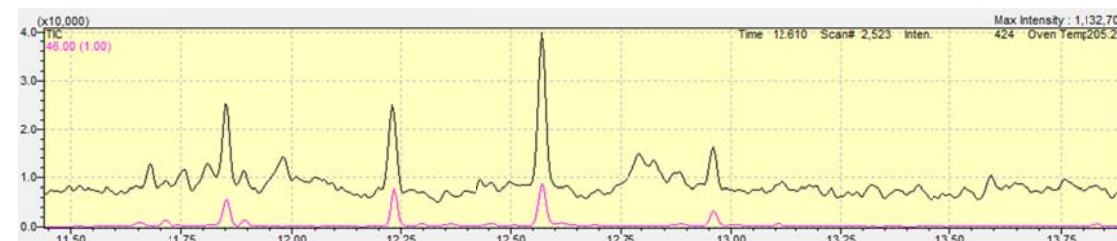
Figure 2.27. The TIC (black) and *m/z* 46 EIC (pink) from the GC-(NICI)-MS following an α-pinene chamber experiment.

Corrections were also made for dilution of the reaction chamber during the denuder-based filter sampling period. Since sampling occurred at 10 L/min, a first order loss rate constant of $0.11 \, hr^{-1}$ was used ($600 \, L \, hr^{-1}/5500 \, L = 0.11 \, hr^{-1}$) to calculate original $RONO_2$ concentrations (A_o from Eq. 2.14). Typical sampling times were 1.5 hr., which corresponds to an 8.5% yield correction.

2.3 Results

The α-pinene and aerosol mass concentrations over a typical seed aerosol

experiment are shown in Fig. 2.28. The aerosol mass increased linearly after

approximately 10 minutes. The slight induction period in aerosol growth is likely a result

of the time needed to create sufficient gas phase product concentrations that could

condense onto the aerosol precursors.
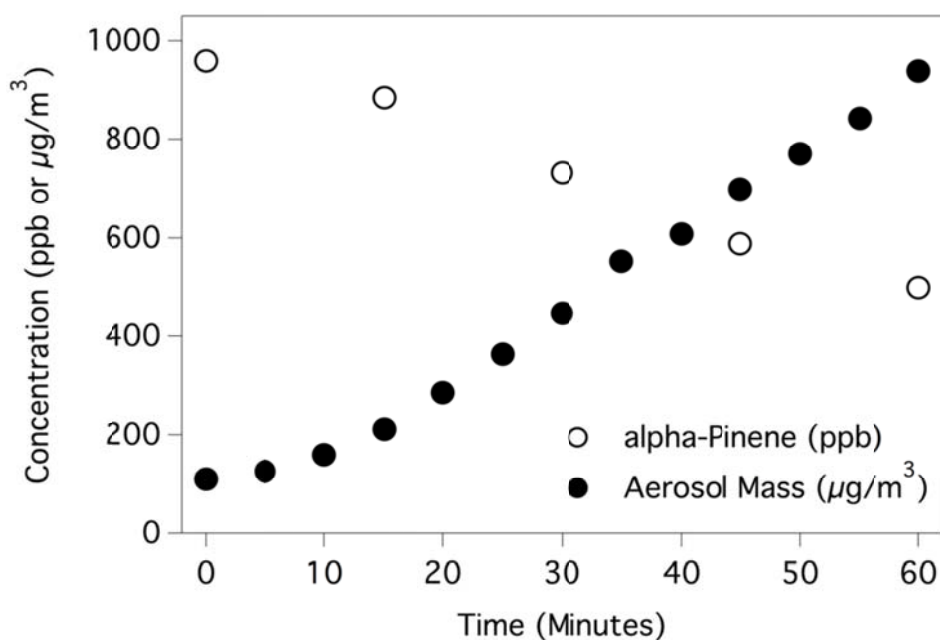
Figure 2.28. The α-pinene and aerosol mass concentrations as a function of time for a neutral seed experiment. The open circles (○) represent α-pinene (ppb) while the closed circles (●) represent the aerosol mass concentration ($\mu g/m^3$). Initial α-pinene and seed aerosol concentrations were 960 ppb and 110 $\mu g/m^3$, respectively.

Measurements made using the NO/NO$_y$ instrument over the course of a reaction chamber experiment are shown in Fig. 2.29. The peaks in NO data correspond to injections of nitric oxide to ensure ozone concentrations were minimized.
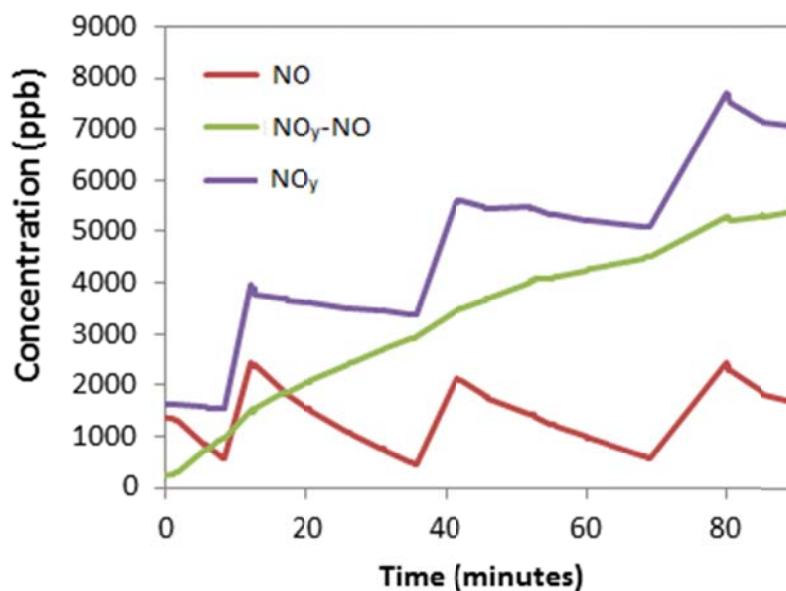
Figure 2.29. The NO, NO$_y$-NO, and NO$_y$ concentrations measured for an α-pinene oxidation experiment. The NO$_y$ concentration measurement does not include HNO$_3$.

The production of secondary organic aerosol (SOA) was also observed in unseeded aerosol experiments. Aerosol mass concentrations in these experiments grew very rapidly and their size distributions were quickly (within 20 minutes) beyond the measureable range of the SMPS (up to 1.0 μm mobility diameter). The fast SOA production from unseeded aerosol experiments is a result of small aerosol number concentrations, an average of 3400 cm^{-3} for unseeded aerosol experiments compared to 76,000 cm^{-3} for seeded experiments, and less surface area for organics to condense onto,

leading to homogenous nucleation of gas phase products. Without final aerosol mass concentration measurements, the aerosol yields were unable to be calculated for the unseeded experiments.

The aerosol yield, defined as the SOA mass produced divided by α-pinene mass consumed, was highly variable in all experiments and was not statistically different based on seed aerosol composition or chamber relative humidity. An average value of $32\pm14\%$ was determined for this study, which is in statistical agreement with several previous studies (Hoffmann et al., 1997; Jaoui and Kamens, 2001; Lee et al., 2006; Noziere et al., 1999). In addition to individual experiments in this study, reported aerosol yields from the OH radical oxidation of α-pinene have a wide range of values, from 4-45% (Noziere et al., 1999; Jaoui and Kamens, 2000), the cause of which is currently unknown (Henry et al., 2012).

A recent study from Henry et al. (2012) could not attribute the variability in aerosol yields from α-pinene oxidation to variations in OH radical concentration, seed aerosol concentration, or the amount of ozone produced from the reaction. Thus it is clear that the aerosol yield from BVOC oxidation is not constant and depends on several factors, some of which may be unknown, indicating that further research into the mechanisms of aerosol production is necessary. Aerosol yields from both this study and Henry et al. (2012) did, however, have a similar trend in aerosol yields based on the amount of SOA produced, as shown in Fig. 2.30. Aerosol yields greater than 100% can be attributed to the incorporation of O and N from gas phase oxidants into aerosol phase products.
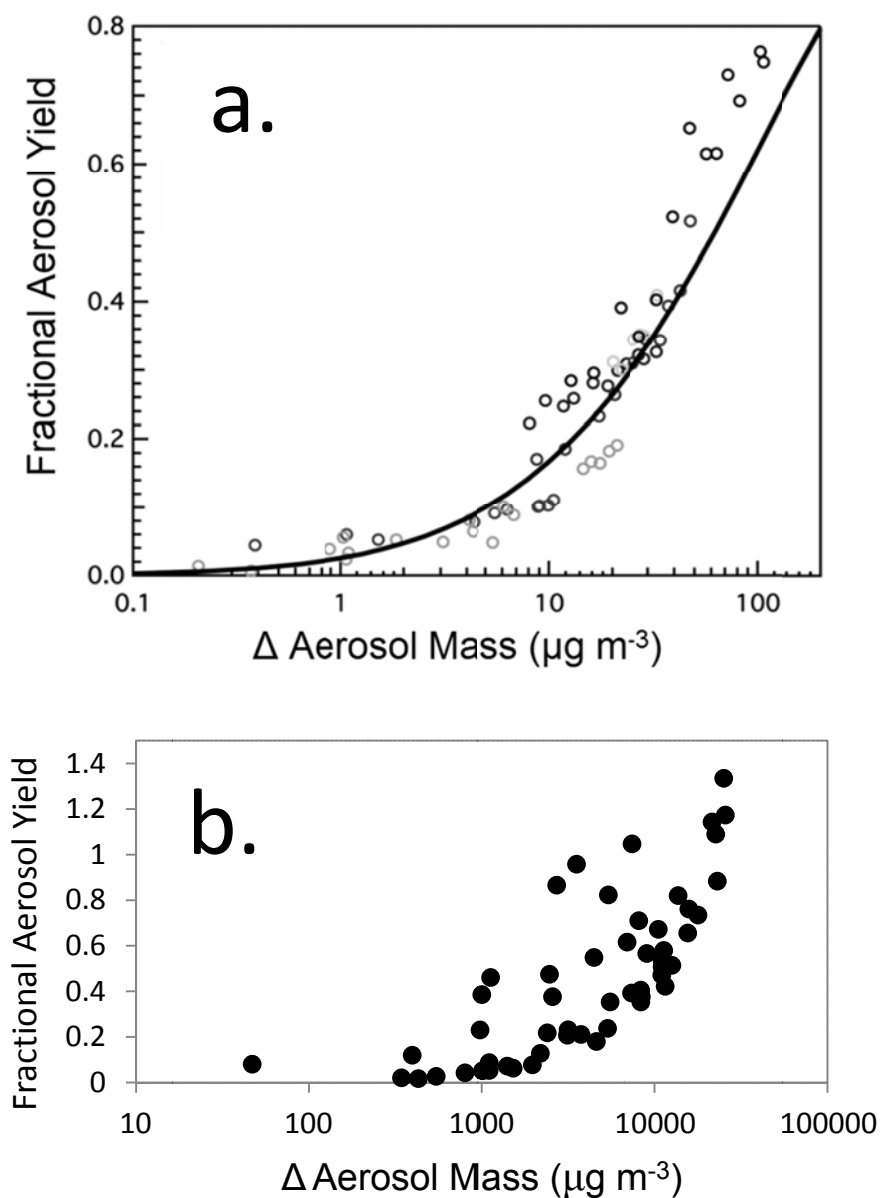
Figure 2.30. The aerosol yields from the OH radical oxidation of α-pinene from (a) Henry et al. (2012) and (b) this study.

2.3.1 Organic Nitrate Yields

Previous studies have determined organic nitrate yields by plotting the measured $RONO_2$ concentration versus $-\Delta[VOC]$ (e.g. O'Brien et al., 1998). This method is useful

if multiple $RONO_2$ measurements can be made over the course of the experiment. In this study, only one organic nitrate measurement could be made at the end of an experiment, due to the high chamber volume needed for sampling (>1000L). Organic nitrate yields were calculated by dividing the total organic nitrate concentration, measured using FT-IR, by the amount of α-pinene consumed. The organic nitrate yields in this study were highly dependent on both the chamber relative humidity (RH) and seed aerosol composition. Single point $RONO_2$ yields for both seed aerosol scenarios plotted against RH are shown in Fig. 2.31 while the unseeded $RONO_2$ yields are shown in Fig. 2.32. The analytical expression used to determine the experimental organic nitrate yields is shown in Eq. 2.16 (both the extraction efficiency and APN absorption cross section relative to the isobutyl nitrate standard were assumed to be unity). The relative uncertainties of the FT-IR and GC-FID signals relative to the blank, 4% and 8%, respectively, were determined using Eq. 2.17. The total measured organic nitrate yield relative uncertainty was determined using Eq. 2.18, which included the combined relative uncertainties of the FT-IR signal, GC-FID signal, FT-IR sensitivity (2%), GC-FID sensitivity (2%), assumed absorption cross section of APNs (7%), extraction volume (0.006%), extraction efficiency (1%), and chamber air sample volume (3%). The propagation of all known uncertainties yielded a relative uncertainty of 12% (Eq. 2.18), which corresponds to an absolute uncertainty (0.032) less than one-half the total uncertainty reported for the organic nitrate branching ratio using the linear regression method (see below).

$$
\frac{RONO_2}{Yield} = \frac{\left(\dfrac{\text{FTIR signal (peak area) - FTIR blank (peak area)}}{\text{FTIR sensitivity (peak area L mol}^{-1})} \times \text{rel. abs. cross section} \times \text{extraction volume (L)} \times \text{extraction efficiency}\right)}{\dfrac{\text{air sample volume (L)} \times 1 \text{ mol air}/24.5 \text{ L}}{\left(\dfrac{\text{FID signal}_{final}\text{ (peak area) - FID signal}_{initial}\text{ (peak area)}}{\text{FID sensitivity (peak area ppb}^{-1})}\right)}} \times 10^9 \text{ ppb} \quad (2.16)
$$

$$
\text{Signal relative uncertainty} = \frac{\left([\text{absolute uncertainty (signal)}]^2 + [\text{absolute uncertainty (blank)}]^2\right)^{1/2}}{\text{measured signal - blank signal}} \quad (2.17)
$$

$$
\text{Relative uncertainty} = \left[\sum_i (\delta a_i / a_i)^2\right]^{1/2} \quad (2.18)
$$

Here $\delta a_i / a_i$ corresponds to the relative uncertainty of a given parameter, i (see above).
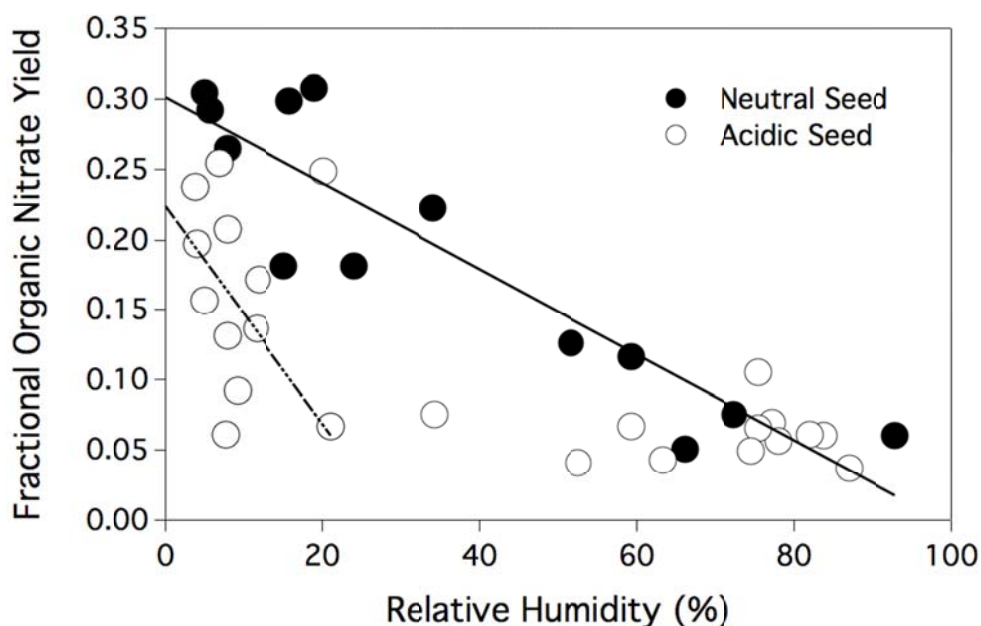
Figure 2.31. The total organic yield as a function of chamber relative humidity for both the acidic seed aerosol ($\circ$) and neutral seed aerosol ($\bullet$) experiments. Each data point represents the organic nitrate yield from a single experiment. The lines shown are regressions used to estimate the 0% RH total $RONO_2$ yield (see text).
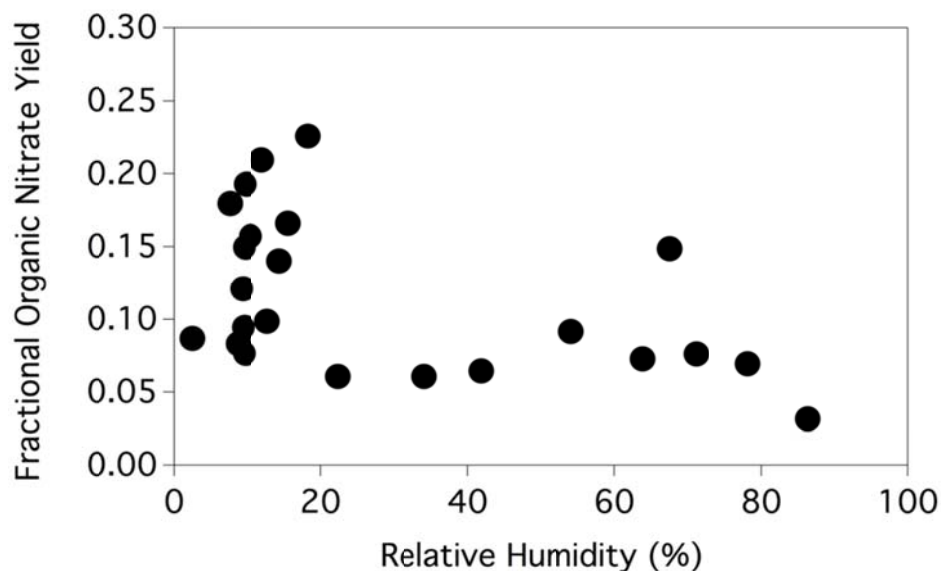
Figure 2.32. The total organic nitrate yield as a function of chamber relative humidity for the unseeded aerosol experiments. Each data point represents the organic nitrate yield from a single experiment.

The decrease in observed total (gas + particle phases) organic nitrate yields with chamber relative humidity is likely the result of gas phase $RONO_2$ partitioning into the particle phase followed by rapid consumption via hydrolysis. Compared to the neutral seed aerosol conditions, the organic nitrate yields from the acidic seed aerosol experiments decrease very rapidly at low relative humidity (~0 to 20% RH) followed by a more mild decrease to total $RONO_2$ yields as low as ~5% as chamber RH goes from 20 to 90%. The neutral seed aerosol experiments have a consistent decrease in total $RONO_2$ yields from low to high RH. The sharp decrease in observed $RONO_2$ yields at low RH indicates that the secondary organic aerosol created in these experiments can readily uptake water under dry conditions to allow for hydrolysis reactions to occur.

The drastic decrease in the total organic nitrate yields with RH from the acidic seed experiments compared to the neutral seed conditions (Fig. 2.31) can be explained by the nature of the hydrolysis reaction under acidic conditions. A reaction scheme for the specific acid-catalyzed hydrolysis of a general β-hydroxy organic nitrate via an S_N1 mechanism is shown in Fig. 2.33. A previous aqueous phase study showed that hydrolysis reaction rates of β-hydroxy nitrates increased with solution acidity (Darer et al. 2011), which, along with the results from this study, indicates that an acid-catalyzed mechanism is likely responsible for particle phase organic nitrate hydrolysis. Additionally, the dominant organic nitrates expected to be produced are tertiary (Fig. 2.1) and, based on hydrolysis lifetimes determined from Darer et al. (2011), which ranged from 3.7 to 40 minutes, have potential to quickly hydrolyze well within the timescales of these experiments. Darer et al. (2011) measured hydrolysis rates for tertiary β-hydroxy nitrates to be much faster than their primary counterparts, with lifetimes as short as 3.7 minutes.
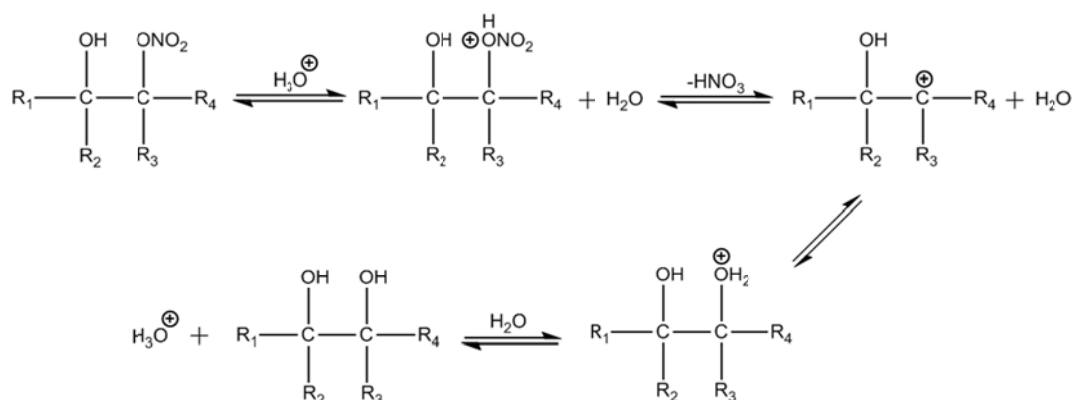
Figure 2.33. The proposed acid-catalyzed S_N1 hydrolysis mechanism responsible for increased particle phase hydrolysis in the acidic seed aerosol experiments.

The total organic nitrate yields for the unseeded aerosol experiments also exhibited a sharp decrease with increasing chamber RH (Fig. 2.32). Assuming the degree of aerosol phase hydrolysis is correlated to particle acidity, it is likely that the uptake of gas phase nitric acid (HNO_3), produced via reaction of OH radical with NO_2 (Eq. 2.19), has influence on the pH of the particles. Particle phase nitric acid may also be produced at the surface from the hydrolysis of NO_2 (Eq. 2.20; Murdachaew et al., 2013).

$$OH \; + \; NO_2 \; \rightarrow \; HNO_3 \tag{2.19}$$

$$2NO_2 + \; H_2O \text{ (surface)} \; \rightarrow \; HNO_3 + \; HONO \tag{2.20}$$

As seen in Figs. 2.31 and 2.32, the $RONO_2$ yields have a higher degree of scatter at dry conditions (low RH). This is attributed to the extreme sensitivity of the organic nitrate yields to aerosol water content and aerosol pH over this range. Additionally, the partitioning of gas phase products will be dependent on the composition and total mass concentration of the particles (Pankow, 1994), the latter of which also varied considerably between experiments.

While we were able to measure neither the aerosol water content nor the aerosol pH in this study, an estimation for aerosol pH can be made by using the Extended-Aerosol Inorganic Model (E-AIM) described by Wexler and Clegg (2002) (http://www.aim.env.uea.ac.uk/aim/aim.php). The E-AIM estimates the acidity of the seed aerosol conditions in this study to be approximately pH~5 for neutral seed aerosol and pH<1 for the acidic seed aerosol. These estimations are only valid for the initial conditions because, once the experiment begins, nitric acid (HNO_3) will be produced (Eqs. 2.19-2.20), influencing the pH of particles throughout the experiment.

Since the observed organic nitrate yields varied greatly with chamber relative humidity, a true $RONO_2$ yield could not be measured for α-pinene oxidation without assumed losses within the aerosol phase. To correct for aerosol phase losses, a linear extrapolation of seed aerosol data at low RH (0 to 20%) was completed to the zero humidity intercept, as seen in Fig. 2.31. We assume that the intercept then represents a no-loss condition, in which case it then represents the branching ratio ($k_A/(k_A+k_B)$; see Fig. 2.1). The resulting linear regressions yielded y-intercepts of 30±4% and 22±6% for the neutral and acidic seed aerosol cases, respectively. These values correspond to a total organic nitrate yield of 26±7%, after combining the standard errors of the y-intercepts. A statistically significant slope from a least squares fit of the unseeded data was unable to be determined, based on the high degree of scatter within the data set, and a total organic nitrate yield could not be reported.

Due to the sharp decrease with RH in the observed $RONO_2$ yields from the acidic seed aerosol experiments, only the low RH (0-20%) data was used for the linear extrapolation to the zero humidity intercept. As displayed in Fig. 2.31, the use of a larger range would underestimate the determined yield. The data point at ~20% RH was omitted from the regression analysis after it was determined that its Cook's distance (2.7) was significantly greater (7.5x) than the value suggested for removal (4/n=0.36, where n is the number of observations). Cook's distance is a standard statistical test used for identifying outliers in a linear regression data set (Cook, 1977).

The determined total organic nitrate yield, 26±7%, represents the $RONO_2$ branching ratio (k_A/k_A+k_B) for α-pinene oxidation under high NO_x conditions (Fig. 2.1), assuming that all peroxy radicals react with NO, and that there are no unknown losses of

organic nitrates. This value is higher than the ~1% reported by Aschmann et al. (2002) but does not statistically differ from the 18±9% determined by Noziere et al. (1999), who also used FT-IR to determine organic nitrate concentrations.

The rapid hydrolysis of organic nitrates in the aerosol phase has very important implications for the fate gas phase NO_x. The formation of organic nitrates creates a temporary sink for gas phase NO_x as further reactions, such as oxidation or photolysis in either the gas or particle phase, may release NO_x back into the gas phase. However, the conversion of $RONO_2$ species to the analogous alcohol within the aerosol phase will convert the nitrooxy group in the organic nitrate to a free nitrate ion, which will remain relatively longer (depending on pH) in the particle phase due to its lower reactivity, effectively eliminating the possibility for further oxidation of organic nitrates and the release of NO_x back into the gas phase. An example of the nitrate ion's low reactivity is demonstrated by its photolysis rate, which, compared to organic nitrates, is at least a couple orders of magnitude smaller (Suarez-Bertoa et al., 2012; Zafiriou and True, 1979; Galbavy et al., 2007). Thus, deposition of the nitrate ion would be the main pathway of α-pinene-derived nitrate removal from the atmosphere. The relatively large organic nitrate yield from a monoterpene reported here (26±7%), along with fast hydrolysis in the aerosol phase, likely makes organic nitrate production from monoterpenes an important sink for NO_x, limiting ozone production.

Additionally, the organic nitrate branching ratio of 26±7% is much larger, by about a factor of 3x, than what would be estimated from the β-hydroxy nitrate branching ratio trend described O'Brien et al. (1998) (see Chapter 1). The large $RONO_2$ yield from

α-pinene may indicate that other non-β-hydroxy nitrate species are contributing to the

RONO$_2$ production from this oxidation pathway.

A likely mechanism for producing more diverse hydroxy nitrate species from α-pinene oxidation by OH/NO involves the gas phase rearrangement of the alkyl radical (Fig. 2.34). Theoretical calculations by Peeters et al. (2001) suggest that rearrangement of the radicals formed from the OH radical oxidation of α-pinene can occur before oxygen can add to the radical, producing at least four different organic nitrate isomers. It is important to note that the proposed organic nitrate products are either tertiary or secondary and, thus, are likely candidates to undergo hydrolysis, based on suggestions from Darer et al. (2011).
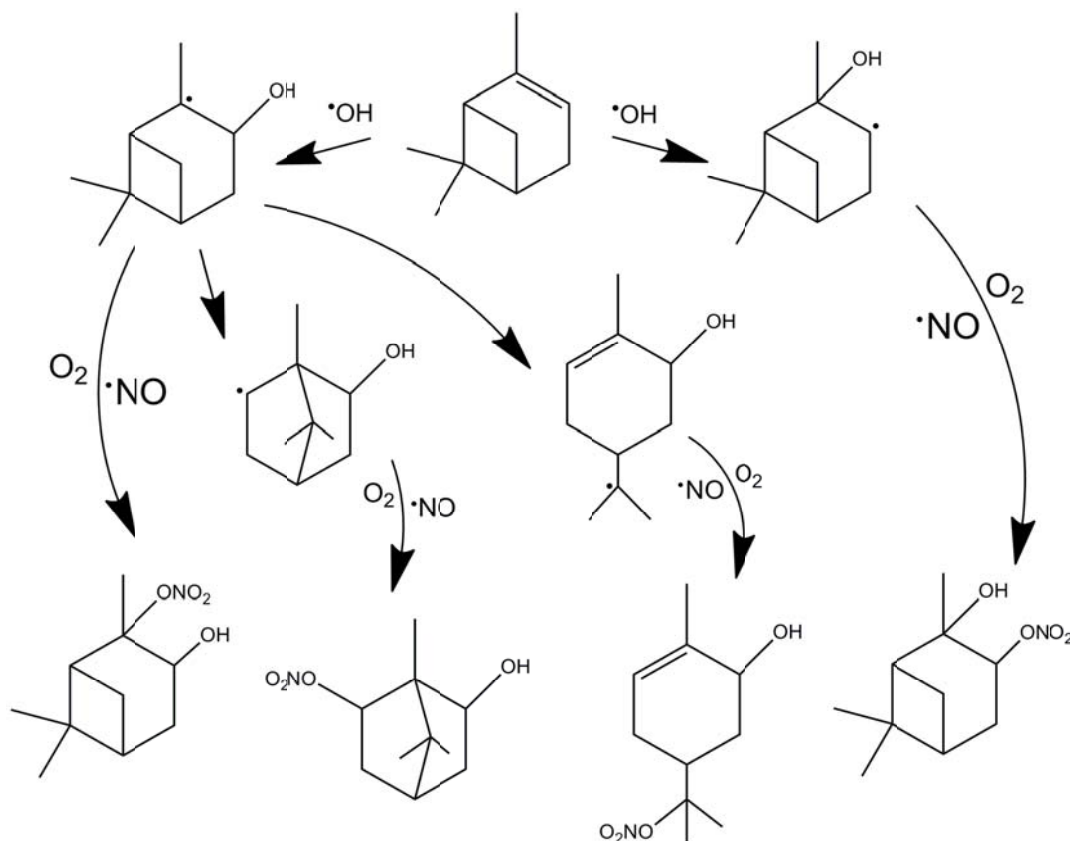
Figure 2.34. The gas phase rearrangement of α-pinene radicals formed from OH radical oxidation and the four organic nitrates isomers produced from each pathway. The proposed chemistry is based on Peeters et al. (2001).

Using the denuder-based filter sampling technique, the organic nitrate yields for the gas and particle phases could be measured separately. The gas phase (A_i) and particle phase (F_i) organic nitrate concentrations from each individual seeded aerosol experiments, along with the RH and total $RONO_2$ yield, are shown in Table 2.2 while the analogous information for the unseeded experiment is shown in Table 2.3.

Table 2.2. Summary of results for the neutral and acidic seed experiments. A_i and F_i correspond to gas phase and particle phase $RONO_2$ concentrations, respectively.

Exp. Date	Seed Aerosol	RH (%)	Δ α-Pinene (ppb)	A_i (ppb)	F_i (μg/m³)	$RONO_2$ Yield (%)
10/17/2011	Neutral	4.90	433.0	9.9	1073	30
11/16/2011	Neutral	5.60	104.0	7.1	202	29
11/19/2011	Neutral	7.80	2026	203	2937	26
11/3/2011	Neutral	15.1	1257	129	879	18
10/24/2011	Neutral	18.9	587.0	30	1319	31
11/14/2011	Neutral	23.9	461.0	38	404	18
6/23/2011	Neutral	34.1	655.0	25	1064	22
11/27/2012	Neutral	51.6	3957	122	3315	13
11/22/2012	Neutral	59.3	3485	104	2656	12
11/15/2012	Neutral	66.0	3146	65	835	5.1
11/9/2012	Neutral	72.3	3455	110	1337	7.6
12/1/2012	Neutral	92.9	3021	56	1108	6.0
6/16/2012	Acidic	3.70	2771	342	2779	24
6/12/2012	Acidic	4.00	3704	132	5267	20
6/7/2012	Acidic	4.90	3680	279	2629	16
5/11/2012	Acidic	6.70	3339	482	3236	25
5/29/2012	Acidic	7.50	576.0	34	15	6.1
5/24/2012	Acidic	7.80	1922	225	1530	21
6/24/2012	Acidic	7.80	556.0	5.2	598	13
9/11/2012	Acidic	9.10	3340	275	290	9.2
6/27/2013	Acidic	11.5	3870	77	3966	14
9/25/2012	Acidic	11.7	4178	128	5188	17
5/19/2012	Acidic	20.1	1166	108	1592	25
8/24/2012	Acidic	21.0	4843	219	932	6.7
8/17/2012	Acidic	34.3	2963	198	229	7.5
8/20/2012	Acidic	52.5	1948	33	413	4.1
8/8/2012	Acidic	59.3	1876	126	0.0	6.7
8/14/2012	Acidic	63.3	4341	135	448	4.3
7/25/2012	Acidic	74.5	4136	188	141	4.9
7/15/2012	Acidic	75.5	1998	132	0.0	6.6
7/22/2012	Acidic	75.5	922.0	97	0.0	11
7/8/2012	Acidic	77.2	348.0	24	0.0	7.0

Table 2.2. Continued.

Exp. Date	Seed Aerosol	RH (%)	Δ α-Pinene (ppb)	Ai (ppb)	Fi (µg/m3)	RONO2 Yield (%)
7/11/2012	Acidic	78.0	2822	161	0.0	5.7
8/5/2012	Acidic	82.0	3480	212	0.0	6.1
7/28/2012	Acidic	83.7	1573	95	0.0	6.0
8/1/2012	Acidic	87.0	3147	117	0.0	3.7

Table 2.3. Summary of results for the unseeded α-pinene oxidation experiments. The A_i and F_i parameters correspond to the concentration of $RONO_2$ in the gas phase and particle phase, respectively.

Exp. Date	Seed Aerosol	RH (%)	Δ α-Pinene (ppb)	A_i (ppb)	F_i (µg/m^3)	$RONO_2$ Yield (%)
5/3/2012	NONE	2.40	3652	186	1152	8.7
3/22/2012	NONE	7.50	2217	132	2339	18
9/19/2012	NONE	8.60	3680	19	2524	8.3
4/23/2012	NONE	9.20	4737	178	3473	12
2/8/2012	NONE	9.40	1187	78	299	9.4
3/13/2012	NONE	9.60	2730	110	2620	15
9/27/2012	NONE	9.60	3749	115	1521	7.7
2/17/2012	NONE	9.70	2515	182	2664	19
2/13/2012	NONE	10.4	1294	74	1134	16
4/17/2012	NONE	12.0	2505	126	3500	21
2/28/2012	NONE	12.8	4212	218	1741	9.9
4/4/2012	NONE	14.4	4082	219	3104	14
1/24/2012	NONE	15.6	640.0	32	660	17
3/9/2012	NONE	18.3	155.0	23	106	23
2/1/2012	NONE	22.3	3648	55	1460	6.1
1/20/2013	NONE	34.1	3142	34	1372	6.1
1/13/2013	NONE	41.9	4445	33	2225	6.4
10/23/2012	NONE	54.2	3475	68	2207	9.2
1/16/2013	NONE	63.8	4445	52	2392	7.3
11/2/2012	NONE	67.4	3152	78	3438	15
1/24/2013	NONE	71.0	2311	47	1134	7.6
1/9/2013	NONE	78.2	3472	50	1680	6.9
11/6/2012	NONE	86.3	4500	45	853	3.2

The particle phase organic nitrate concentrations were used to determine the fractional contribution of $RONO_2$ to SOA produced. Only dry experiments (0-20% RH) were taken into account in the determination, due to rapid particle phase hydrolysis. Assuming a molecular mass of 215 g/mol, the total contribution of $RONO_2$ to the SOA produced was 18±4% by mass, which was determined by plotting the aerosol phase $RONO_2$ concentration against the SOA mass produced from all low RH experiments (Fig. 2.35). The 18±4% relative mass yield is in good agreement with a previous study that also reported an 18% $RONO_2$ aerosol percentage by mass using a flow-tube to study the α-pinene/OH/NO_x system in the absence of seed aerosol (Rollins et al., 2010). This implies in BVOC-impacted areas, organic nitrates are likely to contribute significantly to SOA production, as discussed in previous studies (e.g. Hao et al., 2014).
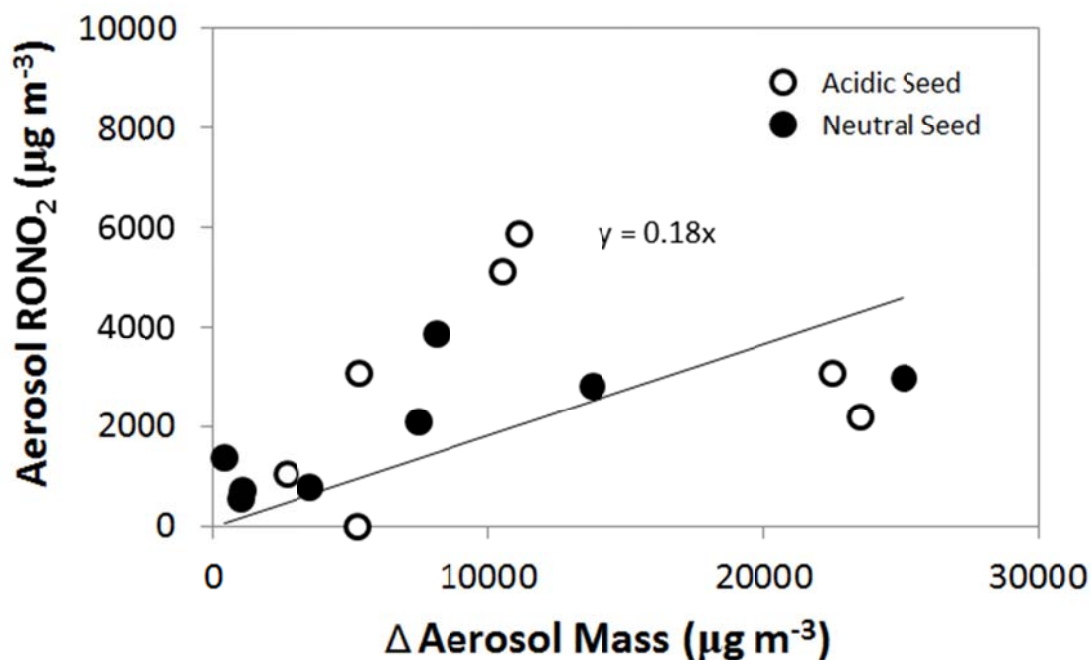
Figure 2.35. The organic nitrate ($RONO_2$) aerosol mass concentration (μg m^{-3}) plotted against total aerosol mass produced (μg m^{-3}) from the seeded aerosol experiments at low RH (0-20%). The slope of the linear regression represents the percentage contribution of $RONO_2$ species to SOA.

Similar to the total organic nitrate yields, the particle phase organic nitrate mass fraction yields were highly dependent on seed aerosol composition and chamber relative humidity. Owing to increased aerosol phase hydrolysis, the particle phase yields from the acidic seed experiments decreased much faster with increasing RH compared to the neutral seed experiments, as shown in Figs. 2.36 and 2.37. In the acidic experiments, particle phase yields fell to ~0% by ~80% RH. Each plot in Figs. 2.36 and 2.37 has the regression confidence limits shown for each data series, which were calculated for each data set using Eq. 2.21:

$$\text{Confidence Limit} = \pm\ t_{n-2} \cdot S_{xy} \cdot \left(\frac{1}{n-2} \ \frac{(x_i - \bar{x})}{\sum (x_i - \bar{x})^2} \right)^{1/2}$$

(2.21)

Here t_{n-2} is the critical t-value for n-2 degrees of freedom, S_{xy} is the standard error of the regression, x_i is a given data point, and $\bar{x}$ is the average value for the data set.
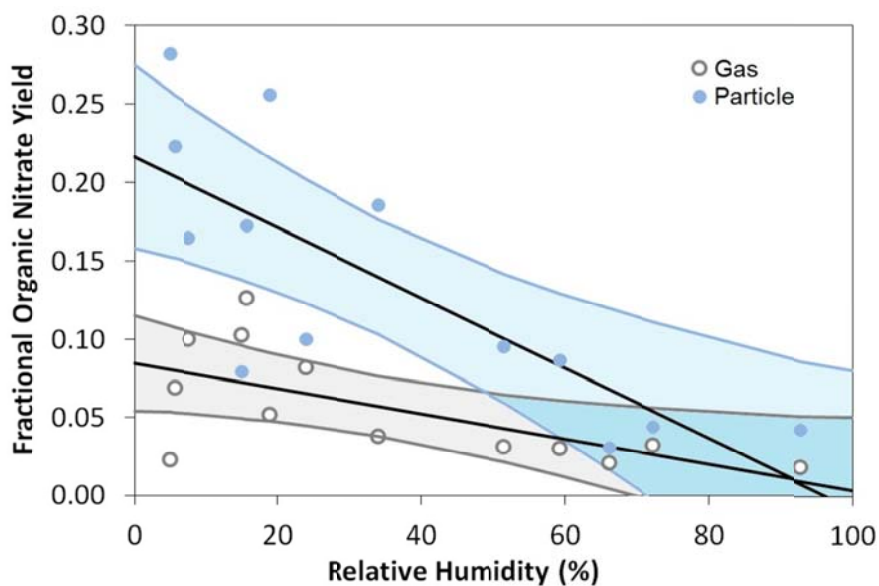
Figure 2.36. Gas and aerosol-phase organic nitrate yields, by phase, for the neutral seed aerosol experiments where open circles (○) represent gas phase yields and closed circles (●) represent particle phase yields. Linear regressions with confidence limits are shown for each data series.
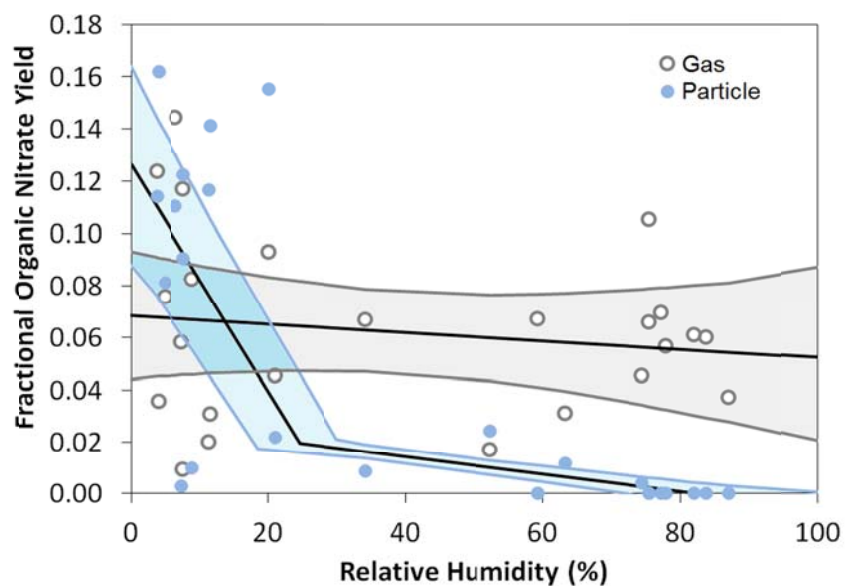
Figure 2.37. Gas and aerosol-phase organic nitrate yields, by phase, for the acidic seed aerosol experiments where open circles (○) represent gas phase yields and closed circles (●) represent particle phase yields. Linear regressions with confidence limits are shown for each data series. The particle phase yield regressions are separated into a low RH and high RH regime.

Interestingly, the gas phase organic nitrate yields also decreased with RH for both the acidic and neutral seed experiments (Figs. 2.36-2.37). Hydrolysis only occurs in the condensed phase, thus, a decrease in both the gas and phase yields can be explained by an apparent non-equilibrium partitioning system where hydrolysis eliminates $RONO_2$ species in the particle phase, causing gas phase $RONO_2$ compounds to continue to partition into the aerosol phase and undergo consumption via hydrolysis.

Support of the apparent non-equilibrium partitioning of organic nitrates can be observed by analysis of the $RONO_2$ F/A ratios at dry (<20% RH) and wet (>20% RH) conditions. As shown in Table 2.4, the organic nitrate F/A ratios are greater than 1.0, meaning partitioning to the particle phase is favored, for all seed aerosol systems when

averaged over the respective humidity range except for the case of acidic seed aerosol at high RH. The inversion of observed RONO$_2$ partitioning for the acidic seed experiments is also observed by inspection of Fig. 2.37. In this scenario, observed F/A ratios less than 1.0 for the acidic seed experiments indicate that an acid-induced increase in the rate of hydrolysis in the particle phase is occurring at a rate that out-competes uptake of gas phase organic nitrates into the aerosol phase at elevated RH.

Table 2.4. The F/A ratio, where F is the particle phase organic nitrate concentration and A is the gas phase organic nitrate concentration, of both the acidic seed and neutral seed experiments averaged over both the low and high humidity ranges.

Relative Humidity	Average F/A (Neutral Seed)	Average F/A (Acidic Seed)
Low (<20%)	4.1	3.2
High (>20%)	2.5	0.3

To estimate an upper limit for the rate of RONO$_2$ loss in this system via particle phase hydrolysis, the uptake rate (R_{in}) of organic nitrates can be calculated using Eq. (2.22), described by Jacob (2000), where r is the radius of the particle, D_g is the gas-phase molecular diffusion coefficient, v is the mean molecular speed, α is the RONO$_2$ mass accommodation coefficient, A is the aerosol surface area per unit volume of air, and $N^{'}$ is the gas phase RONO$_2$ concentration.

$$R_{in} = \left(\frac{r}{D_g} + \frac{4}{v\,\alpha} \right)^{-1} A\, N'$$

(2.22)

Assuming a mass accommodation coeffiecient (α) similar to that for 2-nitrophenol, 0.012 (Muller and Heal, 2002), a D_g of 0.20 cm^2/s (Jacob, 2000), and a calculated v of 1.72×10^4 cm/s, the estimated timescale for uptake into the aerosol phase, τ_{uptake} $((R_{in}/N')^{-1})$, was calculated to be 194s. That value, the lower limit timescale for the loss of RONO$_2$ in our system after partitioning to the particle phase, is much shorter than the combined experimental and sampling timescale of ~2.5 hours. For ambient conditions (Han et al., 2014), an uptake lifetime (τ_{uptake})of 3.43 hours was calculated for organic nitrates, indicating that particle phase partitioning and hydrolysis make deposition a likely removal pathway for gas phase NO$_x$ above coniferous forests.

It is also possible that other aerosol phase chemical reactions, such as through oligomerization, can contribute to the observed apparent non-equilibrium partitioning of organic nitrates by forming less volatile species within the particle. One possible oligomerization reaction of an α-pinene-derived nitrate is via Fischer esterification. An example reaction with pinonic acid, a known α-pinene oxidation product, is shown in Fig. 2.38.
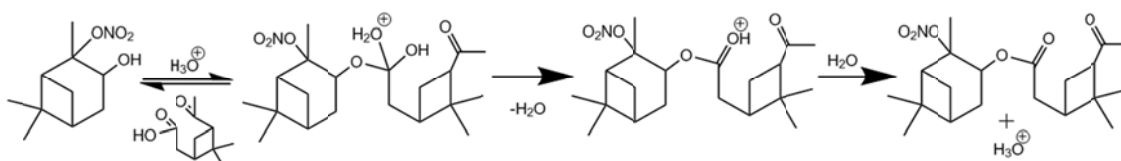
Figure 2.38. A possible oligomerization reaction, via Fischer esterification, of an α-pinene-derived nitrate with pinonic acid, a known α-pinene oxidation product. It is important to note that this reaction product has not yet been observed in chamber or field studies, to date.

To further examine the partitioning of the organic nitrates as a function of aerosol type and humidity, partition coefficients were calculated based on Pankow (1994), which assumes a reversible gas-particle partitioning process involving solubilization of the gas phase component throughout the particle (Eq. 2.23), which is assumed to be a liquid.

$$K_p = \frac{F_i/M}{A} \tag{2.23}$$

For a pure equilibrium, the partition coefficient should be a constant. Calculated partition coefficients are shown as a function of relative humidity in Fig. 2.38. At high humidity, the decrease in apparent K_p is greater than implied by the data shown in Fig. 2.38 because, for elevated chamber RH (see Fig. 2.37), the aerosol phase $RONO_2$ concentration was below the detection limit, and these cases are not plotted. The data in Fig. 2.38, showing larger partition coeffiecients (K_p) at low RH compared to high RH by three orders of magnitude, give further support for an apparent non-equilibrium partitioning system governed by particle phase hydrolysis.
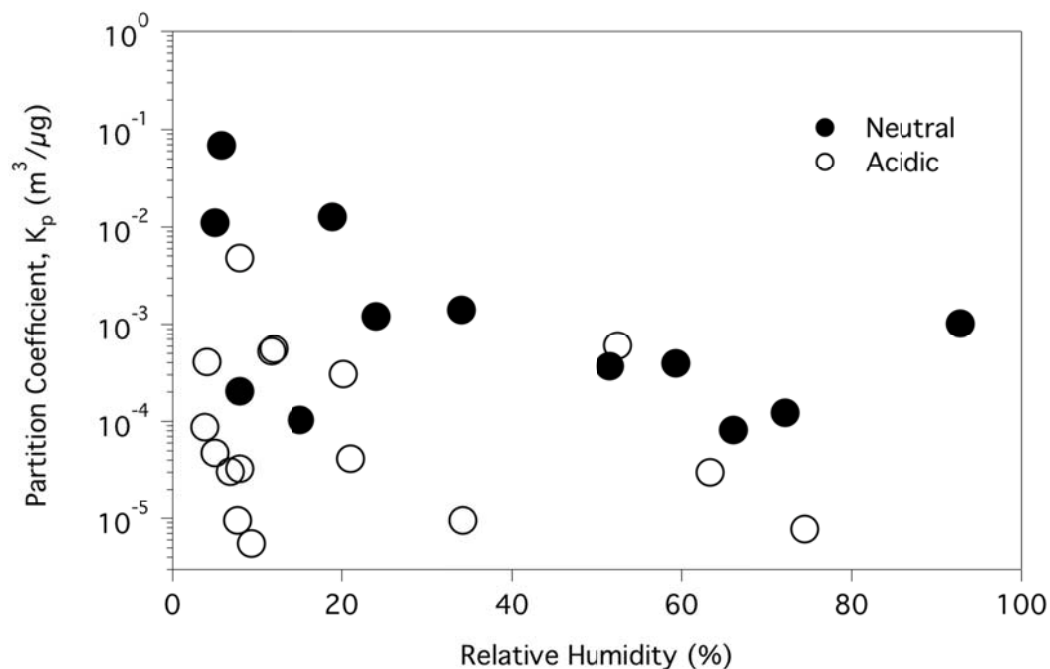
Figure 2.39. Calculated partition coefficients (K_p) from neutral and acidic seed aerosol experiments plotted against experiment relative humidity. Open circles (○) represent the acidic seed experiments while the closed circles (●) represent the neutral seed experiments. It is important to note that this plot does not show eight data points from the acidic seed aerosol data set which have partition coefficients of zero due to the lack of detected $RONO_2$ in the particle phase (see Figure 2.29).

Another factor that may contribute to the observed partitioning is the physical property of the aerosol particle. Recent work has shown that particles can range from "hard" and viscous at low humidity to much "softer" at higher RH where water uptake occurs much more readily (Shiraiwa et al., 2012; Virtanen et al., 2010; You et al., 2012). A previous organic nitrate partitioning study attributed an observed apparent non-equilibrium system to such effects while at very low RH (Perraud et al., 2012). Thus, at low RH, the particles may have a high viscosity, limiting uptake into and diffusion within the bulk particle, rendering the Pankow (1994) model inappropriate. At high RH, the viscosity may be lower due to higher liquid water content and solvation of the particle

phase oxidation products, which may lead to an increase in polar solute dissolution within the particle and hydrolysis chemistry. Thus, the degree of scatter in Fig. 2.38 indicates that multiple physical and chemical processes may affect how low volatility organic nitrates partition between the gas and aerosol phases.

Results from this study indicate that hydrolysis of organic nitrates under acidic conditions is likely a unimolecular (S_N1, E1) mechanism rather than bimolecular (S_N2, E2), as previously suggested (Darer et al., 2011). The increase in hydrolysis under aqueous acidic conditions can be explained by the increased stabilization of the carbocation transition state and better solvation of the leaving group in the S_N1 and E1 mechanisms by the polar protic solvent system. Since the formation of the carbocation is the rate determining step of this reaction, the hydrolysis mechanism should be a first order process, consistent with previously reported data (Hu et al., 2011).

Other previously reported data also implies that organic nitrate hydrolysis is unimolecular under acidic conditions. Darer et al. (2011) showed that tertiary nitrates are the most prone to hydrolysis. This is consistent with a unimolecular mechanism because the steric hindrance of tertiary organic compounds makes it difficult for bimolecular transition states to exist. Also, tertiary carbocations are more stable than their primary and secondary counterparts, which allows for much faster unimolecular reaction rates. Another limitation in the argument for bimolecular hydrolysis of organic nitrates is the unlikelihood of water to attack a carbon center, due to its weak nucleophilicity. Previous studies have shown that the analogous alcohols can form from organic nitrates (Darer et al., 2011; Hu et al., 2011), a product that is much more likely to happen through the S_N1 mechanism.

2.4 Conclusions

The relatively large branching ratio of organic nitrate formation (26±7%) from the OH radical initiated oxidation of α-pinene will limit ozone production, and this knowledge lowers the uncertainty in the ozone production potential from monoterpene emissions. Additionally, the high yield of the assumed hydroxy nitrates compared to previous studies (e.g. O'Brien et al., 1998) indicates that gas phase rearrangement may diversify the functionality of the organic nitrates produced from this reaction.

The dependence of the measured organic nitrate yields on both particle acidity and chamber relative humidity indicates that aerosol phase hydrolysis can control the fate of organic nitrate species, even at low RH. By converting the nitrooxy group of the $RONO_2$ into the nitrate ion, the nitrogen will remain much longer in the particle phase, due to decreased reactivity, and will effectively eliminate the opportunity for the release of NO_x from organic nitrates via particle phase reaction. The ambient aerosol uptake lifetime (τ_{uptake}, Eq. 2.22) for organic nitrates above a coniferous forest was calculated to be 3.43 hours, using aerosol mean diameter and concentrations from Han et al. (2014), which suggests that particle uptake and deposition would be the most likely avenue of removal of $RONO_2$ from the atmosphere.

The chemical mechanism that is most likely responsible for organic nitrate hydrolysis was determined to be a unimolecular mechanism (S_N1, E1). This helps further the knowledge of organic chemistry as no literature has been published on the organic nitrate hydrolysis under acidic conditions. This also gives insight into aerosol phase chemical processing, a large unknown currently shouldered by the atmospheric science community. The identification of particle phase hydrolysis also helps explain the

decrease in organic nitrogen-containing species observed at high ambient RH in a recent field study (Day et al., 2010) and may help explain the overall relative dearth in ambient organic nitrate measurements.

Particle phase hydrolysis can also have a significant impact on the partitioning of organic nitrate compounds. α-Pinene-derived nitrates are favored to partition into the aerosol phase based on their high F/A ratios, however, particle phase hydrolysis leads to the consumption of $RONO_2$ compounds, causing an increase in partitioning of gas phase $RONO_2$ compounds and subsequent loss via hydrolysis. Thanks to the high yields of organic nitrate formation, particle phase partitioning and loss via hydrolysis, the production of $RONO_2$ compounds in coniferous forest environments may be an important sink for gas phase NO_x.

CHAPTER THREE: MASS SPECTROMETRIC ANALYSIS OF PHOTOCHEMICAL
CHAMBER EXPERIMENTS

3.1 Introduction

Previous results from this thesis have shown that, at low RH, organic nitrates are

produced at a 26±7% yield from the OH radical oxidation of α-pinene in high NO_x

conditions. The gas and particle phase products that comprise the remaining 74% from

this study have yet to be identified. Additionally, the effect of chamber relative humidity

and particle acidity on the yields of non-$RONO_2$ products is still unclear for compounds

derived from α-pinene oxidation. While this thesis has shown that α-pinene-derived

organic nitrates can hydrolysis rapidly in the particle phase, their products and explicit

reaction mechanisms are also currently uncertain. Thus, a variety of mass spectrometric

methods were used to help gain knowledge into the many uncertainties of the α-pinene-

derived oxidation products produced from photochemical chamber experiments in this

thesis.

While there have been numerous studies into the oxidation of α-pinene, the

identification of products from the OH radical oxidation of α-pinene under high NO_x

conditions is still incomplete, as 29-46% of products have yet to be identified (Jaoui and

Kamens, 2001). The uncertainty in product identification is related to the large number of

reaction pathways of large cyclic molecules, such as α-pinene, where simple rules

deduced from well-known reactions of smaller molecules do not necessarily apply

(Capouet et al., 2004). The major gas phase product identified from α-pinene oxidation reactions is pinonaldehyde (see below), with yields ranging from 28 to 87% (Hakola et al., 1994; Noziere et al., 1999). In the particle phase, pinonic acid and pinic acid are the major products identified. Additionally, under acidic seed aerosol conditions, organosulfates have been detected in α-pinene chamber experiments (Surratt et al., 2008).

Our objective was the measurement of individual products has been accomplished using both GC-MS and LC-MS methods (see below). The use of GC-MS has been successfully employed in the detection of relatively volatile oxidation species, such as pinonaldehyde, while the use of LC-MS has been applied to the measurement of more highly oxidized species, such as carboxylic acids. GC-MS has also been used to identify more oxidized species, however, a derivatization procedure has been used to replace the acidic proton of carboxylic acids with trimethylsilyl esters before analysis (Jaoui and Kamens, 2001). It is unknown if the Jaoui and Kamens (2001) pre-treatment reaction is specific to carboxylic acids, thus, the development of other methods is necessary for a more direct product analysis that includes investigation of organosulfates, organic nitrates, and other aerosol phase products.

3.2 Experimental

To identify products from the α-pinene oxidation experiments conducted in this thesis (described in Chapter 2), a suite of mass spectrometric techniques was employed. Several products were identified using GC-(EI)-MS, relying on the interpretation of fragmentation patterns and GC retention indices available from NIST. Insight into product functionality was also gathered using GC-(NICI)-MS, described below. The use

of denuder-based filter extracts gave insight into the gas-particle distribution of products using GC-MS. An LC-MS technique was also used as a complimentary mass spectrometric method for particle phase analysis. Additionally, the application of paper spray-mass spectrometry to directly sample filters was investigated, proving to be a useful method for identification of organosulfates and carboxylic acids with minimal sample preparation.

3.2.1 GC-MS

A gas chromatograph coupled to a quadrupole mass spectrometer (GC-MS; QP-2010, Shimadzu, Inc.) was used to identify and/or quantify both gas phase products produced during chamber experiments and off-line denuder-based filter extracts. A GC-MS schematic, shown in gas phase sampling mode (under "LOAD" setting) with a 10mL sample loop, is displayed in Fig. 3.1. The ZB-1701 capillary column (Phenomenex, Inc.) used had a 30 m length, 0.25 mm i.d., and 1.0 μm film thickness. The mobile phase of the ZB-1701 capillary column was 14% cyanopropyl/86% dimethylpolysiloxane polymer. The column oven was kept at 58°C for 5 minutes before being heated to 255°C at a rate of 8°C/minute. The GC-MS was also capable of analyzing liquid phase samples by direct injection, such as the denuder-based filter extracts in this study.
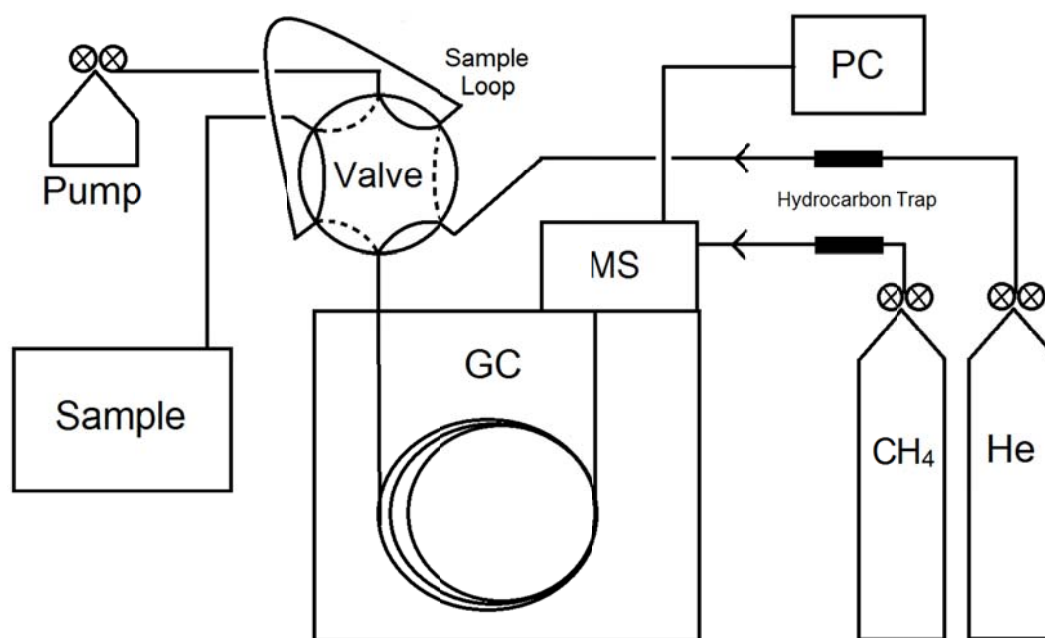
Figure 3.1. Schematic for measuring gas phase α-pinene products using the GC-MS.

The GC-MS is capable of operating in three ionization modes: electron impact (EI), negative mode chemical ionization (NICI), and positive mode chemical ionization (CI). Only the electron impact and negative chemical ionization modes were used in this study. Electron impact involves the ionization of the analyte by impact with a 70 eV electron beam, which is created from a tungsten filament through the application of an electrical current. Once the electron is produced, it is accelerated toward the analyte gas stream by the application of a 70 eV potential. The electron beam will interact with the analyte (M) to displace an outer shell electron (Eq. 3.1). Due to its high energy, EI is known as a hard ionization technique that deposits excess energy into the primary ion, often leading to many ion fragments and low abundance of the molecular ion ($M^{+\cdot}$).

$$M + e\text{-} \rightarrow M^{+\cdot} + 2e\text{-} \tag{3.1}$$

Negative mode chemical ionization (NICI) is a softer ionization technique that will lead to less overall fragmentation, due to the creation of low energy thermal electrons (<15 eV). Similar to EI, an electron beam is originally created, however, in NICI, these high energy electrons interact with the reagent gas (CH_4) to create $CH_4^{+\cdot}$ and thermal electrons (Eq. 3.2). The use of methane as a reagent gas is beneficial because its ionization yields a very low amount of negative ions and, thus, low background signals (Worton et al., 2008).

$$CH_4 + e\text{-} \rightarrow CH_4^{+\cdot} + 2e\text{- (<15eV)} \hspace{4cm} (3.2)$$
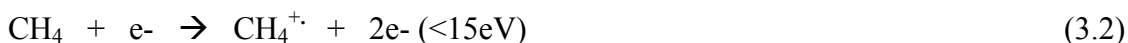
Negative ion mode chemical ionization is especially useful for the detection of compounds containing electron-accepting electronegative species, such as organic nitrates and alkyl halides. When $RONO_2$ compounds accept a thermal electron in NICI, the O-N single bond is the most likely to break, leading to two possible negatively charged fragments: the NO_2^- ion or the RO^- ion (Eqs. 3.3a, 3.3b). The relative yield of the RO^- ion compared to the NO_2^- ion has been found to be proportional to the carbon chain length, for alkyl nitrate species (Worton et al., 2008).

$$RONO_2 + e\text{- (<15eV)} \rightarrow NO_2^- + RO \hspace{3.5cm} (3.3a)$$

$$RONO_2 + e\text{- (<15eV)} \rightarrow RO^- + NO_2 \hspace{3.5cm} (3.3b)$$
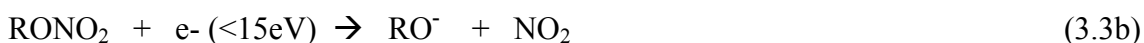
Once the gas phase analyte is ionized, it is extracted into the quadrupole mass spectrometer where ions are separated based on their mass to charge ratio (*m/z*). A quadrupole mass spectrometer consists of four parallel cylindrical rods (Fig. 3.2). Opposite rods are electrically connected to a DC voltage source and a radio-frequency

generator, which applies a 180° out of phase AC voltage to each pair of rods. A given DC

and AC voltage corresponds to the stability of an ion at a certain *m/z* ratio and sweeping a

magnitude of voltages containing the same DC to AC ratio will provide a complete mass

spectrum. The mass resolution of typical quadrupole MS instruments is on the order of

several hundred, meaning that only peaks with *m/z* ratios of no less than 1 amu difference

can be distinguished from each other.
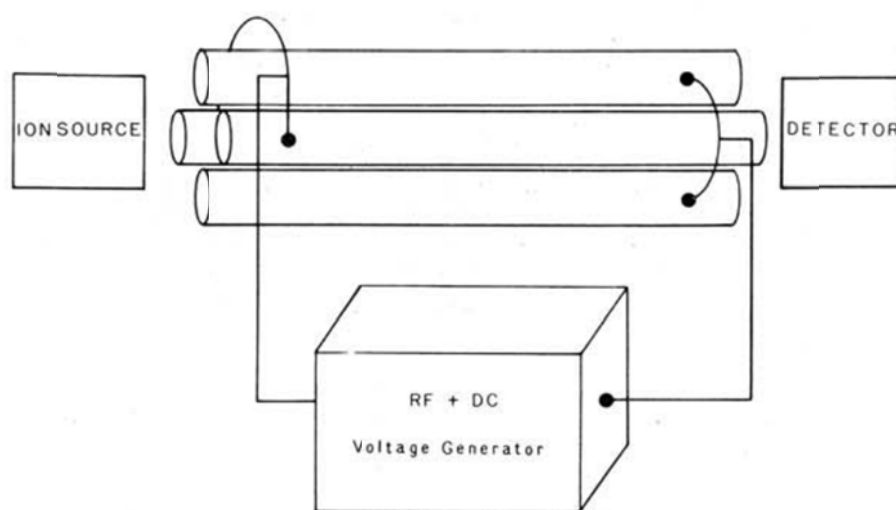
Figure 3.2. The schematic for the quadrupole mass spectrometer. The figure is adapted
from Miller and Denton (1986).

A calibration curve for the GC-MS in negative chemical ionization mode using

isobutyl nitrate, described in Eq. 3.3a, is shown in Fig. 3.3. For quantitative

measurements, the extracted ion current chromatogram (EIC) of *m/z* 46⁻ was used for

peak area calculations, due to the NO_2^- ion's prevalence in organic nitrate ionization.
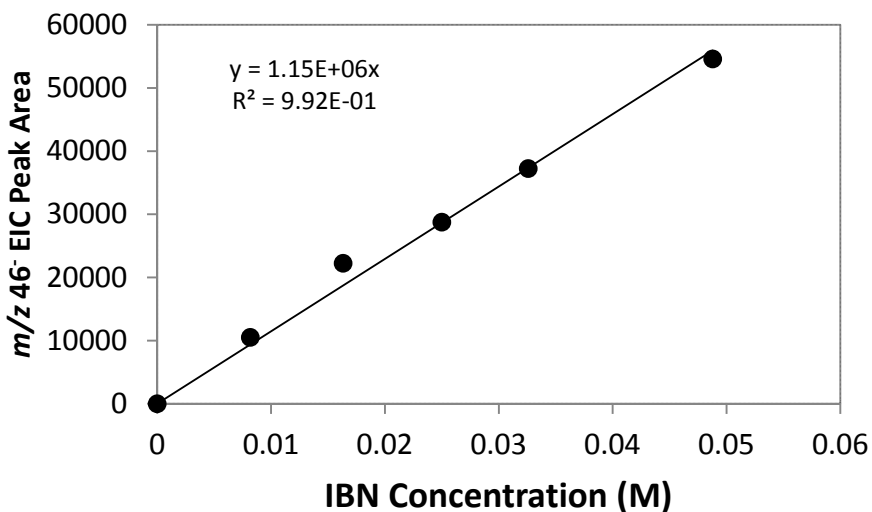
Figure 3.3. The calibration curve for the GC-(NICI)-MS from the liquid injection of isobutyl nitrate (IBN) and integrating the m/z 46⁻ extracted ion current (EIC).

3.2.2 LC-MS

High performance liquid chromatography was coupled to a time of flight mass spectrometer with electrospray ionization (HPLC-(ESI)-TOF) to gather high resolution product information from filter extracts. For this application, reverse-phase liquid chromatography was used to separate compounds by hydrophobic interaction with the column stationary phase and varying the polarity of the mobile phase. Initially, a hydrophilic solvent, in this case 0.1% aqueous acetic acid, was used as the mobile phase to allow organic compounds to interact with the hydrophobic stationary phase. As the mobile phase is shifted to a more hydrophobic gradient by the increasing the concentration of an organic solvent, in this case methanol, hydrophobic compounds within the column will become better solvated and elute with the mobile phase. The use of high pressures in HPLC, compared to normal LC, allows for the use of smaller particle

sizes for the column stationary phase and better sample separation via increased surface area for column-analyte interaction.

To separate analyte species within a sample, this study employed a C_{18} column (3 μm; 2.1 × 150 mm; 3 μm particle size; Waters, Corp.) and a 45 minute mobile phase gradient consisting of 0.1% aqueous acetic acid and methanol. The gradient was as follows: 3% methanol/0.1% aqueous acetic acid for 2 minutes, followed by an increase to 90% methanol in 18 minutes and held for 10 minutes before the gradient was decreased back down to 3% methanol in 5 minutes and then held for 10 minutes, prior to the next injection. The column flow rate was 0.2 mL/min. HPLC conditions were based on Surratt et al. (2008).

Once eluted from the column, the sample was ionized using electrospray ionization (ESI). ESI uses a high voltage (>2.5kV) to create a spray of charged solvent-analyte aerosols that are dried to create ions. Electrospray ionization is considered a soft ionization mechanism and will often yield a molecular ion without extensive fragmentation. However, due to its low energy of ionization, ESI does not readily ionize many functional groups and, traditionally, the technique has been used for analysis of easily ionizable compounds, such as organosulfates and carboxylic acids.

The analysis of ions was accomplished using a high resolution time of flight (TOF) mass spectrometer (Agilent, Inc.) in the negative ion mode. Negative ion mode was used because both organosulfates ($ROSO_3H$) and carboxylic acids (ROOH) easily lose a proton during ESI to form $[M-H]^-$ ions (Surratt et al., 2008). In TOF-MS, ions are accelerated by the application of a voltage across a drift tube of known length. Since all ions will have the same kinetic energy, the velocity of ions within the drift tube will be

inversely proportional to their mass and smaller ions will reach the detector before larger

ones (Fig. 3.4). The relationship equating the potential energy of a charged ion in an

electric field to its kinetic energy is shown in Eq. 3.4. This equation can be manipulated

to show that the mass to charge ratio (m/z) of an ion detected is proportional to its time of

flight within the drift tube (Eq. 3.5). The application of a drift tube with a large length

allows for increased ion time of flight and separation, leading to high mass resolution of

at least 10,000 (Russell and Edmondson, 1997). At mass resolution of >10,000, it is

possible to determine the empirical formulae for ions detected.

$$zU = \tfrac{1}{2}\, m\, (L/t)^2 \tag{3.4}$$

$$m/z = 2\, U\, (t/L)^2 \tag{3.5}$$

Here U is the electric field potential, z is the charge of the ion, m is the mass of the ion, L

is the drift tube length, and t is the time of flight within the drift tube.
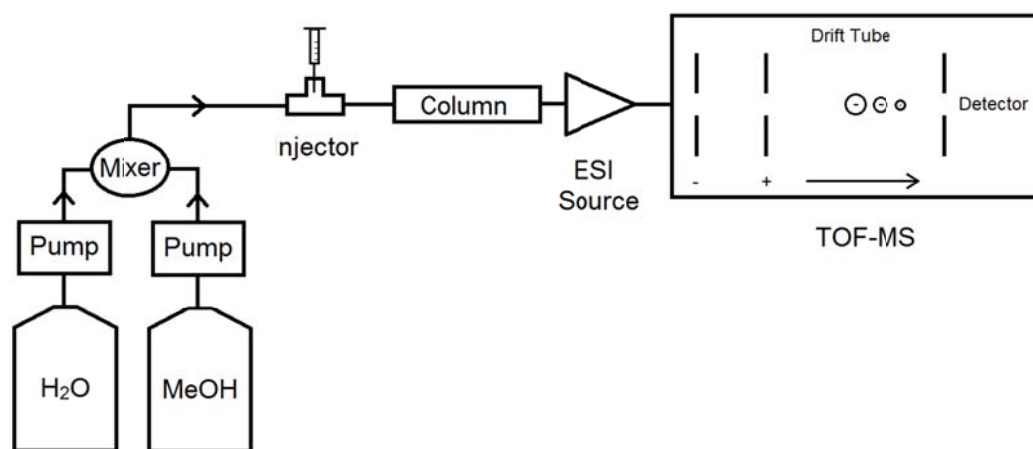
Figure 3.4. The schematic for an LC-(ESI)-TOF mass spectrometer.

3.2.3 PS-MS

Paper spray ionization mass spectrometry (PS-MS) was used for direct analysis of filter samples taken from photochemical chamber experiments. Paper spray mass spectrometry is an ambient ionization method, first developed in R. Graham Cook's laboratory, that involves the application of a high voltage (5 kV) to a paper triangle wetted with small volume of solvent solution (Liu et al., 2010). This method produces an analyte-containing spray originating from the tip of the paper that can be transferred to a mass spectrometer for analysis. The spray created from PS ionization is not unlike those produced from electrospray ionization (ESI) and desorption electrospray ionization (DESI) (Liu et al., 2010).
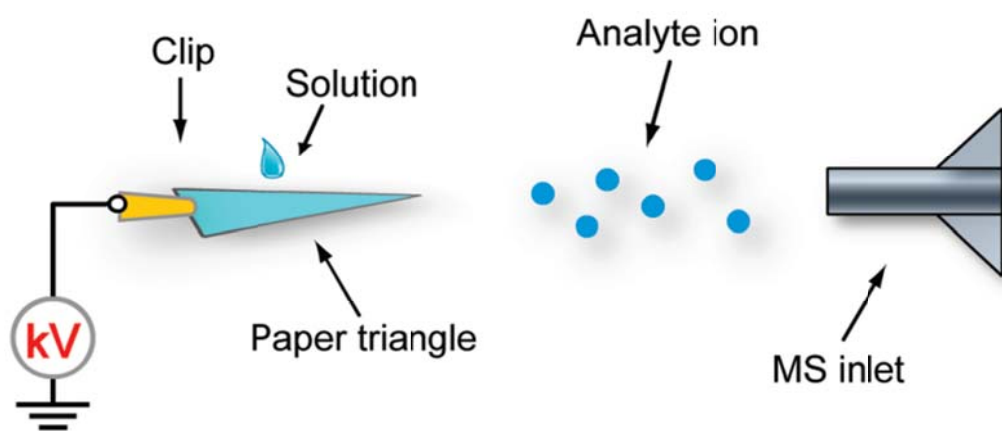
Figure 3.5. The schematic for paper spray ionization mass spectrometry (PS-MS). The figure is adapted from Liu et al. (2010).

Ambient ionization methods have been used for the study of organic aerosol previously, most notably by the Laskin group at Pacific Northwest National Laboratory (e.g. Laskin et al., 2010). A major advantage to ambient sampling techniques is the

minimal sample preparation needed, which limits the possible occurrence of sample artifacts and sample manipulation, and associated chemical transformation of the analyte. Previous applications, however, involved the use of nano-DESI, which desorbs an analyte from an impactor substrate using a solvent bridge formed between two capillaries before transfer to a mass spectrometer (Roach et al., 2010). The direct sampling of organic aerosol from a filter has not yet been accomplished, thus, the successful application of PS-MS to aerosol filter analysis would be a novel approach for particle analysis.

In this study, paper filter samples (Whatman, Inc.) were acquired at the completion of selected chamber experiments for PS-MS analysis. Filters were cut into a triangular shape and 10 uL of methanol was added to the filter before the application of the high voltage needed for paper spray ionization. After ionization, mass spectrometric analysis was accomplished using a quadrupole mass spectrometer (see above) acting as an ion trap for tandem mass spectrometry (MS^2).

In this application of mass spectrometry, static DC voltages are applied at the end caps of the quadrupole to trap ions axially and an AC voltage is applied 180° out of phase on opposite quadrupole electrodes to trap ions radially (Louris et al., 1987). Tandem MS was used to create fragmentation of the molecular ion [M-H]$^-$ within the ion trap and allow for further information on the molecular connectivity of precursor ions. Ion fragments were produced via collision-induced dissociation (CID), which applies an AC voltage on the end caps of the quadrupole to create axial on-resonance movement of ions within the trap. This motion leads to collisions with the bath gas and the absorption of kinetic energy, which induces fragmentation of the ions. Similar to the ESI method

described previously, mass spectrometric analysis was completed in the negative ion mode.

3.3 Results

3.3.1 GC-MS Analysis

GC-MS analysis of denuder-based filter extracts led to the identification of several α-pinene-derived species. A total ion current chromatogram (TIC) from a typical filter extract is shown in Fig. 3.6 and the corresponding peaks identified are shown in Table 3.1. The peaks were identified by interpretation of their mass spectrum and retention indices. The three major products detected in both the gas and particle phase extracts were pinocamphone, campholenic aldehyde, and pinonaldehyde. Pinocamphone and campholenic aldehyde are known condensed phase products of α-pinene-derived chemistry (see Chapter 4) and, due to their high volatility, may be created in the particle phase and partition back into the gas phase. Pinonaldehyde, on the other hand, is a known gas phase oxidation product of α-pinene (see Fig. 3.7) and its presence in both the gas and particle phases indicates that partitioning from the gas to the particle phase has occurred. Additionally, pinonaldehyde was the main yield product in several previous OH radical oxidation studies of α-pinene (e.g. Noziere et al., 1999).
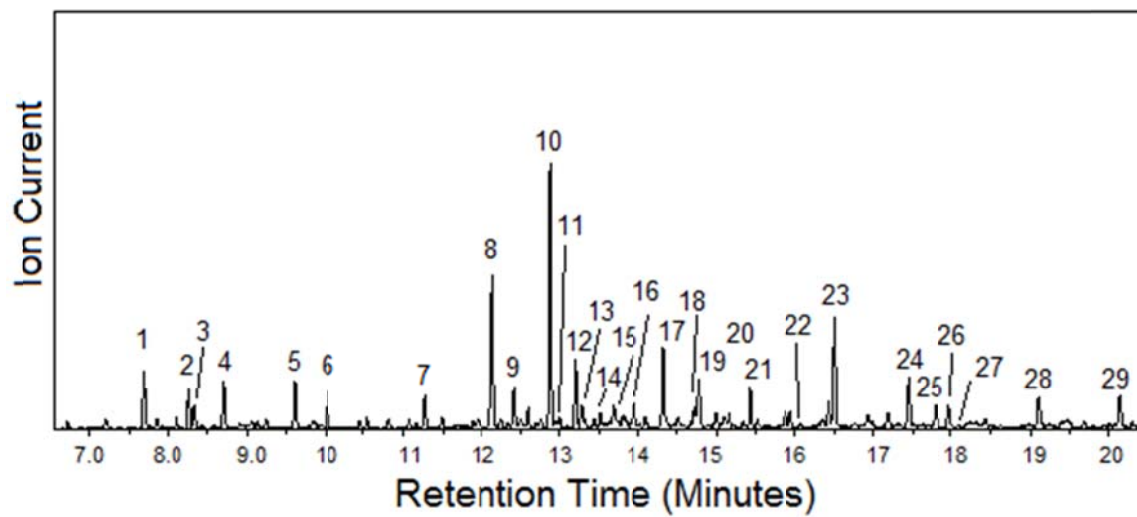
Figure 3.6. The total ion current chromatogram (TIC) of a filter extract from a representative α-pinene oxidation experiment.

Table 3.1. The identified structures that correspond with Fig. 3.6. Products with an asterisk (*) indicate tentatively identified compounds.
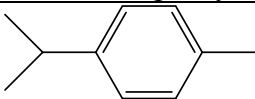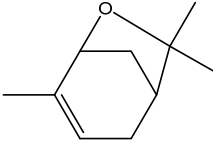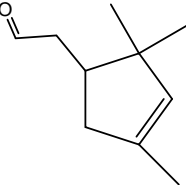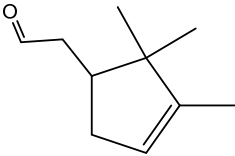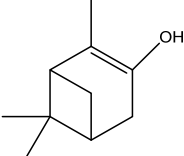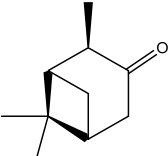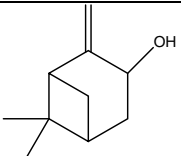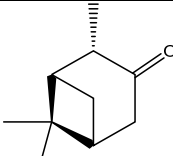
Peak No.	Retention Time (min)	Identified As:	Structure
1	7.69	unknown	unknown
2	8.27	limonene	α-pinene impurity
3	8.34	pentachloroethane	solvent impurity
4	8.71	*para*-cymene	
5	9.61	hexachloroethane	solvent impurity
6	10.03	pinol	
7	11.27	fencholenic aldehyde*	
8	12.14	campholenic aldehyde	
9	12.42	pinocamphenol*	
10	12.88	(Z)-pinocamphone	
11	13.00	pinocarveol	
12	13.19	(E)-pinocamphone	

Table 3.1. Continued.
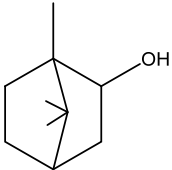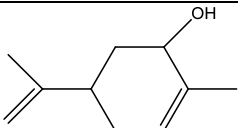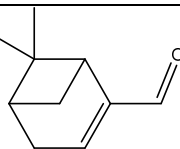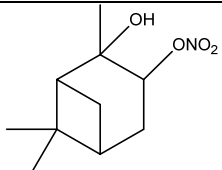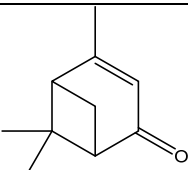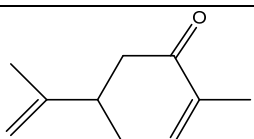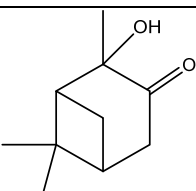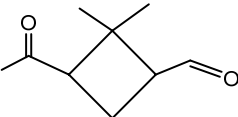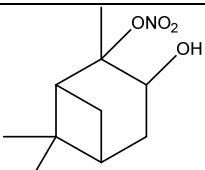
Peak No.	Retention Time (min)	Identified As:	Structure
13	13.28	borneol	
14	13.44	carveol	
15	13.83	myrtenal	
16	14.32	α-pinene-derived nitrate	
17	14.71	verbenone	
18	14.77	carvone	
19	14.99	2-hydroxy-3-pinone	
20	15.16	norpinonaldehyde	
21	15.43	α-pinene-derived nitrate*	

Table 3.1. Continued.

Peak No.	Retention Time (min)	Identified As:	Structure
22	16.07	α-pinene-derived nitrate*	unknown
23	16.51	pinonaldehyde	
24	17.44	unknown	unknown
25	17.80	α-pinene-derived nitrate*	unknown
26	17.98	unknown	unknown
27	18.24	unknown	unknown
28	19.11	unknown	unknown
29	20.15	unknown	unknown
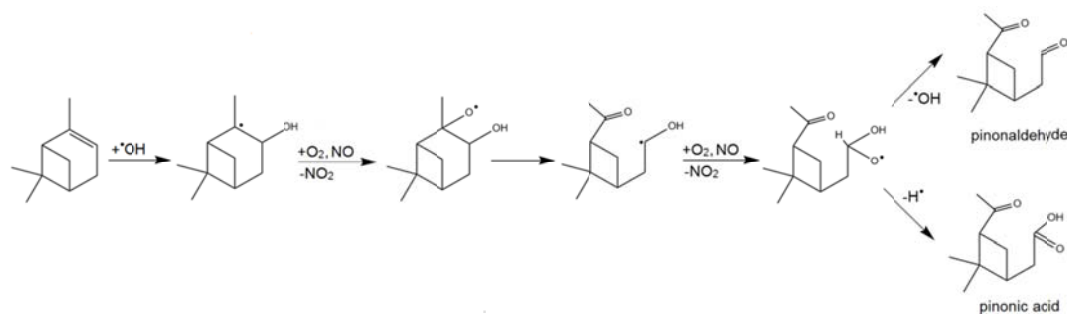
Figure 3.7. A gas phase mechanism for the production of pinonaldehyde from α-pinene. The figure is based on chemistry described in Peeters et al. (2001) and Librando and Tringali (2005).

Minor products identified include *para*-cymene, pinocarveol, borneol, carveol, mrytenal, verbenone, carvone, 2-hydroxy-3-pinone, and norpinonaldehyde. These compounds, which have been identified as α-pinene oxidation products from a previous study (Jaoui and Kamens, 2001), were identified using available standard EI mass spectra

and retention indices from the National Institute of Science and Technology (NIST; http://webbook.nist.gov/chemistry/). In addition, α-pinene oxide was observed in both phases of neutral seed experiments.

Products without known MS spectra were tentatively identified based on comparison to known compounds. For instance, fencholenic aldehyde, which has been identified as a minor condensed phase α-pinene-derived product by Bleier et al. (2013) from the acid-catalyzed rearrangement of campholenic aldehyde, was tentatively identified as the peak at 11.27 minutes (Fig. 3.6), due to its similar fragmentation pattern/retention time to campholenic aldehyde and relatively smaller peak area. Pinocamphenol was tentatively identified due to its similar retention time (12.42 minutes) and fragmentation pattern to its isomer pinocarveol, which was identified at 13.0 minutes (Table 3.1). Pinocamphenol has not yet been identified from α-pinene chamber experiments, however, it is a keto-enol tautomer of pinocamphone and, thus, very likely to exist in a particle phase equilibrium with pinocamphone. Mechanisms for the formation of fencholenic aldehyde and pinocamphenol from known products campholenic aldehyde and pinocamphone, respectively, are shown in Fig. 3.8.
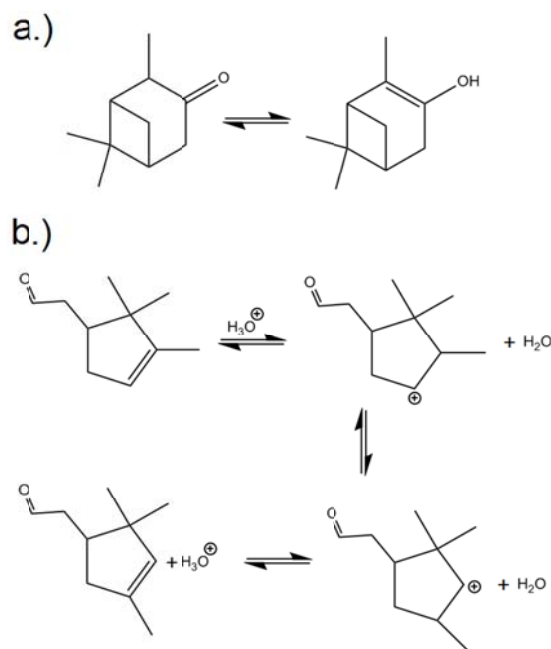
Figure 3.8. The mechanisms for the creation of a.) pinocamphenol and b.) fencholenic aldehyde from known products pinocamphone and campholenic aldehyde, respectively.

The α-pinene-derived nitrates (APNs) were identified based on the presence of an *m/z* 46 in the negative ion mode from GC-(NICI)-MS extracted ion chromatograms (see Chapter 2). Structures for two APNs at 14.32 and 15.43 minute retention times were based on the similarity of MS spectra and retention time to a synthesized α-pinene-derived nitrate standard (see Chapter 4).

Despite the identification of many peaks in the GC-MS spectra, several unknown compounds were left unidentified after analysis. The majority of these compounds had large retention times in the TIC, indicating that they are likely of low-volatility and had increased interaction with the column. Mass spectra for the unknown compounds are shown in Fig. 3.9.
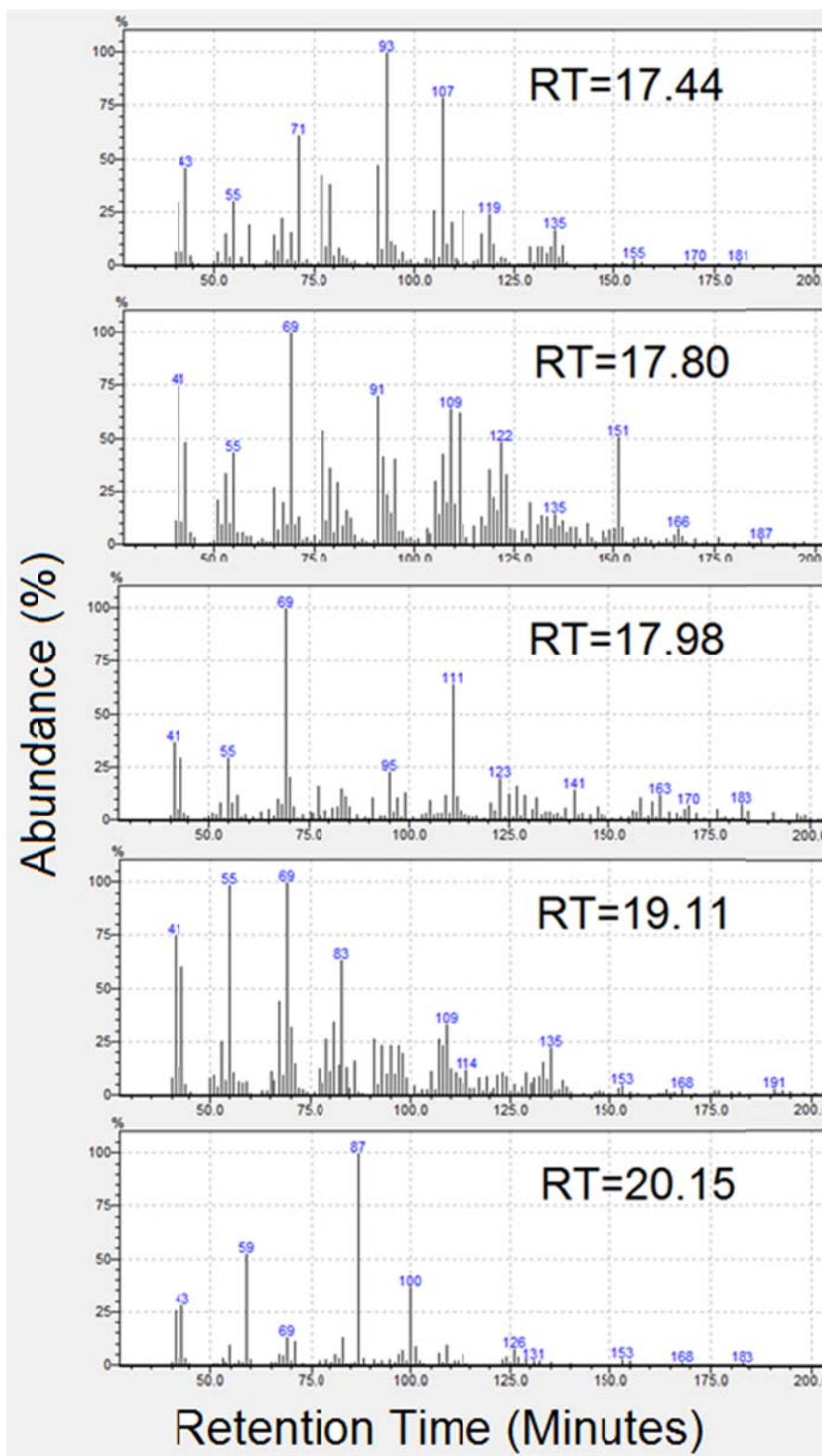
Figure 3.9. The EI mass spectra of the unknown compounds from Table 3.1.

The use of denuder-based filter sampling allowed for separate analysis of gas and particle phase products. Interestingly, nearly all peaks observed in the gas phase were also observed in the particle phase. One exception was *trans*-sobrerol, which is likely to be created in the particle phase and partition to the gas phase. *trans*-Sobrerol is very reactive in the condensed phase (see Chapter 4) and was likely consumed in the particle phase via chemical reactions.

The similarity in observed gas and particle phase products indicates that an equilibrium between the gas and particle phases was present within the chamber experiments. However, based on peak areas from the GC-MS spectra, the particle phase product concentrations were larger than those in the gas phase, which implies that the high aerosol mass loadings of the chamber experiments may have influenced the gas/particle partitioning. The possibility that the particles created were highly viscous, making gas phase compounds "stick" to particles to create a particle phase favored equilibrium is unlikely based on the observed partitioning of pinonaldehyde between phases (see below).

The relative yields (ratio of peak areas) of the two major particle phase products, pinocamphone and campholenic aldehyde, were determined for acidic seed and neutral seed experiments at low RH (<20%) and high RH (>20%). The results, displayed in Fig. 3.10 and 3.11, show that the particle phase concentration of campholenic aldehyde relative to pinocamphone increased with chamber RH. The observed increase is more dramatic in the case of acidic seed aerosol compared to neutral seed aerosol experiments. One explanation for this result is a humidity-dependent increase in particle phase hydrolysis, which is supported by previous studies that indicated that campholenic

aldehyde is a major product of α-pinene-derived hydrolysis chemistry (Iinuma et al., 2009; Bleier et al., 2013). Additionally, Iinuma et al. (2013) observed an increase in campholenic aldehyde yields from α-pinene-derived hydrolysis with decreasing pH, thus, a larger increase in campholenic aldehyde concentrations in the acidic seed experiments compared to neutral seed experiments indicate that an acid-catalyzed mechanism is likely responsible for the observed chemistry in our experiments. Iinuma et al. (2013) also observed pinocamphone as a minor product of α-pinene hydrolysis but did not quantify its concentration as a function of pH. Assuming that the production of pinocamphone and campholenic aldehyde are competitive, and that campholenic aldehyde yields increase with decreasing pH, the relative decrease in pinocamphone concentrations with increasing acidity in our experiments supports the proposed aerosol phase acid-catalyzed hydrolysis chemistry. The acid-catalyzed hydrolysis mechanism for α-pinene oxide is shown in Fig. 3.12.

Acidic Seed Experiments
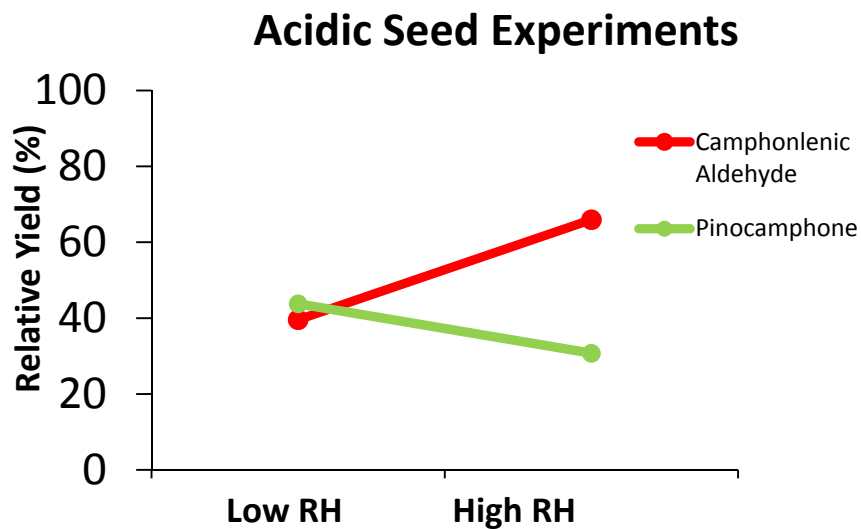
Figure 3.10. Relative yields of the two major particle phase products in acidic seed experiments, pinocamphone and campholenic aldehyde. Data are averaged over the low RH (<20%) and high RH (>20%) experiments.

Neutral Seed Experiments
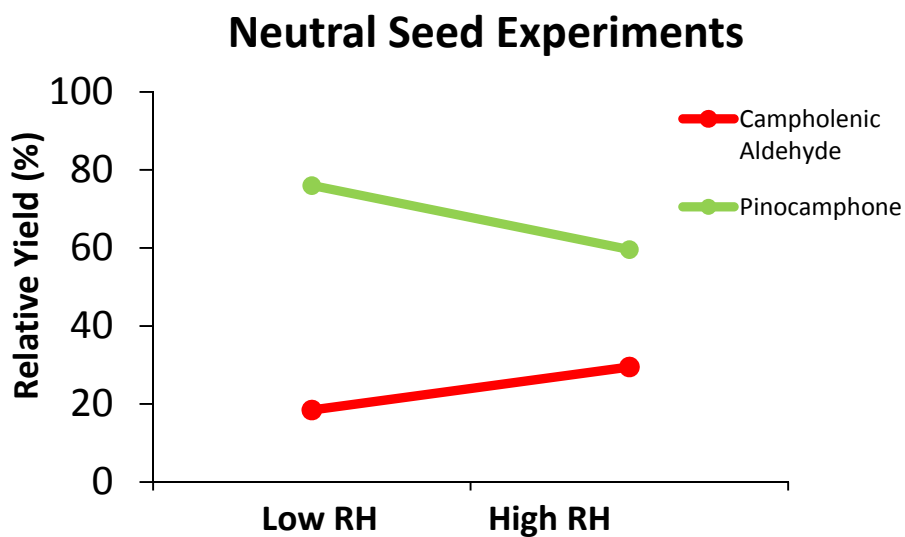
Figure 3.11. Relative yields of the two major particle phase products in neutral seed experiments, pinocamphone and campholenic aldehyde. Data are averaged over the low RH (<20%) and high RH (>20%) experiments.
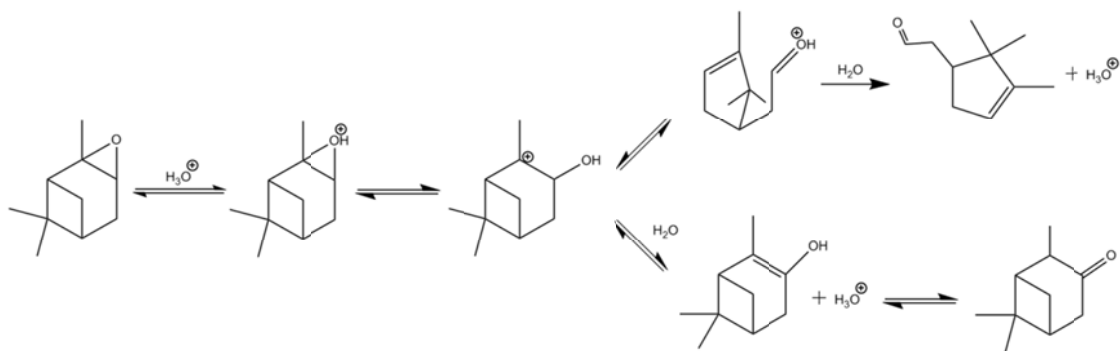
Figure. 3.12. The acid-catalyzed hydrolysis of α-pinene oxide to form campholenic aldehyde (top) and pinocamphone (bottom).

The distribution of the major gas phase product, pinonaldehyde, was also determined. Unlike the $RONO_2$ compounds observed in previous experiments (see Chapter 2), the partitioning of pinonaldehyde was observed to be an equilibrium process, as described by Pankow (1994). This equilibrium is shown in Fig. 3.13, which displays a linear relationship between the particle yield (F/M) of pinonaldehyde and the measured gas phase concentrations (A). In cases of non-equilibrium partitioning, these data are not linear (Perraud et al., 2012). The partition coefficients (K_p) of pinonaldehyde did not vary based on chamber RH or particle acidity, indicating that particle phase reactions likely do not govern the fate of pinonaldehyde. The average K_p of pinonaldehyde from chamber experiments was $1.3 \pm 2 \times 10^{-4}$ m^3 μg^{-1}. This value is an order of magnitude smaller than reported previously (Tillmann et al., 2010), highlighting the need for further studies focusing on the partitioning of α-pinene oxidation products.
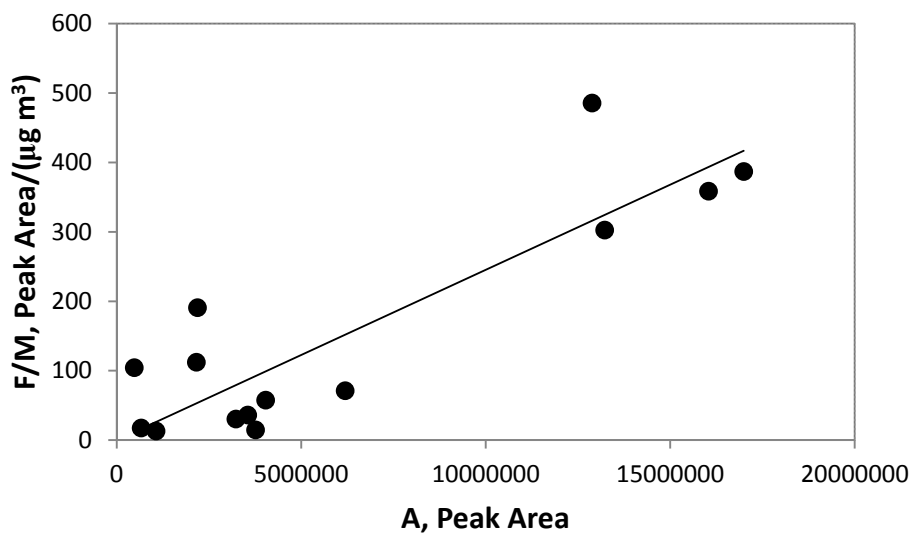
Figure 3.13. The aerosol yield of pinonaldehyde (F/M) plotted versus gas phase pinonaldehyde concentration (A) from both acidic and neutral seed aerosol experiments.

The use of GC-NICI-MS was instrumental in the identification of organic nitrate species. As seen in Chapter 2, the presence of an *m/z* 46 peak in the NICI mass spectrum indicated the presence of an organic nitrate. An extracted ion current chromatogram (EIC) from the GC-NICI-MS of a filter sample shows that there are at least 5 organic nitrates present in the particle phase (Fig. 3.14). Despite the detection of organic nitrates, the elucidation of their isomeric chemical structure was not possible at this time. Corresponding mass spectra for two organic nitrate peaks from the GC-NICI-MS analysis are shown Fig. 3.15. Future studies with synthesized standards would be helpful in the identification and quantification of organic nitrates species.
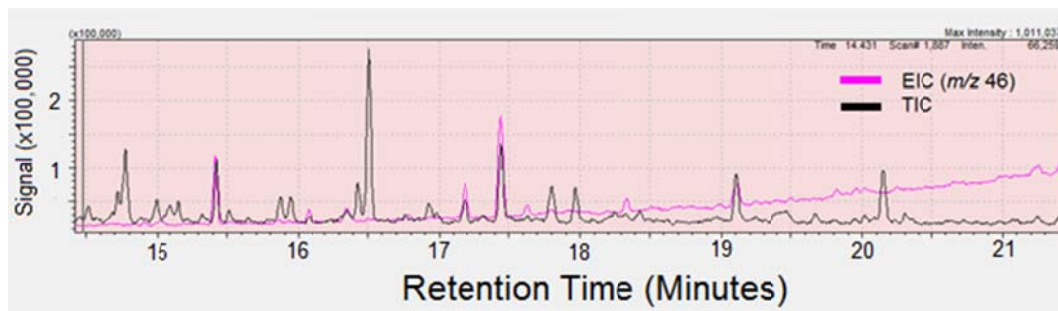
Figure 3.14. The EI-MS TIC and the NICI-MS EIC (*m/z* 46) from of an acidic seed aerosol chamber experiment filter extract.
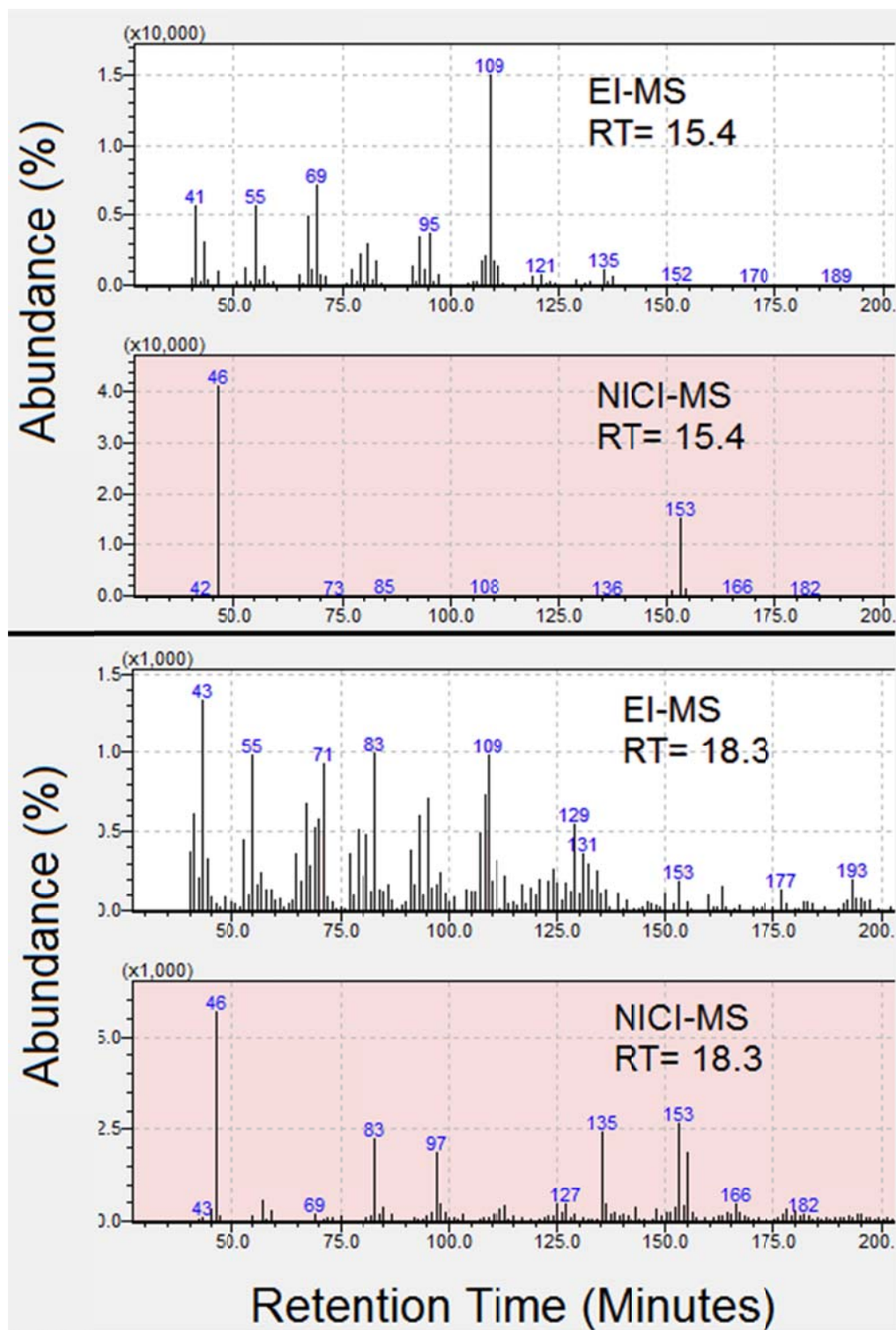
Figure 3.15. The EI and NICI mass spectra for peaks with retention time 15.4 and 18.3 minutes.

3.3.2 LC-MS Analysis

High resolution HPLC-TOF mass spectrometry was used as a complimentary

method to GC-MS in analysis of denuder-based filter extracts, due to its ability to

identify highly oxidized species, in contrast to the GC-based method. The major product

identified from HPLC-TOF analysis was pinonic acid (RT=23.0 minutes; Fig. 3.16),

which accounted for more than half (56%) of the total peak area from all identified

compounds. The observation of a large pinonic acid yield from OH radical initiated α-

pinene oxidation experiments is consistent with previous literature (e.g. Larsen et al.,

2001). A total ion chromatogram (TIC) from an acidic seed chamber experiment is shown

in Fig. 3.16.
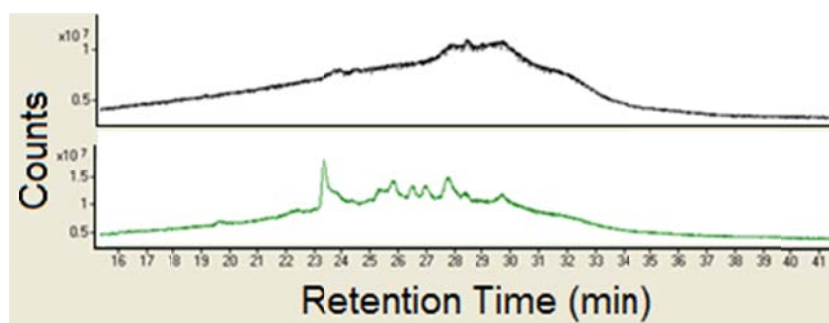
Figure 3.16. The total ion chromatograms (TIC) from an acidic seed aerosol experiment,
shown in green, and a blank, shown in black.

In addition to pinonic acid, several other products were detected, including

carboxylic acids and α-pinene-derived hydroxynitrates (Table 3.2). The carboxylic acids

were identified based on the detection of their exact masses and previous elution times

from reverse-phase liquid chromatography experiments (Glasius et al., 1999; Ma et al.,

2007). A mechanism for pinonic acid formation is shown in Fig. 3.7. While the

carboxylic acids norpinic, hydroxypinonic, hydroxypinalic, norpinalic, and 3-pinalic acid

have been identified in previous α-pinene oxidation experiments using both LC-MS and

GC-MS techniques (Glasius et al., 1999; Jaoui et al., 2005; Ma et al., 2007), the

identification of α-pinene-derived hydroxynitrates has been limited to a single study that

used gas phase atmospheric pressure ionization (Aschmann et al., 2002). To date, there

are no reported studies that have identified hydroxynitrates using mass spectrometry

coupled to separation technique (GC, LC). Thus, the identification of a technique with the

ability to separate and measure individual APNs is extremely valuable in the analysis of

atmospherically relevant organic nitrates.

Table 3.2. The retention times, molecular formulae, structures, and base peaks identified of the particle phase products from an acidic seed α-pinene oxidation experiment using HPLC-ESI(-)-TOF mass spectrometry.
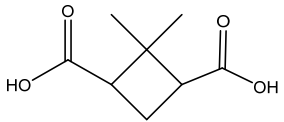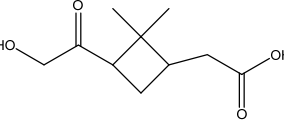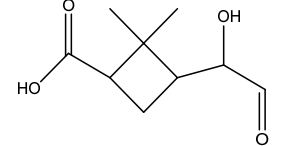
Retention Time (min)	Identified As:	Molecular Formula	Base Peak(s) (m/z)	Structure
19.24	norpinic acid	$C_8H_{12}O_4$	171.0664	
19.36	hydroxypinonic acid	$C_{10}H_{16}O_4$	259.1190 199.0970	
20.62	hydroxypinalic acid	$C_9H_{14}O_4$	185.0818	
21.66	norpinalic acid	$C_8H_{12}O_3$	215.0927 155.0707	

Table 3.2. Continued.

Retention Time (min)	Identified As:	Molecular Formula	Base Peak(s) (m/z)	Structure
21.90	3-pinalic acid	$C_9H_{14}O_3$	169.087	
22.03	APN	$C_{10}H_{17}NO_4$	214.1086 274.1298	unknown
22.57	APN*	$C_{10}H_{17}NO_4$	214.1087 274.1298	
22.86	APN*	$C_{10}H_{17}NO_4$	214.1086	
23.00	pinonic acid	$C_{10}H_{16}O_3$	183.1029	
23.64	APN	$C_{10}H_{17}NO_4$	214.1087 274.1298	unknown
24.39	APN*	$C_{10}H_{17}NO_4$	214.1084	
26.83	norpinonaldehyde	$C_{10}H_{14}O_2$	153.0920	
27.54	pinonaldehyde	$C_{10}H_{16}O_2$	167.1079	

The identification of individual products using HPLC-ESI(-)-TOF was accomplished by analysis of the [M-H]⁻ pseudo molecular ion. The ESI of several compounds (hydroxypinonic acid, norpinalic, and the APNs) also yielded the [M+C₂H₃O₂]⁻ ion, produced from an adduct with the solvent-derived acetate ion. The high resolution of the TOF mass spectrometry technique provided *m/z* information with less than 1 ppm error, allowing for the unambiguous identification of product empirical formulae.

The extracted ion current chromatogram (EIC) of the distinct α-pinene-derived molecular ion, *m/z* 214.1086 ± 0.01%, is shown in Fig. 3.17, displaying 5 clear peaks. The exact mass of the α-pinene-derived nitrate species identified indicates a hydroxynitrate functionality, which is likely to occur from the initial gas phase oxidation of α-pinene under high NO$_x$ conditions (see Chapter 2). The first generation organic nitrate products from α-pinene oxidation can isomerize to form at least four compounds, as described by Peeters et al. (2001) (see Fig. 2.34, Chapter 2). The split peak at ~22.7 minutes is likely from the similarly structured β-hydroxynitrates described earlier (RT = 22.57, 22.86; see Table 3.2) and the peak with the largest elution time is likely the ring-opened tertiary APN, due to the increased interaction with the hydrophobic column from its olefinic functionality. Structures for the proposed APNs are shown in Table 3.2.
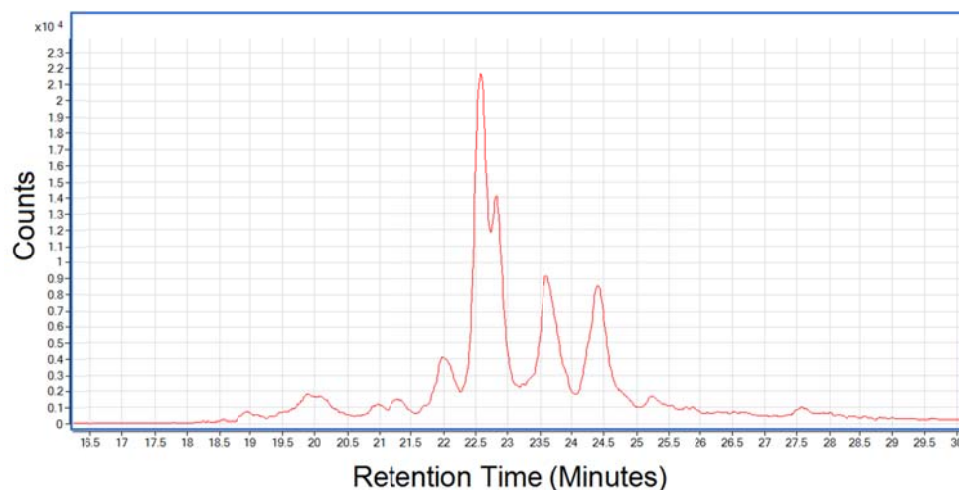
Figure 3.17. The EIC of *m/z* 214.1086 ± 0.01%, the unique α-pinene-derived organic nitrate pseudo molecular ion mass to charge ratio.

The presence of an [M-H]⁻ pseudo molecular ion peak from the ESI of α-pinene-derived nitrates is a surprising result. Previous studies have used ESI-MS to analyze both ambient and chamber samples (e.g. Surratt et al., 2008) but none have reported detection of hydroxynitrates using the soft ionization method, in contrast to the data from this study. One reason for the lack of literature data is the likely small ionization efficiency of hydroxynitrates from ESI. The ionization requires the deprotonation of an alcohol group, which is not a highly favorable process in comparison to carboxylic acids and organosulfates, two compounds that can easily sustain a negative charge. Perhaps assisting this deprotonation is the through the formation of acetate adducts, which had large abundance in the mass spectra of APN species, that can abstract a proton to form acetic acid. It is important to note that the response signal from the APNs was significantly smaller than that of carboxylic acids, such as pinonic acid, which had a measured response 2 orders of magnitude greater than the APNs. In any case, the

identification of molecular ions from ESI(-) ionization is a large step forward in the analysis of atmospherically relevant organic nitrates.

Also surprising was the electrospray ionization of ketone compounds such as pinonaldehyde and norpinonaldehyde (see Table 3.2). Previous studies using LC-MS were unable to detect pinonaldehyde using both electrospray ionization and atmospheric pressure chemical ionization. Similar to other products identified in this study, the main peak observed from the ESI(-) of the ketone compounds was the [M-H]⁻ pseudo molecular ion. Despite the lack of hydroxyl groups for ionization, it is possible that pinonaldehyde may undergo keto-enol tautomerization to produce an alcohol compound necessary for ionization. Similar to APNs, the ionization efficiency of pinonaldehyde using ESI is likely small in comparison to carboxylic acid analogues. One factor that likely contributes to our ability to measure the ketone and organic hydroxynitrate compounds with ESI, in comparison to previous studies, is the large quantity of α-pinene consumed in our chamber experiments.

Contrary to previous studies using LC-ESI(-)-MS, organosulfates were not detected using this mass spectrometry method. The ionization efficiency of organosulfates is currently unknown, thus, it is possible that organosulfate concentrations were below the detection limit of this method. Additionally, the acidity of particles was likely highly variable between experiments and it is uncertain if the pH conditions of the limited sample size analyzed were adequate for organosulfate production.

3.3.3 PS-MS analysis

The use of paper spray ionization was an effective method in the detection of organosulfates. Several organosulfates were identified based on tandem MS experiments and comparison to previous literature (Surratt et al., 2008). The organosulfates identified (Fig. 3.18) have been observed in previous experiments involving OH radical initiated oxidation of α-pinene. The tandem mass spectra of each organosulfate are shown in Fig. 3.19, along with comparison to available tandem mass spectra from Surratt et al. (2008). As seen in Fig. 3.19, there is good agreement with the *m/z* ratios detected from Surratt et al. (2008), although there are small differences in some peak intensities, which can be expected from differing ionization methods. The major carboxylic acid observed in LC-MS studies, pinonic acid, was also observed with the paper spray ionization MS technique (*m/z* = 183).
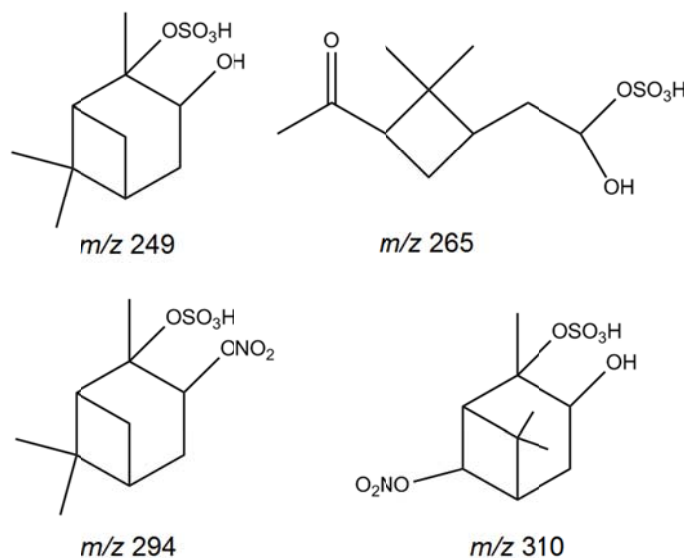
Figure 3.18. The organosulfates detected using paper spray ionization mass spectrometry. The mass to charge ratios detected for the [M-H]⁻ pseudo molecular ion are also listed.
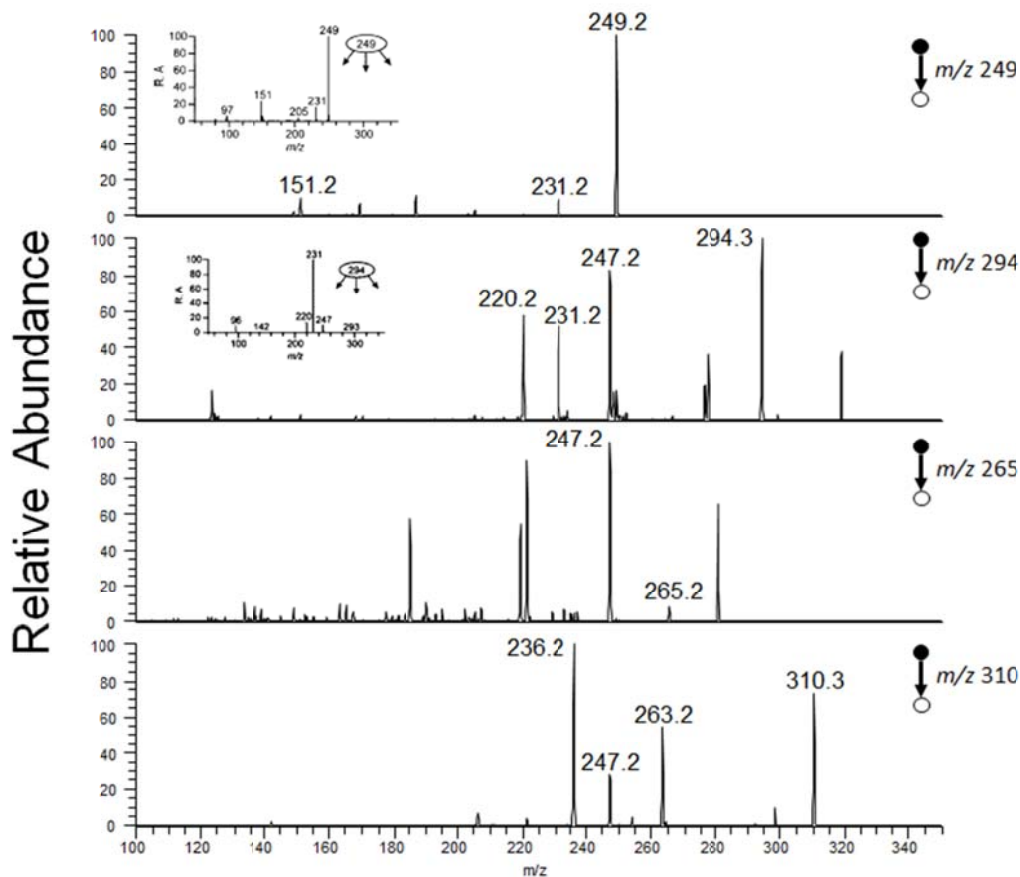
Figure 3.19. The tandem mass spectra of four organosulfates identified from paper spray ionization MS. The corresponding MS from Surratt et al. (2008) are also displayed, where available.

Additionally, water was added directly to a filter to observe the induced condensed phase chemistry. Mass spectra of a blank, wet, and dry filter are shown in Fig. 3.20. The blank filter had very few ions above m/z 160. An increase in peaks at m/z 80, 97, and 125 indicate that the presence of water allowed for increased concentrations of SO_3^-, HSO_4^-, and the $NO_3\text{-}H\text{-}NO_3^-$ adduct. The increase of the nitrate and sulfate anions may be related to an increase in organic nitrates and organosulfates within the sample. Additionally, the presence of both the $NO_3\text{-}H\text{-}NO_3^-$ adduct (m/z=125) and the nitrate ion

(*m/z*=62) in mass spectra indicates that nitric acid was a contributor to aerosol mass concentrations. Further studies investigating the quantification of particle phase nitric acid may be possible using PS-MS. Unfortunately, several other peaks in the mass spectra are still unidentified, highlighting the need for further research into the identification of negative ion fragments of α-pinene oxidation experiments using paper spray ionization.
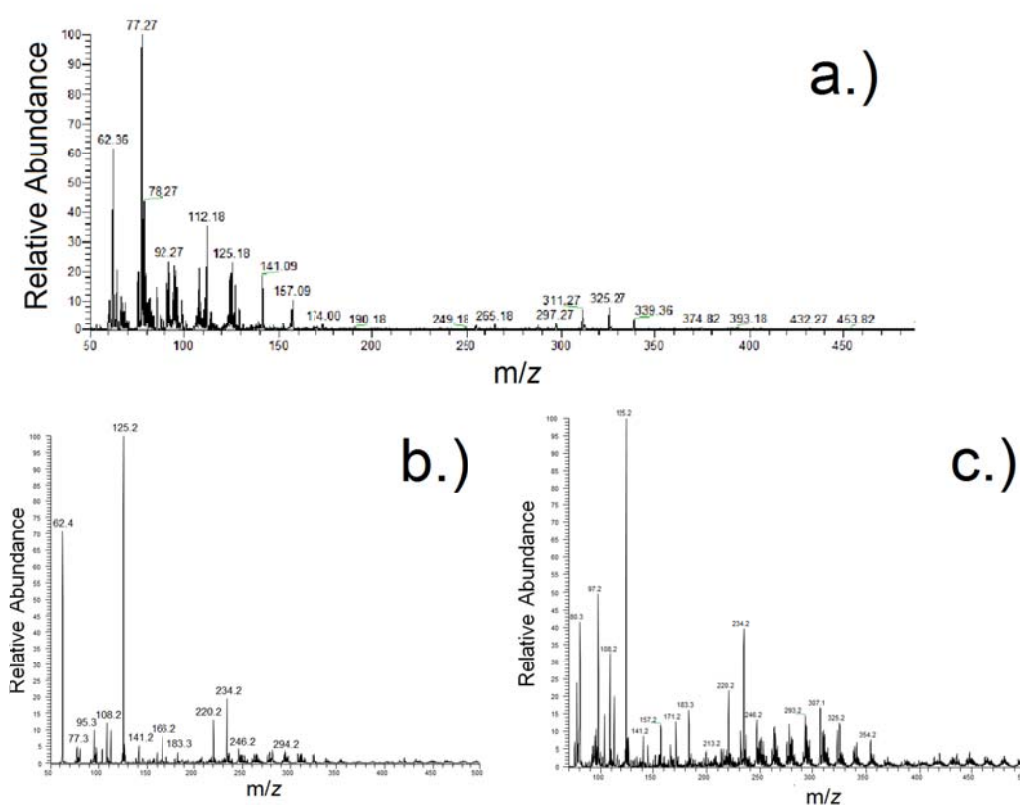
Figure 3.20. The paper spray ionization of a filter sample from a.) a blank, b.) an acidic seed aerosol chamber experiment and c.) the same filter with water added after 60 minutes.

The ability to directly identify organosulfates and carboxylic acids from filter samples is an important step forward in filter analysis. The minimal sample preparation needed decreases the opportunity for samples artifacts and manipulation. While this technique likely needs further development, it is straight-forward and relatively quick and has potential for in-field sample analysis.

3.4 Conclusions

The mass spectrometry experiments described here identified a wide variety of compounds from the OH radical initiated oxidation of α-pinene under high NO_x conditions. GC-MS analysis proved useful in identifying 18 different compounds from α-pinene oxidation, including fencholenic aldehyde, pinocaphenol, and α-pinene-derived nitrates, all of which have not been identified previously from α-pinene chamber experiments. Additionally, GC-MS allowed for detection of pinonaldehyde in the gas and particle phases, which showed that the gas/particle system in chamber experiments exhibited equilibrium partitioning. This supports that the observed non-equilibrium partitioning of APNs in Chapter 2 is derived from particle phase consumption reactions (hydrolysis).

Similar to previous studies, HPLC-ESI(-)-TOF mass spectrometry was useful in the identification of carboxylic acids. Additionally, for the first time, the HPLC-MS method was able to identify α-pinene-derived hydroxynitrates and pinonaldehyde by analysis of the [M-H]⁻ pseudo molecular ion. This has important implications in the future detection of atmospheric hydroxynitrates in complex sample matrices from both

chamber and field studies. The use of authentic standards is needed for quantification of organic nitrates using this technique.

Additionally, an analytical method was adapted to directly analyze filter samples using paper spray ionization mass spectrometry. This technique was able to identify both carboxylic acids and organosulfates from direct analysis of filter samples. The minimal sample preparation of this technique allowed for decreased sample handling, which corresponds to a lower potential for sample artifacts and manipulation that may occur in a traditional filter extraction and derivatization procedure. This ambient ionization method is a quick, effective method for sample analysis and has the potential for filter analysis during field studies.

CHAPTER FOUR: THE ACID-CATALYZED HYDROLYSIS OF ALPHA-PINENE-
DERIVED NITRATES

4.1 Introduction

Previous results described within this thesis suggest that the particle phase

hydrolysis is an important pathway concerning the fate of organic hydroxynitrates.

Despite this knowledge, the hydrolysis rate constants, specific mechanisms, and product

yields are either currently unknown or uncertain for almost all atmospherically relevant

compounds. To expand our knowledge on the hydrolysis-driven particle phase reactivity

of organic nitrates, aqueous phase reactions were studied with various organic nitrate

standards. The hydrolysis rate constants were determined for organic nitrates of differing

functionality over a range of solution pHs, giving insight into the chemical mechanisms

responsible for $RONO_2$ elimination reactions in the particle phase. Typical ambient

aerosol pH values are estimated to be between 1.5 and 4.0 (Zhang et al, 2007), however,

actual aerosol pH values have yet to be measured *in-situ*. Additionally, the hydrolysis of

other α-pinene-derived standards was investigated to gain further insight into the particle

phase chemistry of α-pinene-derived products, such as those created from chamber

experiments.

<u>4.2 Experimental</u>

Organic nitrate hydrolysis reactions were conducted by injecting a known amount

of a standard into a 100 mL buffered solution. The solutions were constantly mixed using

a stir bar. Aliquots of 5mL were taken at varying time points and extracted with 5mL of

tetrachloroethylene (C_2Cl_4) before analysis using FT-IR for organic nitrate quantification

(see Chapter 2) and GC-MS for product identification (see Chapter 3). The solutions used

were buffered at 10 mM buffer concentrations, and pH values ranged from 0.25 to 6.9. A

complete list of pH values and buffer systems used is given in Table 4.1.

Table 4.1. The buffer systems used for hydrolysis reactions and the corresponding pH
values.

pH	Buffer System	Acid pK_a
0.25	HSO_4^-/SO_4^{2-}	2.0
1.0	HSO_4^-/SO_4^{2-}	2.0
2.5	HSO_4^-/SO_4^{2-}	2.0
4.0	CH_3COOH/ CH_3COO^-	4.8
6.9	$H_2PO_4^-/HPO_4^{2-}$	7.2

4.2.1 Nuclear Magnetic Resonance

An α-pinene-derived nitrate standard was synthesized and analyzed for purity

using nuclear magnetic resonance (NMR). NMR is a common technique in organic

structure determination that can differentiate individual atoms within a sample based on

their interaction with RF radiation in a magnetic field. This interaction is heavily

influenced by the connectivity of said atoms, thus, NMR can be used to elucidate the structure of chemical species.

Unlike other spectroscopic methods, such as infrared and UV-Vis, NMR involves the absorption of electromagnetic radiation by atomic nuclei rather than outer electrons. After absorption of electromagnetic radiation in the radio frequency region occurs under an applied magnetic field, nuclei will emit measureable radiation, which is collected using a radio receiver coil. Only atoms with an odd number of protons and/or neutrons, such as ^{1}H and ^{13}C, are capable of nuclear magnetic resonance, due to their non-zero spin.

Since a nucleus can also interact with the magnetic field of nearby electrons and nuclei, the radio frequency of a nucleus' absorption is highly dependent on its surrounding environment, i.e. the connectivity of a molecule. The differences in absorption frequency of nuclei are called chemical shift and can be used to determine the molecular structure of a species. The chemical shift is determined in reference to an internal standard, typically DSS (4,4-dimethyl-4-silapentane-1-sulfonic acid).

4.2.2 α-Pinene-Derived Nitrate Synthesis

The synthesis of the β-hydroxy nitrate derived from α-pinene was based on Pinto et al. (2007). This procedure involves the interaction of bismuth(III), a Lewis acid, with the epoxide ring of α-pinene oxide to weaken the C-O bond and allow the nitrate ion (NO_3^-) to successfully attack the secondary carbon on the epoxide ring. Trace amounts of water within the reaction mixture will then convert the oxygen from the epoxide ring into an alcohol group. This reaction is regioselective, due to its S_N2 mechanistic nature, and,

thus, the corresponding tertiary β-hydroxy nitrate cannot be formed from this pathway.

The S$_N$2 reaction mechanism involved is shown in Fig. 4.1.
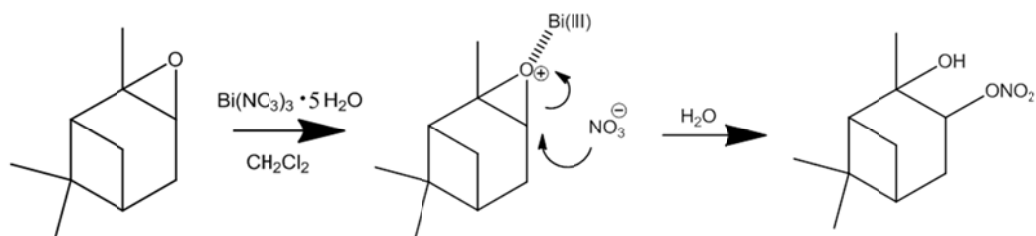
Figure 4.1. The synthesis of the secondary β-hydroxy nitrate derived from α-pinene starting from α-pinene oxide and bismuth(III) nitrate pentahydrate.

The α-pinene-derived nitrate synthesis was accomplished by adding 1 molar equivalent (0.96 mL) of α-pinene oxide (99%, Sigma Aldrich, Inc.) to a 1.5 molar equivalent (0.48 g) solution of bismuth(III) nitrate pentahydrate [Bi(NO$_3$)$_3$·5H$_2$O; Sigma Aldrich, Inc.] in methylene chloride (0.67 mL; CH$_2$Cl$_2$). Prior to use, the bismuth(III) nitrate pentahydrate was dried in an 80°C oven and the methylene chloride was dried using molecular sieves. Drying of the reagents significantly increased the α-pinene-derived nitrate yield from this synthesis. The reaction was stirred under N$_2$ for one hour before vacuum filtration and flash chromatography purification using a 20% solution of ethyl acetate in hexane. The purification of the α-pinene-derived nitrate was confirmed using ^{1}H NMR as all peaks were able to be identified and protons were quantified (Fig 4.3). Synthetic yields of up to ~20% were achieved from this reaction.

The chemical shifts, peak multiplicity and integration of the APN protons in the ^{1}H NMR spectrum (labeled a-i in Fig. 4.3), using deuterated chloroform ($CDCl_3$) as a solvent, were as follows: (a) δ 5.6 (triplet, 1H), (b) δ 5.6 (singlet, 1H), (c) δ 2.4 (triplet of a triplet, 1H), (d) δ 2.2 (triplet, 1H), (e) δ 1.9 (doublet of a doublet, 2H), (f) δ 1.8 (singlet, 3H), (g) δ 1.6 (singlet, 3H), (h) δ 1.5 (singlet, 3H), (i) (doublet of a doublet, 2H).
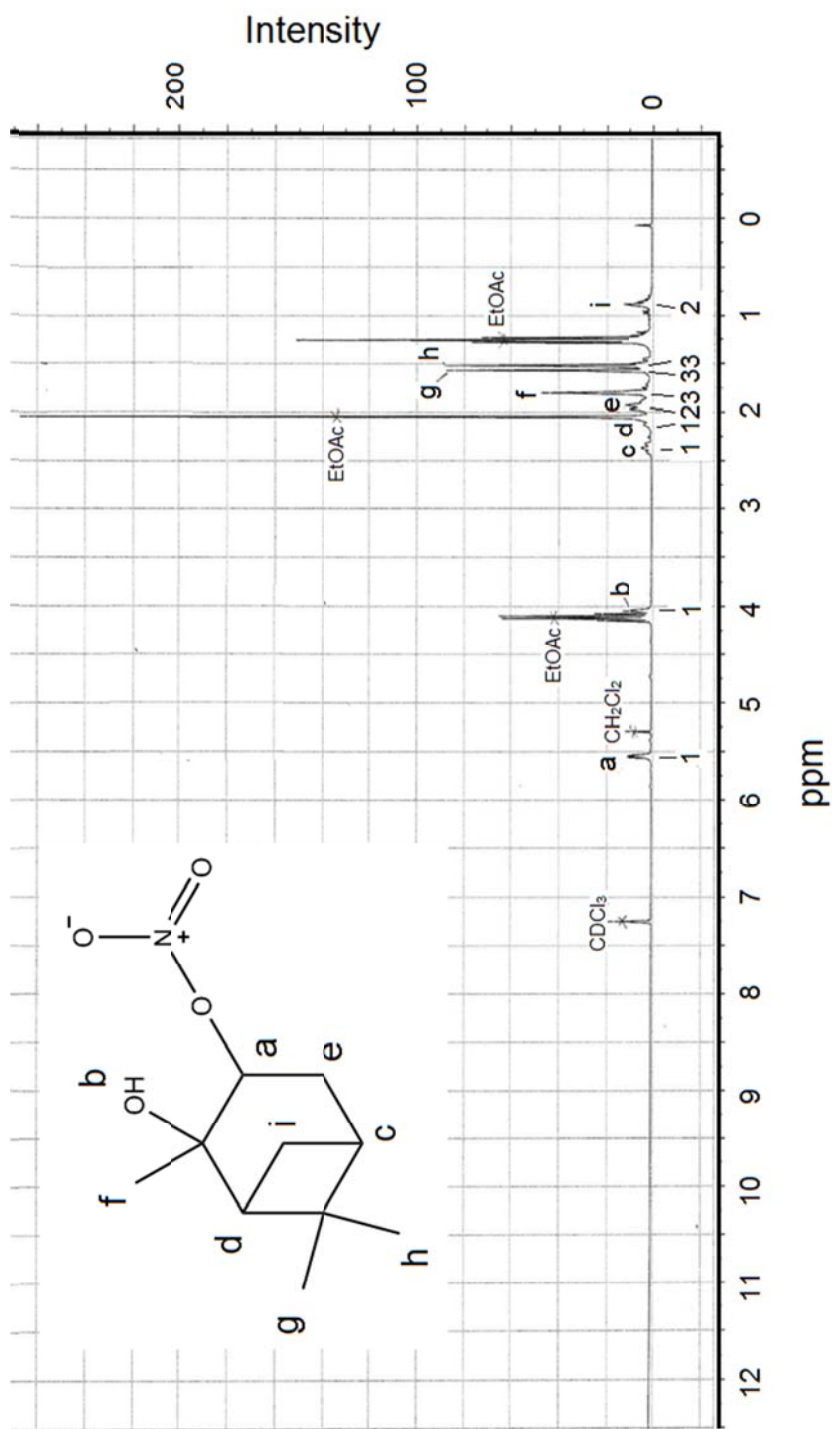
Figure 4.2. The ¹H NMR of the α-pinene-derived nitrate. Hydrogen peaks are labeled a-i as are solvent peaks from ethyl acetate (EtOAc), methylene chloride (CH₂Cl₂), and deuterated chloroform CDCl₃ . The proton integrations are listed below each peak.

4.2.3 Hydrolysis Procedure

Hydrolysis reactions were studied using commercial standards for isopropyl nitrate (IPN; Sigma Aldrich, Inc.) and isobutyl nitrate (IBN; Sigma Aldrich, Inc.), shown in Fig. 4.3, and synthesized standard α-pinene-derived nitrate (APN), shown in Fig. 4.4. Hydrolysis reactions with the commercially available α-pinene oxide (Sigma Aldrich, Inc.), pinanediol (Sigma Aldrich, Inc.), and *trans*-sobrerol (Sigma Aldrich, Inc.) were also completed to compare to the APN-derived chemistry and products (Fig. 4.4).
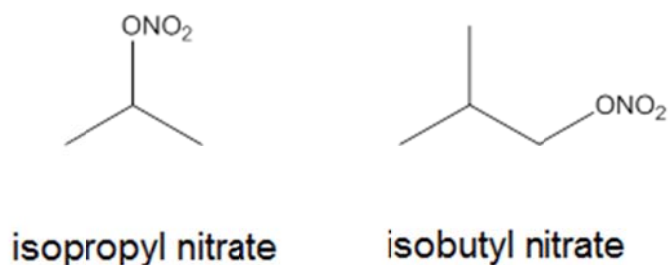
Figure 4.3. The structures for isopropyl nitrate (IPN) and isobutyl nitrate (IBN).
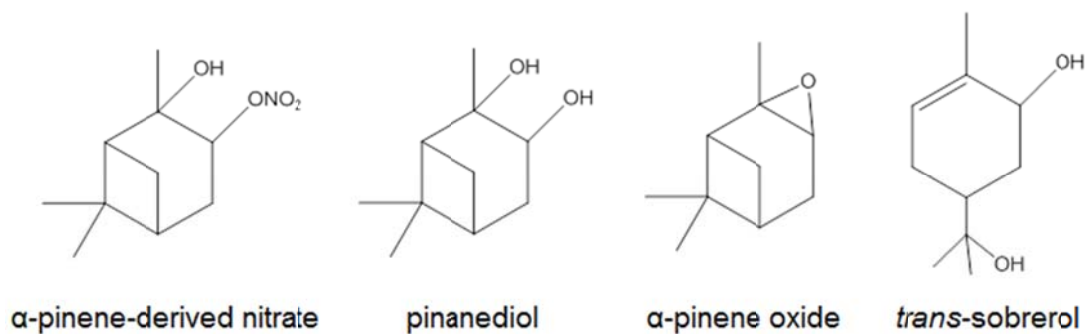
Figure 4.4. The structures for the α-pinene-derived nitrate, pinanediol, α-pinene oxide, and *trans*-sobrerol.

Similar to previous experiments, the asymmetric –NO_2 stretch of organic nitrates in the infrared region (~1640 cm^{-1}) was used to measure $RONO_2$ concentrations. Product analysis was conducted by liquid injection of the C_2Cl_4 extracts into a GC-MS using EI ionization (see Chapter 3 for GC column and oven conditions).

4.3 Results

4.3.1 Hydrolysis Rate Constant Determination

Organic nitrate concentrations, determined using FT-IR, for a typical experiment are shown as a function of time in Fig. 4.5a. Similar to previous determination of first order loss rate constants (see Chapter 2), a linear regression of a plot of $\ln(A_o/A_t)$ against time was created with the slope equal to k, the first order rate constant (Fig. 4.5b). The first order loss is described by Eq. 4.1 and 4.2 below:

$$A_t = A_o \exp(-kt) \tag{4.1}$$

$$\ln(A_o/A_t) = kt \tag{4.2}$$

Here A_t is the concentration of the organic nitrate at time t, A_o is the original concentration of the organic nitrate, and k is the first order loss rate constant.
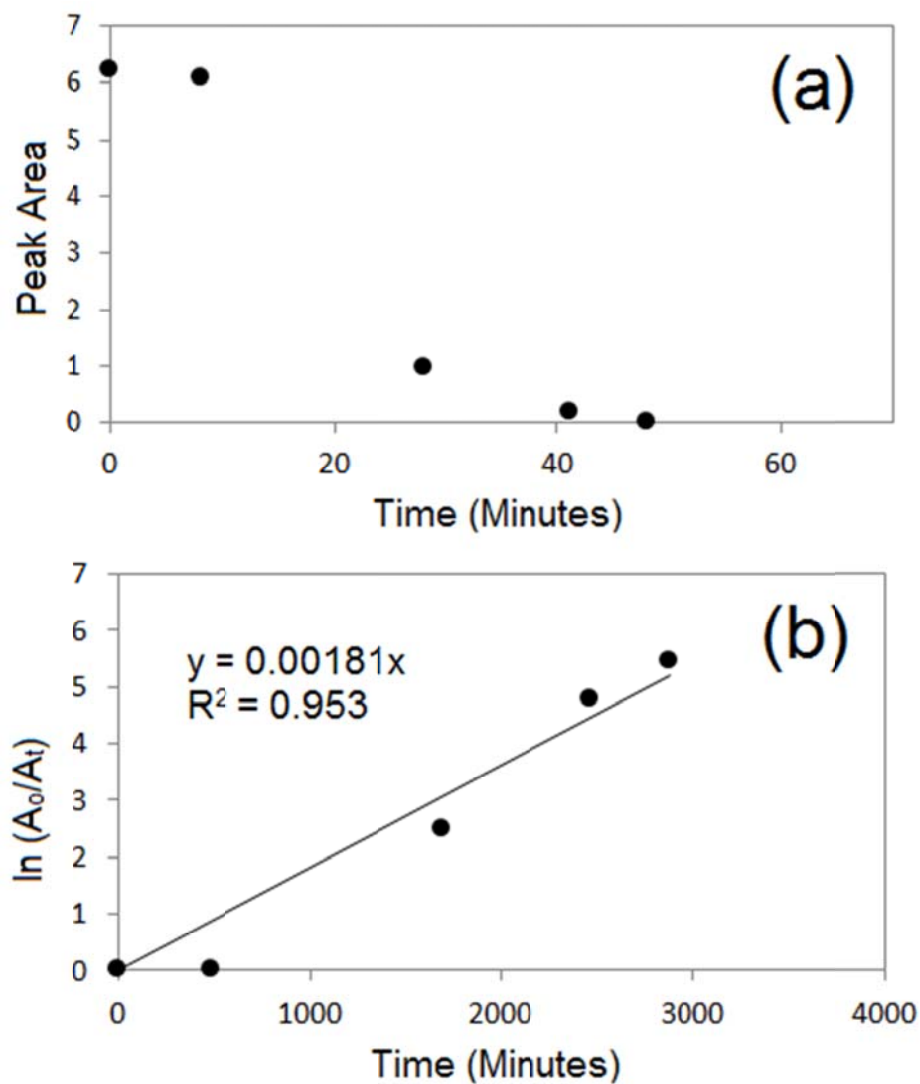
Figure 4.5. (a) The peak area of α-pinene-derived nitrate plotted versus time, in minutes, from a condensed phase hydrolysis reaction at pH 0.25 and (b) the corresponding plot of $\ln(A_o/A_t)$ versus time, in seconds, used to determine the first order hydrolysis rate constant.

4.3.2 pH Dependence of Hydrolysis Rate Constants

As discussed in Chapter 2, particle phase hydrolysis is an important reaction concerning the atmospheric fate of organic nitrates. The consumption of the $RONO_2$ functional group within the aerosol phase has impact on the fate of gas phase NO_x and its

contribution to atmospheric ozone concentrations. In all experiments, the hydrolysis rate constants increased with decreasing pH, as shown in Figs. 4.6 and 4.7. For the α-pinene-derived nitrate, average hydrolysis rate constants ranged from 3.16×10^{-5} s^{-1} at neutral pH (~6.9) to 2.02×10^{-3} s^{-1} at low pH (0.25). The hydrolysis rate constants for isopropyl nitrate and isobutyl nitrate were smaller by more than 2 orders of magnitude, ranging, on average, from 1.23×10^{-7} s^{-1} at neutral pH (~6.9) to 1.1×10^{-5} s^{-1} at low pH (0.25), for isopropyl nitrate and isobutyl nitrate. The error bars in Fig. 4.7 correspond to one standard deviation of replicate measurements.
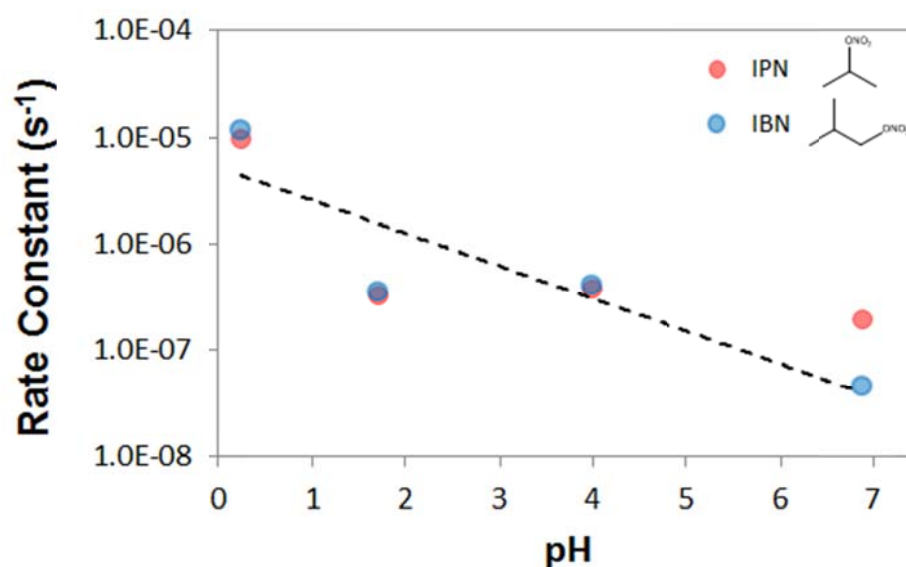
Figure 4.6. The hydrolysis rate constants (s^{-1}) for isopropyl nitrate (IPN; red) and isobutyl nitrate (IBN; blue) as a function of solution pH.
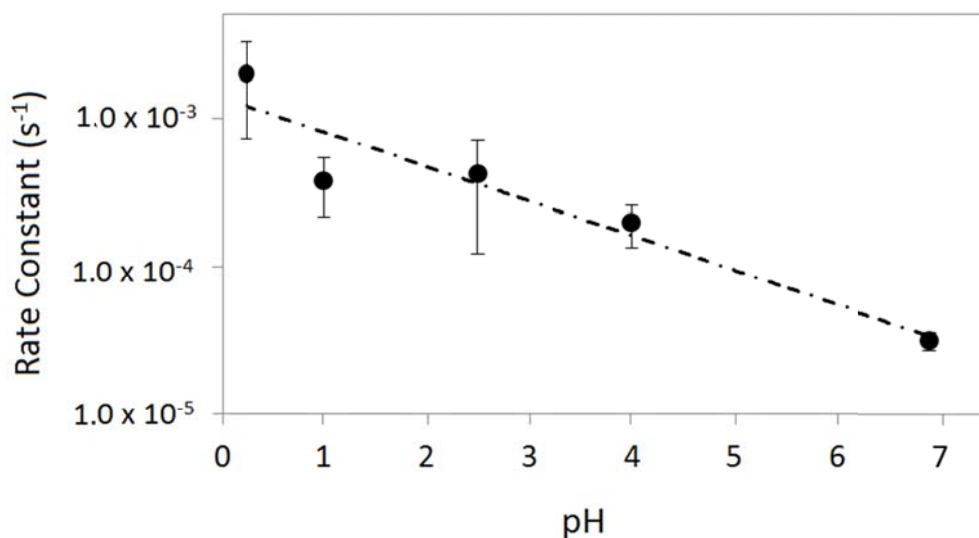
Figure 4.7. The hydrolysis rate constants (s^{-1}) for the α-pinene-derived nitrate as a function of solution pH. The error bars correspond to one standard deviation.

The corresponding hydrolysis lifetimes for the organic nitrates studied are shown in Table 4.2. The α-pinene-derived nitrate had a condensed phase hydrolysis lifetime of 8.3 minutes at low pH (0.25) and a lifetime of 8.8 hours at neutral pH (~6.9). Both of these lifetimes, as well the uptake lifetime of APNs into the particle phase under ambient conditions (3.43 hours; see Chapter 2), are well within the lifetime of an atmospheric aerosol particle. Also, as discussed in Chapter 2, it was shown that complete particle phase hydrolysis of organic nitrates can occur within an hour long experiment, which, combined with the pH dependence of the APN hydrolysis, suggests that the pH of the lab generated aerosol was pH < 4.0. The average lifetimes of isopropyl nitrate and isobutyl nitrate were much larger than for APN, likely due to their smaller size (see below), and ranged from 26 hours at low pH (0.25) to greater than 8 months at neutral pH (~6.9).

Table 4.2. The hydrolysis lifetimes of isopropyl nitrate (IPN), isobutyl nitrate (IBN), and the α-pinene-derived nitrate (APN) at varying pH.

pH	Lifetime		
	IPN	IBN	APN
0.25	28 h	23 h	8.3 min
1.0	N/A	N/A	44 min
1.7	35 d	33 d	N/A
4.0	30 d	28 d	1.3 h
6.9	> 8 mo	> 8 mo	8.8 h

4.3.3 Specific Acid-Catalyzed Hydrolysis Mechanism

The pH dependence of the observed rate constants indicates that the hydrolysis of organic nitrates is a specific acid-catalyzed mechanism. In specific acid-catalyzed mechanisms, the transfer of the H^+ ion from the acid to the reactant is reversible and occurs before the rate determining step. This is in contrast to a general-acid catalyzed mechanism that involves the transfer of the H^+ ion in a process simultaneous with the rate determining step. General acid-catalysis is not dependent on solution pH. The general mechanism for a two-step specific acid-catalyzed reaction is shown in Fig. 4.8. Assuming that protonating the reactant (R) is an equilibrium process, the rate of the reaction can be described analytically as a function of the hydronium ion concentration, $[H^+]$ (Fig. 4.8).

$$\frac{k_1}{k_{-1}} = \frac{[RH^+]}{[R][H^+]} \tag{4.3}$$

$$\text{Rate} = k_2[RH^+] = k_2\left(\frac{k_1}{k_{-1}}[R][H^+]\right) = k_{obs}[R][H^+] \tag{4.4}$$

Figure 4.8. The general mechanism for a two-step specific acid-catalyzed reaction where "r.d.s" indicates the rate determining step. The equilibrium of the hydronium ion (H^+) addition to the reactant (R) is described in Equation (4.3) and the rate of the reaction is described in Equation (4.3).

An observed specific acid-catalyzed mechanism is also consistent with the unimolecular reaction pathway. As seen in step 2 (Fig. 4.8), the rate determining step of the specific acid-catalyzed mechanism is preceded by the reactant's acceptance of the H^+ ion. This is also true for the hydrolysis of $RONO_2$ compounds by unimolecular mechanisms (E1, S_N1), where the rate determining step occurs after accepting the acidic proton, creating products through a carbocation intermediate. See Fig. 4.9 for a proposed mechanistic explanation of the isobutyl nitrate hydrolysis reaction.
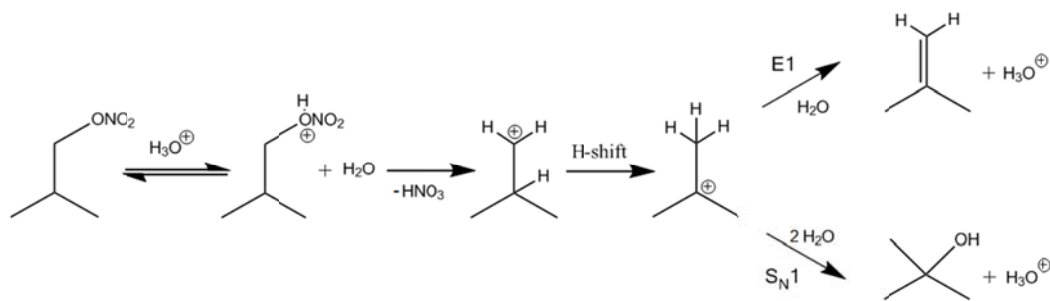
Figure 4.9. The proposed unimolecular mechanism for isobutyl nitrate (IBN) demonstrating the specific acid-catalysis and H-shift rearrangement.

The observed hydrolysis rate constants for isobutyl nitrate and isopropyl nitrate were very similar, as displayed in Fig. 4.6. Previous research has shown that hydrolysis rate constants increase with alkyl substitution of the reactive carbon center (Darer et al., 2011) and, since isobutyl nitrate is a primary organic nitrate and isopropyl nitrate is a secondary organic nitrate, it may be surprising to observe similar rate constants for these two species, at first examination. However, the similarity in observed hydrolysis rate constants can be explained through the inspection of the unimolecular (S_N1, E1) mechanism. The creation of a carbocation intermediate allows for intramolecular rearrangement, and for the primary isobutyl carbocation created through the unimolecular mechanism, a 1,2 H-shift, which is typically less than 4 kcal/mol (Saunders and Cline, 1990), is likely to rapidly occur to produce the more stable tertiary carbocation (Fig. 4.9). Since the rate of unimolecular reactions are proportional to the stability of the carbocation intermediate, the relatively large hydrolysis rate observed for the primary isobutyl nitrate compared to the secondary isopropyl nitrate can easily be explained.

A similar investigation into the hydrolysis rate constants of primary and secondary organic nitrates was reported by Jacobs et al. (2014). Jacobs et al. (2014) investigated the hydrolysis rate constants of a primary and a secondary isoprene-derived nitrate and, similar to this study, found that the primary organic nitrate had a much larger hydrolysis rate constant than expected. In fact, the hydrolysis rate constant was observed to be two orders of magnitude larger than its secondary analogue. This phenomenon was attributed to the resonance stabilization of the primary carbocation to form a much more stable tertiary carbocation, via the unimolecular reaction mechanism, and allow for faster hydrolysis rates (Fig. 4.10).
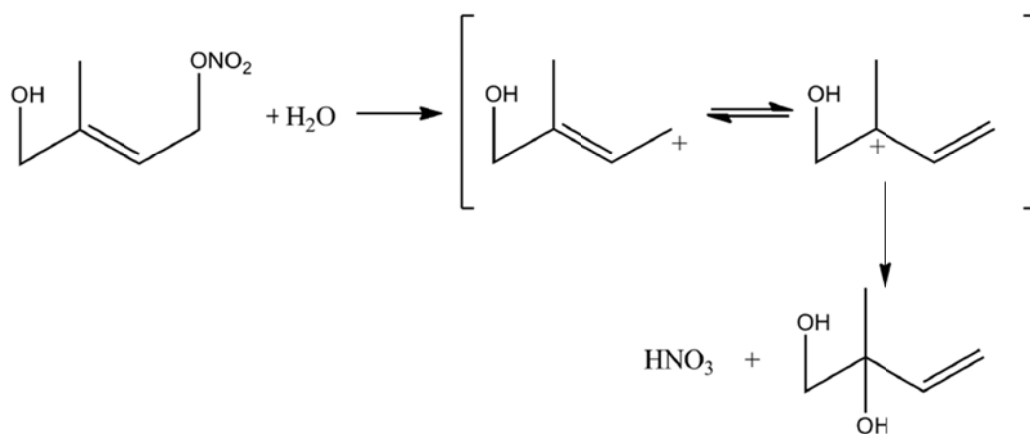
Figure 4.10. The hydrolysis of the primary 1,4-isoprene-derived nitrate showing the resonance stabilization of the carbocation intermediate, as described by Jacobs et al. (2014).

The hydrolysis rate constant for the α-pinene-derived nitrate was much larger than those for isobutyl nitrate and isopropyl nitrate. Similar to the case of isobutyl nitrate, the relatively large hydrolysis rate constant for the APN is likely due to the increased stability of the carbocation intermediate. The increased carbon number of the α-pinene-derived nitrate allows for better stabilization of the positive charge compared to the short-chain isopropyl and isobutyl carbocations and faster hydrolysis in the aqueous phase. The α-pinene-derived nitrate also had a larger hydrolysis rate constant than the secondary isoprene-derived organic nitrate reported by Jacobs et al. (2014), also likely due to the increased stability of the relatively larger APN intermediate.

Hydrolysis rate constants were not determined for α-pinene oxide and pinanediol. *trans*-Sobrerol had a hydrolysis lifetime of ~9 days at pH 1.0. The hydrolysis of α-pinene oxide occurred rapidly within solution and, thus, kinetic data couldn't be acquired. Pinanediol was stable in aqueous solutions at pH 0-7. Under extremely acidic conditions (pH<0), pinanediol hydrolysis occurred at rate much faster than the sampling frequency.

4.3.4 Product Identification

Identification of the hydrolysis reaction products was conducted using GC-(EI)-MS. The hydrolysis of the α-pinene-derived nitrate did not yield the corresponding S_N1 alcohol product, pinanediol (Fig. 4.11). Instead, the major product observed was campholenic aldehyde, accounting for over 90% of the total peak area from all products. Minor products observed included pinol and pinocamphone. Campholenic aldehyde has also been observed as the major product from the hydrolysis of α-pinene oxide from both this study (99% yield) and a recent publication (Bleier et al. 2013), suggesting that a similar mechanism is responsible for the hydrolysis of both APN and α-pinene oxide. Hydrolysis reactions of *trans*-sobrerol and pinanediol led to the formation of pinol as the major product (> 90% yield).

The formation of all three observed products from the hydrolysis of the α-pinene-derived nitrate, pinol, pinocamphone, and campholenic aldehyde, are formed through a unimolecular mechanism involving a tertiary carbocation intermediate (Fig. 4.11), which will be referred to as AP_t^+ interchangeably throughout this thesis. For α-pinene oxide hydrolysis, the reaction is initiated by the protonation of the epoxide, which decreases the C-O bond strength, leading to a break in the epoxide ring and the formation of AP_t^+. The tertiary carbocation, AP_t^+, is also formed from pinanediol after protonation of the tertiary alcohol and subsequent dissociation of water, which is an excellent leaving group. For the APN, the nitrate group is originally protonated to create the strong leaving group HNO_3, which will dissociate to create the corresponding secondary carbocation. From here, the adjacent β-hydroxyl group can form a bond with the carbocation center to create the same protonated epoxide from the α-pinene oxide hydrolysis. Similar to the α-pinene oxide

hydrolysis pathway, this will lead to the formation of campholenic aldehyde, pinol, and

pinocamphone via the AP_t^+ intermediate.
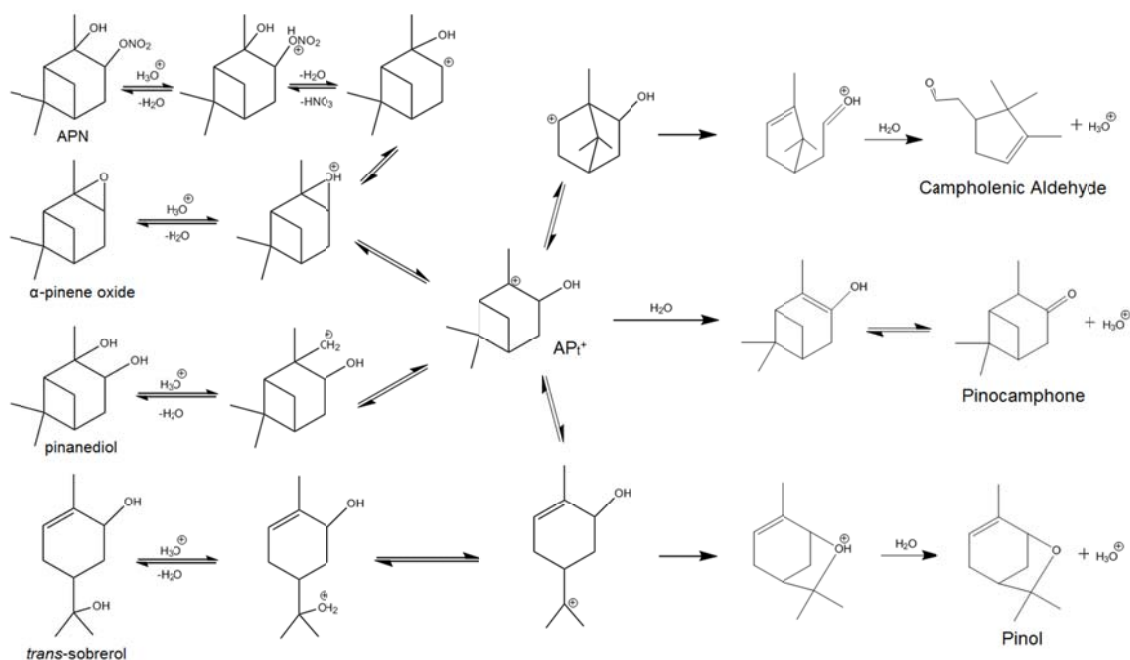
Figure 4.11. The proposed specific acid-catalyzed hydrolysis mechanisms of the α-pinene-derived nitrate (APN), α-pinene oxide, pinanediol, and *trans*-sobrerol.

Once the tertiary carbocation (AP_t^+) is formed, the reaction will either proceed via

an elimination (E1) mechanism or intramolecular rearrangement (Fig. 4.11). Following

the E1 pathway will lead to the formation of pinocamphone. In this mechanism, water

will abstract a β-proton from the AP_t^+ intermediate, causing the formation of a double

bond. The resulting olefinic alcohol product will be in equilibrium with pinocamphone

through keto-enol tautomerization.

Rearrangement of AP_t^+ will lead to the formation of either pinol or campholenic aldehyde (Fig. 4.11). Pinol is formed after the four-membered ring of AP_t^+ breaks to form a double bond and another tertiary carbocation. This rearrangement will be followed by attack from the secondary hydroxyl group to create a protonated pinol compound. The abstraction of the proton by water will complete the acid-catalyzed reaction to create the final pinol product and H_3O^+.

The major product of APN and α-pinene oxide hydrolysis, campholenic aldehyde, is formed by rearrangement of the AP_t^+ intermediate to form a secondary carbocation (Fig. 4.12). The conversion of a tertiary carbocation to a secondary carbocation is usually uphill by about ~10 kcal/mol, however, if the rearrangement leads to the formation of a product much lower in energy, this barrier is not prohibitive (Carey and Sundberg, 2007). After rearrangement to form the secondary carbocation, the free electrons on the oxygen will create a bond with the adjacent carbon to simultaneously form a carbonyl, break the six-membered ring, and create a double bond on the five-membered ring. The final campholenic aldehyde product is formed after water abstracts the remaining acidic proton, reforming H_3O^+ and completing the acid-catalyzed reaction.

The large yields of campholenic aldehyde (> 90%) from the hydrolysis of α-pinene-derived species are related to the molecule's relative stability. Previous theoretical calculations have indicated that campholenic aldehyde has the lowest free energy of a suite of α-pinene-derived species that included α-pinene oxide, pinanediol, pinol, *trans*-sobrerol, and the same APN from this study (Bleier et al., 2013). Thus, the experimental results from this study are consistent with the calculations from Bleier et al. (2013).

The formation of campholenic aldehyde from the hydrolysis of an α-pinene-derived nitrate creates a product that has a vapor pressure estimated to be three orders of magnitude greater than the original organic nitrate. Vapor pressure calculations were accomplished using the EPI Suite available at the Environmental Protection Agency website (http://www.epa.gov/opptintr/exposure/pubs/episuite.htm). Forming more volatile species within a particle may lead to a reduction in aerosol mass by the partitioning of products back into the gas phase. It is important to note that campholenic aldehyde has olefinic functionality and may react further in the particle phase, especially under acidic conditions. Thus, both the gas and particle phase fate of campholenic aldehyde warrants future study to determine the fate of α-pinene-derived species in the atmosphere.

4.4 Conclusions

The large hydrolysis rate constant for the atmospherically-relevant α-pinene-derived nitrate corresponds to a small hydrolysis lifetime, which is well within the atmospheric lifetime of an aerosol particle. Lifetimes ranged from 8.8 hour at neutral pH (~6.9) to 8.3 minutes at low pH (0.25). Coupled with the expected short particle phase uptake lifetime under ambient conditions (3.43 hours; see Chapter 2), the fast hydrolysis of organic nitrates in the condensed phase indicates that particle phase hydrolysis is likely a sink for atmospheric NO_x. The formation of campholenic aldehyde from the APN represents the removal of the $RONO_2$ functionality to form an aldehyde compound that may partition back into the gas phase, due to its estimated vapor pressure to be three orders of magnitude greater that of the APN. Thus the creation of aldehyde species from

particle phase hydrolysis has the potential for decreasing aerosol mass. However, campholenic aldehyde has olefinic functionality and may undergo further reactions under acidic conditions, such as oligomerization, to create low volatility products that remain in the particle phase. Future investigation into the particles phase reactivity of campholenic aldehyde is needed to better understand its impact on secondary organic aerosol mass.

The formation of the similar products from the hydrolysis of four different α-pinene-derived species indicates that unimolecular mechanisms are prevalent in condensed phase reactions, having implication into cloud/fog processing and aerosol chemistry. Since a variety of α-pinene-derived species react through a similar pathway, it is possible that the fate of monoterpene-derived species in the particle phase is governed by a similar unimolecular mechanism (S_N1, E1). Additionally, due to the large dependence of organic nitrate hydrolysis rate constants on solution pH, ranging over several orders of magnitude, the specific acid-catalyzed hydrolysis is likely to be a very important contributor to aerosol phase chemistry at atmospherically-relevant pH values (1.5 – 4.0; Zhang et al., 2007).

CHAPTER FIVE: THE ANALYSIS OF PARTICLE PHASE ORGANIC NITRATES
USING RAMAN MICROSPECTROSCOPY

5.1 Introduction

Results within this thesis describe the production of organic nitrates in the gas

phase and the particle phase reactivity that likely governs their atmospheric fate. Despite

this knowledge, the transition between the gas and particle phases is still uncertain.

Additionally, since recent research has shown that the physical state of an aerosol may be

separated into organic and aqueous sections (You et al., 2012; Song et al., 2012), instead

of a well-mixed particle described by the Pankow (1994) model, it is important to

investigate the partitioning system of organic nitrates in real-time to learn more about the

physical state of organic nitrate-containing particles and how interaction with water

occurs.

The uptake of water to or presence of water in aerosols can lead to the hydrolysis

of particle phase organic nitrates (Chapter 2), however, the real-time observation of such

chemistry has not yet been accomplished. Analysis of samples using spectroscopy is a

promising technique because it does not lead to sample degradation, as opposed to mass

spectrometry, and a partitioning system can be observed without destroying particles.

However, in the case of aerosol particles, the uptake of water happens readily, and

infrared spectroscopy, as described earlier in this thesis, is not an attractive option due to

the large infrared absorption by water. Raman spectroscopy, on the other hand, has a

large potential for analysis of the hydrolysis reactions, due to the minimal Raman scattering activity of water. In addition to organic nitrates and possible products, the nitrate ion also has an active peak in the Raman spectrum, giving potential to the simultaneous measurement of organic nitrates, products, and the nitrate ion created through the hydrolysis reaction.

By coupling the method of Raman spectroscopy with a confocal microscope, recent studies have been able to monitor both physical and chemical changes to aerosol particles with real-time measurements (Ciobanu et al., 2009). Additionally, a Raman imaging technique has been applied to particles, allowing for information on the spatial distribution of compounds within an aerosol particle (Batonneau et al., 2006). Thus, Raman microspectroscopy is a potentially useful technique for investigation of the particle phase hydrolysis of organic nitrates.

Another question raised within this thesis concerns the pH of aerosol particles created in photochemical chamber experiments. As shown in Chapter 4, the rate of organic nitrate hydrolysis is highly dependent on the pH of its environment. However, unlike in the condensed phase studies, the pH of the aerosol particles in chamber experiments (Chapter 2) could not be directly measured. Instead particle pH was calculated using the E-AIM model (Wexler and Clegg, 2002) for pre-experiment conditions. The application of Raman microspectroscopy to directly monitor aerosol particles provides potential in the determination of aerosol pH, by allowing for the measurement of free ions within the aerosol.

<u>5.2 Experimental</u>

Raman microspectroscopy experiments were conducted in collaboration with Prof. Andrew A. Ault at the University of Michigan, Ann Arbor, focusing on isopropyl nitrate, isobutyl nitrate, ethylhexyl nitrate, 2-mononitroglycerin, and α-pinene oxide. Raman spectra of the various standards were recorded using Raman microscopy. The partitioning of the organic standards to inorganic aerosol particles and the resulting chemical reactions under high relative humidity (RH) conditions were also investigated. Particle acidity was varied to investigate the effect on the aerosol phase chemistry. Additionally, inorganic free ion concentrations of laboratory-generated particles were measured to gain insight into aerosol pH.

5.2.1 Raman Spectroscopy

Raman scattering was first discovered by C. V. Raman in 1928 (Raman, 1928). The concept relies on the inelastic scattering of radiation by a compound and its ability to reemit a photon at a different energy than the incoming light. The light source in Raman experiments is usually in the form of laser radiation. When a molecule reemits a photon at a lower frequency than the incoming radiation, it is known as Stokes scattering, and, when the reemitted photon is of higher frequency, it is known as anti-Stokes scattering. As seen in Fig. 5.1., Stokes scattering occurs when a molecule at the ground vibrational level absorbs a photon to reach a virtual state before emitting a photon, while anti-Stokes involves the absorption of radiation by a vibrationally excited molecule before reemitting a photon to the ground vibrational state. Due to much larger concentrations of molecules

at the ground vibrational state compared to the excited state under standard conditions, only the Stokes scattering was measured in this study.
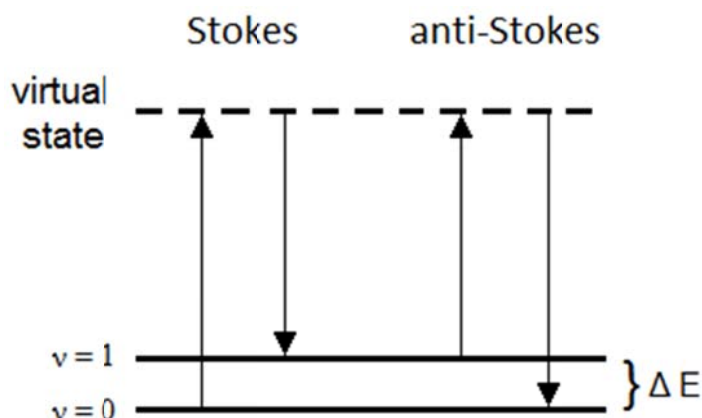
Figure 5.1. The Stokes and anti-Stokes scattering of Raman spectroscopy.

In order to achieve a Raman signal, a molecule must be polarizable, meaning that its electron cloud can be distorted by an external electric field. This is in contrast to infrared spectroscopy where a signal is generated by a change in the dipole moment of a molecule from a vibrational mode. Since molecular vibrations can also change its polarizability, the Raman signal of a molecule can be derived from its vibrational modes. The intensity of the Raman signal is very low, often below 0.001% of the excitation radiation. To overcome this limitation, a band-stop filter is used to reject laser radiation from a sensitive charged-coupled device (CCD) detector.

5.2.2 Raman Microspectroscopy

Coupling a Raman spectrometer (Horiba Scientific) to a confocal microscope allows for Raman imaging at high spatial resolution on the order of 1 μm (Evans and Xie, 2008). A schematic for the Raman microscope is shown in Fig. 5.2.
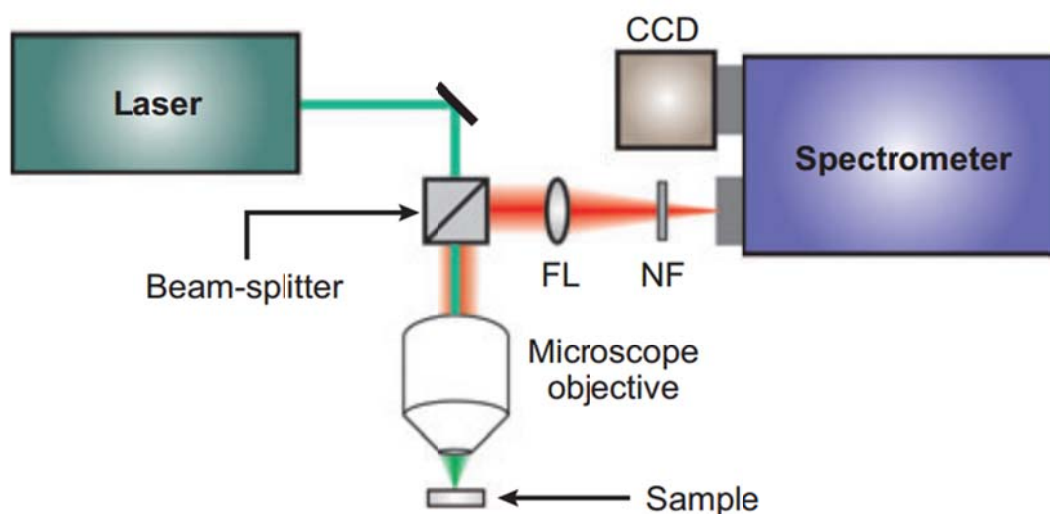
Figure 5.2. The Raman microscope schematic. FL refers to a focusing lens and NF refers to the notch filter. This figure is adapted from Stiles et al. (2008).

Samples were placed on quartz substrates and irradiated with the laser pulse (120 fs), which operated at 532 nm with incident power of 2.5 mW. Backscattered light was directed through a focusing lens (FL) and a notch filter (NF) to reject elastically scattered light. The microscope was used with 10x and 100x (Olympus) objective lenses. This instrument is capable of both optical and Raman microscopy.

Due to the high spatial resolution of this technique, 2D mapping of an aerosol particle can be accomplished using Raman imaging. This occurs when a distinct Raman

shift can be measured with high time resolution to observe its distribution within the aerosol. An example showing the spatial distribution of sulfate (Raman shift = 908 cm^{-1}) in a laboratory-generated seed aerosol particle is shown in Fig. 5.3.
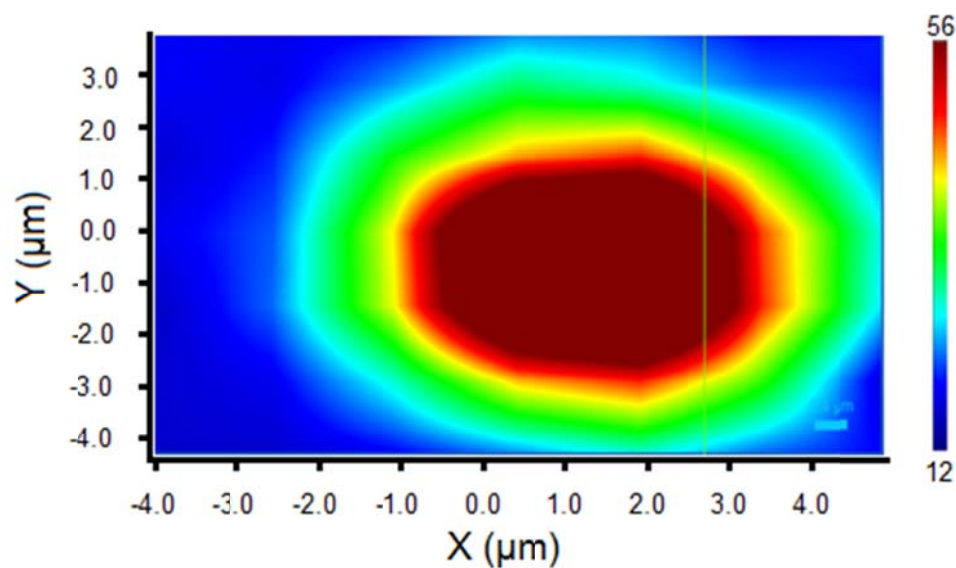
Figure 5.3. The 2D map of sulfate within a laboratory-generated seed particle. The Raman intensity is shown on the right hand side.

5.2.3 Experimental Procedure

Raman spectra of standards were acquired by irradiating a liquid droplet of the given sample on a quartz substrate. A Raman spectrum for isopropyl nitrate was unable to be acquired due to its high volatility.

Experiments were conducted to investigate the physical and chemical state of organic/inorganic mixed aerosol. In these experiments, seed aerosol was impacted on quartz slides using a rotating Micro-Orifice Uniform Deposition Impactor (MSP, Corp.). For more information on impactor theory, see Chapter 2. Seed aerosol was generated by a

laboratory-made atomizer, which operated in similar theory to the aerosol generator

described in Chapter 2. Two types of seed aerosol were used, a neutral seed, which had

an atomizer solution consisting of 15mM ammonium sulfate, and an acidic seed, which

had an atomizer solution consisting of an ammonium sulfate/sulfuric acid mix with

concentrations of 15mM and 50mM, respectively.

Once seed aerosol was created, air streams containing the desired organic

standard were passed over the particles within an RH cell, a small enclosed device with a

quartz window that was used for Raman microspectroscopy measurements. Organic air

streams were created by injecting liquid solutions into a heated glass tee under the flow

of air from a zero-air generator. Water was injected into the RH cell by bubbling air

through an enclosed side-arm Erlenmeyer flask containing ultra-pure water. Relative

humidity (RH) was monitored using an RH sensor and, for the high RH experiments, was

77%, on average. For aerosol pH measurements, deposited seed aerosol was directly

measured using the Raman microscope set-up (Fig. 5.2).

5.3 Results

5.3.1 Fundamental Characterization of Standards

Raman spectra for isobutyl nitrate (Fig. 5.4), ethylhexyl nitrate (Fig. 5.4),

2-mononitroglycerin (Fig. 5.5), and α-pinene oxide (Fig. 5.6) are shown below. Spectra

were acquired by applying a liquid droplet of the pure standard directly onto a quartz

substrate. The Raman spectra of ethylhexyl nitrate and α-pinene oxide have not been

reported previously.
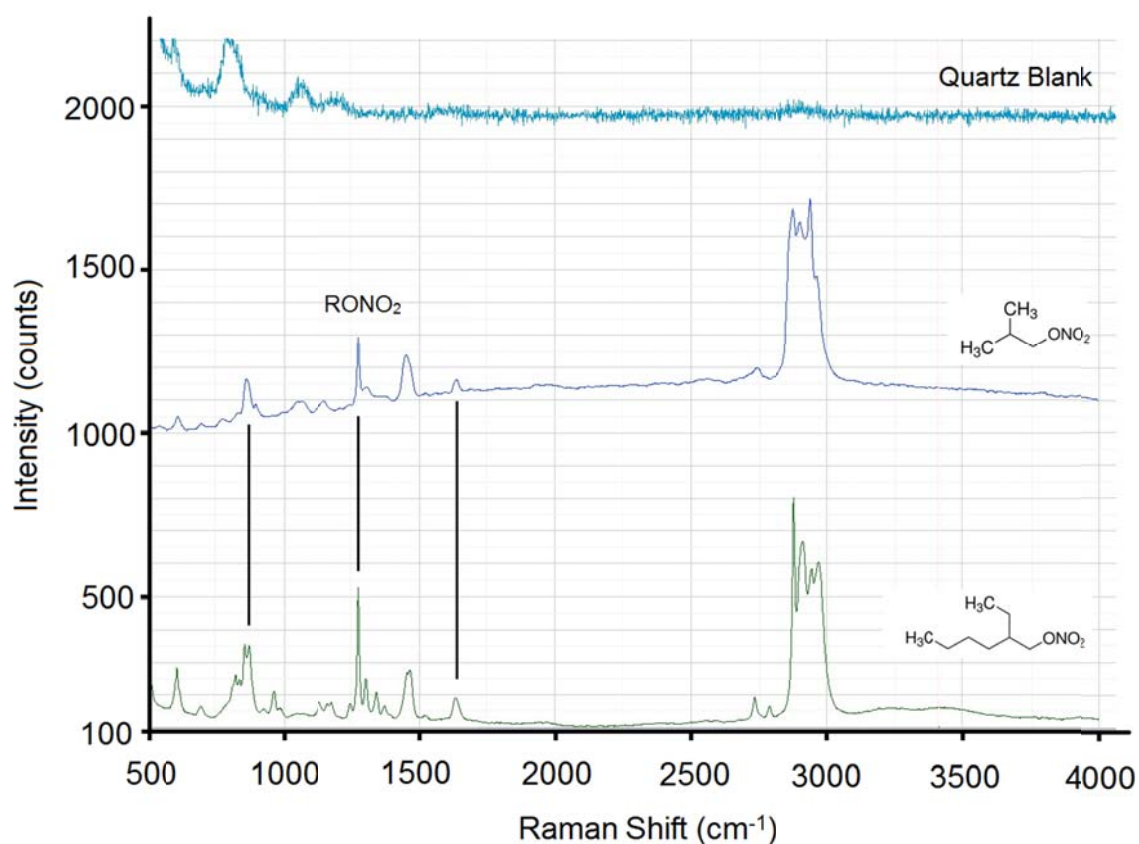
Figure 5.4. The Raman spectrum of (top) the quartz substrate, (middle) isobutyl nitrate, and (bottom) ethylhexyl nitrate. The active $RONO_2$ Raman bands are displayed for isobutyl nitrate and ethylhexyl nitrate.
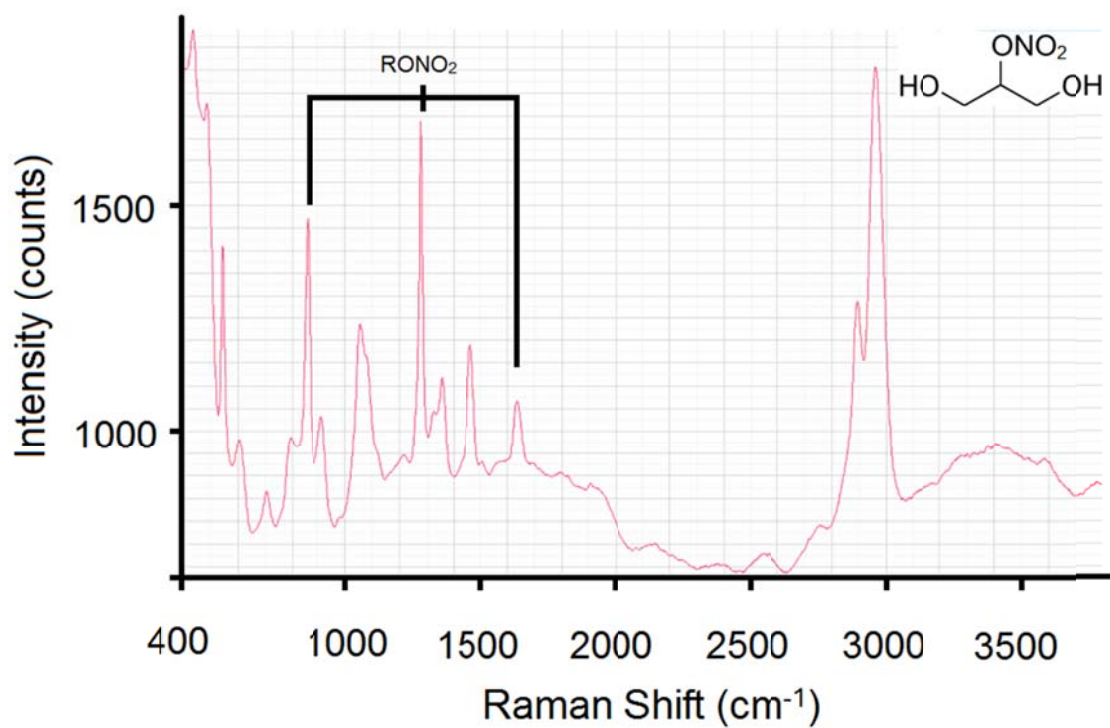
Figure 5.5. The Raman spectrum of 2-mononitroglycerin. The active $RONO_2$ Raman bands are displayed.
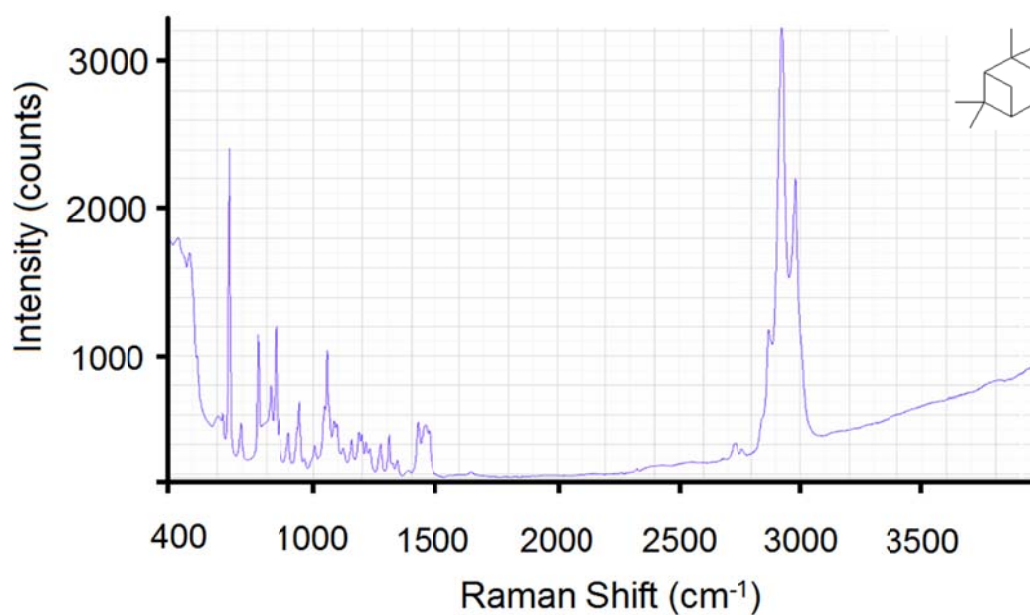
Figure 5.6. The Raman spectrum of α-pinene oxide.

Similar to infrared spectroscopy, organic nitrates have three active Raman shifts, as shown in Fig. 5.4 and 5.5. The most intense $RONO_2$ peak occurs at ~1280 cm^{-1}, in contrast to the 1640 cm^{-1} of the infrared spectrum. In each spectrum, the peaks at ~2800 to 3000 cm^{-1} correspond to organic C-H stretches and the peak at ~1460 cm^{-1} corresponds to -CH$_3$ symmetric deformation. In the 2-mononitroglycerin spectrum (Fig. 5.5), the peak at ~1060 cm^{-1} corresponds to C-O stretching, derived from its multiple alcohol groups. Despite the identification of these Raman shifts, classification of the remaining peaks is still needed for complete fundamental characterization of the vibrational modes of each species.

5.3.2 Aerosol Phase Partitioning of Organics

Of the organic nitrate species, only ethylhexyl nitrate and 2-mononitroglycerin were observed to partition to seed aerosol particles. Isopropyl nitrate and isobutyl nitrate were too volatile to condense onto particles.

The partitioning of ethylhexyl nitrate onto aerosol produced a liquid-liquid phase separation where an inner core consisting of inorganic compounds and outer shell of organic material were simultaneously present. At high relative humidity (~77%), water uptake into particles readily occurred. Instead of partitioning to outside of the particle, water immediately diffused to the inorganic core, diluting the salts to lower the free energy of the sample. Diffusion of ethyl hexyl nitrate to the bulk particle did not occur, regardless of aerosol water content, as would be expected based on its low solubility in water.

The spatial distribution of organics and inorganics within the mixed ethylhexyl nitrate/acidic aerosol particle system (Fig. 5.7) was determined using a Raman imaging technique. Separate 2D maps of the aerosol particle were created for ethylhexyl nitrate and sulfate ion concentrations. The ethylhexyl nitrate map was created using the peak area of the -CH stretching region of ethylhexyl nitrate (2900 cm^{-1}) and the sulfate ion map was created using the peak area of the sulfate stretch (980 cm^{-1}). As seen in Fig. 5.7, the inorganic core and organic shell have distinctly different distributions within the particle.
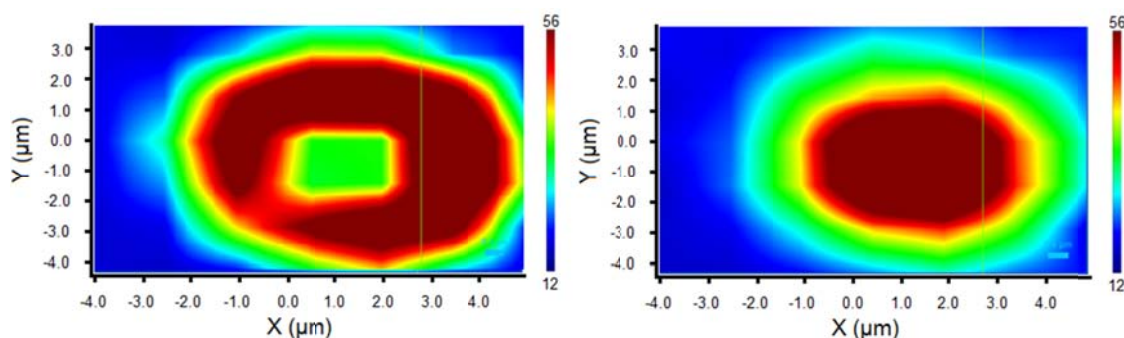
Figure 5.7. An image of the Raman shifts of the organic ethylhexyl nitrate (2900 cm^{-1}) and inorganic sulfate (980 cm^{-1}).

In addition to the Raman images (Fig. 5.7), optical images were also obtained of the ethylhexyl nitrate/acidic seed aerosol system. Shown in Fig. 5.8 is a close-up image of the particle, which was acquired using the 100x objective lens, showing the existence of a third "middle" layer in the ethylhexyl nitrate partitioning system. A separate Raman spectrum was taken for each layer to find that, while the outer layer consisted solely of ethylhexyl nitrate and the inner core consisted solely of inorganics sulfate (980 cm^{-1}) and

ammonium ($\sim$3400 cm^{-1}), the middle layer displayed features of both the organic and

inorganic sections (Fig. 5.9).
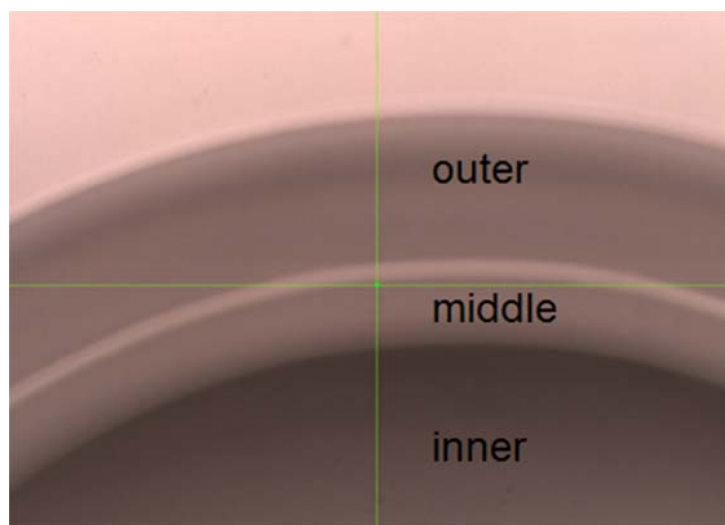
Figure 5.8. An optical image of the ethylhexyl nitrate/acidic seed aerosol system. Three distinct layers are observed.
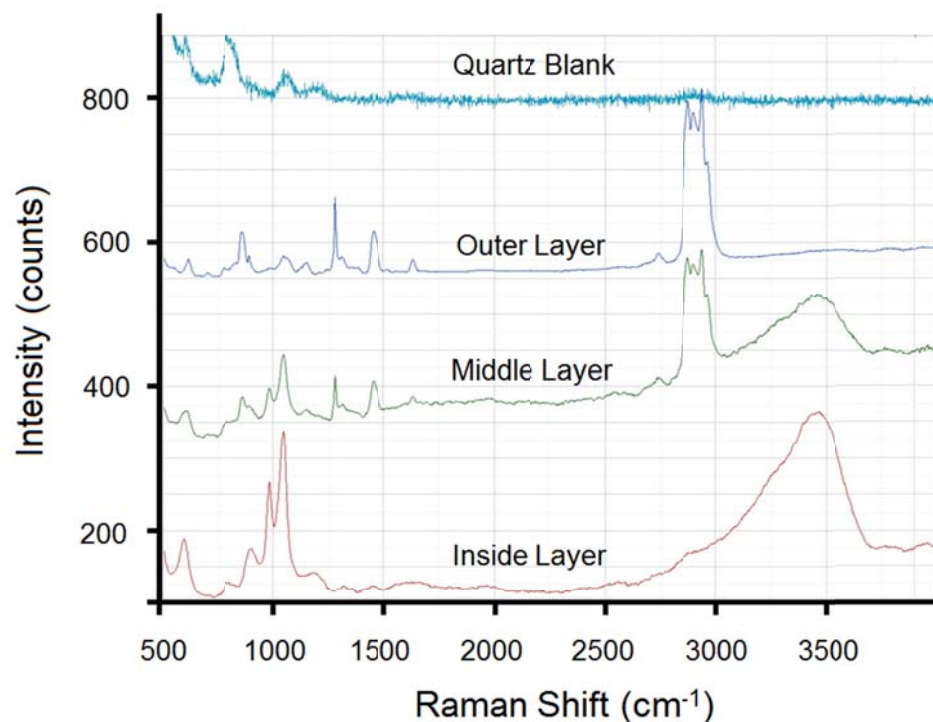
Figure 5.9. The Raman spectrum for the (top) quartz substrate, (middle top) outer shell, (middle bottom) mixed middle layer, and (bottom) inorganic inner core of an ethylhexyl nitrate/acidic seed aerosol system.

The existence of a mixed middle layer, even in the highly organic ethylhexyl nitrate aerosol system, is very important with respect to aerosol phase chemistry as it provides a physical location where organics are free to interact with the aqueous phase. The primary nitrate of ethylhexyl nitrate is much less reactive than organic nitrates containing more functional groups, thus, hydrolysis chemistry was not observed in this particle phase experiment. Despite the lack of observed chemistry in this experiment, the mixed layer, observed here for the first time, is the likely location of particle phase hydrolysis chemistry. Further studies investigating the partitioning system of a more highly reactive organic nitrate are needed to confirm the proposed mixed layer hydrolysis chemistry. It is important to note that ambient particles will uptake a variety of

compounds having differing polarity and this model system may not represent the partitioning of complex atmospheric particles.

Phase separation was not observed in the 2-mononitroglycerin/seed aerosol system at high RH. Instead, a well-mixed particle, similar to the Pankow (1994) model, was observed. This is likely due to the very high water solubility of 2-mononitroglycerin.

5.3.3 Particle Phase Reactivity

Once water vapor was added to the 2-mononitroglycerin/acidic seed aerosol system, H_2O uptake readily occurred and particle phase hydrolysis was observed, indicated by the elimination of the Raman active $RONO_2$ peaks at 1640, 1280 and 850 cm^{-1} in its Raman spectra (Fig. 5.10). The observed hydrolysis occurred very rapidly (within 5 minutes), thus, kinetic data was not able to be gathered from this experiment. Figure 5.10 shows two product spectra from the 2-mononitroglycerin hydrolysis reaction within acidic seed aerosol after 15 minutes. Both products are currently unidentified. However, small peaks at ~1650 (C=C stetch) and ~3100 cm^{-1} (=C-H stretch) in the top spectrum of Fig. 5.10 may indicate the presence of an alkene while, in the middle spectrum, minor peaks at 590, 920, 1180, and 1205 cm^{-1} are consistent with the C-O-S out of phase stretch of an organosulfate. Further investigations into the reaction products of 2-mononitroglycerin are needed to assist the assignment of unknown Raman shifts in Fig. 5.10. The use LC-MS to help identify products, coupled with synthesized authentic standards, would be very helpful in the determination of 2-mononitroglycerin hydrolysis products.
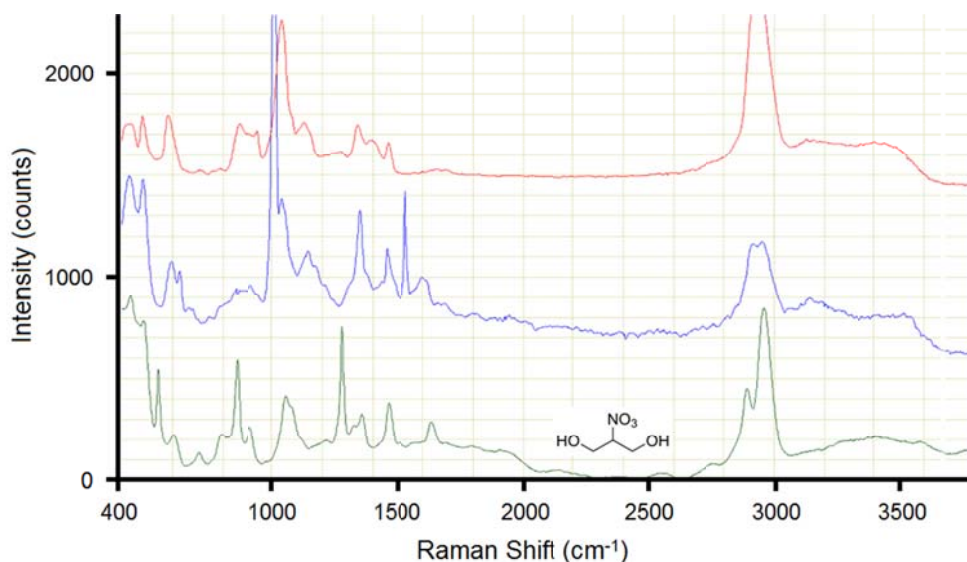
Figure 5.10. The Raman spectrum of (bottom) 2-mononitroglycerin and (middle, top) two unknown hydrolysis reaction products from the 2-mononitroglycerin/acidic seed/water vapor aerosol system.

The particle phase reactivity of α-pinene oxide under increased aerosol water content was also investigated to gain insight into the particle phase reactivity of an α-pinene-derived standard. The α-pinene oxide system was also used as a proof of principle test system. α-Pinene oxide is known to hydrolyze very quickly in aqueous conditions, as shown in Chapter 4 of this thesis, thus, it was chosen as a proxy for α-pinene-derived aerosol chemistry. In separate experiments, α-pinene oxide partitioned to neutral and acidic seed and the addition of water vapor to the system led to chemical reactions within the aerosol, as observed by the drastic change in the Raman spectra of aerosol particles after water was introduced into the particle phase. The Raman spectra of

α-pinene oxide and the reaction products within neutral and acidic seed are shown in Fig. 5.11.
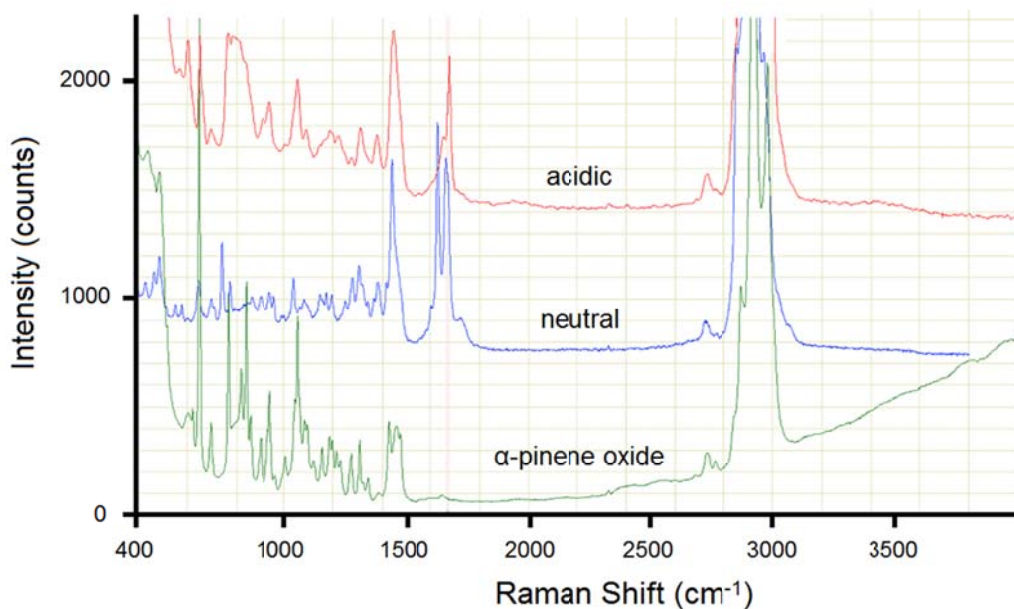
Figure 5.11. The Raman spectrum for (bottom) pure α-pinene oxide, (middle) the α-pinene oxide hydrolysis reaction in neutral seed aerosol, and (top) the α-pinene oxide hydrolysis reaction in acidic seed aerosol.

Similar to the case of 2-mononitroglycerin, the hydrolysis of α-pinene oxide was so rapid that kinetic data could not be gathered for the particle phase reaction. Notable changes in the neutral seed Raman spectra include the appearance of peaks at 1620 and 1680 cm^{-1}, both of which are in the C=C stretch region. In addition, a minor peak at 1730 cm^{-1} indicates the existence of a C=O group. The observed vibrations (C=C, C=O) are not inconsistent with the production of campholenic aldehyde, the main hydrolysis product observed form α-pinene-derived species in Chapter 4. Additionally, the presence

of more Raman peaks in the neutral seed hydrolysis reaction compared to the acidic seed

reactions, shown most notably in the C=C stretch region (1600-1700 cm^{-1}), indicate that

the product distribution of α-pinene oxide hydrolysis products decreases with increasing

acidity. The characterization of all Raman-active peaks is needed to determine the

complete product distribution from the particle phase hydrolysis of α-pinene oxide. It is

important to note that the use of other analytical techniques, such as LC-MS and GC-MS,

have greater potential for individual product identification.

5.3.4 The Determination of Aerosol pH

Many inorganic ions, such as sulfate (SO$_4$$^{2-}$) and ammonium (NH$_4$$^+$), have Raman

active lines. One example, shown in Fig. 5.12, is the acidic seed aerosol system from this

study, which consisted of a (NH$_4$)$_2$SO$_4$/H$_2$SO$_4$ mixture. In Fig. 5.12, the well-known

stretches of sulfate (980 cm^{-1}), bisulfate (1050 cm^{-1}), and ammonium (~3000-3500 cm^{-1})

are displayed. The ability to differentiate both the sulfate and bisulfate peaks in the

Raman spectrum is very useful because it allows for the simultaneous measurement of

both ion concentrations within an aerosol particle. Since sulfate and bisulfate are in

equilibrium with [H$^+$] (Eq. 5.1), the distribution of sulfate and bisulfate ions is directly

proportional to the H$^+$ concentration of their environment. The equilibrium of the ionic

system is described by Eq. 5.2, where the equilibrium constant (K$_A$) is equal to the ratio

of activities of each ion in solution (α$_i$). In high ionic strength solutions, such as an

aerosol particle, the activity coefficients (γ$_i$) of each ion can deviate from unity, thus,

knowledge of an ion's concentration in solution is not sufficient information when

performing calculations involving the equilibrium constant equation (Eq. 5.2). If the

concentration and activity coefficient of the hydronium ion (H^+) are known, the pH of a solution can be calculated using Eq. 5.3.
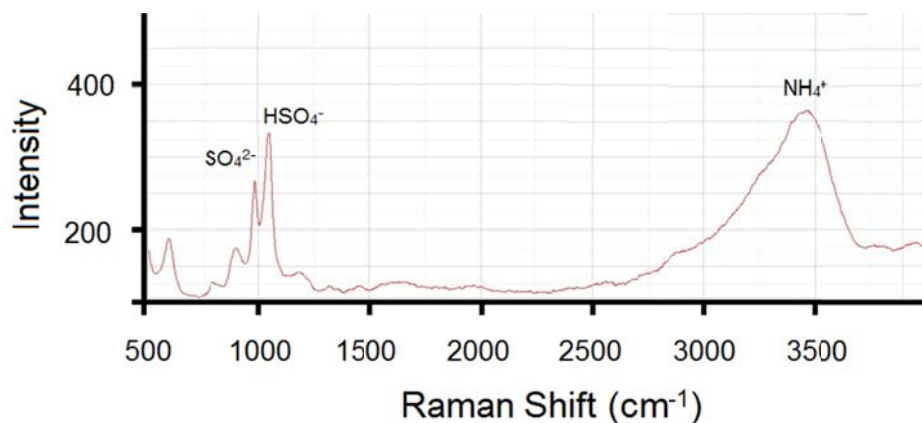
Figure 5.12. The Raman spectrum of the acidic seed aerosol [$(NH_4)_2SO_4/H_2SO_4$]. The sulfate, bisulfate, and ammonium peaks are labeled.

$$HSO_4^- \longleftrightarrow H^+ + SO_4^{2-} \tag{5.1}$$

$$K_A = \alpha_{H+}\,\alpha_{SO4=}\,/\alpha_{HSO4-} = [H^+]\gamma_{H+}[SO_4^{2-}]\,\gamma_{SO4=}/[\,HSO_4^-]\,\gamma_{HSO4-} \tag{5.2}$$

$$pH = -\log(\alpha_{H+}) = -\log([H^+]\,\gamma_{H+}) \tag{5.3}$$

To calculate the aerosol pH of the system, peak heights of the sulfate and bisulfate Raman active lines were used, along with the known relative sensitivities of Raman signal to both ions (Chen and Irish, 1971), to determine relative concentrations of the two ions. The [H^+] concentration of the system was calculated using Eq. 5.3 and experimentally determined activity coefficients for each ion in aqueous solution (Kielland, 1937). The determination of the activity coefficients was based on an

estimated ionic strength of 0.10 M, which was derived from the concentration of the

solution used in the aerosol atomizer (see Surratt et al. (2008); Chapter 2). Once the H^+

activity coefficient and concentration was determined, an aerosol pH of -0.017 was

calculated. This pH value is much lower than expected, given the atomizer solution's

measured pH (1.2), which was determined using a pH meter.

This experiment represents the first time that the pH of an aerosol particle has

been measured *in-situ*. Previous methods investigating aerosol pH involved extracting

filters with H_2O and measuring ion concentrations (Offenberg et al., 2009), a process that

will be influenced by the solvent pH and won't be representative of individual particles.

Since aerosol phase chemical processes are expected to be highly dependent on pH, such

as the hydrolysis reactions described in Chapter 4, it is very important to accurately know

the pH values for aerosol in chamber experiments, for example. One such example is

shown by Surratt et al. (2008), who found that organosulfate formation in photochemical

chamber experiments only occurred when the seed aerosol atomizer solution contained

H_2SO_4. Surratt et al. (2008) were unable to quantify aerosol pH. By providing a method

for determining aerosol pH, the correlation between organosulfate production and particle

phase [H+] concentration can be better understood. This is also useful information for

condensed phase studies, which can now be developed to mimic aerosol pH conditions

and provide much clearer insight into particle phase processing.

Additionally, this technique may also have potential for measurement of ambient

aerosol pH. While ambient aerosol consist of many different compounds, the presence of

liquid-liquid separation within a particle, as observed in this experiment, allows for the

investigation of only the inorganic core. Since sulfates are believed to be the most

abundant anion contributing to fine particulate matter, there is hope that measurement of the SO_4^{2-}/HSO_4^- system is possible and the pH of ambient aerosol can be determined *in-situ.*

Further studies other inorganic systems are needed to determine aerosol pH under more basic conditions. One candidate is the carbonate system (HCO_3/CO_3^-), which has a pK_A at 6.37. Additionally, the evolution of particle phase acidity with relative humidity also warrants study.

5.4 Conclusions

The use of Raman microspectroscopy in this study allowed for the measurement of both organic and inorganic compounds within the aerosol phase. Additionally, for the first time, Raman spectra were obtained for ethylhexyl nitrate and α-pinene oxide, which provides the ground work needed for the fundamental characterization of the vibrational modes of each species. The identification of all peaks in the corresponding Raman spectra is incomplete at this time.

While volatile short chain compounds, such as isopropyl nitrate and isobutyl nitrate, did not partition to aerosol in this study, larger compounds, such as ethylhexyl nitrate and α-pinene oxide, and the multi-functional 2-mononitroglycerin experienced uptake to laboratory-generated particles. Raman imaging of the organic/inorganic particles showed a well-mixed particle, in the case of 2-mononitroglycerin, at increased RH. This physical phenomenon is attributed to the high water solubility of 2-mononitroglycerin. Ethylhexyl nitrate, on the other hand, did not form well-mixed

particles, instead creating a liquid-liquid phase separated particle that contained an organic shell and an inorganic core. Despite the presence of an organic shell, water uptake occurred by rapidly diffusing through the organic layer and into the inorganic core. As atmospheric reaction products have a large range of polarity, the uptake to ambient particles may yield very different aerosol physical properties than those observed in a controlled laboratory setting. However, it is important to note that liquid-liquid phase separation has been observed in aerosol particle samples collected from Atlanta, GA (You et al., 2012).

Ethylhexyl nitrate/acidic seed particles remained phase separated, even at high RH values. The use of optical imaging, coupled to Raman spectroscopy, allowed for the detection of a third layer in between the inorganic core and organic shell. This middle layer contained both inorganic and organic peaks in its Raman spectrum, indicating that a mixed layer may exist in aerosol, providing a physical location for reactions between organics, water, and inorganic ions to occur. This mixed layer has not been observed previously, however, it may be specific to the chemical nature of this system, which includes a relatively hydrophobic species. Due to the low reactivity of the primary nitrate of ethylhexyl nitrate, an aerosol phase hydrolysis reaction was not observed. To study the potential reactivity that may occur within the mixed layer of an aerosol, the partitioning of more reactive organic nitrates warrants further study. Additionally, experiments investigating the partitioning of compounds with a wide range of volatility and polarity are necessary to better understand the chemistry that may occur in the layers of a liquid-liquid phase separated particle.

Aerosol phase reactions were observed for 2-mononitroglycerin and α-pinene oxide at elevated RH, both of which occurred very rapidly, thus, kinetic information was not able to be gathered for either reaction. Raman spectra of the 2-mononitroglycerin reaction indicate that the hydrolysis of the organic nitrate functionality occurred. Product peaks in the Raman spectrum have yet to be identified. However, Raman peaks not inconsistent with organosulfates were observed. Further identification of hydrolysis product functionality is needed.

Particle phase reactions of α-pinene oxide were studied within both neutral and acidic seed aerosol at high RH as a proof of principle model system for particle phase reactions of α-pinene-derived species. Aerosol phase chemistry was observed while maintaining the physical integrity of the particle. The analysis of Raman spectra indicate that C=C and C=O bonds were potentially created, which may indicate the production of campholenic aldehyde (see Chapter 4). The further identification of Raman peaks in product spectra would be helpful in understanding the functional groups created in the hydrolysis of an α-pinene-derived standard.

The pH of laboratory-generated aerosol particles was measured *in-situ*, for the first time, using the Raman microspectroscopy technique. Relative concentrations of the SO_4^{2-}/HSO_4^- system were measured using the Raman peaks at 980 and 1050 cm^{-1}, respectively, allowing for the calculation of aerosol pH. For the acidic seed aerosol generated in this experiment, a pH=-0.017 was calculated. This value, which was lower than the aerosol generator solution's pH (1.2), has implications into the particle phase chemistry of photochemical chamber experiments, specifically, the production of aerosol

phase organosulfates (Surratt et al., 2008). Further studies using other inorganic ion

systems are warranted for the measurement of aerosol pH under more basic conditions.

CHAPTER SIX: CONCLUSIONS AND FUTURE DIRECTIONS

6.1 Conclusions

Research described within this thesis has provided valuable insight into the gas phase formation and particle phase reactivity of α-pinene-derived organic nitrates. Under high NO_x conditions, the organic nitrate branching ratio from the OH radical oxidation of α-pinene was determined to be 26±7%. This value helps to lower the large uncertainty in the reported $RONO_2$ yield from this pathway, which have values ranging from ~1% (Aschmann et al., 2002) and 19% (Noziere et al., 1999). The determined $RONO_2$ yield value is very important for modeling the ozone production potential of BVOC-impacted environments.

Once produced in the gas phase, α-pinene-derived organic nitrates readily partition to aerosol particles and undergo chemical reactions that affect their atmospheric fate, such as hydrolysis. Organic nitrates rapidly hydrolyzed in the particle phase of photochemical reaction chamber experiments, on timescales less than 2.5 hours, to remove the $RONO_2$ functionality from α-pinene-derived species. Particle phase hydrolysis was found to increase with both chamber relative humidity and particle acidity. Additionally, hydrolysis occurred even at low RH (< 20%), indicating that this reaction is important at most ambient atmospheric conditions and that partitioning of

organic nitrates to particles, estimated to occur within 3.43 hours above coniferous forests (see Chapter 2), is likely a sink for $RONO_2$ compounds.

In the hydrolysis mechanism, the $RONO_2$ functionality is removed to produce the nitrate ion (NO_3^-). The nitrate ion is much less reactive than $RONO_2$ compounds, with effectively zero vapor pressure, and, thus, will likely remain in the aerosol phase, except at very low pH, when a significant fraction exists as HNO_3. Thus, removal of the nitrate ion from the atmosphere will likely be from dry and wet deposition. This has implications on the fate of anthropogenic NO_x and ozone, specifically, in the presence of sufficient acidic aerosol, the production of monoterpene-derived nitrates may be a permanent NO_x sink.

From condensed phase studies, the mechanism of organic nitrate hydrolysis under acidic conditions was determined to be unimolecular (S_N1, E1), giving insight into the chemistry of aerosol phase processing. For α-pinene-derived nitrates, the main product created from hydrolysis is campholenic aldehyde (> 90% yield), which is formed through the rearrangement of a carbocation intermediate. The same product is formed from the hydrolysis of other α-pinene-derived species, such as α-pinene oxide and pinanediol, indicating that the hydrolysis chemistry identified in this thesis is not specific to organic nitrates and has broader implications in aerosol phase processing.

Additionally, the rate of organic nitrate hydrolysis increases with decreasing pH, indicating that organic nitrate hydrolysis occurs through a specific acid-catalyzed mechanism. The first step in a specific acid-catalyzed reaction involves the reversible addition of a proton to $RONO_2$ followed by the rate determining step of reaction. The identification of the mechanistic pathways of organic nitrates under acidic aqueous

conditions also gives insight into fundamental chemistry concepts as there is currently a lack of mechanistic research into organic nitrate hydrolysis in acidic environments.

Since the reaction of $RONO_2$ compounds was observed to be directly related to pH, the measurement of aerosol acidity is very important. Thus, a method was developed for measuring the pH of laboratory-generated aerosol particles, for the first time, using a Raman microscpectroscopic technique. Information about aerosol pH is extremely useful in understanding the chemistry of photochemical chamber experiments, such as the pH levels that produce organosulfates (Surratt et al., 2008), and for developing condensed phase studies that try to simulate aerosol phase chemistry.

Additionally, the detection of α-pinene-derived nitrates was also accomplished by using HPLC-ESI(-)-TOF mass spectrometry, for the first time. This has important implications on the detection of organic hydroxynitrates in complex samples matrices from filter and denuder extracts in both field and chamber studies. Five α-pinene-derived isomers were observed the LC-MS study.

6.2 Future Directions

In respect to photochemical chamber experiments, several adjustments could be made in terms of the measurements gathered. Since aerosol phase chemistry is highly dependent on acidity, it would be beneficial to measure the particle phase nitric acid concentrations in such experiments. Due to the large amount of NO_2 present in chamber experiments, large nitric acid concentrations were likely created through both gas (OH + NO_2 → HNO_3) and particle phase (H_2O + $2NO_2$ → HNO_3 + HONO) reactions. Correlations between particle phase HNO_3 concentrations and organic nitrate hydrolysis

should be investigated. To measure free nitrate concentrations within aerosol, collected filters can be extracted with slightly basic water and analyzed using ion chromatography. Additionally, as seen in Chapter 3, paper spray ionization has potential for the analysis of nitrate ion concentrations.

The extent of particle phase hydrolysis within chamber experiments also had a dependency on chamber relative humidity. However, the aerosol water content of particles was not measured in experiments. One method that can be used to determine aerosol water content involves drying particles prior to measurement with the SMPS, such as through the use of a diffusion dryer, and comparing the aerosol mass concentration to measurements made without use of the dryer (Nguyen et al., 2014). Similar to the measured HNO_3 concentrations, a correlation between aerosol water content and organic nitrate hydrolysis should be investigated.

Another method that has potential for investigating the acidity and composition of aerosol particles is Raman microspectroscopy. After depositing particles onto quartz substrates using an impactor, Raman microspectroscopy can be used to identify inorganics, such as sulfate and nitrate ions, as well as organics, such as organic nitrates, within single aerosol particles. Coupling this technique with optical imaging may reveal physical information about the particles created in photochemical reaction chamber experiments, or in ambient particles, such as liquid-liquid phase separation within aerosols. Particles from photochemical reaction chamber experiments have not been analyzed using this method, to date, and further development of this method is needed. For ambient aerosol, if aged particles become highly viscous, the uptake of water and polar organics could lead to multiphase particles.

In addition to the α-pinene/OH radical chemistry, many other BVOC oxidation systems also warrant further investigation. Recent literature (e.g. Pratt et al., 2012) suggests that the nitrate radical ($NO_3^{\cdot}$) is very important to organic nitrate formation in forest environments. Curiously, α-pinene does not have a large $RONO_2$ yield or aerosol yield from the reaction with nitrate radical but its isomer, β-pinene, has both a large organic nitrate yield and aerosol yield from the same reaction (Fry et al., 2014). Further investigations into the chemical mechanisms behind this phenomenon are warranted. Additionally, there are currently no reported organic nitrate yields from reaction of the nitrate radical with sesquiterpenes, such as β-caryophyllene.

While studies within this thesis were able to provide insight into the fate of organic nitrates within the particle phase, the fate of organic nitrates in the gas phase is still uncertain. Currently there is a large uncertainty in the reported NO_x recycling efficiency, or the amount of NO_x released compared to amount of NO_x consumed from oxidation, of isoprene-derived nitrates, ranging from +50% (Paulot et al., 2009) to +24% (Lee et al., 2014). There is currently no data on the NO_x recycling efficiency of α-pinene-derived nitrates. Thus, chamber studies involving the measurement of NO_2 yields from the OH radical oxidation of α-pinene-derived nitrate standards are needed.

Since the gas and particle phase reactivity of organic nitrates is very structure dependent, the synthesis of other α-pinene-derived standards, such as those shown in Fig. 6.1, would be very useful to study in both condensed phase hydrolysis and gas phase oxidation experiments. In this thesis, five hydroxynitrate isomers derived from α-pinene were identified using HPLC-TOF MS, while the number of proposed structures only accounts for four α-pinene-derived nitrate species (see Chapter 4). Thus, further research

into the α-pinene oxidation system is needed. Synthesized standards of the analogous α-pinene-derived organosulfates would also be useful. Purified standards would allow for the identification and quantification of individual organic nitrate and organosulfate reaction products from both condensed phase and chamber experiments.
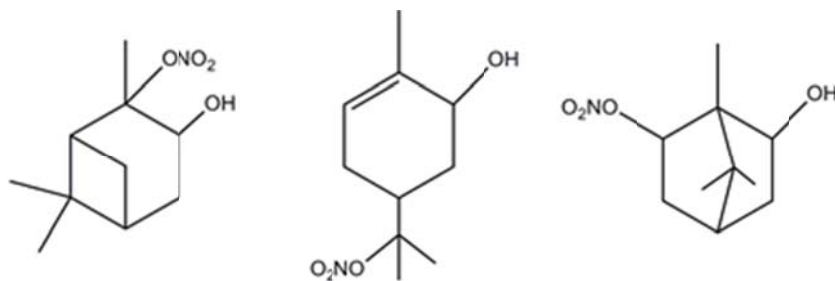
Figure 6.1. α-Pinene-derived nitrate compounds.

LIST OF REFERENCES

LIST OF REFERENCES

Altwegg, K., H. Balsiger, A. Bar-Nun, J. J. Berthelier, A. Bieler, P. Bochsler, C. Briois, U. Calmonte, M. Combi, J. De Keyser, P. Eberhardt, B. Fiethe, S. Fuselier, S. Gasc, T. I. Gombosi, K. C. Hansen, M. Hassig, A. Jackel, E. Kopp, A. Korth, L. Leroy, U. Mall, B. Marty, O. Mousis, E. Neefs, T. Owen, H. Reme, M. Rubin, T. Semon, C. Y. Tzou, H. Waite, and P. Wurz, 2015, 67P/Churyumov-Gerasimenko, a Jupiter family comet with a high D/H ratio: Science, v. 347, p. 3.

Araujo, J. A., B. Barajas, M. Kleinman, X. P. Wang, B. J. Bennett, K. W. Gong, M. Navab, J. Harkema, C. Sioutas, A. J. Lusis, and A. E. Nel, 2008, Ambient particulate pollutants in the ultrafine range promote early atherosclerosis and systemic oxidative stress: Circulation Research, v. 102, p. 589-596.

Arey, J., S. M. Aschmann, E. S. C. Kwok, and R. Atkinson, 2001, Alkyl nitrate, hydroxyalkyl nitrate, and hydroxycarbonyl formation from the NOx-air photooxidations of C-5-C-8 n-alkanes: Journal of Physical Chemistry A, v. 105, p. 1020-1027.

Aschmann, S. M., R. Atkinson, and J. Arey, 2002, Products of reaction of OH radicals with alpha-pinene: Journal of Geophysical Research-Atmospheres, v. 107, p. 7.

Atkinson, R., and J. Arey, 2003, Atmospheric degradation of volatile organic compounds: Chemical Reviews, v. 103, p. 4605-4638.

Atkinson, R., W. P. L. Carter, and A. M. Winer, 1983, Effects of temperature and pressure on alkyl nitrate yields in the nox photooxidations of normal-pentane and normal-heptane: Journal of Physical Chemistry, v. 87, p. 2012-2018.

Atlas, E., 1988, Evidence For Greater-than-or-equal-to-c-3 Alkyl Nitrates In Rural And Remote Atmospheres: Nature, v. 331, p. 426-428.

Avzianova, E. V., and P. A. Ariya, 2002, Temperature-dependent kinetic study for ozonolysis of selected tropospheric alkenes: International Journal of Chemical Kinetics, v. 34, p. 678-684.

Baker, J. W., and D. M. Easty, 1950, Hydrolysis of organic nitrates: Nature, v. 166, p. 156-156.

Barnes, I., K. H. Becker, and T. Zhu, 1993, near uv absorption-spectra and photolysis products of difunctional organic nitrates - possible importance as NO(x) reservoirs: Journal of Atmospheric Chemistry, v. 17, p. 353-373.

Batonneau, Y., S. Sobanska, J. Laureyns, and C. Bremard, 2006, Confocal microprobe Raman imaging of urban tropospheric aerosol particles: Environmental Science & Technology, v. 40, p. 1300-1306.

Bleier, D. B., and M. J. Elrod, 2013, Kinetics and Thermodynamics of Atmospherically Relevant Aqueous Phase Reactions of alpha-Pinene Oxide: Journal of Physical Chemistry A, v. 117, p. 4223-4232.

Bruns, E. A., V. r. Perraud, A. Zelenyuk, M. J. Ezell, S. N. Johnson, Y. Yu, D. Imre, B. J. Finlayson-Pitts, and M. L. Alexander, 2010, Comparison of FTIR and Particle Mass Spectrometry for the Measurement of Particulate Organic Nitrates: Environmental Science & Technology, v. 44, p. 1056-1061.

Cahill, T. M., V. Y. Seaman, M. J. Charles, R. Holzinger, and A. H. Goldstein, 2006, Secondary organic aerosols formed from oxidation of biogenic volatile organic compounds in the Sierra Nevada Mountains of California: Journal of Geophysical Research-Atmospheres, v. 111, p. 14.

Cairnssmith, A. G., 1978, Precambrian solution photochemistry, inverse segregation, and banded iron formations: Nature, v. 276, p. 807-808.

Canfield, D. E., 2005, The early history of atmospheric oxygen: Homage to Robert A. Garrels, Annual Review of Earth and Planetary Sciences: Annual Review of Earth and Planetary Sciences, v. 33: Palo Alto, Annual Reviews, p. 1-36.

Carey, F. A., and Sundberg, R. J., Advanced Organic Chemistry, Part A: Structure and Mechanisms, Springer Science, New York, NY, 2007.

Carlton, A. G., C. Wiedinmyer, and J. H. Kroll, 2009, A review of Secondary Organic Aerosol (SOA) formation from isoprene: Atmospheric Chemistry and Physics, v. 9, p. 4987-5005.

Carrington, R. A. G., 1960, The infra-red spectra of some organic nitrates: Spectrochimica Acta, v. 16, p. 1279-1293.

Catling, D. C., and M. W. Claire, 2005, How Earth's atmosphere evolved to an oxic state: A status report: Earth and Planetary Science Letters, v. 237, p. 1-20.

Chan, K. M., D. D. Huang, Y. J. Li, M. N. Chan, J. H. Seinfeld, and C. K. Chan, 2013, Oligomeric products and formation mechanisms from acid-catalyzed reactions of methyl vinyl ketone on acidic sulfate particles: Journal of Atmospheric Chemistry, v. 70, p. 1-18.

Chen, H., and D. E. Irish, 1971, Raman spectral study of bisulfate-sulfate systems. II. Constitution, equilibriums, and ultrafast proton transfer in sulfuric acid: Journal of Physical Chemistry, v. 75, p. 2672-2681.

Chen, X. H., D. Hulbert, and P. B. Shepson, 1998, Measurement of the organic nitrate yield from OH reaction with isoprene: Journal of Geophysical Research-Atmospheres, v. 103, p. 25563-25568.

Ciobanu, V. G., C. Marcolli, U. K. Krieger, U. Weers, and T. Peter, 2009, Liquid-Liquid Phase Separation in Mixed Organic/Inorganic Aerosol Particles: Journal of Physical Chemistry A, v. 113, p. 10966-10978.

Cook, R. D., 1977, Detection of influential observation in linear-regression: Technometrics, v. 19, p. 15-18.

Darer, A. I., N. C. Cole-Filipiak, A. E. O'Connor, and M. J. Elrod, 2011, Formation and Stability of Atmospherically Relevant Isoprene-Derived Organosulfates and Organonitrates: Environmental Science & Technology, v. 45, p. 1895-1902.

Darnall, K. R., W. P. L. Carter, A. M. Winer, A. C. Lloyd, and J. N. Pitts Jr. (1976), Importance of RO2 + NO in alkyl nitrate formation from C4-C6 alkane photooxidations under simulated atmospheric conditions, J. Phys. Chem., 80, 1948 – 1960.

Daumit, K. E., A. J. Carrasquillo, J. F. Hunter, and J. H. Kroll, 2014, Laboratory studies of the aqueous-phase oxidation of polyols: submicron particles vs. bulk aqueous solution: Atmospheric Chemistry and Physics, v. 14, p. 10773-10784.

Day, D. A., S. Liu, L. M. Russell, and P. J. Ziemann, 2010, Organonitrate group concentrations in submicron particles with high nitrate and organic fractions in coastal southern California: Atmospheric Environment, v. 44, p. 1970-1979.

Day, D. A., P. J. Wooldridge, M. B. Dillon, J. A. Thornton, and R. C. Cohen, 2002, A thermal dissociation laser-induced fluorescence instrument for in situ detection of NO2, peroxy nitrates, alkyl nitrates, and HNO3: Journal of Geophysical Research-Atmospheres, v. 107.

De Moraes, C. M., W. J. Lewis, P. W. Pare, H. T. Alborn, and J. H. Tumlinson, 1998, Herbivore-infested plants selectively attract parasitoids: Nature, v. 393, p. 570-573.

Denlinger, M. C., 2005, The origin and evolution of the atmospheres of Venus, Earth and Mars: Earth Moon and Planets, v. 96, p. 59-80.

Ellison, G. B., J. M. Herbert, A. B. McCoy, J. F. Stanton, and P. G. Szalay, 2004, Unimolecular rearrangement of trans-FONO to FNO2. A possible model system for atmospheric nitrate formation: Journal of Physical Chemistry A, v. 108, p. 7639-7642.

Elrod, M. J., 2011, Kinetics Study of the Aromatic Bicyclic Peroxy Radical plus NO Reaction: Overall Rate Constant and Nitrate Product Yield Measurements: Journal of Physical Chemistry A, v. 115, p. 8125-8130.

EPA, 2010: Quantitative Health Risk Assessment for Particulate Matter. http://www.epa.gov/ttn/naaqs/standards/pm/data/PM_RA_FINAL_June_2010.pdf

EPA, 2011. Second External Review Draft of the Integrated Science Assessment of Ozone and related Photochemical Oxidants (EPA/600/R-10/076B).

Espada, C., J. Grossenbacher, K. Ford, T. Couch, and P. B. Shepson, 2005, The production of organic nitrates from various anthropogenic volatile organic compounds: International Journal of Chemical Kinetics, v. 37, p. 675-685.

Espada, C., and P. B. Shepson, 2005, The production of organic nitrates from atmospheric oxidation of ethers and glycol ethers: International Journal of Chemical Kinetics, v. 37, p. 686-699.

Evans, C. L., and X. S. Xie, 2008, Coherent Anti-Stokes Raman Scattering Microscopy: Chemical Imaging for Biology and Medicine, Annual Review of Analytical Chemistry: Annual Review of Analytical Chemistry, v. 1: Palo Alto, Annual Reviews, p. 883-909.

Finlayson-Pitts, B. J., and J. N. Pitts, Chemistry of the upper and lower atmosphere: Theory, experiments, and applications, Academic Press, San Diego, CA, 2000.

Fuchs, N. A., On the stationary charge distribution on aerosol particles in a bipolar ionic atmosphere. Geofis. pura appl., 56 (1963), p. 185

Galbavy, E. S., C. Anastasio, B. Lefer, and S. Hall, 2007, Light penetration in the snowpack at Summit, Greenland: Part 2 nitrate photolysis: Atmospheric Environment, v. 41, p. 5091-5100.

Gess, R. W., 2013, The earliest record of terrestrial animals in Gondwana: A scorpion from the Famennian (Late Devonian) Witpoort Formation of South Africa: African Invertebrates, v. 54, p. 373-379.

Glasius, M., M. Duane, and B. R. Larsen, 1999, Determination of polar terpene oxidation products in aerosols by liquid chromatography-ion trap mass spectrometry: Journal of Chromatography A, v. 833, p. 121-135.

Goldstein, A. H., and I. E. Galbally, 2007, Known and unexplored organic constituents in the earth's atmosphere: Environmental Science & Technology, v. 41, p. 1514-1521.

Greene, C. R., and R. Atkinson, 1992, Rate constants for the gas-phase reactions of O3 with a series of alkenes at 296-K+/-2-K: International Journal of Chemical Kinetics, v. 24, p. 803-811.

Guenther, A. B., X. Jiang, C. L. Heald, T. Sakulyanontvittaya, T. Duhl, L. K. Emmons, and X. Wang, 2012, The Model of Emissions of Gases and Aerosols from Nature version 2.1 (MEGAN2.1): an extended and updated framework for modeling biogenic emissions: Geoscientific Model Development, v. 5, p. 1471-1492.

Hakola, H., J. Arey, S. M. Aschmann, and R. Atkinson, 1994, Product formation from the gas-phase reactions of OH radicals and O3 with a series of monoterpenes: Journal of Atmospheric Chemistry, v. 18, p. 75-102.

Hallquist, M., J. C. Wenger, U. Baltensperger, Y. Rudich, D. Simpson, M. Claeys, J. Dommen, N. M. Donahue, C. George, A. H. Goldstein, J. F. Hamilton, H. Herrmann, T. Hoffmann, Y. Iinuma, M. Jang, M. E. Jenkin, J. L. Jimenez, A. Kiendler-Scharr, W. Maenhaut, G. McFiggans, T. F. Mentel, A. Monod, A. S. H. Prevot, J. H. Seinfeld, J. D. Surratt, R. Szmigielski, and J. Wildt, 2009, The formation, properties and impact of secondary organic aerosol: current and emerging issues: Atmospheric Chemistry and Physics, v. 9, p. 5155-5236.

Han, Y. M., Y. Iwamoto, T. Nakayama, K. Kawamura, and M. Mochida, 2014, Formation and evolution of biogenic secondary organic aerosol over a forest site in Japan: Journal of Geophysical Research-Atmospheres, v. 119, p. 259-273.

Hao, L. Q., A. Kortelainen, S. Romakkaniemi, H. Portin, A. Jaatinen, A. Leskinen, M. Komppula, P. Miettinen, D. Sueper, A. Pajunoja, J. N. Smith, K. E. J. Lehtinen, D. R. Worsnop, A. Laaksonen, and A. Virtanen, 2014, Atmospheric submicron aerosol composition and particulate organic nitrate formation in a boreal forestland-urban mixed region: Atmospheric Chemistry and Physics, v. 14, p. 13483-13495.

Henry, K. M., T. Lohaus, and N. M. Donahue, 2012, Organic Aerosol Yields from alpha-Pinene Oxidation: Bridging the Gap between First-Generation Yields and Aging Chemistry: Environmental Science & Technology, v. 46, p. 12347-12354.

Hinds, W.C. 1982, Aerosol Technology: Properties, Behavior, and Measurement of Airborne Particles. New York: John Wiley & Sons, p. 114.

Hoffmann, T., J. R. Odum, F. Bowman, D. Collins, D. Klockow, R. C. Flagan, and J. H. Seinfeld, 1997, Formation of organic aerosols from the oxidation of biogenic hydrocarbons: Journal of Atmospheric Chemistry, v. 26, p. 189-222.

Holm, T., 1999, Aspects of the mechanism of the flame ionization detector: Journal of Chromatography A, v. 842, p. 221-227.

Hu, K. S., A. I. Darer, and M. J. Elrod, 2011, Thermodynamics and kinetics of the hydrolysis of atmospherically relevant organonitrates and organosulfates: Atmospheric Chemistry and Physics, v. 11, p. 8307-8320.

Hudman, R. C., D. J. Jacob, O. R. Cooper, M. J. Evans, C. L. Heald, R. J. Park, F. Fehsenfeld, F. Flocke, J. Holloway, G. Hubler, K. Kita, M. Koike, Y. Kondo, A. Neuman, J. Nowak, S. Oltmans, D. Parrish, J. M. Roberts, and T. Ryerson, 2004, Ozone production in transpacific Asian pollution plumes and implications for ozone air quality in California: Journal of Geophysical Research-Atmospheres, v. 109, p. 19.

Iinuma, Y., O. Boge, A. Kahnt, and H. Herrmann, 2009, Laboratory chamber studies on the formation of organosulfates from reactive uptake of monoterpene oxides: Physical Chemistry Chemical Physics, v. 11, p. 7985-7997.

Iinuma, Y., Kahnt, A., Mutzel, A., Boge, O., and Herrmann, H.: Ozone-Driven Secondary Organic Aerosol Production Chain, Environmental Science & Technology, 47, 3639-3647, 10.1021/es305156z, 2013.

IPCC, 2007: Climate Change 2007: The Physical Science Basis. Contribution of Working Group I to the Fourth Assessment Report of the Intergovernmental Panel on Climate Change [Solomon, S., D. Qin, M. Manning, Z. Chen, M. Marquis, K.B. Averyt, M.Tignor and H.L. Miller (eds.)]. Cambridge University Press, Cambridge, United Kingdom and New York, NY, USA.

IPCC, 2013: Climate Change 2013: The Physical Science Basis. Contribution of Working Group I to the Fifth Assessment Report of the Intergovernmental Panel on Climate Change [Stocker, T.F., D. Qin, G.-K. Plattner, M. Tignor, S.K. Allen, J. Boschung, A. Nauels, Y. Xia, V. Bex and P.M. Midgley (eds.)]. Cambridge University Press, Cambridge, United Kingdom and New York, NY, USA, 1535 pp, doi:10.1017/CBO9781107415324.

Jacob, D. J., 2000, Heterogeneous chemistry and tropospheric ozone: Atmospheric Environment, v. 34, p. 2131-2159.

Jacobs, M. I., W. J. Burke, and M. J. Elrod, 2014, Kinetics of the reactions of isoprene-derived hydroxynitrates: gas phase epoxide formation and solution phase hydrolysis: Atmospheric Chemistry and Physics, v. 14, p. 8933-8946.

Jaoui, M., and R. M. Kamens, 2001, Mass balance of gaseous and particulate products analysis from alpha-pinene/NOx/air in the presence of natural sunlight: Journal of Geophysical Research-Atmospheres, v. 106, p. 12541-12558.

Jaoui, M., T. E. Kleindienst, M. Lewandowski, J. H. Offenberg, and E. O. Edney, 2005, Identification and quantification of aerosol polar oxygenated compounds bearing carboxylic or hydroxyl groups. 2. Organic tracer compounds from monoterpenes: Environmental Science & Technology, v. 39, p. 5661-5673.

Jerrett, M., R. T. Burnett, C. A. Pope, K. Ito, G. Thurston, D. Krewski, Y. L. Shi, E. Calle, and M. Thun, 2009, Long-Term Ozone Exposure and Mortality: New England Journal of Medicine, v. 360, p. 1085-1095.

Jimenez, J. L., M. R. Canagaratna, N. M. Donahue, A. S. H. Prevot, Q. Zhang, J. H. Kroll, P. F. DeCarlo, J. D. Allan, H. Coe, N. L. Ng, A. C. Aiken, K. S. Docherty, I. M. Ulbrich, A. P. Grieshop, A. L. Robinson, J. Duplissy, J. D. Smith, K. R. Wilson, V. A. Lanz, C. Hueglin, Y. L. Sun, J. Tian, A. Laaksonen, T. Raatikainen, J. Rautiainen, P. Vaattovaara, M. Ehn, M. Kulmala, J. M. Tomlinson, D. R. Collins, M. J. Cubison, E. J. Dunlea, J. A. Huffman, T. B. Onasch, M. R. Alfarra, P. I. Williams, K. Bower, Y. Kondo, J. Schneider, F. Drewnick, S. Borrmann, S. Weimer, K. Demerjian, D. Salcedo, L. Cottrell, R. Griffin, A. Takami, T. Miyoshi, S. Hatakeyama, A. Shimono, J. Y. Sun, Y. M. Zhang, K. Dzepina, J. R. Kimmel, D. Sueper, J. T. Jayne, S. C. Herndon, A. M. Trimborn, L. R. Williams, E. C. Wood, A. M. Middlebrook, C. E. Kolb, U. Baltensperger, and D. R. Worsnop, 2009, Evolution of Organic Aerosols in the Atmosphere: Science, v. 326, p. 1525-1529.

Kanakidou, M., J. H. Seinfeld, S. N. Pandis, I. Barnes, F. J. Dentener, M. C. Facchini, R. Van Dingenen, B. Ervens, A. Nenes, C. J. Nielsen, E. Swietlicki, J. P. Putaud, Y. Balkanski, S. Fuzzi, J. Horth, G. K. Moortgat, R. Winterhalter, C. E. L. Myhre, K. Tsigaridis, E. Vignati, E. G. Stephanou, and J. Wilson, 2005, Organic aerosol and global climate modelling: a review: Atmospheric Chemistry and Physics, v. 5, p. 1053-1123.

Klason, P., and T. Carlson, 1907, The alkali saponification of alkyl nitrates: An article on the constitution of saltpeter acid: Berichte Der Deutschen Chemischen Gesellschaft, v. 40, p. 4183-4191.

Kleinman, L. I., P. H. Daum, Y. N. Lee, L. J. Nunnermacker, S. R. Springston, J. Weinstein-Lloyd, and J. Rudolph, 2002, Ozone production efficiency in an urban area: Journal of Geophysical Research-Atmospheres, v. 107, p. 12.

Kielland, J., 1937, Individual Activity Coefficients of Ions in Aqueous Solutions: Journal of the American Chemical Society, v. 59, p. 1675-1678.

Köhler, H.: The nucleus in and the growth of hygroscopic droplets, Trans Farad Soc, 32, 1152–1161, 1936.

Laskin, J., A. Laskin, P. J. Roach, G. W. Slysz, G. A. Anderson, S. A. Nizkorodov, D. L. Bones, and L. Q. Nguyen, 2010, High-Resolution Desorption Electrospray Ionization Mass Spectrometry for Chemical Characterization of Organic Aerosols: Analytical Chemistry, v. 82, p. 2048-2058.

Lamarque, J. F., P. Hess, L. Emmons, L. Buja, W. Washington, and C. Granier, 2005, Tropospheric ozone evolution between 1890 and 1990: Journal of Geophysical Research-Atmospheres, v. 110, p. 15.

Larsen, B. R., D. Di Bella, M. Glasius, R. Winterhalter, N. R. Jensen, and J. Hjorth, 2001, Gas-phase OH oxidation of monoterpenes: Gaseous and particulate products: Journal of Atmospheric Chemistry, v. 38, p. 231-276.

Laskin, J., A. Laskin, P. J. Roach, G. W. Slysz, G. A. Anderson, S. A. Nizkorodov, D. L. Bones, and L. Q. Nguyen, 2010, High-Resolution Desorption Electrospray Ionization Mass Spectrometry for Chemical Characterization of Organic Aerosols: Analytical Chemistry, v. 82, p. 2048-2058.

Lee, A., A. H. Goldstein, J. H. Kroll, N. L. Ng, V. Varutbangkul, R. C. Flagan, and J. H. Seinfeld, 2006, Gas-phase products and secondary aerosol yields from the photooxidation of 16 different terpenes: Journal of Geophysical Research-Atmospheres, v. 111, p. 25.

Lee, L., A. P. Teng, P. O. Wennberg, J. D. Crounse, and R. C. Cohen, 2014, On Rates and Mechanisms of OH and O-3 Reactions with Isoprene-Derived Hydroxy Nitrates: Journal of Physical Chemistry A, v. 118, p. 1622-1637.

Lei, H., and J. X. L. Wang, 2014, Sensitivities of NOx transformation and the effects on surface ozone and nitrate: Atmospheric Chemistry and Physics, v. 14, p. 1385-1396.

Li, P., J. Y. Xin, Y. S. Wang, S. G. Wang, G. X. Li, X. C. Pan, Z. R. Liu, and L. L. Wang, 2013, The acute effects of fine particles on respiratory mortality and morbidity in Beijing, 2004-2009: Environmental Science and Pollution Research, v. 20, p. 6433-6444.

Librando, V., and G. Tringali, 2005, Atmospheric fate of OH initiated oxidation of terpenes. Reaction mechanism of alpha-pinene degradation and secondary organic aerosol formation: Journal of Environmental Management, v. 75, p. 275-282.

Liu, B. Y. H., and K. W. Lee, 1975, Aerosol generator of high stability: American Industrial Hygiene Association Journal, v. 36, p. 861-865.

Liu, J. J., H. Wang, N. E. Manicke, J. M. Lin, R. G. Cooks, and Z. Ouyang, 2010, Development, Characterization, and Application of Paper Spray Ionization: Analytical Chemistry, v. 82, p. 2463-2471.

Lockwood, A. L., P. B. Shepson, M. N. Fiddler, and M. Alaghmand, 2010, Isoprene nitrates: preparation, separation, identification, yields, and atmospheric chemistry: Atmospheric Chemistry and Physics, v. 10, p. 6169-6178.

Loreto, F., and V. Velikova, 2001, Isoprene produced by leaves protects the photosynthetic apparatus against ozone damage, quenches ozone products, and reduces lipid peroxidation of cellular membranes: Plant Physiology, v. 127, p. 1781-1787.

Luke, W. T., R. R. Dickerson, and L. J. Nunnermacker, 1989, Direct measurements of the photolysis rate coefficients and henry law constants of several alkyl nitrates: Journal of Geophysical Research-Atmospheres, v. 94, p. 14905-14921.

Lyons, T. W., C. T. Reinhard, and N. J. Planavsky, 2014, The rise of oxygen in Earth's early ocean and atmosphere: Nature, v. 506, p. 307-315.

Ma, Y., T. Luciani, R. A. Porter, A. T. Russell, D. Johnson, and G. Marston, 2007, Organic acid formation in the gas-phase ozonolysis of alpha-pinene: Physical Chemistry Chemical Physics, v. 9, p. 5084-5087.

Martin, R. S., T. A. Mather, and D. M. Pyle, 2007, Volcanic emissions and the early Earth atmosphere: Geochimica Et Cosmochimica Acta, v. 71, p. 3673-3685.

Mickley, L. J., D. J. Jacob, B. D. Field, and D. Rind, 2004, Climate response to the increase in tropospheric ozone since preindustrial times: A comparison between ozone and equivalent CO2 forcings: Journal of Geophysical Research-Atmospheres, v. 109, p. 18.

Muller, B., and M. R. Heal, 2002, Mass accommodation coefficients of phenol, 2-nitrophenol, and 3-methylphenol over the temperature range 278-298 K: Journal of Physical Chemistry A, v. 106, p. 5120-5127.

Muller, J. F., J. Peeters, and T. Stavrakou, 2014, Fast photolysis of carbonyl nitrates from isoprene: Atmospheric Chemistry and Physics, v. 14, p. 2497-2508.

Murdachaew, G., M. E. Varner, L. F. Phillips, B. J. Finlayson-Pitts, and R. B. Gerber, 2013, Nitrogen dioxide at the air-water interface: trapping, absorption, and solvation in the bulk and at the surface: Physical Chemistry Chemical Physics, v. 15, p. 204-212.

Ng, N. L., P. S. Chhabra, A. W. H. Chan, J. D. Surratt, J. H. Kroll, A. J. Kwan, D. C. McCabe, P. O. Wennberg, A. Sorooshian, S. M. Murphy, N. F. Dalleska, R. C. Flagan, and J. H. Seinfeld, 2007, Effect of NOx level on secondary organic aerosol (SOA) formation from the photooxidation of terpenes: Atmospheric Chemistry and Physics, v. 7, p. 5159-5174.

Nguyen, T. K. V., Petters, M. D., Suda, S. R., Guo, H., Weber, R. J., and Carlton, A. G., 2014, Trends in particle-phase liquid water during the Southern Oxidant and Aerosol Study: Atmospheric Chemistry and Physics, v. 14, p. 10911-10930.

Nielsen, T., A. H. Egelov, K. Granby, and H. Skov, 1995, Observations on particulate organic nitrates and unidentified components of NOy: Atmospheric Environment, v. 29, p. 1757-1769.

Noziere, B., I. Barnes, and K. H. Becker, 1999, Product study and mechanisms of the reactions of alpha-pinene and of pinonaldehyde with OH radicals: Journal of Geophysical Research-Atmospheres, v. 104, p. 23645-23656.

O'Brien, J. M., E. Czuba, D. R. Hastie, J. S. Francisco, and P. B. Shepson, 1998, Determination of the hydroxy nitrate yields from the reaction of C(2)-C(6) alkenes with OH in the presence of NO: Journal of Physical Chemistry A, v. 102, p. 8903-8908.

Pankow, J. F., 1994, An absorption-model of gas-particle partitioning of organic-compounds in the atmosphere: Atmospheric Environment, v. 28, p. 185-188.

Paulot, F., J. D. Crounse, H. G. Kjaergaard, J. H. Kroll, J. H. Seinfeld, and P. O. Wennberg, 2009, Isoprene photooxidation: new insights into the production of acids and organic nitrates: Atmospheric Chemistry and Physics, v. 9, p. 1479-1501.

Peeters, J., L. Vereecken, and G. Fantechi, 2001, The detailed mechanism of the OH-initiated atmospheric oxidation of alpha-pinene: a theoretical study: Physical Chemistry Chemical Physics, v. 3, p. 5489-5504.

Perraud, V., E. A. Bruns, M. J. Ezell, S. N. Johnson, Y. Yu, M. L. Alexander, A. Zelenyuk, D. Imre, W. L. Chang, D. Dabdub, J. F. Pankow, and B. J. Finlayson-Pitts, 2012, Nonequilibrium atmospheric secondary organic aerosol formation and growth: Proceedings of the National Academy of Sciences of the United States of America, v. 109, p. 2836-2841.

Pinto, R. M. A., J. A. R. Salvador, and C. Le Roux, 2007, Bismuth(III) salts mediated regioselective ring opening of epoxides: an easy route to halohydrins and beta-hydroxy nitrates: Tetrahedron, v. 63, p. 9221-9228.

Possanzini, M., A. Febo, and A. Liberti, 1983, NEW DESIGN OF A HIGH-PERFORMANCE DENUDER FOR THE SAMPLING OF ATMOSPHERIC POLLUTANTS: Atmospheric Environment, v. 17, p. 2605-2610.

Prinn, R. G., R. F. Weiss, B. R. Miller, J. Huang, F. N. Alyea, D. M. Cunnold, P. J. Fraser, D. E. Hartley, and P. G. Simmonds, 1995, ATMOSPHERIC TRENDS AND LIFETIME OF CH3CCL3 AND GLOBAL OH CONCENTRATIONS: Science, v. 269, p. 187-192.

Raaschou-Nielsen, O., Z. J. Andersen, R. Beelen, E. Samoli, M. Stafoggia, G. Weinmayr, B. Hoffmann, P. Fischer, M. J. Nieuwenhuijsen, B. Brunekreef, W. W. Xun, K. Katsouyanni, K. Dimakopoulou, J. Sommar, B. Forsberg, L. Modig, A. Oudin, B. Oftedal, P. E. Schwarze, P. Nafstad, U. De Faire, N. L. Pedersen, C. G. Ostenson, L. Fratiglioni, J. Penell, M. Korek, G. Pershagen, K. T. Eriksen, M. Sorensen, A. Tjonneland, T. Ellermann, M. Eeftens, P. H. Peeters, K. Meliefste, M. Wang, B. Bueno-de-Mesquita, T. J. Key, K. de Hoogh, H. Concin, G. Nagel, A. Vilier, S. Grioni, V. Krogh, M. Y. Tsai, F. Ricceri, C. Sacerdote, C. Galassi, E. Migliore, A. Ranzi, G. Cesaroni, C. Badaloni, F. Forastiere, I. Tamayo, P. Amiano, M. Dorronsoro, A. Trichopoulou, C. Bamia, P. Vineis, and G. Hoek, 2013, Air pollution and lung cancer incidence in 17 European cohorts: prospective analyses from the European Study of Cohorts for Air Pollution Effects (ESCAPE): Lancet Oncology, v. 14, p. 813-822.

Raman, C. V, 1928, A new radiation: Indian Journal of Physics, 2, 387-98.

Roach, P. J., J. Laskin, and A. Laskin, 2010, Nanospray desorption electrospray ionization: an ambient method for liquid-extraction surface sampling in mass spectrometry: Analyst, v. 135, p. 2233-2236.

Rollins, A. W., J. D. Smith, K. R. Wilson, and R. C. Cohen, 2010, Real Time In Situ Detection of Organic Nitrates in Atmospheric Aerosols: Environmental Science & Technology, v. 44, p. 5540-5545.

Rubinstein, C. V., P. Gerrienne, G. S. de la Puente, R. A. Astini, and P. Steemans, 2010, Early Middle Ordovician evidence for land plants in Argentina (eastern Gondwana): New Phytologist, v. 188, p. 365-369.

Russell, D. H., and R. D. Edmondson, 1997, High-resolution mass spectrometry and accurate mass measurements with emphasis on the characterization of peptides and proteins by matrix-assisted laser desorption/ionization time-of-flight mass spectrometry: Journal of Mass Spectrometry, v. 32, p. 263-276.

Saunders, M., and G. W. Cline, 1990, Experimental and theoretical-studies of nonadditivity of multiple isotopic-substitution on equilibria: Journal of the American Chemical Society, v. 112, p. 3955-3963.

Scanion, J. T., and D. E. Willis, 1985, Calculation of flame ionization detector relative response factors using the effective carbon number concept: Journal of Chromatographic Science, v. 23, p. 333-340.

Schurath, U. 1984, Entstehung und Verbreitung von anthropogenem Ozon in der Bundesrepublik Deutschland, Wissenschaft und Umwelt 2/1984.

Scott, C. E., A. Rap, D. V. Spracklen, P. M. Forster, K. S. Carslaw, G. W. Mann, K. J. Pringle, N. Kivekas, M. Kulmala, H. Lihavainen, and P. Tunved, 2014, The direct and indirect radiative effects of biogenic secondary organic aerosol: Atmospheric Chemistry and Physics, v. 14, p. 447-470.

Seinfeld, J. H., and Pandis, S. N., Atmospheric Chemistry and Physics, from Air Pollution to Climate Change, John Wiley, New York, 1998.

Sharkey, T. D., and E. L. Singsaas, 1995, Why plants emit isoprene: Nature, v. 374, p. 769-769.

Shaw, G. H., 2008, Earth's atmosphere - Hadean to early Proterozoic: Chemie Der Erde-Geochemistry, v. 68, p. 235-264.

Shepson, P. B., E. Mackay, and K. Muthuramu, 1996, Henry's law constants and removal processes for several atmospheric beta-hydroxy alkyl nitrates: Environmental Science & Technology, v. 30, p. 3618-3623.

Shiraiwa, M., L. D. Yee, K. A. Schilling, C. L. Loza, J. S. Craven, A. Zuend, P. J. Ziemann, and J. H. Seinfeld, 2013, Size distribution dynamics reveal particle-phase chemistry in organic aerosol formation: Proceedings of the National Academy of Sciences of the United States of America, v. 110, p. 11746-11750.

Sillman, S., and D. Y. He, 2002, Some theoretical results concerning O-3-NOx-VOC chemistry and NOx-VOC indicators: Journal of Geophysical Research-Atmospheres, v. 107, p. 15.

Skalska, K., J. S. Miller, and S. Ledakowicz, 2010, Trends in NOx abatement: A review: Science of the Total Environment, v. 408, p. 3976-3989.

Song, M., C. Marcolli, U. K. Krieger, A. Zuend, and T. Peter, 2012, Liquid-liquid phase separation and morphology of internally mixed dicarboxylic acids/ammonium sulfate/water particles: Atmospheric Chemistry and Physics, v. 12, p. 2691-2712.

Suarez-Bertoa, R., B. Picquet-Varrault, W. Tamas, E. Pangui, and J. F. Doussin, 2012, Atmospheric Fate of a Series of Carbonyl Nitrates: Photolysis Frequencies and OH-Oxidation Rate Constants: Environmental Science & Technology, v. 46, p. 12502-12509.

Sun, K., Y. Qu, Q. Wu, T. T. Han, J. W. Gu, J. J. Zhao, Y. L. Sun, Q. Jiang, Z. Q. Gao, M. Hu, Y. H. Zhang, K. D. Lu, S. Nordmann, Y. F. Cheng, L. Hou, H. Ge, M. Furuuchi, M. Hata, and X. G. Liu, 2014, Chemical characteristics of size-resolved aerosols in winter in Beijing: Journal of Environmental Sciences-China, v. 26, p. 1641-1650.

Surratt, J. D., Y. Gómez-González, A. W. H. Chan, R. Vermeylen, M. Shahgholi, T. E. Kleindienst, E. O. Edney, J. H. Offenberg, M. Lewandowski, M. Jaoui, W. Maenhaut, M. Claeys, R. C. Flagan, and J. H. Seinfeld, 2008, Organosulfate Formation in Biogenic Secondary Organic Aerosol: The Journal of Physical Chemistry A, v. 112, p. 8345-8378.

Taylor, S. R., 2001, Does the lunar composition retain a memory from the early solar nebula: Meteoritics & Planetary Science, v. 36, p. 1567-1569.

Thornton, J. A., P. J. Wooldridge, R. C. Cohen, M. Martinez, H. Harder, W. H. Brune, E. J. Williams, J. M. Roberts, F. C. Fehsenfeld, S. R. Hall, R. E. Shetter, B. P. Wert, and A. Fried, 2002, Ozone production rates as a function of NOx abundances and HOx production rates in the Nashville urban plume: Journal of Geophysical Research-Atmospheres, v. 107, p. 17.

Tillmann, R., M. Hallquist, A. M. Jonsson, A. Kiendler-Scharr, H. Saathoff, Y. Iinuma, and T. F. Mentel, 2010, Influence of relative humidity and temperature on the production of pinonaldehyde and OH radicals from the ozonolysis of alpha-pinene: Atmospheric Chemistry and Physics, v. 10, p. 7057-7072.

Trainer, M., D. D. Parrish, P. D. Goldan, J. Roberts, and F. C. Fehsenfeld, 2000, Review of observation-based analysis of the regional factors influencing ozone concentrations: Atmospheric Environment, v. 34, p. 2045-2061.

Trenberth, K. E., J. T. Fasullo, and M. A. Balmaseda, 2014, Earth's Energy Imbalance: Journal of Climate, v. 27, p. 3129-3144.

Treves, K., and Y. Rudich, 2003, The atmospheric fate of C-3-C-6 hydroxyalkyl nitrates: Journal of Physical Chemistry A, v. 107, p. 7809-7817.

Tuazon, E. C., and R. Atkinson, 1990, A product study of the gas-phase reaction of isoprene with the oh radical in the presence of NOx: International Journal of Chemical Kinetics, v. 22, p. 1221-1236.

Tuazon, E. C., R. Atkinson, H. Macleod, H. W. Biermann, A. M. Winer, W. P. L. Carter, and J. N. Pitts, 1984, Yields of glyoxal and methylglyoxal from the nox-air photooxidations of toluene and m-xylene and p-xylene: Environmental Science & Technology, v. 18, p. 981-984.

Ueno, Y., 1976, Studies of salt-solution aerosols .13. Effect of surface-active substances on stability of aqueous salt solution aerosols: Atmospheric Environment, v. 10, p. 409-413.

Vingarzan, R., 2004, A review of surface ozone background levels and trends: Atmospheric Environment, v. 38, p. 3431-3442.

Vione, D., V. Maurino, C. Minero, and E. Pelizzetti, 2003, The atmospheric chemistry of hydrogen peroxide: A review: Annali Di Chimica, v. 93, p. 477-488.

Virtanen, A., J. Joutsensaari, T. Koop, J. Kannosto, P. Yli-Pirila, J. Leskinen, J. M. Makela, J. K. Holopainen, U. Poschl, M. Kulmala, D. R. Worsnop, and A. Laaksonen, 2010, An amorphous solid state of biogenic secondary organic aerosol particles: Nature, v. 467, p. 824-827.

Walker, J. C. G., 1982, The earliest atmosphere of the earth: Precambrian Research, v. 17, p. 147-171.

Wang, S. C., and R. C. Flagan, 1990, Scanning electrical mobility spectrometer: Aerosol Science and Technology, v. 13, p. 230-240.

Wayne 1992, Atmospheric chemistry: the evolution of our atmosphere, J. Photochem. Photobiol. A: Chem., 62 (1992) 379-396.

Wexler A. S. Constant humidity solutions. In CRC Handbook of Chemistry and Physics, 73rd edition, D. R. Lide, editor, 1992.

Wexler, A. S., and S. L. Clegg, 2002, Atmospheric aerosol models for systems including the ions H+, NH4+, Na+, SO42-, NO3-,Cl-, Br-, and H2O: Journal of Geophysical Research-Atmosheres, v. 107, p. 14.

Wiedensohler, A., An approximation of the bipolar charge distribution for particles in the submicron size range, J. Aerosol Sci. Technol., 19 (1986), p. 387.

Wild, M., D. Folini, C. Schar, N. Loeb, E. G. Dutton, and G. Konig-Langlo, 2013, The global energy balance from a surface perspective: Climate Dynamics, v. 40, p. 3107-3134.

Worton, D. R., G. P. Mills, D. E. Oram, and W. T. Sturges, 2008, Gas chromatography negative ion chemical ionization mass spectrometry: Application to the detection of alkyl nitrates and halocarbons in the atmosphere: Journal of Chromatography A, v. 1201, p. 112-119.

You, Y., L. Renbaum-Wolff, M. Carreras-Sospedra, S. J. Hanna, N.i Hiranuma, S. Kamal, M. L. Smith, X. Zhang, R. J. Weber, J. E. Shilling, D. Dabdub, S. T. Martin, and A. K. Bertram, 2012, Images reveal that atmospheric particles can undergo liquid–liquid phase separations: Proceedings of the National Academy of Sciences of the United States of America, v. 109, p. 13188-13193.

You, Y., L. Renbaum-Wolff, and A. K. Bertram, 2013, Liquid-liquid phase separation in particles containing organics mixed with ammonium sulfate, ammonium bisulfate, ammonium nitrate or sodium chloride: Atmospheric Chemistry and Physics, v. 13, p. 11723-11734.

Zafiriou, O. C., and M. B. True, 1979, Nitrate photolysis in seawater by sunlight: Marine Chemistry, v. 8, p. 33-42.

Zhang, Q., J. L. Jimenez, D. R. Worsnop, and M. Canagaratna, 2007, A case study of urban particle acidity and its influence on secondary organic aerosol: Environmental Science & Technology, v. 41, p. 3213-3219.

Zhao, Y. L., K. N. Houk, and L. P. Olson, 2004, Mechanisms of peroxynitrous acid and methyl peroxynitrite, ROONO (R = H, Me), rearrangements: A conformation-dependent homolytic dissociation: Journal of Physical Chemistry A, v. 108, p. 5864-5871.

APPENDIX

APPENDIX

A gas chromatograph coupled to an electron capture detector (GC-ECD; Shimadzu, Inc.) was used to measure gas phase organic nitrate compounds during the denuder calibration study. A GC-ECD schematic is displayed in Fig. A.1 and the column specifications for the RTX-1701 capillary column (Restek, Inc.) used were 30 m length, 0.25 mm i.d., and 1.0 μm film thickness. The mobile phase of the ZB-1701 capillary column was a 14% cyanopropyl/86% dimethylpolysiloxane polymer. The column oven was kept at 30°C for 5 minutes before heated to 225°C at a rate of 20°C/minute.
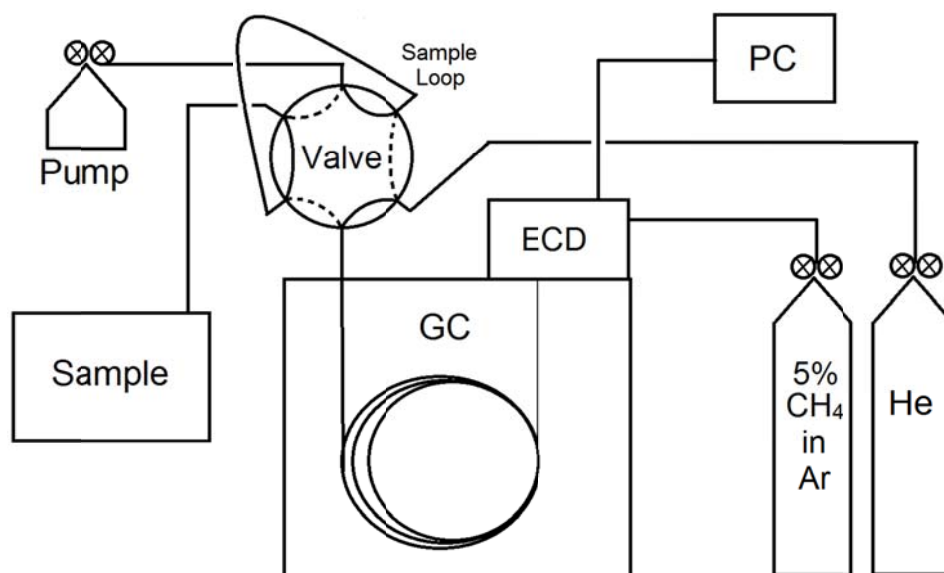
Figure A.1. The schematic for the GC-ECD.

Electron capture detectors are useful in the detection of electron-accepting electronegative compounds, such as organic nitrates and alkyl halides. Within an ECD, a radioactive Ni-63 β-emitting source is used to ionize the make-up gas, this study used 5% CH_4 in Ar, to generate free electrons and produce a standing current between two electrodes. When electronegative compounds, such as $RONO_2$ species, enter the detector, they readily accept the free electrons and cause a decrease in observed current. A schematic is shown in Fig. A.2. A calibration curve for the GC-ECD using isopropyl nitrate is shown in Fig. A.3.
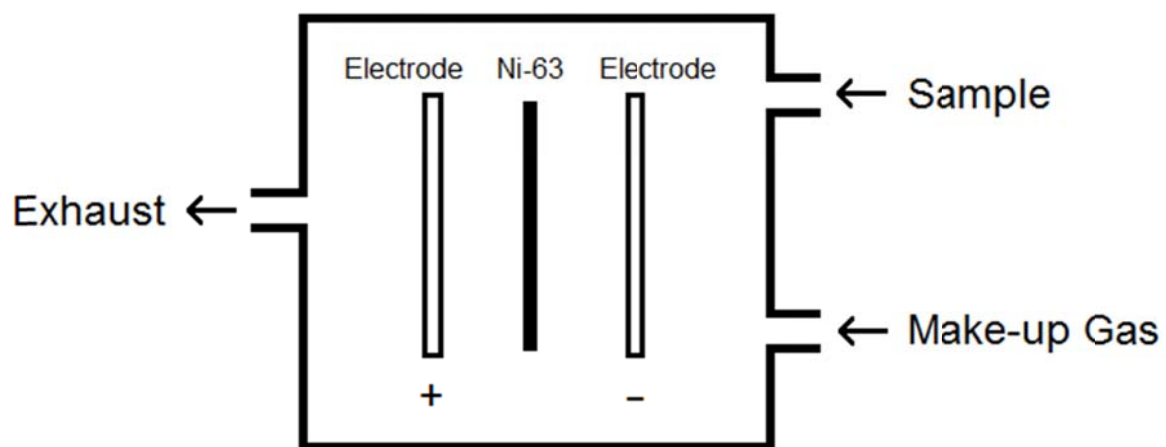
Figure A.2. The schematic for an electron capture detector (ECD).
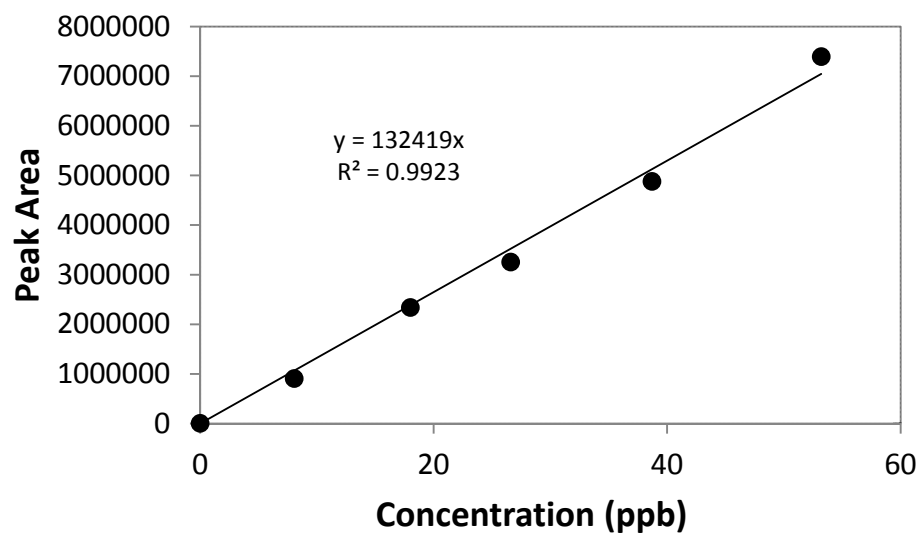
Figure A.3. A calibration curve for the GC-ECD using gas phase isopropyl nitrate.

VITA

VITA

Joel David Rindelaub was born on March 6, 1987 to George and Mary Ann Rindelaub. He grew up in St. Cloud, MN as the middle of three Rindelaub boys, which meant he was involved in sports and learned to play the piano, two requirements of the household, seemingly. Joel attended Cathedral High School in St. Cloud, MN and, in addition to being a GPA 4.0 student, he was a percussionist in the school's concert band and a letter winner in football, hockey, and baseball, earning the school's AAA award for excellence in the arts, academics, and athletics. Despite being selected in the 2005 NAHL entry draft, Joel followed his interests in mathematics and chemistry to Gustavus Adolphus College in St. Peter, MN where he majored in ACS chemistry while playing collegiate hockey. After an REU experience with Paula K. Hudson at California State University, Fullerton in the summer of 2008, Joel decided that he wanted to continue studying atmospheric chemistry and entered Purdue University as a graduate student in 2009. At Purdue, Joel focused his work on the atmospheric chemistry of α-pinene, using laboratory studies to gain insight into the formation and fate of α-pinene-derived nitrates, with implications into environmental air quality and climate. In addition to the atmospheric sciences, Joel has strong interest in astrochemistry/biology, music, sports, religion, philosophy, comedy, performance art, language, and culture. He aspires to become a research scientist and help improve the public communication of science.

PUBLICATION

The photochemical production of organic nitrates from α-pinene and loss via
acid-dependent particle phase hydrolysis

Joel D. Rindelaub [a, *], Kevin M. McAvey [a], Paul B. Shepson [a, b, c, *]

[a] Department of Chemistry, Purdue University, West Lafayette, IN, USA
[b] Department of Earth, Atmospheric, and Planetary Sciences, Purdue University, West Lafayette, IN, USA
[c] Purdue Climate Change Research Center, Purdue University, West Lafayette, IN, USA

HIGHLIGHTS

- High NO_x photochemical oxidation of α-pinene produced a 26 ± 7% organic nitrate yield.
- Organic nitrates hydrolyzed quickly in the particle phase.
- Partitioning and hydrolysis of organic nitrates may be an atmospheric sink for NO_x.

ARTICLE INFO

ABSTRACT

The hydroxyl radical oxidation of α-pinene under high NO_x conditions was studied in a photochemical reaction chamber to investigate organic nitrate ($RONO_2$) production and fate between the gas and particle phases. We report an organic nitrate yield of 26 ± 7% from the oxidation of this monoterpene in the presence of nitric oxide (NO). However, the apparent organic nitrate yield was found to be highly dependent on both chamber relative humidity (RH) and seed aerosol acidity, likely as a result of particle phase hydrolysis. The particle phase loss of organic nitrates is believed to increase the gas to particle partitioning within the system, leading to decreased $RONO_2$ yields in both the gas and particle phases at elevated RH and an apparent non-equilibrium partitioning mechanism. The hydrolysis of particle phase organic nitrates in this study, starting at low chamber relative humidity, implies that aerosol partitioning of organic nitrates may be an important sink for atmospheric NO_x and may have a significant impact on regional air quality.

1. Introduction

Global annual biogenic volatile organic compound (BVOC) emissions are estimated at ~1000 Tg/yr (Guenther et al., 2012), accounting for ~88% of all non-methane VOC emissions (Goldstein and Galbally, 2007). The oxidation of BVOCs can lead to secondary organic aerosol (SOA) formation, which impacts visibility, human health, and climate forcing. An important contributing SOA precursor is α-pinene with annual emissions estimated at ~66 Tg/yr (Guenther et al., 2012).

One specific group of BVOC oxidation products of interest is organic nitrates ($RONO_2$), due to their impact on regional air quality. An important oxidation pathway of α-pinene is initiated by the OH radical, which proceeds via addition across the double bond for ~90% of initiated reactions (Peeters et al., 2001), as shown in Scheme 1, α-Pinene-derived nitrates (APNs) are formed by the radical addition of O_2 and subsequent reaction with NO, nitric oxide (Reactions 1–3). The organic nitrate yield from the radical termination step (Reaction 3a) has a large range of reported values, from ~1% (Aschmann et al., 2002) to 18 ± 9% (Noziere et al., 1999), which contributes to a high degree of uncertainty in the α-pinene ozone production efficiency. This chain termination step (Reaction 3a) inhibits ozone production while the NO oxidation step (Reaction 3b) represents ozone production.

The production of organic nitrates creates low volatility compounds that are more hydrophilic than their precursor VOCs, and thus may play an important role in SOA formation, chemistry, and cloud condensation nuclei/ice nuclei activity as ambient measurements have indicated that 17–23% of molecules in organic aerosol

* Corresponding authors. 560 Oval Dr., West Lafayette, IN 47907, USA.
E-mail addresses: jrindela@purdue.edu (J.D. Rindelaub), pshepson@purdue.edu (P.B. Shepson).

J.D. Rindelaub et al. / Atmospheric Environment 100 (2015) 193—201
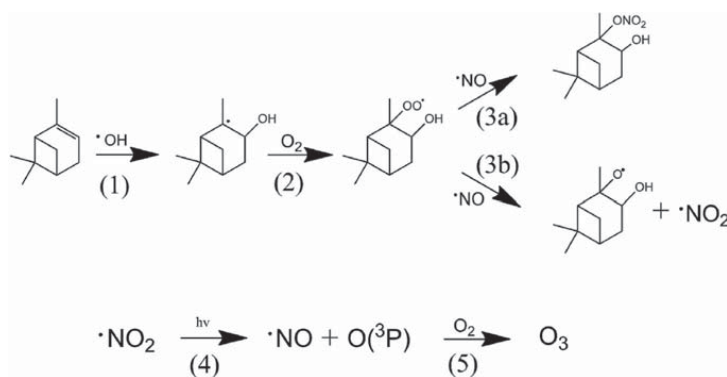
Scheme 1. An example mechanistic pathway for the hydroxyl radical initiated oxidation of α-pinene in the presence of NO$_x$ and subsequent ozone formation pathway.

contain the RONO$_2$ functional group (Rollins et al., 2013). Also, the formation of organic nitrates heavily influences gas phase NO$_x$ lifetimes and ozone concentrations (Browne and Cohen, 2012). Since NO$_x$, ozone, and particulate matter are all potentially harmful and regulated by local and national organizations internationally, the formation and fate of organic nitrates have great importance when assessing air quality and the impact on human health and climate.

Once produced, gas phase oxidation of organic nitrates may release NO$_x$ back into the gas phase and effectively transport ozone production potential to remote locations (Paulot et al., 2009, 2012). Additionally, organic nitrates have been shown to readily partition into the particle phase by a possible non-equilibrium mechanism (Perraud et al., 2012). Once in the particle phase, continued chemical reactions can occur, likely affecting the fate of organic nitrates in the atmosphere. Thus, partitioning and gas and aerosol phase chemistry of organic nitrates is of interest with respect to the fate of anthropogenic NO$_x$.

Of possible reactions in the particle phase, those governed by water are of interest due to its high tropospheric concentration and prevalence within aerosol particles (e.g. Veselovskii et al., 2000). Biogenically-derived SOA has been shown to increase the hygroscopicity of inorganic seed particles in laboratory studies (Bertram et al., 2011; Smith et al., 2012). Also, studies of condensed phase chemistry have shown that organic nitrates can hydrolyze readily under aqueous conditions with rate constants positively correlated to solution acidity (Darer et al., 2011; Hu et al., 2011). A recent chamber study by Liu et al. (2012) attributes a decrease in organic nitrate production to particle phase hydrolysis and suggests that this mechanism can explain the decrease in nitrogen-containing organic species observed in both laboratory (Nguyen et al., 2011) and field measurements (Day et al., 2010) under increased humidity. Particle phase hydrolysis may also be in part responsible for the scarcity of ambient BVOC-derived nitrate measurements.

Currently, in addition to the uncertainty in production yields for α-pinene-derived nitrate species, there are no known studies published that focus on the humidity dependent chemistry of particle phase organic nitrates from α-pinene-based reactions. Thus, in an effort to improve our understanding of the production and fate of organic nitrates from BVOC oxidation, we investigated their formation in both the gas and particles phases from the OH radical oxidation of α-pinene in a photochemical reaction chamber in the presence of NO$_x$. This experiment was conducted as a function of chamber relative humidity and seed aerosol acidity. This data set aims to provide valuable information concerning the hydrolysis chemistry of organic nitrates and how the reactivity of particle phase organic nitrates may impact air quality.

2. Experimental

Experiments were conducted using a 5.5 m^3 Teflon photochemical reaction chamber equipped with a mixing fan and UV lights (maximum output at 340 nm), described previously by Chen et al. (1998) and Lockwood et al. (2010). Three sets of experiments containing different seed aerosol conditions were completed as a function of chamber relative humidity, acidic seed, neutral seed, and the case without seed aerosol. The various seed aerosol types were created using an aerosol generator (3076, TSI, Inc.) and its output was passed through a Kr-85 aerosol neutralizer (TSI, Inc.) before injection into the chamber. A 15 mM (NH$_4$)$_2$SO$_4$ aerosol generator solution was used for the neutral seed aerosol experiments and a 30 mM MgSO$_4$/50 mM H$_2$SO$_4$ solution was used for the acidic seed aerosol experiments. The seed aerosol conditions were based on Surratt et al. (2008). According to the Extended-Aerosol Inorganics Model (E-AIM; http://www.aim.env.uea.ac.uk/aim/aim.php) described by Wexler and Clegg (2002), the pH of the neutral seed aerosol for high humidity conditions is estimated to start at close to pH = 5 while the acidic seed is estimated at pH < 1. However, once the experiment begins, HNO$_3$ will be produced (see below) and partition to the aerosol phase, and so the pH likely becomes more acidic through the experiment, for the "neutral seed" case. To maintain distinction between the two seed aerosol cases, the term "neutral seed" will be used even though the seed aerosol may actually be slightly acidic. Typical seed aerosol mass concentrations ranged from 50 to 150 μg/m^3 and number concentrations ranged from approx. 5.0 $\times$ 10^4 to 1.5 $\times$ 10^5 cm^{-3}. Large initial seed aerosol concentrations were effective in keeping the SOA within the measureable range of the scanning mobility particle sizer (SMPS; see below) over the course of the experimental timescale. Hydrogen peroxide, the OH radical precursor, and ultra-pure water were gently bubbled into the chamber under hydrocarbon-free air before the addition of the seed aerosol and α-pinene. Chamber water concentrations were measured using a LICOR-7000. The α-pinene (98%, Sigma Aldrich, Inc.) was introduced into the chamber by injection through a glass tee under heat while nitric oxide was similarly injected under N$_2$ without heat.

Real-time measurements were made using several instruments. The α-pinene concentrations were measured using a gas chromatograph-flame ionization detector (GC-FID; HP-5980), NO/NO$_y$ (nitric oxide/all reactive nitrogen oxide species) concentrations were measured with a Thermo NO/NO$_y$ detector (Model 42, Thermo, Inc.), and an SMPS (Model 3062, TSI, Inc.) was used to determine size-resolved particle concentrations. The SMPS was

calibrated with polystyrene latex spheres (PSLs) and both aerosol and sheath flow rates were monitored prior to use. Nitric oxide concentrations were kept above 100 ppb to keep ozone concentrations low and ensure the hydroxyl radical was the sole initial oxidizing agent. Selected experiments were conducted using isooctane as a reactive tracer compound to determine that OH radical concentrations in the chamber ranged from 1×10^6 cm^{-3} to 1×10^7 cm^{-3}.

After injection, the contents of the chamber were allowed to mix for 10 min before the fan was turned off for the duration of the experiment. The experiment was initiated (time = 0) when the UV lamps were turned on and the experiment was terminated when approximately half of the initial α-pinene was consumed, in an effort to focus on first generation products. Organic nitrate yields were not dependent on the fractional amount of α-pinene consumed. Typical experiment lengths were 1 h. All sampling lines were heated PFA Teflon (120 °C) except for the copper aerosol sampling line. The chamber was flushed continuously under irradiation with at least five chamber volumes of hydrocarbon-free air prior to each experiment.

Denuder-based filter samples were acquired at the completion of each experiment for off-line analysis. Gas phase compounds were sampled at 10 L/min and adsorbed onto the surface of the XAD-4 coated annular denuder (20 cm, URG, Inc.) while particle phase compounds were collected on a filter pack containing a Teflon filter (47 mm, VWR, Inc.) and a carbon-infused back-up filter (Grade 72, VWR, Inc.), which was used to capture gas phase negative artifacts arising from the front filter. The gas phase collection efficiency was determined by measuring the concentration of an isopropyl nitrate standard (99%, Sigma Aldrich) both upstream and downstream of the denuder. The collection efficiency was ≥98%. The denuder was extracted in a 50:30:20 acetonitrile:hexane:methylene chloride solution and extracts were dried to ~50% of their original volume before transfer to tetrachloroethylene (C$_2$Cl$_4$) to prevent losses during drying. Filters were placed in tetrachloroethylene (≥99.9%, Sigma—Aldrich) and sonicated for 45 min.

Blank samples were acquired from the chamber prior to the experiment using only the filter pack.

Organic nitrate quantification was accomplished through use of a Brucker Tensor FT-IR spectrometer (Brucker, Inc.). FT-IR has been successfully employed in several previous laboratory and field studies for organic nitrate quantification (Laurent and Allen, 2004; Dekermenjian et al., 1999; Noda et al., 2000; Hallquist et al., 1999; Nielsen et al., 1998). As the full complement of α-pinene-derived nitrate standards are currently unavailable, quantification of organic nitrate products using a GC-based method was not possible for this study. Additionally, FT-IR presents the advantage of detecting all organic compounds with the RONO$_2$ functionality and does not require that they quantitatively pass through a column. Filter and denuder extracts were analyzed in a 1 cm liquid cell and organic nitrate concentrations were determined using the asymmetric $-$NO$_2$ stretch at ~1640 cm^{-1} (Nielsen et al., 1995). The asymmetric $-$NO$_2$ stretch at ~1640 cm^{-1} is unique to organic nitrates and does not have any known interferences from other oxidized nitrogen species (Roberts, 1990). Typical spectra for both a filter extract and blank extract in tetrachloroethylene (C$_2$Cl$_4$) are shown in Fig. 1. Tetrachloroethylene was chosen as a solvent because it has minimal absorption features in the infrared region. However, as observed in the IR spectra (Fig. 1), bands from weaker absorption features are more prominent in liquid phase spectra. The non-organic nitrate bands in Fig. 1 are of solvent origin.

While traditionally there are three distinct bands used to quantify organic nitrate in the infrared spectrum (1645, 1280, and 845 cm^{-1}), a recent study by Bruns et al. (2010) did not reveal a significant difference in quantitative results when integrating over one absorption band compared to the use of all three. Since no APN standards are currently available, the absorption cross section of the organic nitrate products at ~1640 cm^{-1} was assumed to be identical to that from an isopropyl nitrate standard. A previous study analyzing molecular extinction coefficients of alkyl nitrates observed a standard deviation of less than 7% among the compounds studied (Carrington, 1960), indicating that variability in the
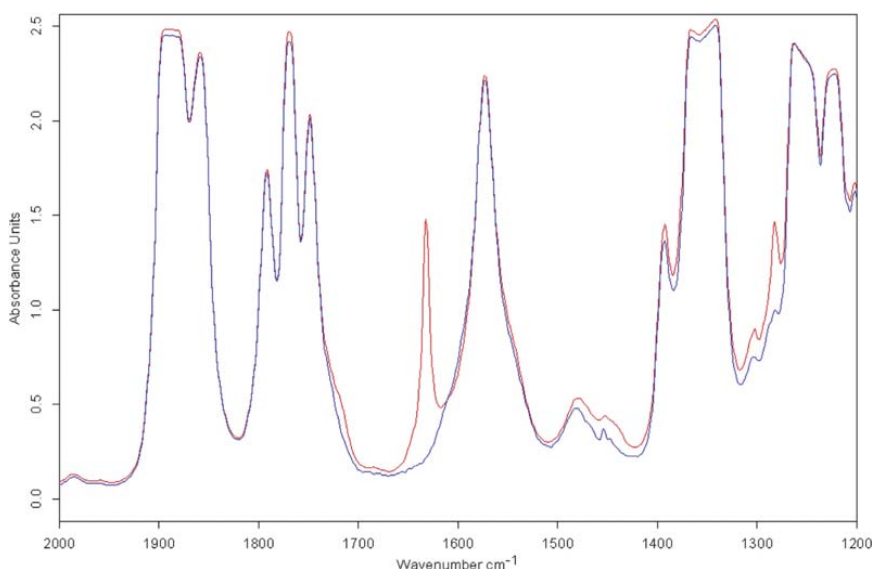

Fig. 1. The FT-IR spectra of a filter sample extracted in C$_2$Cl$_4$ (red) and a filter blank (blue). The peak at ~1640 cm^{-1} corresponds to the asymmetric $-$NO$_2$ stretch of organic nitrates. (For interpretation of the references to color in this figure legend, the reader is referred to the web version of this article.)

absorption cross section of organic nitrates in our study is likely not a significant source of error.

Organic nitrate yield values were corrected for chamber wall loss and consumption by OH radicals. The gas phase wall loss rate constants were determined by observing the loss of an α-pinene-derived nitrate product after the completion of experiments, via GC–(NICI)–MS, a technique that identifies organic nitrates using the m/z 46 ion in the negative ion mode (Worton et al., 2008). Particle phase wall loss rates were determined in a similar manner from the SMPS data. Wall loss rate constants, 2.28×10^{-4} s^{-1} and 8.0×10^{-5} s^{-1} for the gas and particle phases, respectively, were not influenced by chamber RH. Final yield values were determined by accounting for product loss via wall partitioning based on Tuazon et al. (1984). Due to the uncertainty in the NO$_x$ recycling efficiency of organic nitrates from further gas phase oxidation, ranging from +50% (Paulot et al., 2009) to −23% (Lee et al., 2014), the consumption of α-pinene-derived nitrates by the OH radical was not taken into account for the calculation of the total organic nitrate yield. However, it is important to note that, because most of the organic nitrates produced are saturated, the yield calculation including a rate constant for product consumption by OH, estimated from the EPI Suite provided online by the EPA (http://www.epa.gov/opptintr/exposure/pubs/episuite.htm), did not have a significant impact on the final yield values, i.e. shifting the assumed OH rate constant by an order of magnitude corresponded to less than a 2% difference in final yield values.

3. Results and discussion

3.1. Photochemical reaction chamber experiments

Typical α-pinene and aerosol mass concentrations over the length of a seed aerosol experiment are shown in Fig. 2. Relatively high starting concentrations of α-pinene were used to produce organic nitrate concentrations measureable by offline FT-IR analysis. Several experiments yielded organic nitrate concentrations close to or below the detection limit of the instrument, especially at high chamber RH (see discussion below). Nitric oxide concentrations were maintained at levels high enough to ensure that all α-pinene consumption occurred via reaction with OH, and that RO$_2$ isomerization and self-reactions did not compete with the RO$_2$ + NO pathway (Capouet et al., 2004; Atkinson et al., 2006). Despite relatively high NO$_2$ concentrations created in the chamber,
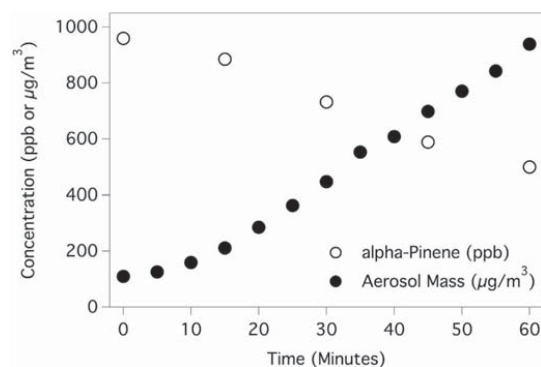
we calculate that the RO + NO$_2$ reaction pathway will have less than a 1% contribution to the total RONO$_2$ yield, largely because the predominant alkoxy radicals rapidly decompose to produce a carbonyl compound and HO$_2$, based on reaction rate constant assumptions from Atkinson et al. (1997, 2006), Nakamura et al. (2000), and Orlando et al. (2003). SOA production occurred within 10 min, after which the aerosol mass concentration increased approximately linearly throughout the experiment. The slight induction period needed for SOA production is related to the time needed to build up sufficient partial pressures of low volatility oxidation products that would support aerosol growth.

The SOA production from experiments without seed aerosol also increased rapidly. However, with much smaller chamber aerosol number concentrations and less surface area on which to condense, organic material from the gas phase reaction underwent homogeneous nucleation to form new particles that quickly grew out of the measurable range for the SMPS (up to 1.0 μm mobility diameter). Thus, we were unable to calculate aerosol yields for the unseeded experiments. The density of SOA produced was assumed to be 1.25 g/cm^3, based on (Ng et al., 2006). The aerosol yield from all seed aerosol experiments was 34 ± 12% and didn't statistically differ based on seed aerosol composition or chamber relative humidity. While previous studies have shown that the aerosol yield from this type of reaction can be highly variable, as highlighted by Henry et al. (2012), the calculated yield from this experiment is in statistical agreement with several previous studies (Hoffmann et al., 1997; Jaoui and Kamens, 2001; Lee et al., 2006; Noziere et al., 1999).

3.1.1. Determination of the organic nitrate branching ratio

The organic nitrate branching ratio, $k_{3a}/(k_{3a} + k_{3b})$ (see Scheme 1), is typically determined from a yield plot of [RONO$_2$] produced throughout the experiment vs. $-\Delta$[BVOC], under the assumption that every RO$_2$ radical reacts with NO. For these experiments, however, only one data point is produced per experiment due to the large sample volumes required for analysis. The single point total organic nitrate yields (gas + aerosol) calculated from 58 separate experiments, shown in Figs. 3 and 4, were found to be highly dependent on chamber relative humidity, even at low RH (Figs. 3 and 4).

We propose (see discussion below) that this results from humidity dependent consumption of RONO$_2$ in the aerosol phase after production in the gas phase via Reaction 3a (Scheme 1). The higher

Fig. 2. The α-pinene and aerosol mass concentrations as a function of time for a neutral seed experiment. The open circles ($\circ$) represent α-pinene (ppb) while the closed circles ($\bullet$) represent the aerosol mass concentration (μg/m^3). Initial α-pinene and seed aerosol concentrations were 960 ppb and 110 μg/m^3, respectively.

Fig. 3. The total organic yield as a function of chamber relative humidity for both the acidic seed aerosol ($\circ$) and neutral seed aerosol ($\bullet$) experiments. Each data point represents the organic nitrate yield from a single experiment. The lines shown are regressions used to estimate the 0% RH total RONO$_2$ yield (see text).

Fig. 4. The total organic nitrate yield as a function of chamber relative humidity for the unseeded aerosol experiments. Each data point represents the organic nitrate yield from a single experiment.

degree of scatter under dry conditions in Figs. 3 and 4 is believed to be a result of the extreme sensitivity of the organic nitrate yields to chamber RH over this range and c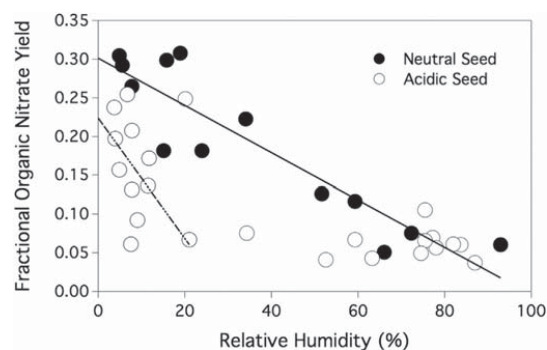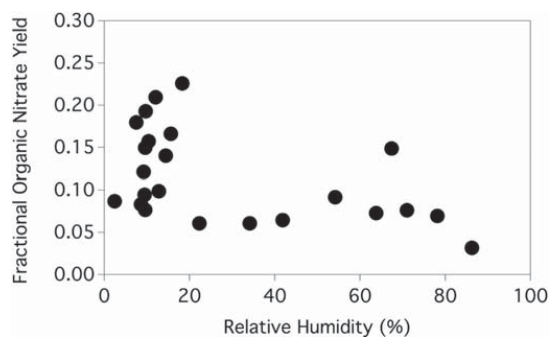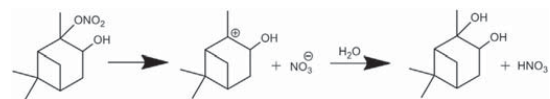orresponding variations in aerosol water content and aerosol pH. Since hydrolysis is highly dependent on pH (see Scheme 2), the aerosol water content, seed aerosol composition and partitioning of gas phase HNO_3 created via Reaction 6 (see below) are all expected to influence the observed $RONO_2$ yields.

Additionally, the partitioning of gas phase products will be dependent on the composition and total mass concentration of the particles (Pankow, 1994), which also varied considerably between experiments. Thus, due to several processes and variables mentioned, including the uncertainty in aerosol liquid water content under dry conditions, a high amount of variability would be expected in the measured organic nitrate yields over the low humidity range.

$$OH + NO_2 \rightarrow HNO_3 \tag{6}$$

On the assumption that the 0% RH yield value would represent the true initial total $RONO_2$ yield (i.e. representing no losses within the aerosol phase), we conducted a linear extrapolation of the seed aerosol low humidity yield data, from 0 to 20% RH, to the zero humidity intercept. The low humidity data from 0 to 20% RH was used for a linear regression analysis of the acidic seed data because, as shown in Fig. 3, the observed yield is very humidity dependent over this range, and the use of a larger range would underestimate the yield. The acidic seed data point at ~20% RH was omitted from the least squares fit after analysis of its Cook's distance (Cook, 1977). A linear regression of the data yielded y-intercepts of 30 ± 4% and 22 ± 6% for the neutral and acidic seed aerosol cases, respectively. The regression lines are shown in Fig. 3. Combining the standard errors of the y-intercepts, we report a 26 ± 7% total organic nitrate yield from this oxidation pathway of α-pinene. Due to the high degree of scatter in the unseeded data at

low RH (Fig. 4) and the lack of a statistically significant slope from a least squares fit, an analogous linear extrapolation from the unseeded plot was not conducted. Table 1 shows results from both the acidic and neutral seed experiments where the A_i and F_i parameters correspond to the concentration of $RONO_2$ in the gas phase and particle phase in ppb and $\mu g/m^3$, respectively. Table 2 shows the analogous results for the unseeded experiments. Assuming that all peroxy radicals react with NO (Scheme 1), and that there are no unknown losses of organic nitrates, the yield then corresponds to the branching ratio. The 26 ± 7% total organic nitrate yield reported here is higher than the ~1% reported by Aschmann et al. (2002) but does not statistically differ from the 18 ± 9% determined by Noziere et al. (1999), who also used FT-IR to determine organic nitrate concentrations.

The organic nitrate contribution to total particle mass was also determined for experiments in the 0–20% RH range. As stated previously, this calculation, which is the ratio of total organic nitrate mass in the particle phase to the total SOA mass produced, could only be assessed for seeded aerosol experiments as the final aerosol mass concentrations for unseeded experiments could not be determined. The calculated mass fraction of organic nitrates in the particle phase, assuming an organic nitrate molecular weight of 215 g/mole, is 18 ± 4% for the seeded aerosol experiments, the same value (18%) reported by (Rollins et al., 2010) from an α-pinene/NO_x irradiation flow-tube study in the absence of seed aerosol.

Table 1

Summary of results for the neutral seed [$(NH_4)_2SO_4$] and acidic seed [$MgSO_4/H_2SO_4$] α-pinene oxidation experiments. The A_i and F_i parameters correspond to the concentration of $RONO_2$ in the gas phase and particle phase, respectively.

Exp. date	Seed aerosol	RH (%)	Δ α-pinene (ppb)	A_i (ppb)	F_i ($\mu g/m^3$)	$RONO_2$ yield (%)
10/17/2011	Neutral	4.90	433.0	9.9	1073	30
11/16/2011	Neutral	5.60	104.0	7.1	202	29
11/19/2011	Neutral	7.80	2026	203	2937	26
11/3/2011	Neutral	15.1	1257	129	879	18
10/24/2011	Neutral	18.9	587.0	30	1319	31
11/14/2011	Neutral	23.9	461.0	38	404	18
6/23/2011	Neutral	34.1	655.0	25	1064	22
11/27/2012	Neutral	51.6	3957	122	3315	13
11/22/2012	Neutral	59.3	3485	104	2656	12
11/15/2012	Neutral	66.0	3146	65	835	5.1
11/9/2012	Neutral	72.3	3455	110	1337	7.6
12/1/2012	Neutral	92.9	3021	56	1108	6.0
6/16/2012	Acidic	3.70	2771	342	2779	24
6/12/2012	Acidic	4.00	3704	132	5267	20
6/7/2012	Acidic	4.90	3680	279	2629	16
5/11/2012	Acidic	6.70	3339	482	3236	25
5/29/2012	Acidic	7.50	576.0	34	15	6.1
5/24/2012	Acidic	7.80	1922	225	1530	21
6/24/2012	Acidic	7.80	556.0	5.2	598	13
9/11/2012	Acidic	9.10	3340	275	290	9.2
6/27/2013	Acidic	11.5	3870	77	3966	14
9/25/2012	Acidic	11.7	4178	128	5188	17
5/19/2012	Acidic	20.1	1166	108	1592	25
8/24/2012	Acidic	21.0	4843	219	932	6.7
8/17/2012	Acidic	34.3	2963	198	229	7.5
8/20/2012	Acidic	52.5	1948	33	413	4.1
8/8/2012	Acidic	59.3	1876	126	0.0	6.7
8/14/2012	Acidic	63.3	4341	135	448	4.3
7/25/2012	Acidic	74.5	4136	188	141	4.9
7/15/2012	Acidic	75.5	1998	132	0.0	6.6
7/22/2012	Acidic	75.5	922.0	97	0.0	11
7/8/2012	Acidic	77.2	348.0	24	0.0	7.0
7/11/2012	Acidic	78.0	2822	161	0.0	5.7
8/5/2012	Acidic	82.0	3480	212	0.0	6.1
7/28/2012	Acidic	83.7	1573	95	0.0	6.0
8/1/2012	Acidic	87.0	3147	117	0.0	3.7

Scheme 2. The condensed phase hydrolysis mechanism at neutral pH of a proposed α-pinene-derived organic nitrate to form the corresponding alcohol product, pinanediol. This S_N1 mechanism is in competition with the E1 mechanism, which would form an olefinic elimination product.

Table 2
Summary of results for the unseeded α-pinene oxidation experiments. The A_i and F_i parameters correspond to the concentration of $RONO_2$ in the gas phase and particle phase, respectively.

Exp. date	Seed aerosol	RH (%)	Δ α-pinene (ppb)	A_i (ppb)	F_i ($\mu g/m^3$)	$RONO_2$ yield (%)
5/3/2012	NONE	2.40	3652	186	1152	8.7
3/22/2012	NONE	7.50	2217	132	2339	18
9/19/2012	NONE	8.60	3680	19	2524	8.3
4/23/2012	NONE	9.20	4737	178	3473	12
2/8/2012	NONE	9.40	1187	78	299	9.4
3/13/2012	NONE	9.60	2730	110	2620	15
9/27/2012	NONE	9.60	3749	115	1521	7.7
2/17/2012	NONE	9.70	2515	182	2664	19
2/13/2012	NONE	10.4	1294	74	1134	16
4/17/2012	NONE	12.0	2505	126	3500	21
2/28/2012	NONE	12.8	4212	218	1741	9.9
4/4/2012	NONE	14.4	4082	219	3104	14
1/24/2012	NONE	15.6	640.0	32	660	17
3/9/2012	NONE	18.3	155.0	23	106	23
2/1/2012	NONE	22.3	3648	55	1460	6.1
1/20/2013	NONE	34.1	3142	34	1372	6.1
1/13/2013	NONE	41.9	4445	33	2225	6.4
10/23/2012	NONE	54.2	3475	68	2207	9.2
1/16/2013	NONE	63.8	4445	52	2392	7.3
11/2/2012	NONE	67.4	3152	78	3438	15
1/24/2013	NONE	71.0	2311	47	1134	7.6
1/9/2013	NONE	78.2	3472	50	1680	6.9
11/6/2012	NONE	86.3	4500	45	853	3.2

3.1.2. Humidity dependence of organic nitrate yields

As discussed above, the total organic nitrate yields were highly dependent on chamber relative humidity, as seen in Figs. 3 and 4. The total (gas + particle phases) organic nitrate yield decreased rapidly as RH was increased from 0 to ~20% in both the unseeded and seeded aerosol conditions, followed by a less pronounced drop from 20 to 90% RH to total yields as low as 5%. Despite our lack of knowledge of the relationship between aerosol liquid water content of the SOA created and chamber relative humidity, the strong inverse correlation between organic nitrate concentration and the presence of water vapor within the chamber indicates that the SOA particles created may have a high potential for both water and acid uptake, leading to organic nitrate hydrolysis in the particle phase. Hydrolysis of organic nitrates has been previously reported for aqueous phase laboratory studies (Darer et al., 2011; Hu et al., 2011) and is believed to be responsible for decreased organic nitrate aerosol concentrations in a recent chamber study (Liu et al., 2012). Our findings add further evidence for the importance of the hydrolysis reaction in particle phase chemistry and help provide an explanation for the decrease in organic nitrogen-containing species observed at high ambient RH in a recent field study (Day et al., 2010). The decrease in organic nitrate yields with humidity was observed with all three types of seed aerosol experiment sets.

A reaction mechanism for the proposed condensed phase hydrolysis of an α-pinene-derived nitrate at neutral pH is shown in Scheme 2. The hydrolysis mechanism to form the corresponding alcohol likely proceeds via unimolecular nucleophilic substitution (S_N1) rather than bimolecular nucleophilic substitution (S_N2) as suggested previously (Darer et al., 2011). Instead of occurring in a single step initiated by nucleophilic attack, the S_N1 mechanism occurs in two separate steps where first the leaving group, in this case the nitrate anion, detaches from the molecule to form a carbocation, which is followed by the attachment of the nucleophile, in this case water, at the available site. As water is a weak nucleophile, it is more likely that it will attach to an available carbocation rather than attack a carbon center carrying a weakly induced dipole. Previous laboratory studies indicate that tertiary organic nitrates are much more susceptible to hydrolysis than similar primary species (Darer et al., 2011). This phenomenon is consistent with the S_N1 mechanism as the steric hindrance of tertiary organic compounds makes it difficult for an S_N2 transition state to exist. Also, the carbocation intermediates formed from tertiary organics are much more stable than their primary counterparts, allowing for much faster S_N1 reaction rates. As the major organic nitrate products produced from this oxidation pathway are expected to be both tertiary and secondary (Scheme 3), partitioning to and hydrolysis in the particle phase is a feasible explanation for decreased organic nitrate yields as a function of chamber humidity.

Unfortunately, standards are unavailable for the expected organic nitrate products and the applicable aqueous phase lifetimes are currently unknown. The reported lifetimes for tertiary β-hydroxy-organic nitrates in the aqueous phase at neutral pH are less than 1 h (Darer et al., 2011), which would fall within the experimental timescale. Due to the acidic nature of the aerosol in these experiments, the hydrolysis rates in this study are likely much faster than those determined by Darer et al. (2011). However, a recent chamber study investigating the hydrolysis of trimethylbenzene-derived organic nitrate compounds, which were predicted to be primarily tertiary organic nitrates, reported a particle phase lifetime of ~6 h (Liu et al., 2012). It is also important to note that nucleophilic attack by the bisulfate ion (HSO_4^-) on the carbocation created via the S_N1 mechanism (Scheme 2) may be responsible for creating particle phase organosulfates, such as the m/z 249 compound detected by Surratt et al. (2008).

Further evidence to support organic nitrate hydrolysis via the S_N1 mechanism is shown by the difference in organic nitrate yields between the neutral and the acidic seed aerosol as a function of chamber RH. The particle phase organic nitrate yields in the acidic seed case decreases more rapidly with RH, and to below the detection limit by ~80% RH, than for the neutral seed case (see Figs. 5 and 6 for the gas and particle phase yields for each case), while the particle phase organic nitrate yields only dropped to ~4% in the neutral seed experiments at similar relative humidity. The gas phase yields had a stronger dependence on RH in the acidic seed experiments compared to those with neutral seed.

The dependence of the organic nitrate yield on both chamber water content and seed aerosol acidity supports the proposed mechanism as organic nitrate hydrolysis rates are known to increase with solution acidity (Hu et al., 2011), providing evidence
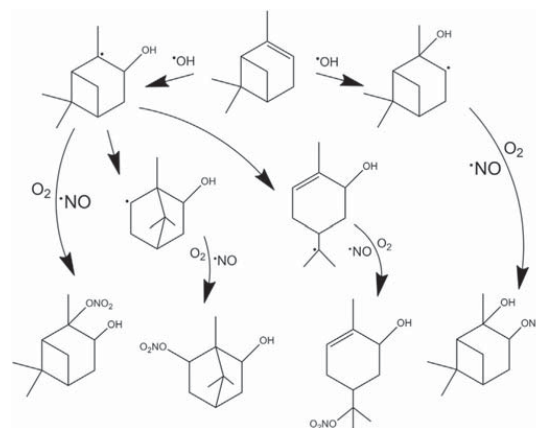
Scheme 3. The OH radical addition to α-pinene, the possible gas phase rearrangements of the radicals formed, and the four organic nitrates isomers produced from each pathway. The proposed chemistry is based on Peeters et al. (2001).

that reactions that eliminate the $RONO_2$ functionality, such as hydrolysis, are likely acid-catalyzed. Additionally, the aqueous acidic conditions in this study provide a polar protic solvent system which favors S_N1 and E1 mechanisms by allowing for increased stabilization of the transition state and better solvation of the leaving group, leading to an increase in both carbocation formation and product creation. Since the formation of the carbocation is the rate determining step of this reaction, the hydrolysis mechanism should be a first order process, consistent with previously reported data (Hu et al., 2011).

In the case of the unseeded aerosol experiments, the total organic nitrate yield showed a similar trend as the seeded aerosol experiments when RH was increased (Fig. 4). If the degree of organic nitrate hydrolysis within the timescale of these experiments is related to particle acidity, the behavior of the unseeded and neutral seed $RONO_2$ yield plots must be influenced by the uptake of HNO_3 to the particle phase, produced either in the gas phase (Reaction 6) or at the surface (Atkinson et al., 1976; Murdachaew et al., 2013).

3.1.3. Gas-particle partitioning of monoterpene-derived organic nitrates

Using denuder-based filter sampling allowed for separate analysis of both the gas and particle phase products, as shown in Figs. 5 and 6. The F_i/A_i ratio of organic nitrates in the system, where F_i and A_i are the particle and gas phase concentrations, respectively, was greater than 1.0 for all seed aerosol systems when averaged over the low humidity range (0–20% RH). At elevated RH, only the acidic seed aerosol case revealed F_i/A_i ratios below 1.0, shown in Table 3.

This phenomenon is also observed by inspecting the linear regressions of both the gas and particle phase organic nitrate yield data shown in Figs. 5 and 6. While the apparent particle phase organic nitrate yields decrease more rapidly than the gas phase yields with RH for both the neutral and acidic seed aerosol scenarios, the decrease is much more dramatic in the acidic seed scenario (Fig. 6), leading to F_i/A_i ratios less than 1.0 at elevated humidity (>20% RH). The rapid decrease with RH in the acidic seed particle phase $RONO_2$ yield values indicates that an acid-induced increase in the rate of hydrolysis in the particle phase is occurring at a rate that out-competes uptake of gas phase organic nitrates into the aerosol phase at elevated RH.
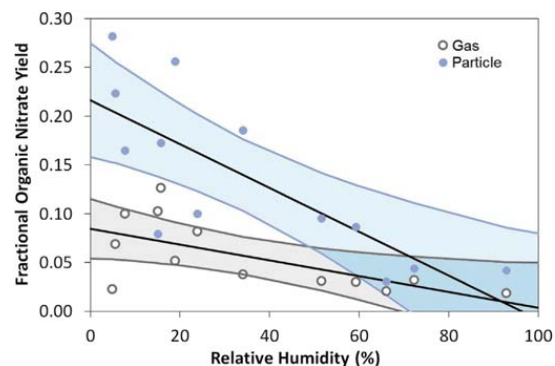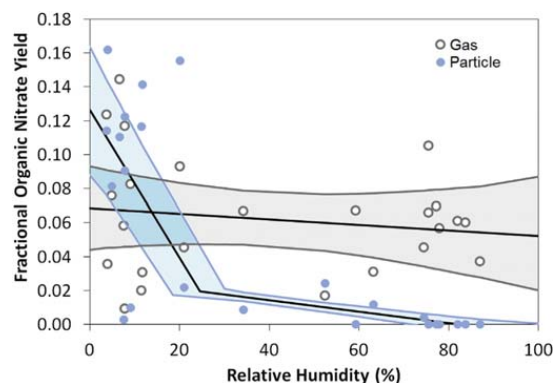

Fig. 6. Gas and aerosol-phase organic nitrate yields, by phase, for the acidic seed aerosol experiments where open circles (○) represent gas phase yields and closed circles (●) represent particle phase yields. Linear regressions with confidence limits are shown for each data series. The particle phase yield regressions are separated into a low RH and high RH regime.

These measurements, along with the aerosol mass concentrations (M), can enable calculation of the gas-aerosol partition coefficient, K_p, as described by Pankow (1994) and Eq. (1).

$$K_p = \frac{F_i/M}{A_i} \tag{1}$$

However, this assumes simple gas-aerosol partitioning without losses on the timescale of equilibration. Calculated values of K_p in this study vary from an estimated 7.3×10^{-6} $m^3/\mu g$ maximum at high RH (estimated from the FT-IR organic nitrate detection limit) to the order of 10^{-2} $m^3/\mu g$ at low RH, reflecting the impact of rapid consumption in the aerosol phase, and a non-equilibrium system. The highest measured partition coefficients at low RH correspond to saturated vapor pressures of roughly one to two orders of magnitude lower than what is estimated for α-pinene-derived organic nitrates (Pankow, 1994; Pankow and Asher, 2008). This could arise from a number of phenomena, including non-equilibrium partitioning into low viscosity particles, chemical processing of the organic nitrates in the aerosol phase (thus lowering their vapor pressure), and/or contributions to total organic nitrates from secondary oxidation in the gas phase.

To estimate an upper limit for the rate of $RONO_2$ loss in our system via particle phase hydrolysis, the uptake rate (R_{in}) of organic nitrates was calculated using Eq. (2) described by Jacob (2000), where r is the radius of the particle, D_g is the gas phase molecular diffusion coefficient, v is the mean molecular speed, α is the $RONO_2$ mass accommodation coefficient, A is the aerosol surface area per unit volume of air, and N' is the gas phase $RONO_2$ concentration.

$$R_{in} = \left(\frac{r}{D_g} + \frac{4}{v\alpha}\right)^{-1} AN' \tag{2}$$

Fig. 5. Gas and aerosol-phase organic nitrate yields, by phase, for the neutral seed aerosol experiments where open circles (○) represent gas phase yields and closed circles (●) represent particle phase yields. Linear regressions with confidence limits are shown for each data series.

Table 3
The F/A ratio, where F is the particle phase organic nitrate yield and A is the gas phase organic nitrate yield, of both the acidic seed and neutral seed experiments averaged over both the low and high humidity ranges.

Relative humidity	Average F/A (neutral seed)	Average F/A (acidic seed)
Low (<20%)	4.1	3.2
High (>20%)	2.5	0.3

Assuming a mass accommodation factor (α) similar to that for 2-nitrophenol, 0.012 (Muller and Heal, 2002), a D_g of 0.2 cm^2/s (Jacob, 2000), and a calculated v of 1.72×10^4 cm/s, the estimated timescale for uptake into the aerosol phase, τ_{uptake} (R_{in}/N'), was calculated to be 194s. That value, the lower limit timescale for the loss of RONO$_2$ in our system after partitioning to the particle phase, is much shorter than the combined experimental and sampling timescale of ~2.5 h. Support of an apparent non-equilibrium partitioning system can be seen by examining the decrease in both the gas and particle organic nitrate yields as a function of RH in the acidic seed aerosol case. Acidic particle phase organic nitrate yields decreased to ~0% at high humidity (>60% RH) while the gas phase yields decreased to ~6%. The decrease in apparent particle phase organic nitrate yields can be explained by hydrolysis in the aerosol phase, where the consumption of organic nitrates causes further partitioning of gas phase organic nitrates into the particle phase, followed by subsequent hydrolysis, lowering the apparent yields for both phases. We note that the condensed phase chemical reaction of organic nitrates to form less volatile species within aerosol, such as through oligomerization, also is likely to contribute to the observed apparent non-equilibrium partitioning.

Under typical tropospheric conditions, hydrolysis will likely be important as relative humidity is most often above the range where this study began to observe RONO$_2$ hydrolysis (0—10% RH), meaning that water interaction with SOA particles may occur even at very low RH. For aerosols in many moderately populated environments, the pH can be very low, e.g. on the order of 1.0 (Koutrakis et al., 1988), which also will have a large effect on hydrolysis chemistry. The degree of scatter in the plotted data indicate that multiple physical and chemical processes may affect how low volatility organic nitrates, such as those derived from monoterpene oxidation, partition between the gas and aerosol phases.

3.2. Atmospheric implications

The high degree of organic nitrate partitioning and hydrolysis in the particle phase, even under low RH conditions, may have an important impact on NO$_x$, O$_3$, and regional air quality. Organic nitrates are an important sink for gas phase NO$_x$; however, further reactions, such as oxidation or photolysis in either the gas or particle phase, may release NO$_x$ back into the gas phase, leading to an effectively longer NO$_x$ lifetime. The transformation of organic nitrates to the analogous alcohol within the aerosol will convert the nitrooxy group in the organic nitrate to the nitrate ion, which will remain relatively longer (depending on pH) in the particle phase due to its lower reactivity. For instance, organic nitrate photolysis rates are at least a couple orders of magnitude faster than those for the nitrate ion (Suarez-Bertoa et al., 2012; Zafiriou and True, 1979; Galbavy et al., 2007). This production of the nitrate ion would effectively eliminate the possibility for further oxidation of organic nitrates and the release of NO$_x$. Thus, deposition of the nitrate ion would be the main pathway of α-pinene-derived nitrate removal from the atmosphere, and the relatively large organic nitrate yield from a monoterpene reported here (26 ± 7%), along with fast hydrolysis in the aerosol phase, likely makes organic nitrate production in coniferous forests an important sink for NO$_x$, limiting ozone production. The organic nitrate yield values, partition coefficients, and hydrolysis rate constants would then be important components needed to assess NO$_x$ sequestration and nitrogen deposition.

4. Conclusion

The organic nitrate yield from the OH radical initiated oxidation of α-pinene in the presence of nitric oxide (NO) was found to be 26 ± 7%. The concentration of organic nitrates present after interaction with particles was found to be highly dependent on relative humidity and seed aerosol acidity for both the gas and particle phase products. An increase in seed aerosol acidity also led to decreased observed organic nitrate yields at elevated RH, supporting previous observations that the hydrolysis mechanism is acid-catalyzed. The consumption of organic nitrates in the particle phase by hydrolysis perturbed the gas/particle partitioning of the system, allowing for increased partitioning from the gas phase into the particle phase, hydrolysis, and a decrease in both the determined gas and particle phase organic nitrate yields. Since this study observed a large yield of organic nitrate formation from α-pinene, and a sharp decrease in total organic nitrate yields with increasing RH, starting at low chamber RH, the partitioning of relatively soluble α,β-hydroxy-organic nitrates into the particle phase may be an important sink for gas phase NO$_x$ in forest environments, as the formation of the more stable alcohol and less reactive nitrate ion is expected to readily occur via hydrolysis.

References

Aschmann, S.M., Atkinson, R., Arey, J., 2002. Products of reaction of OH radicals with alpha-pinene. J. Geophys. Research-Atmospheres 107 (7). http://dx.doi.org/10.1029/2001jd001098.

Atkinson, R., Perry, R.A., Pitts, J.N., 1976. Rate constants for reactions of OH radical with NO$_2$ (M = AR) and N-2) and SO$_2$ (m = AR). J. Chem. Phys. 65, 306—310. http://dx.doi.org/10.1063/1.432770.

Atkinson, R., 1997. Atmospheric reactions of alkoxy and beta-hydroxyalkoxy radicals. Int. J. Chem. Kinet. 29, 99—111. http://dx.doi.org/10.1002/(sici)1097-4601(1997)29:2<99::aid-kin3>3.0.co;2-f.

Atkinson, R., Baulch, D.L., Cox, R.A., Crowley, J.N., Hampson, R.F., Hynes, R.G., Jenkin, M.E., Rossi, M.J., Troe, J., 2006. Evaluated kinetic and photochemical data for atmospheric chemistry: volume II — gas phase reactions of organic species. Atmos. Chem. Phys. 6, 3625—4055.

Bertram, A.K., Martin, S.T., Hanna, S.J., Smith, M.L., Bodsworth, A., Chen, Q., Kuwata, M., Liu, A., You, Y., Zorn, S.R., 2011. Predicting the relative humidities of liquid-liquid phase separation, efflorescence, and deliquescence of mixed particles of ammonium sulfate, organic material, and water using the organic-to-sulfate mass ratio of the particle and the oxygen-to-carbon elemental ratio of the organic component. Atmos. Chem. Phys. 11, 10995—11006. http://dx.doi.org/10.5194/acp-11-10995-2011.

Browne, E.C., Cohen, R.C., 2012. Effects of biogenic nitrate chemistry on the NO$_x$ lifetime in remote continental regions. Atmos. Chem. Phys. 12, 11917—11932. http://dx.doi.org/10.5194/acp-12-11917-2012.

Bruns, E.A., Perraud, V., Zelenyuk, A., Ezell, M.J., Johnson, S.N., Yu, Y., Imre, D., Finlayson-Pitts, B.J., Alexander, M.J., 2010. Comparison of FTIR and particle mass spectrometry for the measurement of particulate organic nitrates. Environ. Sci. Technol. 44, 10556—1061. http://dx.doi.org/10.1021/es9029864.

Carrington, R.A.G., 1960. The infrared spectra of some organic nitrates. Spectrochim. Acta 16, 1279—1293.

Capouet, M., Peeters, J., Noziere, B., Muller, J.F., 2004. Alpha-pinene oxidation by OH: simulations of laboratory experiments. Atmos. Chem. Phys. 4, 2285—2311.

Chen, X., Hulbert, D., Shepson, P.B., 1998. Measurement of the organic nitrate yield from OH reaction with isoprene. J. Geophys. Res. 103, 25563—25568. http://dx.doi.org/10.1029/98JD0148.

Cook, R.D., 1977. Detection of influential observation in linear-regression. Technometrics 19, 15—18. http://dx.doi.org/10.2307/1268249.

Darer, A.I., Cole-Filipiak, N.C., O'Connor, A.E., Elrod, M.J., 2011. Formation and stability of atmospherically relevant isoprene-derived organosulfates and organonitrates. Environ. Sci. Technol. 45, 1895—1902. http://dx.doi.org/10.1021/es103797z.

Day, D.A., Liu, S., Russell, L.M., Ziemann, P.J., 2010. Organonitrate group concentrations in submicron particles with high nitrate and organic fractions in coastal Southern California. Atmos. Environ. 44, 1970—1979. http://dx.doi.org/10.1016/j.atmosenv.2010.02.045.

Dekermenjian, M., Allen, D.T., Atkinson, R., Arey, J., 1999. FTIR analysis of aerosol formed in the photooxidation of naphthalene. Aerosol Sci. Technol. 30, 273—279. http://dx.doi.org/10.1080/027868299304624.

Galbavy, E.S., Anastasio, C., Lefer, B., Hall, S., 2007. Light penetration in the snowpack at Summit, Greenland: part 2 nitrate photolysis. Atmos. Environ. 41, 5091–5100. http://dx.doi.org/10.1016/j.atmosenv.2006.01.066.

Goldstein, A.H., Galbally, I.E., 2007. Known and unexplored organic constituents in the earth's atmosphere. Environ. Sci. Technol. 41, 1514–1521. http://dx.doi.org/10.1021/es072476p.

Guenther, A.B., Jiang, X., Heald, C.L., Sakulyanontvittaya, T., Duhl, T., Emmons, L.K., Wang, X., 2012. The model of emissions of gases and aerosols from nature version 2.1 (MEGAN2.1): an extended and updated framework for modeling biogenic emissions. Geosci. Model Dev. 5, 1471–1492. http://dx.doi.org/10.5194/gmd-5-1471-2012.

Hallquist, M., Wangberg, I., Ljungstrom, E., Barnes, I., Becker, K.H., 1999. Aerosol and product yields from NO3 radical-initiated oxidation of selected monoterpenes. Environ. Sci. Technol. 33, 553–559. http://dx.doi.org/10.1021/es980292s.

Henry, K.M., Lohaus, T., Donahue, N.M., 2012. Organic aerosol yields from alpha-pinene oxidation: bridging the gap between first-generation yields and aging chemistry. Environ. Sci. Technol. 46, 12347–12354. http://dx.doi.org/10.1021/es302060y.

Hoffmann, T., Odum, J.R., Bowman, F., Collins, D., Klockow, D., Flagan, R.C., Seinfeld, J.H., 1997. Formation of organic aerosols from the oxidation of biogenic hydrocarbons. J. Atmos. Chem. 26, 189–222. http://dx.doi.org/10.1023/a:1005734301837.

Hu, K.S., Darer, A.I., Elrod, M.J., 2011. Thermodynamics and kinetics of the hydrolysis of atmospherically relevant organonitrates and organosulfates. Atmos. Chem. Phys. 11, 8307–8320. http://dx.doi.org/10.5194/acp-11-8307-2011.

Jacob, D.J., 2000. Heterogeneous chemistry and tropospheric ozone. Atmos. Environ. 34, 2131–2159. http://dx.doi.org/10.1016/s1352-2310(99)00462-8.

Jaoui, M., Kamens, R.M., 2001. Mass balance of gaseous and particulate products analysis from alpha-pinene/NOₓ/air in the presence of natural sunlight. J. Geophys. Research-Atmospheres 106, 12541–12558. http://dx.doi.org/10.1029/2001jd900005.

Koutrakis, P., Wolfson, J.M., Spengler, J.D., 1988. An improved method for measuring aerosol strong acidity – results from a 9-Month study in St. Loius, Missouri and Kingston, Tennesee. Atmos. Environ. 22, 157–162. http://dx.doi.org/10.1016/0004-6981(88)90308-3.

Laurent, J.P., Allen, D.T., 2004. Size distributions of organic functional groups in ambient aerosol collected in Houston, Texas. Aerosol Sci. Technol. 38, 82–91. http://dx.doi.org/10.1080/02786820390229561.

Lee, A., Goldstein, A.H., Kroll, J.H., Ng, N.L., Varutbangkul, V., Flagan, R.C., Seinfeld, J.H., 2006. Gas-phase products and secondary aerosol yields from the photooxidation of 16 different terpenes. J. Geophys. Research-Atmospheres 111 (25). http://dx.doi.org/10.1029/2006jd007050.

Lee, L., Teng, A.P., Wennberg, P.O., Crounse, J.D., Cohen, R.C., 2014. On rates and mechanisms of OH and O-3 reactions with isoprene-derived hydroxy nitrates. J. Phys. Chem. A 118, 1622–1637. http://dx.doi.org/10.1021/jp4107603.

Liu, S., Shilling, J.E., Song, C., Hiranuma, N., Zaveri, R.A., Russell, L.M., 2012. Hydrolysis of organonitrate functional groups in aerosol particles. Aerosol Sci. Technol. 46, 1359–1369. http://dx.doi.org/10.1080/02786826.2012.716175.

Lockwood, A.L., Shepson, P.B., Fiddler, M.N., Alaghmand, M., 2010. Isoprene nitrates: preparation, separation, identification, yields, and atmospheric chemistry. Atmos. Chem. Phys. 10, 6169–6178.

Muller, B., Heal, M.R., 2002. Mass accommodation coefficients of phenol, 2-nitrophenol, and 3-methylphenol over the temperature range 278–298 K. J. Phys. Chem. A 106, 5120–5127. http://dx.doi.org/10.1021/jp013559+.

Murdachaew, G., Varner, M.E., Phillips, L.F., Finlayson-Pitts, B.J., Gerber, R.B., 2013. Nitrogen dioxide at the air-water interface: trapping, absorption, and solvation in the bulk and at the surface. Phys. Chem. Chem. Phys. 15, 204–212. http://dx.doi.org/10.1039/c2cp42810e.

Nakamura, T., Busfield, W.K., Jenkins, I.D., Rizzardo, E., Thang, S.H., Suyama, S., 2000. Thermal decomposition mechanisms of tert-alkyl peroxypivalates studied by the nitroxide radical trapping technique. J. Org. Chem. 65, 16–23. http://dx.doi.org/10.1021/jo990680s.

Ng, N.L., Kroll, J.H., Keywood, M.D., Bahreini, R., Varutbangkul, V., Flagan, R.C., Seinfeld, J.H., Lee, A., Goldstein, A.H., 2006. Contribution of first- versus second-generation products to secondary aerosols formed in the oxidation of biogenic hydrocarbons. Environ. Sci. Technol. 40, 2283–2297. http://dx.doi.org/10.1021/es052269u.

Nguyen, T.B., Laskin, J., Laskin, A., Nizkorodov, S.A., 2011. Nitrogen-containing organic compounds and oligomers in secondary organic aerosol formed by photooxidation of isoprene. Environ. Sci. Technol. 45, 6908–6918. http://dx.doi.org/10.1021/es201611n.

Nielsen, T., Egelov, A.H., Granby, K., Skov, H., 1995. Observations on particulate organic nitrates and unidentified components of NOᵧ. Atmos. Environ. 29, 1757–1769. http://dx.doi.org/10.1016/1352-2310(95)00098-j.

Nielsen, T., Platz, J., Granby, K., Hansen, A.B., Skov, H., Egelov, A.H., 1998. Particulate organic nitrates: sampling and night/day variation. Atmos. Environ. 32, 2601–2608. http://dx.doi.org/10.1016/s1352-2310(97)00483-4.

Noda, J., Hallquist, M., Langer, S., Ljungstrom, E., 2000. Products from the gas-phase reaction of some unsaturated alcohols with nitrate radicals. Phys. Chem. Chem. Phys. 2, 2555–2564. http://dx.doi.org/10.1039/b000251h.

Noziere, B., Barnes, I., Becker, K.H., 1999. Product study and mechanisms of the reactions of alpha-pinene and of pinonaldehyde with OH radicals. J. Geophys. Research-Atmospheres 104, 23645–23656. http://dx.doi.org/10.1029/1999jd900778.

Orlando, J.J., Tyndall, G.S., Wallington, T.J., 2003. The atmospheric chemistry of alkoxy radicals. Chem. Rev. 103, 4657–4689. http://dx.doi.org/10.1021/cr020527p.

Pankow, J.F., 1994. An absorption-model of gas-particle partitioning of organic-compounds in the atmosphere. Atmos. Environ. 28, 185–188. http://dx.doi.org/10.1016/1352-2310(94)90093-0.

Pankow, J.F., Asher, W.E., 2008. SIMPOL.1: a simple group contribution method for predicting vapor pressures and enthalpies of vaporization of multifunctional organic compounds. Atmos. Chem. Phys. 8, 2773–2796.

Paulot, F., Crounse, J.D., Kjaergaard, H.G., Kroll, J.H., Seinfeld, J.H., Wennberg, P.O., 2009. Isoprene photooxidation: new insights into the production of acids and organic nitrates. Atmos. Chem. Phys. 9, 1479–1501.

Paulot, F., Henze, D.K., Wennberg, P.O., 2012. Impact of the isoprene photochemical cascade on tropical ozone. Atmos. Chem. Phys. 12, 1307–1325. http://dx.doi.org/10.5194/acp-12-1307-2012.

Peeters, J., Vereecken, L., Fantechi, G., 2001. The detailed mechanism of the OH-initiated atmospheric oxidation of alpha-pinene: a theoretical study. Phys. Chem. Chem. Phys. 3, 5489–5504. http://dx.doi.org/10.1039/b106555f.

Perraud, V., Bruns, E.A., Ezell, M.J., Johnson, S.N., Yu, Y., Alexander, M.L., Zelenyuk, A., Imre, D., Chang, W.L., Dabdub, D., Pankow, J.F., Finlayson-Pitts, B.J., 2012. Nonequilibrium atmospheric secondary organic aerosol formation and growth. Proc. Natl. Acad. Sci. U S A 109, 2836–2841. http://dx.doi.org/10.1073/pnas.1119909109.

Roberts, J.M., 1990. The atmospheric chemistry of organic nitrates. Atmos. Environ. Part a-General Top. 24, 243–287. http://dx.doi.org/10.1016/0960-1686(90)90108-y.

Rollins, A.W., Smith, J.D., Wilson, K.R., Cohen, R.C., 2010. Real time in situ detection of organic nitrates in atmospheric aerosols. Environ. Sci. Technol. 44, 5540–5545. http://dx.doi.org/10.1021/es100926x.

Rollins, A.W., Pusede, S., Wooldridge, P., Min, K.E., Gentner, D.R., Goldstein, A.H., Liu, S., Day, D.A., Russell, L.M., Rubitschun, C.L., Surratt, J.D., Cohen, R.C., 2013. Gas/particle partitioning of total alkyl nitrates observed with TD-LIF in bakersfield. J. Geophys. Research-Atmospheres 118, 6651–6662. http://dx.doi.org/10.1002/jgrd.50522.

Smith, M.L., Bertram, A.K., Martin, S.T., 2012. Deliquescence, efflorescence, and phase miscibility of mixed particles of ammonium sulfate and isoprene-derived secondary organic material. Atmos. Chem. Phys. 12, 9613–9628. http://dx.doi.org/10.5194/acp-12-9613-2012.

Suarez-Bertoa, R., Picquet-Varrault, B., Tamas, W., Pangui, E., Doussin, J.F., 2012. Atmospheric fate of a series of carbonyl nitrates: photolysis frequencies and OH-oxidation rate constants. Environ. Sci. Technol. 46, 12502–12509. http://dx.doi.org/10.1021/es302613x.

Surratt, J.D., Gomez-Gonzalez, Y., Chan, A.W.H., Vermeylen, R., Shahgholi, M., Kleindienst, T.E., Edney, E.O., Offenberg, J.H., Lewandowski, M., Jaoui, M., Maenhaut, W., Claeys, M., Flagan, R.C., Seinfeld, J.H., 2008. Organosulfate formation in biogenic secondary organic aerosol. J. Phys. Chem. A 112, 8345–8378. http://dx.doi.org/10.1021/jp802310p.

Tuazon, E.C., Atkinson, R., Macleod, H., Biermann, H.W., Winer, A.M., Carter, W.P.L., Pitts, J.N., 1984. YIELDS of glyoxal and methylglyoxal from the NOₓ-air photo-oxidations of toluene and M-xylene and p-xylene. Environ. Sci. Technol. 18, 981–984. http://dx.doi.org/10.1021/es00130a017.

Veselovskii, I.A., Cha, H.K., Kim, D.H., Choi, S.C., Lee, J.M., 2000. Raman lidar for the study of liquid water and water vapor in the troposphere. Appl. Phys. B-Lasers Opt. 71, 113–117.

Wexler, A.S., Clegg, S.L., 2002. Atmospheric aerosol models for systems including the ions H+, NH4+, Na+, SO42-, NO3-,Cl-, Br-, and H₂O. J. Geophys. Research-Atmospheres 107 (14). http://dx.doi.org/10.1029/2001jd000451.

Worton, D.R., Mills, G.P., Oram, D.E., Sturges, W.T., 2008. Gas chromatography negative ion chemical ionization mass spectrometry: application to the detection of alkyl nitrates and halocarbons in the atmosphere. J. Chromatogr. A 1201, 112–119. http://dx.doi.org/10.1016/j.chroma.2008.06.019.

Zafiriou, O.C., True, M.B., 1979. NITRATE photolysis in seawater by sunlight. Mar. Chem. 8, 33–42. http://dx.doi.org/10.1016/0304-4203(79)90030-6.